Department Biologie II

Humanbiologie und Bioimaging

Ludwig-Maximilians-Universität München

Analysis of the Barr body with super-resolution microscopy

Implications for a structural role of Xist RNA in mammalian X chromosome inactivation

Daniel Smeets

Dissertation der Fakultät für Biologie

der Ludwig-Maximilians-Universität München

Eingereicht am 16. Juli 2013

Analysis of the Barr body with super-resolution microscopy

Dissertation der Fakultät für Biologie
der Ludwig-Maximilians-Universität München

vorgelegt von:
Dipl. Biol. Daniel Smeets
aus Koblenz

Gutachter:
Prof. Dr. Heinrich Leonhardt
Prof. Dr. Thomas Cremer

Eingereicht am: 16. Juli 2013
Tag der mündlichen Prüfung: 22. November 2013

Wo kämen wir hin, wenn alle sagten, wo kämen wir hin, und niemand ginge,
um einmal zu schauen, wohin man käme, wenn man ginge?

Kurt Marti
Schweizer Schriftsteller

Table of contents

List of figures

List of tables

1 Summary

X chromosome inactivation (XCI) in female mammalian cells is an ideal model system to study the relationship of epigenetic regulation and higher-order chromatin structure. However, light microscopic studies of chromosomal organization have long been limited by the diffraction barrier of optical resolution. Super-resolution 3D-structured illumination microscopy (3D-SIM) – one of several recent techniques that circumvent this limitation – enables multicolor optical sectioning of entire cells with eightfold-improved volumetric resolution compared to conventional fluorescence imaging methods. In the present work, 3D-SIM has been applied to analyze higher-order chromatin structure of the Barr body in mammalian nuclei, a characteristic hallmark of XCI, with yet unprecedented detail.

First, the increased resolution prompted to reappraise the potential detrimental effect of the DNA-FISH procedure on chromatin structure. Comparative analyses revealed slight deteriorations at the resolution level of 3D-SIM, especially within more decondensed euchromatin sites within the nuclear interior. In contrast, overall nuclear morphology and the nuclear envelope as well as heterochromatic sites in general maintained well preserved. The results suggest that DNA-FISH studies can benefit from a combination with super-resolution microscopy. In particular, when keeping in mind the current developments of the FISH technique with increasingly small and higher-complexity probes.

The compact shape of the Barr body led to the assumption of a contribution of this special higher-order chromatin structure to the establishment and maintenance of the silenced state in the inactive X chromosome (Xi). However, a confirmation of this view has always been hampered by the restrictions of conventional light microscopy. In this work, the 3D chromosomal organization of the Xi and autosomes has been investigated with 3D-SIM in various human and mouse somatic cells and in mouse embryonic stem cell (ESC) lines. The precise subchromosomal localization of a variety of factors involved in XCI in different developmental states was qualitatively and quantitatively assessed utilizing combined immunofluorescence, EdU- pulse and RNA-/DNA-FISH labeling protocols and novel data analysis tools customized for the special requirements of 3D-SIM. The results demonstrate that all autosomes are made of a three-dimensional interconnected network of chromatin domains (CDs, or topology associated domains, TADs) of highly-variable shape and dynamics. CDs/TADs are comprised of a compacted chromatin core enriched with repressive marks, which is collectively proposed to be the functionally passive chromatin compartment (PNC). This PNC is surrounded by a 50 – 150 nm locally defined, less compacted perichromatin region (PR) that is enriched with active histone modifications and pervaded by a three-dimensional interchromatin (IC) network. The PR and the IC are collectively referred to as being the functionally relevant active nuclear compartment (ANC) that harbors all major nuclear processes, including transcription and replication. 3D-SIM data

revealed that the Barr body maintains this principle compartmentalization and that it is still pervaded by a narrow ANC network, which is able to fulfill its functional role as a hub for replication or rarely occurring expression of XCI-escape genes. Live-cell super-resolution imaging on HeLa H2B-GFP cells confirmed that the observed chromatin features do not reflect fixation artifacts.

Xist RNA, the key factor of XCI, has been found to be preferentially located as distinct discernible foci within the ANC throughout the entire volume of the Barr body. Here, it is tightly associated with a Xi-specific form of the nuclear matrix protein SAF-A, which confirms a previously suggested role for this Xi-enriched protein in Xist RNA spreading. In contrast, Xist RNA shows no spatial correlation with repressive Xi-enriched histone marks that are found within compacted chromatin sites. This specific localization of Xist RNA reflects an intrinsic feature as it is already present during early spreading in differentiating female ESCs, where it precedes chromatin compaction concomitant with RNA Polymerase II exclusion. Its localization is further confirmed in a male ESC line carrying an inducible Xist transgene on an autosome, but where Xist RNA fails to form a true autosomal Barr body, which is less compacted and maintains transcriptional activity. Last, Xist RNA shows no direct association with PRC2, the mediator of H3K27me3, which is in contrast to the generally believed direct recruitment model of PRC2 to the Xi by Xist RNA.

The data collected in this work reflects further support and a refinement of the not unequivocally accepted CT-IC (chromosome territory - interchromatin compartment) model of higher-order chromosome architecture. In addition, a first attempt has been made to integrate these findings with a recently growing number of studies using chromosome conformation capturing (3C)-based techniques and to complement them on the single-cell level.

Finally, a novel model for Xist RNA function in XCI is presented, which proposes a sequence-independent structural role for gene silencing and the formation of a repressive chromatin compartment.

2 Introduction

An overview about the current state of knowledge in the three main topics that were relevant for this thesis shall be given in the following. These are (I) epigenetic gene regulation, and in particular the influence of higher-order chromatin architecture in gene activity, (II) mammalian X chromosome inactivation (XCI), which has been used a model system for epigenetically repressed chromatin, and (III) super-resolution microscopy with a brief overview about its types and current developments and with a special emphasis on 3D-structured illumination microscopy (3D-SIM), which has been used as the main tool to analyze both.

2.1 Chromatin, nuclear architecture and gene regulation

The human body consists of over 200 different cell types, all of which fulfill unique functions that have to be skillfully orchestrated in space and time in the course of development as well as for daily maintenance. The many different cellular functions are achieved by the interplay of every cell's unique composition of up to 10,000s of different proteins encoded in the DNA sequence, which is packaged into chromatin and chromosomes within the nucleus. While all cells of an individual contain the identical genetic information of roughly 30,000 protein-coding genes, only a subset of these is active at the same time. Instead, every cell's individual gene expression is tightly regulated and largely controlled by epigenetic mechanisms (from the greek word "*epi*" for "*above*" or "*over*"), which act on different levels.

2.1.1 Chromatin and its modifications

In all eukaryotic cells, DNA is stored within the nucleus in a highly organized manner in the form of chromatin, which is collectively composed of DNA, RNA and proteins. 147 bp-long stretches of the naked double-helical DNA string are wrapped 1.75 times around an octamer of histones to form the nucleosomes, representing the lowest level of DNA compaction (Richmond and Davey, 2003; Watson and Crick, 1953). One histone octamer is built up of the four core histone proteins H2A, H2B, H3 and H4, which pair-wise interact to form the barrel-like histone particle (Luger et al., 1997). Individual nucleosomes are connected by linker DNA of variable length, typically between 10 and 80 bp, which can be observed in its most decondensed form as the typical "beads-on-a-string" conformation under the electron microscope (Olins and Olins, 1974). Association of the 10 nm "beads-on-a-string" fiber with H1 through the linker DNA leads to a further increase in compaction. For long, it has been proposed that this step causes the formation of a "30 nm chromatin fiber", which in turn was thought to be the basic building entity of all higher-order chromatin folding structures (Adkins et al., 2004; Tremethick, 2007). However, the presence of such a 30 nm fiber *in vivo* became more and

more doubted and their presence might actually not even be necessary to explain all higher-order chromatin conformations (Bian and Belmont, 2012; Fussner et al., 2011; Maeshima et al., 2010). Undisputedly, the highest degree of compaction that chromatin is able to acquire is the mitotic metaphase chromosome, which in mammals is about 10,000 – 20,000-fold more compacted than naked DNA, or in more physiological terms about 50-fold increased compared to interphase euchromatic regions (Belmont, 2006). How higher-order chromatin folding is organized on the level between the mitotic chromosome and the 10 nm fiber is still elusive until today and subject to speculation due to a lack of falsifiable *in vivo* experimental evidence. Still, chromatin is not compacted evenly throughout the interphase nucleus, with more compacted heterochromatin being preferentially localized at the nuclear periphery attached to the nuclear lamina or around nucleoli and decondensed euchromatin being preferentially located within the interior of the nucleus (Cremer et al., 2006; Gilchrist et al., 2004; Guelen et al., 2008).

The most basal level of epigenetic control is the direct modification of DNA bases. In vertebrates, the only nucleic base that can be subjected to modification is cytosine within a CpG dinucleotide, typically by covalently attaching a methyl-group, resulting in 5-Methylcytosine. Commonly, 5-Methylcytosine contributes to only around 1% of all nucleic bases of the genome, with mostly gene promoters within so called CpG-islands being susceptible for methylation, which in turn is linked to long-term transcriptional silencing (for reviews see Bird, 2002; Koh and Rao, 2013; Law and Jacobsen, 2010; Ooi et al., 2009). Recently, also other forms of DNA-modification have been discovered in mammals, including 5-Hydroxymethylcytosine, which has been proposed to be involved in de-methylation or in lineage-specific gene regulation, but its exact function still remains to be determined (Branco et al., 2012; Shen and Zhang, 2013; Szwagierczak et al., 2010).

Histones consist of a basic C-terminal part that mediates their interaction with DNA and a flexible N-terminal end of variable length that is capable to receive a wide range of post-translational modifications, which are important targets and players in epigenetic gene regulation. The interplay of these modifications is sometimes collectively referred to as “histone code”. Modifications include (amongst others) methylation, acetylation, phosphorylation and ubiquitination at various – though specific – amino acids of the histone tails. Again, specific modifications are mediated by specific modifying enzymes and recognized by specific readers. This network is highly interactive and interconnected and certain histone modifications, for example, are causing alterations in DNA-modifications, or vice versa. They may also act in another direction and cause local changes in chromatin compaction, which increases accessibility for transcription factors or the transcription machinery, again mediating activating chromatin modifications (Bannister and Kouzarides, 2011; Kouzarides, 2007). For instance, de-acetylation of histone 4 at lysine 16 (H4K16ac) causes a tighter binding of the histones to DNA, due to the loss of steric hindrance and the negatively charged acetyl-

group (Shogren-Knaak et al., 2006). This in turn leads to a locally higher chromatin condensation, which blocks the accessibility of underlying genes for the transcription machinery and thus collectively leads to transcriptional silencing. Important examples for transcriptionally active histone modifications, which are enriched in decondensed euchromatic sites, are the acetylation of histone 3 at lysine 16 (H3K16ac) and tri-methylation of histone 3 at lysine 4 (H3K4me3) or at lysine 36 (H3K36me3). Typical examples for transcriptionally silent histone modifications, enriched in compacted heterochromatin, are tri-methylation of histone 3 at lysine 9 or lysine 27 (H3K9me3, H3K27me3), as well as ubiquitination of H2AK119. The latter two are also typical markers for the facultative heterochromatin of the inactive X chromosome.

In addition to the canonical histone proteins, there are also a variety of histone variants, which can be incorporated in a cell type- or gene-specific manner into certain nucleosomes in order to regulate associated gene expression. A commonly known example is the incorporation of macroH2A into sites of repressed chromatin. The inactive X chromosome (Xi)-enriched macroH2A has been shown to be tightly bound to chromatin, with only a minor free fraction, and has been hypothesized to be involved in long-term gene silencing of the Xi and as a barrier against induced reprogramming (Gaspar-Maia et al., 2013; Pasque et al., 2011; Ratnakumar et al., 2012). H2A possesses also a variety of other variants including the H2A.Z family, of which one novel alternative splicing form, H2A.Z.2.2, has recently been discovered that has been shown to cause massive nucleosome instability and that has been hypothesized to be involved in primate-specific neuronal development (Bönisch et al., 2012).

2.1.2 Nuclear architecture

The role of higher-order chromatin arrangements in transcriptional gene regulation became widely recognized. Apart from being organized into eu- and heterochromatin according to their degree of compaction and enrichment of active or repressive chromatin markers, chromatin is further distributed in a non-random fashion within the interphase nucleus. Individual chromosomes occupy only a restricted volume, the so called chromosome territory (CT) (Cremer and Cremer, 2010). In cell types with round nuclei, like lymphocytes or ES cells, individual CTs occupy a gene density-dependent position, with gene-rich CTs being preferentially located within the interior and gene-poor CTs at the nuclear periphery (Bickmore and van Steensel, 2013; Küpper et al., 2007; Mayer et al., 2005). In cell types with flat nuclei, like fibroblasts, CT positioning is rather size-dependent, with bigger CTs being more peripheral (Bolzer et al., 2005). The same characteristic preferential behavior can be observed in sub-chromosomal domains, like single chromosome arms, which also appear as independent non-overlapping entities after fluorescence *in situ* hybridization (FISH) staining (Dietzel et al., 1998). Interestingly, the latter observation using FISH could recently be confirmed with chromosome

conformation capture (3C)-based techniques showing that the centromeres act as barriers that separate interactions of inactive chromatin between opposing chromosome arms (Kalhor et al., 2012; Sexton et al., 2012). Single gene loci have also been reported to be relocated after their transcriptional activation or silencing. In particular, some genes have been observed to move away from the peripheral heterochromatin after activation and, in agreement, some genes have been observed to move towards the facultative heterochromatin next to the nuclear lamina or around the nucleoli after induced transcriptional silencing (Hewitt et al., 2004; Kosak et al., 2002; Williams et al., 2006). Yet, other examples have been found, which claim the opposite cases or do not find any change in transcription status after forced tethering to the lamina, for instance (Finlan et al., 2008; Kumaran and Spector, 2008; Reddy et al., 2008; Williams et al., 2006). In fact, close inspection of the transcription status at the nuclear lamina found that this nuclear region is not a uniformly silenced chromatin environment and effects on transcription may be rather gene-specific than genome-wide, and especially the areas around the nuclear pore complexes may serve as small-scale transcriptionally active micro-domains (Arib and Akhtar, 2011; Capelson et al., 2010; Deniaud and Bickmore, 2009; Egecioglu and Brickner, 2011). Nevertheless, gene distributions reflect only their preferential localization. Chromatin compaction is highly dynamic and its degree is probably highly variable, thus sites of decondensed chromatin can readily be found at the nuclear periphery, and vice versa for heterochromatin in the nuclear interior. Consequently, repositioning effects of individual gene loci may occur on a much smaller scale as previously thought. There is a clear correlation between chromatin compaction and transcriptional activity. Yet, which one comes first and whether transcriptional activity causes chromatin decompaction or the other way round may probably never be ultimately answered and most likely it is a mutually active feedback rather than a strict cause-consequence relationship that connects these two mechanisms (Krijger and De Laat, 2013; Misteli, 2013).

According to the CT-IC (Interchromatin) model of chromatin organization, chromatin of all CTs is pervaded by DNA-free, 3D interconnected channel system of variable shape and dynamic behavior, which harbors all major nuclear processes and also large macromolecular complexes, like splicing speckles or PML bodies (Cremer and Cremer, 2010; Lanctôt et al., 2007). Based on electron microscopic studies since the 1970s and experiments using conventional light microscopy, it has been proposed that at the border zone between sites of compacted, inaccessible and transcriptionally repressed chromatin and the IC, small-scale decondensed chromatin loops can form and protrude within the IC space. This locally confined zone of 50 – 150 nm around compacted chromatin has been termed perichromatin region (PR) and has been suggested being the place where fundamental nuclear processes, like transcription and replication are taking place (Albiez et al., 2006; Fakan and Hancock, 1974; Markaki et al., 2010; Rouquette et al., 2010). Yet, the current CT-

IC model of chromatin architecture has not been commonly accepted, because of these methodological constraints, and novel super-resolution light microscopy developments as applied in the present work will certainly help to experimentally test its predictions.

Recent studies using 3C-based approaches revealed that chromatin is composed of functional domains within a size-range between ~ 200 kb – 1 Mb, which have been termed topology associated domains (TADs) (Dixon et al., 2012; Lieberman-Aiden et al., 2009; Nora et al., 2012) and became also known as chromatin domains (CDs) as identified in earlier studies using replication labeling and conventional light microscopy (Kireev et al., 2008; Sadoni et al., 2004). According to these modern high-throughput studies, individual TADs share, but do not rely on many chromatin features, like enrichment of specific histone modifications or gene density, and are conserved throughout different cell types and even different species. One of these studies, carried out in the X inactivation center (XIC), the genomic locus important for XCI, revealed that Xist and its antagonist Tsix are located within different TADs (Nora et al., 2012) (for detailed description about the role of Xist and Tsix see Section 2.2.4, p. 12). In general, this mechanism is intriguing as it offers an explanation how different chromatin environments may be maintained within close proximity, but at the same are able to form long-range *in cis* and *in trans* interactions (for recent reviews see Bickmore and van Steensel, 2013; Krijger and de Laat, 2013). Yet, studies generated with 3C-based approaches are reflecting population-wide averages of hundreds of thousands of cells. Thus, how CDs/TADs are spatially organized and dynamically behave on the single cell level still remains to be determined.

Part of the present work was to determine whether super-resolution microscopy could contribute to unravel the nature and spatial organization of individual TADs/CDs on the single cell level and to integrate the results from novel 3C-based approaches into a refined model view of higher-order nuclear architecture. To date, most data about nuclear architecture on the single cell level has been generated using FISH. Recent super-resolution imaging methods, in particular 3D-SIM (see Section 2.3.3, p. 23, and Section 3.3, p. 61) promise to contribute outstandingly to the understanding of proposed small-scale chromatin reorganization upon alteration of transcriptional activity or help unravel the role of the nuclear pore complex as an active microenvironment in the nuclear periphery. Yet, FISH requires a DNA denaturation step, preserving chromatin structure as seen with conventional microscopy, but possibly causing detrimental effects on a smaller scale, only visible with super-resolution imaging. Thus, the general applicability of FISH with studies at 3D-SIM resolution has been addressed here. Further, 3D-SIM has been used to analyze the spatial organization of essential nuclear processes, like replication and transcription, as well as the spatial architecture of repressed and active histone marks in the context of the CT-IC model.

2.2 X chromosome inactivation (XCI)

An extensively studied example of epigenetic gene regulation resulting in higher-order chromatin changes is XCI. As a consequence of Y chromosomal gene loss during mammalian evolution, the X chromosome faced a two-fold transcriptional up-regulation, which would result in a lethal gene dose in females if not counteracted. XCI is the evolutionary reaction in female mammalian cells that causes transcriptional down-regulation of the surplus X chromosome compared to male cells and ensures equal dosages of most X-linked genes in both sexes. In placental mammals, the choice whether the paternal or the maternal X chromosome gets inactivated occurs at a very early stage during embryogenesis independently in every cell and requires several cell divisions, but gets stably maintained and inherited to all subsequent daughter cells. The Xi differs substantially from its active counterpart (Xa) in terms of gene activity, chromatin compaction, composition of histone- and DNA-modifications, shape and nuclear positioning. However, all these differences are solely the result of different epigenetic modifications, as the underlying DNA-sequences are basically identical between the two X chromosomes.

2.2.1 Brief history of the Lyon hypothesis

In her famous hypothesis from 1961, Mary F. Lyon has been the first to propose the concept of random X chromosome inactivation as the mechanism of dosage compensation in female mammals, which has later been termed “Lyon hypothesis” and celebrated a widely recognized 50th anniversary in 2011 (Lyon, 1961). Mary Lyon could rely on earlier studies, mainly from the neuroanatomists Murray Barr and Ewart Bertram in 1949 who provided a first hint for a cytological difference between cells of male and female individuals of the same species (Barr and Bertram, 1949). They discovered a nuclear body that was present only in female and not in male neuronal cells in cats, which they termed “sex chromatin” and which was later named “Barr body” (see Figure 2-1). Their discovery fell in a time, where detailed chromosomal analyses for sex determination (e.g. in sports or intersex disorders) was still impossible and became soon a widely used diagnostics tool. Other important foundations for Lyon’s hypothesis has been the work of Susumu Ohno who identified the single condensed (“heteropyknotic”) Barr body present in female rat cells as actually being one single X chromosome (Ohno et al., 1959). Still, he left the question unaddressed whether the observed heteropyknotic X chromosome was of paternal or maternal origin. Additional analyses by various other scientists at that time carried out in human and mouse individuals with sex chromosome anomalies (e.g. XO Turner syndrome, or XXY Klinefelter syndrome) confirmed the expected difference in number of observable Barr bodies. These studies also clarified that XO individuals are viable, and even fertile in mice, thus showing that the presence of one X chromosome is absolutely sufficient for development in females. XXY individuals, showing a male phenotype but infertility, gave

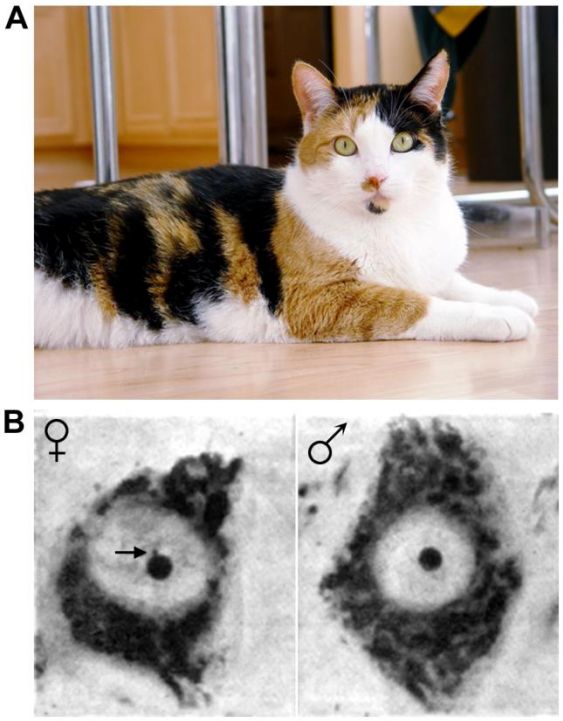

Figure 2-1 Female mammals are mosaics for their inactivated X chromosome. (A) So called calico cats are always females and display a patchy distribution of X-linked fur color genes. Paternal and maternal X chromosomes encode either black or red fur color. An independent gene encodes for patchiness (colored or white). Picture taken from http://en.wikipedia.org/wiki/Calico_cat. **(B)** First evidence for a cytological difference between cells of male and female individuals came from the discovery of the Barr body (black arrow), which is present only in female cells (here, cat neuronal cells stained with Cresyl violet) (Barr and Bertram, 1949).

the final prove that it is the Y chromosome that determines the male phenotype and not the presence of only one X chromosome (Polani et al., 1954; Welshons and Russell, 1959). A last piece of evidence came from studies in mice with sex linked mutations in fur color genes showing that females, which were heterozygous for these mutations, displayed a patchy distribution of mutant and wild-type fur color (Dickie, 1954; Lyon, 1960). This pointed towards a random inactivation of either the mutated or the wild-type carrying X chromosome during early timepoints in development independently in every cell. However, it was not before Mary Lyon who brought all the available pieces of evidence together to formulate her hypothesis "(1) that the heteropyknotic X chromosome can be either paternal or maternal in origin in different cells of the same animal; (2) that it is genetically inactivated" (Lyon, 1961) (for further review on the history of XCI and Mary Lyon see Harper, 2011; Lee, 2011).

2.2.2 Evolution of XCI

Since Mary Lyon's hypothesis, a lot of progress has been made towards the understanding of this fundamental process. As mentioned above, XCI in *Eutheria* (placental mammals) has evolved as a consequence of the loss of most Y-linked genes during evolution, thus sex determination and dosage compensation are intimately linked. In the beginning, the Proto-XY sex chromosomes were identical in gene composition and did not face any dosage imbalances compared to all other autosome pairs. Sex determination occurred solely by environmental influences like breeding temperature, which is still the case today for some reptiles, like turtles or crocodiles and has probably been the case for all ancestors of modern fish, birds and reptiles, including dinosaurs (Crews, 2003; Miller et al., 2004).

At some point, one of the two Proto-XY chromosomes acquired a sex determining gene, i.e. *SRY* on the Y chromosome in mammals has been found to be the key regulator of testis development (Sinclair et al., 1990; Waters et al., 2007; Wilhelm and Koopman, 2006). This sex-linked acquisition led to the development of chromosomal, instead of environmental, sex determination. Obviously,

this mechanism has evolved several times independently, probably due to its advantages over environmental sex determination during times of global climate changes or other large-scale environmental changes. The result was the formation of two distinct Proto-X and Proto-Y chromosomes (or Proto-Z and Proto-W in birds and snakes), which were otherwise still identical and did not need any dosage compensation mechanisms compared to the autosomes. In birds, for example, the homogametic sex is the ZZ males, in contrast to the ZW females. Gradually, mutations and genes favoring only the heterogametic sex (XY males in mammals, ZW females in birds) accumulated around the sex determining region of the Proto-Y, steadily limiting the options for meiotic recombinations between the Proto-X and Y-chromosomes (or Z- and W chromosomes, respectively). This led to a rapid and still ongoing loss of Y-chromosomal genes along with an accumulation of X-chromosomal genes, resulting with more than 1,000 active X-linked and only around 100 Y-linked genes, of which only 78 are male-specific, in humans today (for review see Charlesworth, 1996; Gribnau and Grootegoed, 2012). Meiotic recombinations between the two chromosomes are only possible within the small pseudo-autosomal region, which can be traced back to its autosomal ancestors. Ultimately, the inability for meiotic recombination may lead to a complete loss of the Y-chromosome (Graves, 2006).

Heterogeneous development of the two sex chromosomes always results in a sudden imbalance of linked gene dosages. In mammals, the Y-chromosomal degradation resulted in a sudden imbalance between the single X chromosome and the diploid autosomes in male individuals. There was also an imbalance between the single X males and the double X females, which had to be compensated. In mammals, this resulted in the general two-fold up regulation of all X-linked genes to ensure equal dosages between the X and autosomes in males (Deng et al., 2011). However, it is still unclear which mechanism caused this large-scale up-regulation and maybe it is only true for dosage-sensitive genes instead of the entire X-chromosome (Pessia et al., 2012; for review see Schulz and Heard, 2013). In any case, in females one of the two X-chromosomes had to be concomitantly transcriptionally shut down to equalize X-linked gene dosages between males and females. Thus, chromosomal sex determination and dosage compensation are two tightly linked mechanisms, which have probably co-evolved (Payer and Lee, 2008).

In other species, dosage compensation has been achieved in various different manners. In the invertebrate *Drosophila melanogaster*, the females carry an XX and the males and XY karyotype, like mammals do. However, dosage compensation is achieved in males by a two-fold transcriptional up regulation of their X-linked genes, leaving transcription levels in females unchanged (Straub and Becker, 2007). In *Caenorhabditis elegans*, males carry an XO and hermaphrodites an XX karyotype. Unlike mammals, where females inactivate one entire X-chromosome, hermaphrodite *C. elegans* individuals down-regulate both X-chromosomes by half to ensure equal doses between sexes (Meyer

et al., 2004) (for detailed review about X chromosome dosage compensation see Payer and Lee, 2008).

2.2.3 XCI during development

XCI is a mechanism that is occurring at a very early stage of embryo development in mammals, as it has already been claimed in Lyon's hypothesis. At what stage and how exactly XCI is taking place can, however, be very different in different species. Most data about the XCI process has been generated in mice, whereas relatively little is known about XCI in humans. In *Monotremata*, the most ancestral mammalian lineage, it is still unclear if and to what degree dosage compensation is accomplished between the sex chromosomes and how sex determination is realized, but it may still be closely related to the mechanisms in birds, although *Monotremata* already share the XY system of therian mammals (marsupials and placental mammals) (Escamilla-Del-Arenal et al., 2011; Gruetzner et al., 2006; Wallis et al., 2007). Yet, a recent study revealed no sequence homology between the sex chromosomes of the monotreme platypus (*Ornithorhynchus anatinus*) and therian mammals, which argues for the emergence of therian XY chromosomes, including *SRY*, after the separation from the monotreme lineage about 165 million years ago (Veyrunes et al., 2008). In marsupials, XCI is imprinted, with always the paternal X (Xp) being silenced in all cells. This is unlike placental mammals, which demonstrate random inactivation of either paternal or maternal X chromosome (Xm) in every cell individually. While the complete randomness of XCI is a characteristic in most eutherian

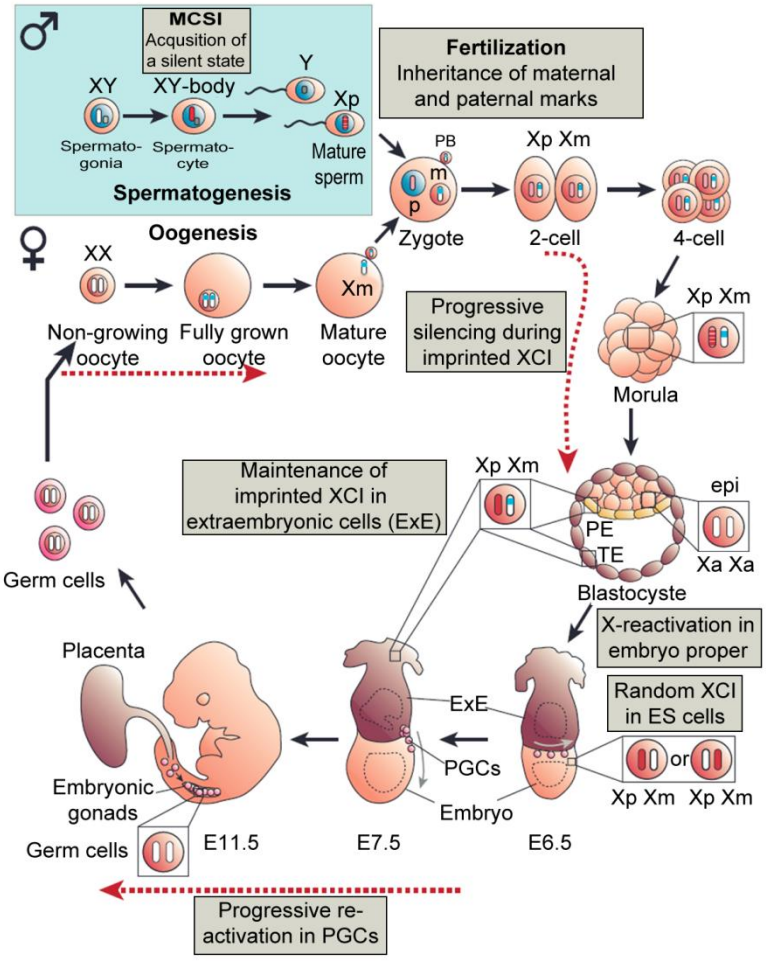

Figure 2-2 Life cycle of XCI in mice. This scheme illustrates the temporal order of XCI during embryogenesis in mice. It starts with meiotic sex chromatin inactivation (MSCI) during spermatogenesis resulting in a pre-inactivated Xp. Xp remains silent throughout development in all extraembryonic (ExE) tissues. Both X chromosomes get reactivated in the embryo proper at the Blastocyste stage, followed by random XCI, which is stably inherited henceforth. Only in primordial germ cells (PGCs), which later develop into mature oocytes, both X chromosomes get reactivated. For further details see main text. Figure adapted and modified from (Payer and Lee, 2008).

mammals, including humans and rabbits, a mixture of imprinted and random XCI seems to be additionally evolved in mice (Migeon, 2002; Moreira de Mello et al., 2010; Okamoto et al., 2011).

The XCI cycle in mice starts with the spermatogenesis in adult males, where the Xp gets pre-silenced by a process called meiotic sex chromosome inactivation (Greaves et al., 2006). After fertilization of the oocyte and generation of the zygote, the Xp remains partially silent until the formation of the morula (Okamoto et al., 2004). This pre-inactivation of the Xp has been proposed to be responsible for imprinted XCI in mice at these very early stages of embryogenesis (Huynh and Lee, 2003; for review see Payer and Lee, 2008). In the extra-embryonic lineages, i.e. the primitive endoderm and the trophoectoderm, the Xp remains silent throughout development (Takagi and Sasaki, 1975). Only in cells of the inner cell mass in the blastocyst that are going to develop into the embryo proper, both X chromosomes get re-activated again and subsequent random XCI is proceeding in every cell individually (Mak et al., 2004; Okamoto et al., 2004). Once the choice has been made, whether the Xp or the Xm gets silenced in a respective cell, it gets stably inherited to all subsequent daughter cells of the animal. Only in primordial germ cells, which later bring rise to the oocytes, the imprinting gets erased, both X chromosomes get re-activated again and another round of the XCI cycle is ready to begin (for review see Escamilla-Del-Arenal et al., 2011; Lee and Bartolomei, 2013; Schulz and Heard, 2013) (see also Figure 2-2).

2.2.4 Xist RNA and initiation of chromosome-wide silencing

In all placental mammals, the key initiator of XCI is the long non-coding (lnc) Xist RNA (*X inactive specific transcript*) that is exclusively expressed on the Xi and spreads *in cis* along the entire chromosome subsequently inducing gene silencing (Borsani et al., 1991; Brockdorff et al., 1991; Brown et al., 1991a). The region around the genomic Xist locus is called X inactivation center (XIC) and contains several other lncRNAs that are important for the regulation of Xist RNA (Brown et al., 1991b) (see Figure 2-3). LncRNAs are more and more recognized as a widely distributed mechanism for large-scale gene regulation and imprinting (both of which include XCI) in various species ranging from yeast to humans (for recent reviews see Brockdorff, 2013; Lee and Bartolomei, 2013). They usually act by recruiting gene silencing machineries, like Polycomb repressive complex 2 (PRC2) that subsequently mediate methylation of H3K27, to specific sites either *in cis* or *in trans*. Apart from Xist RNA in XCI, other lncRNA have recently been described fulfilling these roles, e.g. Kcnqt1ot1 silences a cluster of imprinted genes on mouse chromosome 7 or the lncRNA HOTAIR that is transcribed in the human HOXC locus on chromosome 12, but is recruiting PRC2 *in trans* to the human HOXD locus on chromosome 2 (Pandey et al., 2008; Rinn et al., 2007). In marsupials, there is no Xist RNA homologue and it has been unclear for decades how XCI is initiated in this mammalian lineage. Recently, a female-specific lncRNA called Rsx has been identified, which coats the marsupial Xi *in cis* and is able

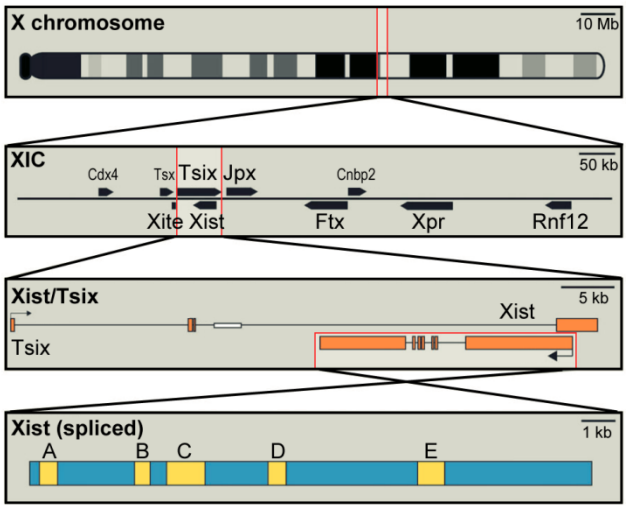

Figure 2-3 Location and composition of the mouse X inactivation center and the Xist gene locus. The XIC has been shown to be divided into two TADs, the Tsix and the Xist-TAD (Nora et al., 2012). Xite, Tsx and Tsix collectively inhibit Xist and are enhanced by pluripotency factors. Xist is inhibited by Tsix and pluripotency factors. Jpx and Ftx enhance Xist *in cis*, Xpr and Rnf12 enhance Xist *in trans*. The Xist transcript contains 5 repeat regions (yellow). The stem-loop containing RepeatA is essential to induce gene silencing and also contains an independent transcript, RepA, another enhancer of Xist expression. Repeats C – E have been shown to be collectively essential for Xist RNA localization, with Repeat C playing to the most important part. Figure modified after (Pontier and Gribnau, 2011).

to induce gene silencing, thus linking it functionally to the eutherian Xist RNA (Grant et al., 2012). In another recent study, a lncRNA with yet unknown function termed XACT has been discovered that is coating the Xa only in human – but not in mouse – embryonic stem cells (ESCs), thus suggesting a human-specific role for XCI initiation and further emphasizing the rapid evolution and variety of this kind of epigenetic regulation (Vallot et al., 2013).

In mice, Xist RNA is a 17 kb long (19 kb in humans) capped, spliced and polyadenylated transcript that circumvents nuclear export and is comprised of several repetitive units, called Repeats A – E. Any of these repeat regions has been predicted to form elaborate secondary structures, which are proposed to be the essential components for potential multimerization and recruitment of silencing machinery, rather than their actual sequence (Arthold et al., 2011; Duszczyk et al., 2011; Maenner et al., 2010). It has been suggested that different repeat regions function independently to ensure overall Xist RNA function. At the very 5' end, the Repeat A region has been proven to be the only component required for gene silencing, via direct or indirect PRC2 recruitment (Brockdorff, 2011; Wutz et al., 2002). Using protein nucleic acids (PNAs) or locked nucleic acids (LNAs) that disrupt Xist RNA binding *in vivo*, it has been demonstrated that it is mainly the Repeat C region that is important to mediate the localization of Xist RNA to the Xi (Beletskii et al., 2001; Sarma et al., 2010). Further, it has been discovered that the Repeat A region produces a 1.6 kb small transcript independently of Xist RNA, called RepA, that is probably able to interact with PRC2 as well via a 28-nt repetitive motif and recruit it to the Xi (Zhao et al., 2008). This interaction mediates H3K27me3 accumulation at the Xist promoter, which paradoxically leads to a Xist RNA up-regulation at the Xi and, in agreement, deletion of the Repeat A region has been shown to prevent the expression of Xist RNA (Sun et al., 2006). However, this is somewhat contradictory as PRC2 deletion embryos still demonstrate XCI and other studies provided evidence that PRC2 was still recruited to the Xi in Repeat A deletion models, just less efficiently (Kohlmaier et al., 2004; Schoeftner et al., 2006).

The major antagonist of Xist RNA is its reverse transcript Tsix, which negatively regulates Xist RNA expression and is transcribed on the (future) Xa before and during the onset of XCI (Lee and Lu, 1999; Lee et al., 1999). The inhibition effect is mainly displayed by transcriptional silencing of the Xist-locus through accumulation of a repressive chromatin conformation, mediated either by Dnmt3a recruitment followed by Xist-promoter methylation and/or disruption of RepA/PRC2 recruitment to the Xist promoter (Sado et al., 2006; Sun et al., 2006). Also, Xist/Tsix RNA duplex formation has been indicated to induce transcript degradation via the RNA interference pathway (Ogawa et al., 2008). In a recent study using chromosome conformation capturing, it could be shown that the genes for Xist and Tsix are located within different TADs, which may offer an intriguing explanation of how their opposing chromatin environments can be maintained in this close proximity (Nora et al., 2012).

In undifferentiated ESCs, prior to XCI, Xist activity is inhibited by the presence of the pluripotency factors Oct4, Sox2 and Nanog, which directly repress Xist expression (Donohoe et al., 2009; Navarro et al., 2008). Moreover, other pluripotency factors, like Rex1, Klf-4 and c-Myc inhibit Xist RNA expression by induction of Tsix expression either directly or by binding to Xite, an enhancer of Tsix (Navarro et al., 2010). This mechanism tightly links differentiation to XCI and ensures that the onset of XCI is inhibited in pluripotent undifferentiated ESCs. In addition, all inhibitory factors act synergistically as a threshold that has to be overcome in order to initiate XCI. Contrarily, there are also factors that activate Xist RNA expression, either *in cis* or *in trans*. Among these, one trans-acting factor that is located within the XIC, is the lncRNA Jpx, which has been proven to induce massive cell death upon heterozygous deletion in female cells due to an inability to up-regulate Xist RNA and XCI onset (Tian et al., 2010). A second long-range cis-acting activator of Xist RNA is the E3 ubiquitin ligase Rnf12, which has been demonstrated to induce Xist-spreading even in male cells upon over-expression. In contrast, female Rnf12$^{-/-}$ mutant cells failed to induce XCI. These observations indicate that Rnf12 acts in a dosage-dependent manner and only the double-dosage that is present in females (and mimicked by the over-expression in male cells) is sufficient for its Xist activating function (Barakat et al., 2011; Jonkers et al., 2009). Other Xist RNA activators are for example the lncRNA Ftx and the pairing element Xpr. Still, it is largely unknown how all of those Xist activators achieve their function. Regardless, it is already clear that they play a key role in the X chromosome counting process due to their dosage dependency and location on the X chromosome (Monkhorst et al., 2008; Monkhorst et al., 2009). All these regulation mechanisms are tightly controlled and it is crucial to ensure their proper timing during development and to find a mechanism to inactivate one, and only one, of the two X chromosomes. To start the XCI process during differentiation, there has to be some sort of introduced imbalance and control mechanism to start Xist expression on the future Xi and meanwhile maintain Tsix expression on the future Xa. It has been proposed that there is a transient pairing event between the two X chromosomes that initiates the XCI choice by transiently down-

regulating Tsix on the future Xi and probably involves the Xpr elements within the XIC (Augui et al., 2007; Bacher et al., 2006; Masui et al., 2011). However, how this pairing (which would involve large-scale chromatin rearrangements) is initiated, how the two XICs are able to find each other within the interphase nucleus and how the crosstalk between the two X chromosomes is mediated is until today still unclear. The possibility remains that XCI choice is controlled by a yet unknown trans-acting mechanism that would work independently of X chromosome pairing.

2.2.5 Xist RNA spreading, gene silencing and Barr body formation

Once the choice to inactive one of the two X chromosomes has been made, Xist RNA expression is highly up-regulated on the Xi and spreading along the entire chromosome *in cis* begins (Sun et al., 2006). Experiments with MS2-tagged transgenic Xist RNA in living ES cells illustrated that spreading is indeed a gradual process starting from the XIC ultimately leading to the coverage of the entire chromosome with a constant amount of Xist RNA (Ng et al., 2011). FRAP-experiments in the same system indicated that there is a constant transcription-dependent turnover of Xist RNA over the entire chromosome with stable on-off rate and a half-life time of 4 – 6 h, which has already been suggested in earlier studies using transcription-inhibiting Actinomycin D in fully differentiated somatic cells (Clemson et al., 1996). Earlier studies using qRT-PCR revealed a copy number of about 300 – 1,000 Xist RNA transcripts in mouse differentiated cells (Buzin et al., 1994; Sun et al., 2006). These findings indicate the necessity for constant Xist RNA expression for long-term maintenance of XCI even in fully differentiated cells and are in agreement with reports about partial loss of long-term silencing modifications upon conditional knock-out of Xist RNA in somatic cells (Csankovszki et al., 2001).

Xist RNA is able to spread also into autosomal chromatin in X:autosome translocations or introduced as an ectopic transgene and is able to induce autosomal gene silencing, though less efficiently than on the X chromosome (Lee and Jaenisch, 1997; White et al., 1998). This observation gave rise to the speculation that some X chromosomal sequence-specific properties may facilitate Xist RNA spreading and possibly act as waystations for chromosome-wide transcriptional repression. Popular candidates have always been the repetitive LINE-1 elements and early discoveries that LINE-1 sequences are about two-fold enriched on the X chromosome compared to all other autosomes supported this view (Lyon, 1998; Lyon, 2003). Yet, the so called LINE-1 hypothesis remains controversy as some studies found support for this view, e.g. showing in a comparative study that transgenic Xist RNA expression on three different autosomes was able to silence those autosomes more efficiently that contained a high proportion of LINE-1 sequences (Chow et al., 2010; Tang et al., 2010), whereas others found no correlation and discovered e.g. rodent species without any LINE-1 sequence homologues at all but normal XCI (Cantrell et al., 2009). Also, experiments on metaphase spreads showed that Xist RNA is

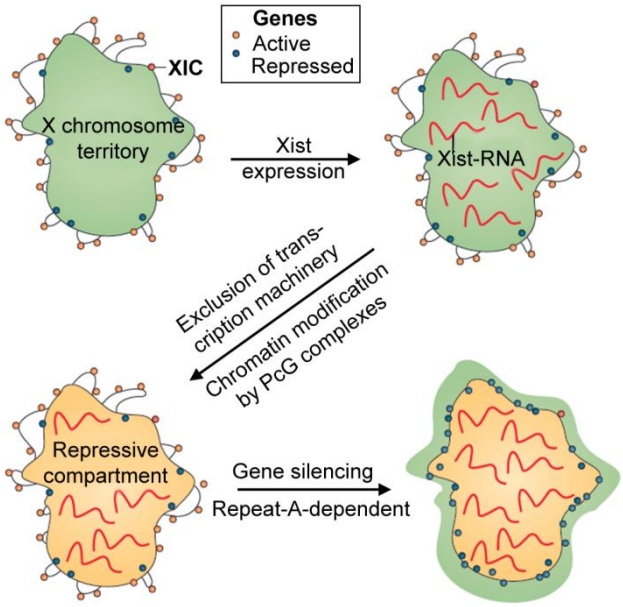

Figure 2-4 Current model view about the establishment of a Xist RNA induced silent compartment. Spreading of Xist RNA causes the establishment of a silenced nuclear compartment, characterized by exclusion of transcription machinery, depletion of active and enrichment of repressive chromatin marks. Potentially, accumulation of LINE-1 sequences supports this building of a repressive chromatin environment. It also leads to gene silencing by Repeat-A-dependent recruitment of PRC2 (whether directly or indirectly is not yet clear). Genes are located outside the silenced, inaccessible Xist RNA delineated chromatin block, irrespective their transcriptional activity. This prevailing view may, however, be a bit over-simplistic and has already been questioned in more recent studies. Figure adapted and modified after (Wutz, 2011).

mainly located within gene-rich, G- light bands and thus reciprocal to LINE-1 sequences, which are by nature gene-poor (Duthie et al., 1999). In this context, it has also been speculated that Xist RNA induces the formation of a repressive inner Barr body core containing mainly repetitive elements, including LINE-1, and an outer decondensed rim containing all X-linked genes irrespective of their transcriptional status (Chaumeil et al., 2006; Clemson et al., 2006). Yet, this view may be over-simplistic and more recent data raised doubts concerning this model by showing that X-linked genes can be found throughout the entire volume of the Barr body (Calabrese et al., 2012; Teller et al., 2011). Nevertheless, using EM data, the observation that the Xi forms a unique higher-order repressed chromatin structure pervaded by channels of decondesed chromatin reaching from its periphery argues in the same direction as the latter two studies (Rego et al., 2008). In summary, the formation of a repressed chromatin compartment, maybe with the help of LINE-1 and other repetitive elements, is one of the key features of Xist RNA function. This view of a potential structural role of Xist RNA has been supported by a study applying allele-specific 4C comparing the Xi and Xa, which revealed that the Xi forms a unique random folding structure that is dependent on the presence of Xist RNA, but is at least partially independent of transcription *per se* (Splinter et al., 2011). Whether this involves a direct interaction of Xist RNA with LINE-1 sequences or if they just act as large-scale building blocks for the formation of a repressive compartment remains debatable and it has been hypothesized that it may not be possible to settle this issue before higher resolution data becomes available (Arthold et al., 2011) (see also Figure 2-4).

Recently, it has been proposed by Jeannie Lee and coworkers that Xist RNA is tethered co-transcriptionally to a so called nucleation center within the XIC on the Xi via the bivalent adaptor protein YY1, which contains RNA- and DNA-binding motifs and has been proposed to interact with the Repeat C motif of Xist RNA (Jeon and Lee, 2011). This mechanism may explain the restriction of Xist RNA *in cis* to the chromosome where it is transcribed from. However, it leaves the question open

as to how spreading is mediated and where exactly Xist RNA is spreading to. Several studies hinted towards a role for the nuclear matrix scaffold protein SAF-A (also called hnRNP U) in Xist RNA attachment and spreading. SAF-A:GFP fusion proteins are enriched at the Xi in a Xist RNA dependent manner and specific knock-down of SAF-A led to a release of Xist RNA from the Xi (Hasegawa et al., 2010; Helbig and Fackelmayer, 2003; Pullirsch et al., 2010). Also, a functional link between Xist RNA and SATB1, a key component in the establishment of chromatin loops said to be essential for the establishment of a repressive chromatin environment, further supports the idea of an involvement of the nuclear matrix and a repressive higher-order chromatin structure in Xist RNA spreading (Agrelo et al., 2009). A role for SAF-A and the nuclear matrix in XCI is intriguing as it may provide a sequence-independent scaffold for Xist RNA propagation *in cis* after its initial tethering by YY1. One of the initial observations that Xist RNA maintains its territorial localization on the Xi even after excessive DNase treatment provides further evidence for this view (Clemson et al., 1996; for review see Hasegawa and Nakagawa, 2011; Tattermusch and Brockdorff, 2011).

The presence of Xist RNA leads to a cascade of silencing modifications on the Xi. One of the earliest visible effects is the removal of active RNA Polymerase II (RNAP II) from the Xi – whether in an active manner or passively by chromatin compaction is not yet known (Chaumeil et al., 2006; Clemson et al., 2006; Okamoto et al., 2004). This is followed by the Xist RNA dependent recruitment of PRC2, which in turn mediates the Xi-enriched histone modification H3K27me3 (Mak et al., 2002; Plath et al., 2003). This recruitment has always been considered to be a direct interaction between Xist RNA and PRC2, however, as has been pointed out in a recent review, there is still a commonly unrecognized possibility for an indirect recruitment mechanism involving yet unknown factors or mechanisms (Brockdorff, 2013). In line with this, it could have been shown that chromatin compaction is a general prerequisite for H3K27me3 accumulation, leading to speculations about PRC2 being recruited to the Xi subsequently to Xist RNA-induced chromatin compaction (Yuan et al., 2012). In differentiating mouse ESCs, ChIP experiments against H3K27me3 followed by high-throughput sequencing demonstrated that the first targets of transcriptional silencing are the promoters of actively transcribed genes, which concomitantly lose the active histone modification H3K4me3 (Marks et al., 2009). Next, H3K27me3 is known to recruit PRC1 to the Xi, which catalyzes the enrichment of H2AK119ub1 at the Xi during early differentiation (De Napoles et al., 2004; Fang et al., 2004). Other changes in histone modification composition include the accumulation of H3K9me3 and loss of the active mark H3K4ac (Heard et al., 2001; Jeppesen and Turner, 1993). Gene silencing occurs synergistically after the establishment of these histone modifications and the establishment of a repressive higher-order chromatin compartment. Another Xi-enriched marker is the histone variant macroH2A. Although its exact role in XCI is still unclear, and macroH2A knock-out mice are in fact viable and fertile, which indicates to its dispensability for XCI (Tanasijevic and Rasmussen, 2011).

Nonetheless, one study showed that it inhibits reprogramming to a pluripotent state in somatic mammalian:*Xenopus* oocyte fusions, thus linking it to long-term gene silencing (Pasque et al., 2011). Last, DNA-methylation is the absolutely essential modification for stable long-term gene inactivation. It has been shown that SmcHD1 acts synergistically with Dnmt1 to establish and maintain DNA methylation within the promoters of X-linked genes (Blewitt et al., 2008; Hellman and Chess, 2007) (for detailed reviews see Arthold et al., 2011; Hall and Lawrence, 2010; Jeon et al., 2012).

After the XCI process, a significant number of genes is able to escape gene silencing – at least partially. Studies in inter-species hybrid cells or mouse crosses found that in humans 15% of all X-linked genes are escapees, compared to only 3% in mice (Carrel and Willard, 2005; Yang et al., 2010). Expression of individual escape genes may vary significantly and genes are commonly considered escapees when their expression level on the Xi reaches 10% of that on the Xa. In humans, escape genes are mostly clustered, with most of them being located on the short X chromosome arm in a region that reflects highest homology to the Y chromosome. In contrast, mouse escape genes display no clustering hinting towards a regulation on the single gene level rather than on a higher-order chromatin organization level like in humans. Generally, escape genes contribute significantly to inter-sex polymorphisms. On the molecular level, lncRNAs as well as the chromatin insulator CTCF may be involved in the establishment of an active chromatin environment and protect escape genes from surrounding repressive chromatin marks (Filippova et al., 2005; Li and Carrel, 2008) (for review about escape genes see Berletch et al., 2011).

XCI is an intensely studied mechanism and a lot of progress has been made since its discovery by Mary Lyon over 50 years ago. Yet, crucial aspects are still unclear, which is mainly due to the RNA nature of Xist as the key regulator of XCI, which makes it difficult to analyze with most standard laboratory techniques. Also, the resolution of conventional light microscopy is not suited to answer important questions in this context. It is still not known, for example, if and to what extent Xist RNA multimerization is taking place and if there is a variation in Xist RNA concentration along the interphase Xi or if it is just distributed evenly throughout the Barr body. Further, PRC2 is commonly thought to be directly recruited by Xist RNA to the Xi, which has in fact never been unequivocally proven, though the possibility of an indirect recruitment is usually disregarded. Despite the claim of one recent study showing the necessity for YY1 for Xist RNA tethering, still the question of its propagation *in cis* remains unsolved. The same is true for the question of sequence specificity, e.g. for LINE-1, which has been proposed, but is still highly controversial. And last, the Xist RNA-induced formation of a repressive compacted compartment is a currently widely accepted model, but it completely neglects the fact that such a re-organization would involve large-scale chromosome-wide re-organization, which is not well in agreement with models of higher-order chromatin organization arguing for a restriction in such chromatin movements in interphase.

In the present work, these open questions have been addressed with the help of super-resolution 3D-SIM, which has the potential to circumvent some of the earlier restrictions due to limited resolution and now allows a re-appraisal of these open questions.

2.3 Super-resolution microscopy

For decades, fluorescence light microscopy has been one of the major tools to study higher-order chromatin organization as well as the XCI process. It offers the possibility to specifically visualize literally any protein or DNA-sequence of interest, either in fixed or in living cells. Further, multi-color labeling and axial sectioning bear the potential to analyze the spatial and temporal relationship of any given structure within its three-dimensional cellular context. Yet, the biggest drawback of light microscopy is its limited resolution, which is constrained to a distance of half the wavelength of the applied light as described by the so called Abbe limit (Abbe, 1873). In absolute terms, the closest resolvable distance between two adjacent objects can be as small as about 200 – 300 nm in lateral (x,y) and 500 – 800 nm in axial (z) direction. The Barr body and most biological structures are rather in the range of tens to a few hundred nanometers, and thus escape a closer inspection with light microscopy (see Figure 2-5).

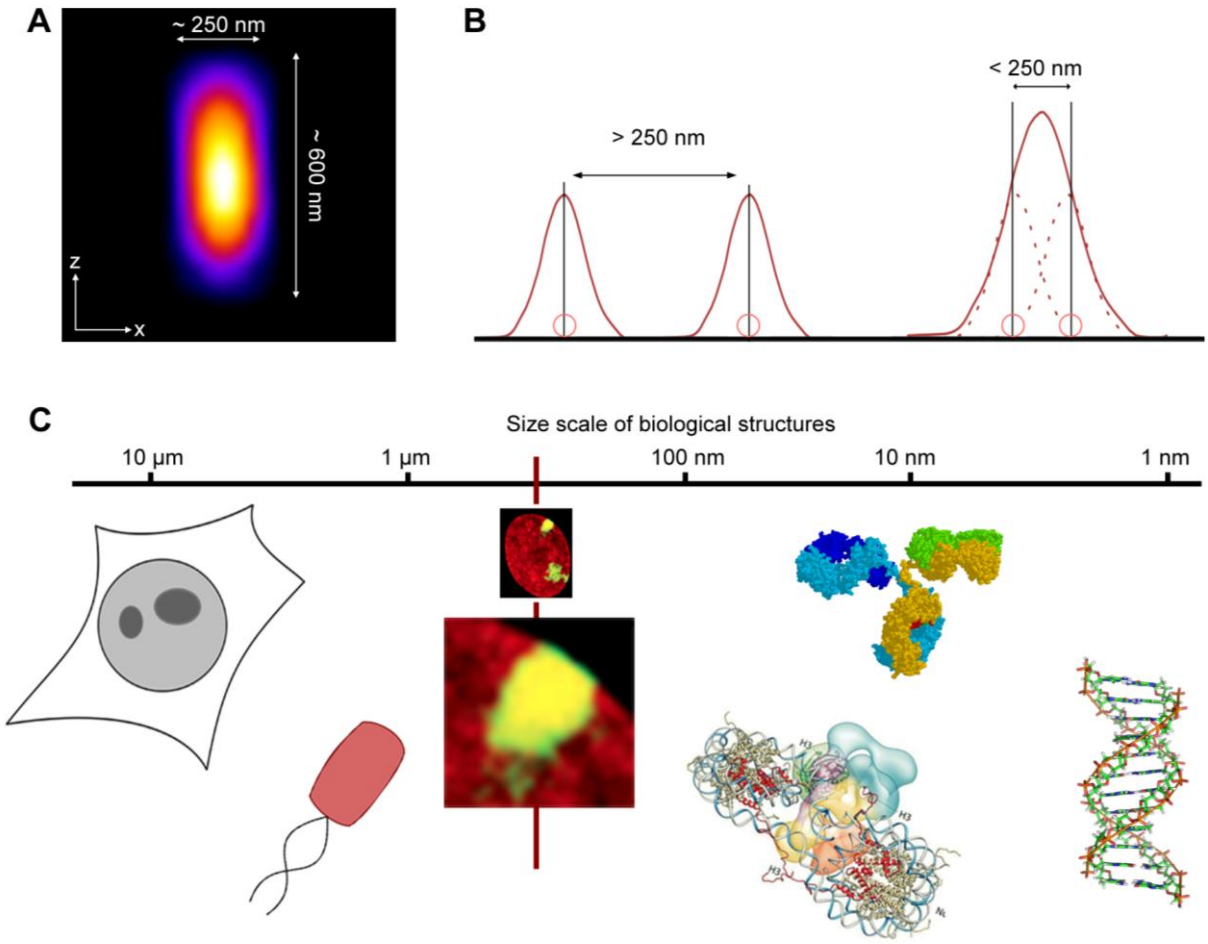

Figure 2-5 Most biological structures are below the level of resolution of light microscopy. (A) Depicted is the smallest volume that visible light can possibly be focused to using conventional microscopy. **(B)** Thus all objects that are smaller than this will always appear as having this diffraction-limited volume using a light microscope. Two sub-diffraction sized objects can be separated by light microscopy, when the distance between their intensity peaks is bigger than the diffraction limit (~ 250 nm). When the distance between the objects is smaller, their two diffraction limited signals merge and the two objects

will appear as one. **(C)** Size scale of various biological structures, ranging from an entire cell to bacteria, sub-cellular structures like the Barr body (image from Teller et al., 2011), protein complexes like PRC2 (image from Ciferri et al., 2012), single proteins like an IgH antibody (image from http://www.utc.fr/~friboule/images/anticorps/igg2a.gif) and the naked DNA fiber (image from http://commons.wikimedia.org/wiki/File:A-DNA,_B-DNA_and_Z-DNA.png). Red line indicates the limit of resolution of conventional light microscopy. Figure inspired by (Huang et al., 2010).

In the past decade, several new techniques have emerged that are able to circumvent this long-thought ultimate physical barrier, but that are still able to preserve the advantages of light microscopy at the same time. These techniques are collectively called super-resolution microscopy and include localization microscopy approaches (PALM/STORM and their derivates), stimulated emission depletion (STED) microscopy and SIM. In the following chapter a short overview over these revolutionary techniques shall be given (for detailed reviews see Huang et al., 2010; Schermelleh et al., 2010; Smeets et al., 2013a, *in press*).

2.3.1 Single molecule localization microscopy (PALM/STORM)

Photoactivated localization microscopy (PALM) or stochastic optical reconstruction microscopy (STORM) are – among many other derivates – the two most common examples of the single molecule localization techniques. These techniques try to separate the emission events of individual fluorophores within a sample, localize them one by one with high precision by, e.g. applying a Gaussian fit or simple centroid determination and generate a projection of these individual spot positions in order to achieve super-resolution information. In PALM/STORM, individual emission events are separated temporally, which means that only a small subset of all present fluorophores within the sample are emitting at any given acquisition timepoint. This allows to separately detect closely adjacent molecules that would otherwise be below the resolvable distance. By acquiring long time-lapse series, super-resolution images can be generated from the pointillistic projections of individual localization spots (Betzig et al., 2006; Hess et al., 2006; Rust et al., 2006) (see also Figure 2-6). The localization accuracy is typically in the range of 10 – 20 nm, but is in principle solely limited by the number of collected photons, whereas the structural resolution depends on the labeling density and typically reaches 50 nm in routine applications. PALM/STORM based techniques are capable of multi-color imaging and can be used with many standard dyes, but typically require non-standard fluorescent proteins, although for best performance photoswitchable or photoactivatable dyes with customized photochemical properties are required (Dempsey et al., 2011; Gunkel et al., 2009; Kaufmann et al., 2012). An even bigger disadvantage is, however, the lack of 3D information, which restricts PALM/STORM to studies of molecules and processes that are within 50 – 100 nm (using TIRF objectives) to the coverslips, e.g. cellular or nuclear membrane, adhesion molecules. By introducing various point spread function (PSF)-manipulating lenses or mirrors into the light path, e.g. creating an astigmatism, or in combination with confocal scanning methods, it has already been demonstrated that it is possible to circumvent this lack in z-depth to some extent (Huang et al., 2008a; Huang et al.,

2008b). Live-cell acquisitions are, by nature, also only possible in a very limited manner and restricted to both very flat (z-depth) and slow processes close to the coverslip, but have nonetheless been performed, e.g. in living bacteria or mammalian nuclei (Jones et al., 2011; Uphoff et al., 2013; Wombacher et al., 2010) (for reviews see Henriques et al., 2011; Herbert et al., 2012; Manley et al., 2011).

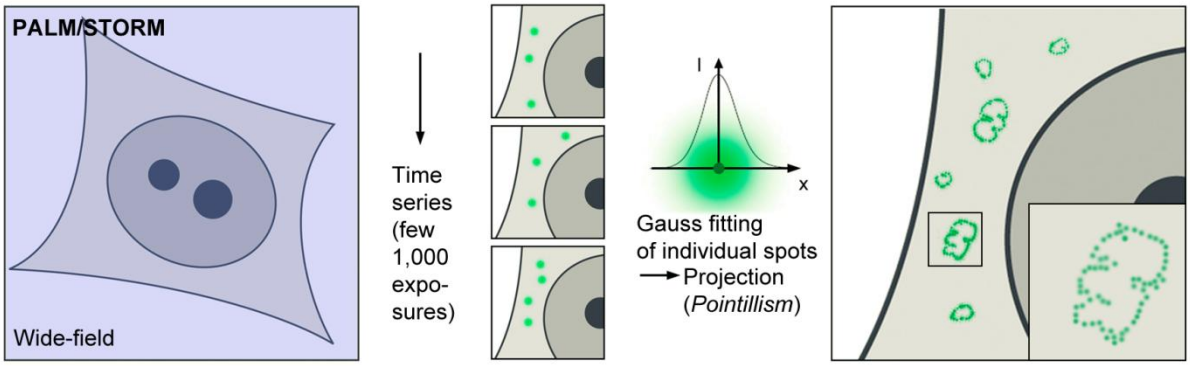

Figure 2-6 Schematic illustration of the single molecule localization microscopy principle. Fluorophores are not emitting all at once, but are temporarily separated from each other (by various means). Only a small fraction of fluorophores is emitting at any given timepoint. By acquiring long time-series, closely adjacent – otherwise unresolvable – single fluorophore molecules can be individually observed. The position of individual spots can be determined at high precision using Gaussian fitting and a pointillistic projection can be generated from these individual spot positions. The resolution is dependent on the labeling density, quantum yield and length of the time series. Figure adapted and modified after (Schermelleh et al., 2010).

2.3.2 Stimulated emission depletion (STED)

The size and shape of the PSF defines the resolvable volume of a microscope. STED actively reduces the diameter of the PSF laser cone by superimposing it with a second, donut-shaped depletion laser. The depletion laser de-excites all fluorophores into the non-fluorescent ground-state before they are able to emit any photons. This leaves only fluorophores right in the center of the donut-shape susceptible for emission, which effectively results in a re-shaped sub-diffraction sized PSF. A super-resolution image can be acquired by scanning the entire image area (analogous to confocal microscopy) with this manipulated PSF. By increasing the intensity of the depletion laser into saturation, the fraction of depleted fluorophores that are pushed back into ground-state in the periphery of the excitation beam tends to 100%. Thus, the diameter of the manipulated PSF, and in consequence the achievable resolution, is only dependent on the intensity of the depletion laser (Hell, 2007; Hell and Wichmann, 1994; Klar and Hell, 1999) (see also Figure 2-7). However, in reality other factors influence the level of achievable resolution as well. These are mainly the photostability and spectral properties of the applied fluorophores and mechanical stability or alignment precision of the two laser beams. In absolute terms, STED is able to reach a resolution down to about 6 nm under optimal conditions, e.g. in imaging extremely photostable diamonds (Rittweger et al., 2009). In

biological samples, a lateral resolution of about 20 nm could be achieved with experimental setups using inorganic dyes, while commercial setups typically achieve 50 – 70 nm. STED has already been demonstrated to work with a wide variety of standard fluorescence dyes and proteins (e.g. Moneron et al., 2010; Wildanger et al., 2009). Yet, multi-color imaging is only possible in a very limited fashion. Always two laser lines with widely separated emission wavelengths are necessary to image one fluorophore, which makes it very difficult to impossible to image more than two different fluorophores within the same sample (Kempf et al., 2013; Schmidt et al., 2008). Classical STED offers no increased axial resolution over conventional microscopy. Nonetheless, combining it with other setups, like for example two opposing objects (4Pi), STED imaging of entire mitochondoria has been demonstrated to achieve a resolution of 30 nm in all three spatial dimensions (isoSTED; Schmidt et al., 2009). Yet again, as already mentioned for localization super-resolution microscopy, an increased z-resolution for STED imaging has only been achieved by highly specialized labs and is still far from becoming an out-of-the-box tool for the standard researcher. In principle, live-cell applications are also possible using STED, but are limited by the acquisition speed, consisting of the scanning speed and the image area. Besides these restrictions, live-cell STED has already been performed, e.g. in imaging neural vesicle movements with about 60 nm resolution, but under the shortcoming of scanning only a relatively small image area (Moneron et al., 2010; Westphal et al., 2008) (for recent reviews see Huang et al., 2009, 2010; Lidke and Lidke, 2012; Schermelleh et al., 2010).

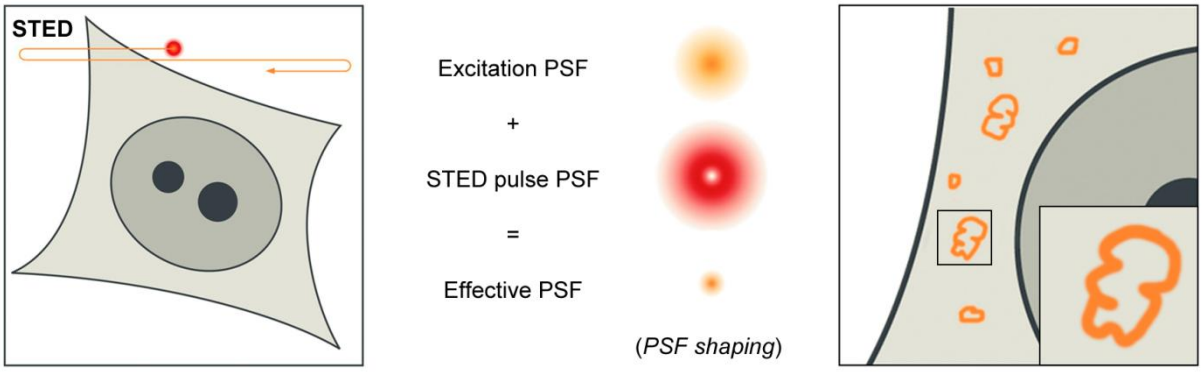

Figure 2-7 Schematic illustration of the STED principle. The diffraction limited excitation laser PSF gets superimposed with a second, donut-shaped depletion laser of very high intensity. The depletion laser pushes all underlying fluorophores into the non-fluorescent ground state, resulting in a sub-diffraction sized PSF. SR information can be obtained by scanning the entire image area with the modified sub-diffraction PSF. Figure adapted and modified after (Schermelleh et al., 2010).

2.3.3 Structured illumination microscopy (SIM)

Despite its moderate resolution improvement, 3D-SIM undisputedly offers a series of advantages compared to the other super-resolution techniques, like multicolor imaging using conventional dyes and fluorescent proteins, its 3D-sectioning capability of over 10 µm in depth and the possibility to acquire large fields of view with rapid speed, a prerequisite for live-cell super-resolution imaging. All

this makes it extremely useful in applications where large objects like entire mammalian nuclei shall be analyzed in the context of their spatial environment, as desired in this work. A detailed description of the basic principles of 3D-SIM, the system setup, sample preparation, acquisition and data evaluation can be found in Section 3.3 (p. 61).

2.4 Aim of this work

The goal of the present work was to analyze higher-order chromatin structure in mammalian nuclei, especially focusing on XCI as a model system for epigenetically silenced chromatin, using super-resolution 3D-SIM imaging. This required adaptation and optimization of immunofluorescence and RNA-/DNA-FISH protocols tailored for the special requirements of 3D-SIM. To quantify the resulting data, novel analyses tools have been developed, which e.g. allow comparing the degree of chromatin compaction between different nuclear volumes, different samples or different cell types by dividing the entire nucleus in an unbiased fashion into different chromatin density classes in 3D. This approach also allows quantifying the preferred localization of certain histone modifications or Xist RNA in respect to functional chromatin compartments. To analyze the degree of spatial correlation between different signals, a 3D-SIM adapted work-flow based on Pearson's and Manders' colocalization coefficients has been generated and applied. At a later stage, this work-flow has been expanded with the possibility to quantify mean distances between signals.

Are 3D-FISH studies generally suited for analyses with super-resolution 3D-SIM?

To analyze the impact of the DNA-FISH treatment and especially the heat denaturation step, on chromatin structure, several DAPI-stained C2C12 nuclei shall be imaged with 3D-SIM with their positions on the glass slide being stored. The cells are going to be unmounted, subjected to (mock-) 3D-FISH and imaged a second time. This will allow monitoring possible changes in chromatin preservation before and after FISH treatment without taking variations of individual cells into account. Using the chromatin density classification tool will allow the quantification of the results of many single-cell measurements. Combining this approach with an Immuno-staining against proteins of the nuclear envelope makes it possible to judge the degree of preservation of nuclear proteins and to assess the potential of 3D-FISH for super-resolution studies of nuclear architecture.

A novel role for Xist RNA in XCI?

First, several immunofluorescence (IF) and EdU replication labeling experiments are being performed to assess the spatial chromatin organization of the Barr. DNA-FISH using an X chromosome paint, as well as DAPI, are being used to visualize the Barr body at 3D-SIM resolution and to assess its architecture in the context of the CT-IC model. Live-cell super-resolution experiments in HeLa H2B-

GFP cells will serve as a control to exclude any possible artifacts due to formaldehyde-fixation or incomplete chromatin coverage of DAPI on the appearance of chromatin structure. RNA-FISH against Xist in human and mouse somatic cells allows quantifying its occurrence on the Xi and its location in respect to functional nuclear compartments and thus to draw conclusions about its role in XCI. RNA-Immuno-FISH against Xist RNA and SAF-A, or SAF-A:hrGFP, a nuclear matrix scaffold protein, will be performed in somatic cells to address and quantify their degree of spatial correlation and test the hypothesis of a role for SAF-A in Xist RNA propagation. Analyzing the localization of Xist RNA in respect to Xi-enriched repressive histone marks, H3K27me3 and macroH2A1, will provide further evidence about its position in respect to chromatin, which might allow functional implications.

XCI, and especially Xist RNA spreading, is a cellular process that occurs very early during embryo development, therefore experiments using XX ESCs or an inducible transgenic Xist RNA on an autosome in male ESCs shall be used to test whether the localization of Xist RNA in respect to chromatin is an intrinsic feature or whether it is not acquired before full differentiation.

Last, it shall be assessed whether Xist RNA shows spatial correlation with PRC2 at XCI initiation in an inducible Xist transgene ES cell line. A direct recruitment model of PRC2 by Xist RNA is commonly accepted although it has never been clearly verified.

3 Materials and Methods

3.1 Cell culture

All cell culture work has been performed under sterile conditions using a laminar flow cabinet to avoid possible contamination of cells. Cells have been incubated in a humified 37°C / 5% CO_2-incubator, somatic cells usually in p100 tissue culture dishes and ES cells usually in T25 tissue culture flasks. All used media, solutions and other substances have been prepared or kept under sterile conditions in freshly autoclaved glass bottles. Cells have been constantly kept under proliferating conditions and were split according to the recommendations in Table 3-1 before they reached full confluency and either seeded to a fresh tissue culture dish with fresh medium for further cultivation or seeded onto coverslips for fixation.

Table 3-1 Cell lines used in this work

Cell line	Cell type	Medium	Splitting ratio
3E ESC	Mouse male embryonic stem cells carrying a doxycyclin-inducible Xist-transgene on Autosome 17	ESC-medium (on Feeder cells)	Split 1:20 – 1:30 every 2nd day Change medium daily
C127	Mouse mammary gland carcinoma cells	DMEM + 10% FCS + Gentamycin	Split 1:10 – 1:12 every 2nd day
C2C12	Mouse myoblast cells	DMEM + 20% FCS + Gentamycin	Split 1:20 – 1:30 every 2nd day
Feeder cells	Mitomycin-treated MEF cells	ESC- or DMEM medium	- - -
HeLa H2B-GFP	Stably expressing H2B-GFP	DMEM + 10% FCS + Gentamycin	Split 1:8 – 1:10 every 2nd day
HeLa Kyoto	Human cervix carcinoma cells (immobilized)	DMEM + 10% FCS + Gentamycin	Split 1:8 – 1:10 every 2nd day
HFb	Human primary fibroblasts	DMEM + 10% FCS + Gentamycin	Split 1:3 – 1:5 every 2nd day

MEF	Mouse primary embryonic fibroblasts	DMEM + 10% FCS + Gentamycin	Split 1:3 – 1:5 every 2nd day
RPE-1	Human retina pigment epithelial cells	DMEM/Ham's F12 + 10% FCS + Gentamycin	Split 1:8 – 1:10 every 2nd day
tr36 ESC	Mouse male embryonic stem cells carrying a doxycyclin-inducible Xist-transgene on Autosome 11	N2B27 + 2i ESC-medium (for feeder-free conditions)	Split 1:20 – 1:30 every 2nd day Change medium daily
XX ESC (clone 16.7)	Mouse female embryonic stem cells	N2B27 + 2i ESC-medium (for feeder-free conditions)	Split 1:20 – 1:30 every 2nd day Change medium daily

3.1.1 Thawing cells

Material:

- Laminar flow cabinet
- CO_2 incubator
- 37°C water bath
- Cryo-vial from liquid N_2 tank containing desired cell line
- Cell culture medium (see Table 3-1 and 6-3)
- 15 ml Falcon tube
- Centrifuge
- p100 tissue dish
- Serological pipettes (2 ml / 5 ml / 10 ml)
- Pipette aid

Method:

- Take out the desired deep-frozen cryo-vial from the liquid N_2 tank
- Place the cryo-vial in a water bath at 37°C until the content becomes liquid
- Prepare a 15 ml falcon tube with 4 ml of the appropriate fresh cell culture medium
- Transfer the freshly thawed cells from the cryo-vial into the prepared falcon tube
- Centrifuge for 3 - 5 min. at 94 g
- Discard the supernatant containing the toxic DMSO
- Rock the falcon tube gently a few times to dissolve the cell pellet

- Resuspend the cells in 10 ml of fresh cell culture medium and transfer them to a new p100 culture dish
- Incubate cells at 37°C and under 5 % CO_2 atmosphere in a CO_2-incubator for further passaging

3.1.2 Passaging somatic cells

All volumes correspond to a standard p100 tissue culture dish.

Material:

- Laminar flow cabinet
- CO_2 incubator
- Cell culture medium (see Table 3-1 and 6-3)
- 1x PBS (cell culture grade)
- Trypsin/EDTA
- p100 tissue dish
- Serological pipettes (5 ml / 10 ml / 25 ml)
- Pipette aid
- Phase contrast microscope

Method:

- Aspirate and discard old medium from tissue dish containing the desired cell line
- Wash with 10 ml sterile 1x PBS
- Aspirate PBS and add 1 ml Trypsin/EDTA. Make sure to distribute it evenly over the entire dish.
- Aspirate Trypsin/EDTA briefly until there is just a thin layer of liquid left over the cells
- Incubate at 37°C in the CO_2-incubator for about 3 - 5 min.
- Prepare a fresh p100 dish with 10 ml (or less) of fresh cell culture medium in the meantime
- Rock the dish with the trypsinized cells gently with the palm of your hand until you see a film of detached cells running down the dish. Check proper detachment of the cells under the phase contrast microscope if necessary.
- Resuspend cells in an appropriate volume of fresh cell culture medium (depending on the desired dilution ratio. Minimum 6 ml)
- Transfer the desired ratio of cells into the new dish
- Incubate at 37°C and 5 % CO_2 in the CO_2-incubator until needed or before the cells become confluent

Notes:

- A p100 dish can collect a total volume of about 10 - 12 ml. The volumes used to resuspend the trypsinized cells and also the prepared fresh medium should be chosen accordingly to not over exceed the dish's capacity
- During the entire procedure cells should never be allowed to dry out
- Cell dishes, which accidently become over confluent should be replaced by freshly thawed aliquots

3.1.3 Cultivating embryonic stem cells

ESCs can be cultivated either on mitomycin-inhibited MEF feeder cells in ESC medium containing LIF or under feeder-free conditions on gelatinized flasks in N2B27 medium supplemented with LIF and the two kinase inhibitors (2i) CHIR99021, against GSK3β, and PD0325901, against MEK1/2.

XX ESCs and tr36 ESCs have been grown under feeder-free conditions and 3E ESCs have been grown on feeder cells (kindly provided by Brockdorff Lab, University of Oxford, UK). To induce transgenic Xist-expression, 2 µg/ml Doxycyclin has been added directly to the cell culture dish and once induced cells have been kept under Doxycyclin-induction constantly. For differentiation of XX ESCs, exactly 10,000 cells have been seeded per cm^2, LIF has been removed from the medium, and after one day of further cultivation, 2i has been removed as well and cells have been grown in MEF medium corresponding to somatic cells (see Section 3.1.2, p. 28).

ESC medium and N2B27 2i, and especially the supplement LIF, are very expensive and should thus be used carefully and only for the actual culturing (*not for, e.g. splitting, diluting, etc.*).

ESCs are typically cultivated in gelatinized T25 tissue culture flasks.

Feeder conditions:

Material:

- Laminar flow cabinet
- CO_2 incubator
- Mitomycin-treated MEF feeder cells
- Cell culture medium, MEF and ESC medium (see Table 3-1 and 6-3)
- 1x PBS (cell culture grade)
- Trypsin/EDTA
- T25 flasks
- Serological pipettes (5 ml / 10 ml / 25 ml)
- Pipette aid
- Phase contrast microscope

Method:

- Prepare feeder cells in a fresh T25 flask at about 60% confluency one day prior to ESCs seeding in MEF medium and incubate them at 37°C/ 5% CO_2
- Aspirate and discard old medium from tissue flask containing the ESCs
- Wash with 10 ml sterile 1x PBS
- Aspirate 1x PBS and add 1 ml Trypsin/EDTA. Make sure to distribute it evenly over the entire dish.
- Aspirate Trypsin/EDTA briefly until there is just a thin layer of liquid left over the cells
- Incubate at 37°C in the CO_2-incubator for about 3 - 5 min.
- Rock the dish with the trypsinized cells gently with the palm of your hand until you see a film of detached cells running down the dish. Check proper detachment of the cells under the phase contrast microscope if necessary.
- Resuspend trypsinized cells in 10 ml MEF medium and transfer to a 50 ml falcon tube
- Centrifuge for 5 min. at 94 g
- Discard supernatant and resuspend cells in 10 ml fresh MEF medium
- Aspirate old medium from feeder cell flask and add 7 ml ESC medium (containing LIF)
- Add 7 µl Doxycyclin (2 mg/ml) to the flask in order to start Xist-transgene expression if desired
- Split ESCs 1:20 – 1:30 as desired in new flask, containing feeders and incubate at 37°C/ 5% CO_2 until needed
- Change medium the next day

Feeder-free conditions:

Material:

- Laminar flow cabinet
- CO_2 incubator
- Gelatine solution (0.2%)
- Cell culture medium, MEF and N2B27 2i medium (see Table 3-1 and 6-3)
- 1x PBS (cell culture grade)
- Trypsin/EDTA
- Doxycyclin (2 mg/ml)
- T25 flasks
- Serological pipettes (5 ml / 10 ml / 25 ml)
- Pipette aid
- Phase contrast microscope

Method:

- Add 7 ml Gelatine solution (0.2%) to a new T25 flask and incubate under sterile conditions in the CO_2 incubator at 37°C for at least 30 min.
- Aspirate and discard old medium from tissue flask containing the ESCs
- Wash with 10 ml sterile 1x PBS
- Aspirate 1x PBS and add 1 ml Trypsin/EDTA. Make sure to distribute it evenly over the entire dish.
- Aspirate Trypsin/EDTA briefly until there is just a thin layer of liquid left over the cells
- Incubate at 37°C in the CO_2-incubator for about 3 - 5 min.
- Rock the dish with the trypsinized cells gently with the palm of your hand until you see a film of detached cells running down the dish. Check proper detachment of the cells under the phase contrast microscope if necessary.
- Resuspend trypsinized cells in 10 ml MEF medium and transfer to a 50 ml falcon tube
- Centrifuge for 5 min. at 94 g
- Discard supernatant and resuspend cells in 10 ml fresh MEF medium
- Aspirate gelatin solution from flask and add 7 ml N2B27 medium (containing LIF and 2i)
- Add 7 µl Doxycyclin (2 mg/ml) to the flask in order to start Xist-transgene expression if desired
- Split ESCs 1:20 – 1:30 as desired in new flask and incubate at 37°C/ 5% CO_2 until needed
- Change medium the next day

In order to differentiate XX ESCs, seed them at a density of 10,000 cells/ cm² in N2B27 containing 2i, without LIF for one day. After one day, change medium to MEF medium and cultivate them as somatic cells (see Section 3.1.2, p. 28).

3.1.4 Freezing cells

Material:

- Laminar flow cabinet
- Freezing medium
- 1x PBS (cell culture grade)
- Trypsin/EDTA
- Cell culture medium (see Table 3-1 and 6-3)
- 50 ml falcon tube
- 1.8 ml cryo-vial
- Serological pipettes (5 ml / 10 ml)
- Pipette aid
- Phase contrast microscope
- Isopropanol- / polystyrene box
- -80°C freezer
- Liquid N_2 tank

Method:

- Let cells grow to a density of about 80% in desired number of p100 cell culture dishes
- Prepare freezing medium and appropriate number of labeled cryo-vials (e.g. 2x 1.8 ml cryo-vials per p100 dish with ~ 80% confluency)
- Aspirate and discard old medium from tissue dish containing the desired cell line
- Wash with 10 ml sterile 1x PBS
- Aspirate 1x PBS and add 1 ml Trypsin/EDTA. Make sure to distribute it evenly over the entire dish.
- Aspirate Trypsin/EDTA briefly until there is just a thin layer of liquid left over the cells
- Incubate at 37°C in the CO_2-incubator for about 3 - 5 min.
- Rock the dish with the trypsinized cells gently with the palm of your hand until you see a film of detached cells running down the dish. Check proper detachment of the cells under the phase contrast microscope if necessary.
- Resuspend trypsinized cells in 10 ml cell culture medium and transfer to a 50 ml falcon tube
- Centrifuge for 5 min. at 94 g

- Discard supernatant and resuspend cells in 1 ml freezing medium (containing DMSO) per cryo-vial (i.e. 2 ml for one p100 dish)
- Transfer cells to cryo-vials
- Place the cryo-vials in an appropriate container (e.g. Isopropanol container, polystyrene box) in a -80°C freezer over night
- Transfer the cryo-vials into a liquid N_2 tank for long-term storage

3.1.5 Seeding cells on coverslips

Only borosilicate coverslips (#1.5) with a high-precision thickness of 0.170 mm ± 0.005 mm should be used to minimize intensity variations due to local thickness differences, which interferes with the structured illumination pattern during 3D-SIM acquisition. Prior to use, the coverslips should be thoroughly cleaned from dust by washing with dH_2O and storing them in 80% EtOH (abs.) at 4°C until use.

Material:

- Laminar flow cabinet
- CO_2 incubator
- 1x PBS (cell culture grade)
- Trypsin/EDTA
- Cell culture medium (see Table 3-1 and 6-3)
- 6-well plate
- Borosilicate coverslips of desired size (#1.5, high precision, 0.170 mm ± 0.005 mm)
- 80% EtOH (abs.)
- Serological pipettes (5 ml / 10 ml)
- Pipette aid
- Watchmaker forceps

Method:

- Let cells grow to a density of about 80% in a p100 cell culture dish
- Prepare a fresh 6-well plate under the laminar flow cabinet and dry one coverslip per well from the EtOH by placing them upright into the wells
- Aspirate and discard old medium from tissue dish containing the desired cell line
- Wash with 10 ml sterile 1x PBS
- Aspirate 1x PBS and add 1 ml Trypsin/EDTA. Make sure to distribute it evenly over the entire dish.

- Aspirate Trypsin/EDTA briefly until there is just a thin layer of liquid left over the cells
- Incubate at 37°C in the CO_2-incubator for about 3 - 5 min.
- Prepare 1-2 ml of fresh cell culture medium in each well
- Resuspend trypsinized cells in 10 ml fresh cell culture medium
- Transfer the desired ratio of cells into the 6-well plate (the surface area of one well of a 6-well plate is ~1/6 the area of a p100 dish. A factor 6 has to be multiplied to the desired splitting ratio)
- Allow the cells to attach over night at 37°C in the CO_2-incubator
- The cells are ready for fixation or further treatment the next morning

Notes:

- Do not flame the coverslip with a Bunsen burner as this may lead to a considerable deterioration of coverslip thickness
- In case of seeding ESCs, gelatinized coverslips should be used to assure proper cell attachment. Incubate the coverslips in 0.2% gelatine/1x PBS for at least 30 min at 37°C in the CO_2-incubator directly before use. Remove the gelatine solution just directly before adding fresh medium and do not let it dry out.
- ESCs should be seeded in the lowest possible density just one night before fixation, to keep the colony size as small as possible. Large colonies lead to more out-of-focus stray light, which seriously compromises the reconstruction quality
- Cells should be allowed enough time to attach properly to the coverslip surface. An incomplete attachment or highly variable distances between the coverslip surface and the actual specimen can cause intensity variations during the acquisition and/or create refractive index mismatches, which both cause lead to reconstruction artifacts and a considerable decreased resolution gain.
- Dying and stressed cells can increase unspecific antibody binding due to debris and other floating particles and may have an increased unspecific uptake of DNA-dyes (e.g. DAPI), which both compromises reconstruction and image quality. Healthy cells are therefore of great importance for successful super-resolution imaging.

3.2 Labeling cells for 3D-SIM super-resolution imaging

Unless otherwise stated, all protocols described in this work are optimized for 3D-SIM super-resolution microscopy. Microscopic imaging generally requires thorough and painstaking sample preparation to obtain clean and artifact-free image data. While this is already true for conventional light microscopy, it is even more so for the entire super-resolution 3D-SIM procedure (Bennett et al., 2009; Markaki et al., 2013).

The following aspects are of importance and need to be considered: **(1)** the structural preservation of the specimen during fixation, permeabilization, and labeling procedure. As 3D-SIM offers an 8-fold increased volumetric resolution over conventional microscopy, all applied labeling techniques should reflect the spatial context as close as possible to the state in the living cell and keep all perturbances to the morphology of the cells to a minimum (due to e.g. fixation, denaturation, mechanical forces). **(2)** The quality of the detection, given by the labeling specificity, labeling density, and signal-to-background ratio. **(3)** The choice of fluorophores in terms of brightness and photostability and **(4)** the optical properties and cleanness of the sample components and the immersion oil to avoid or counteract optical aberrations and refractive index mismatches (Smeets et al., 2013a, *in press*).

3.2.1 Immunofluorescence

Absolute cleanness of all applied solutions is of utmost importance and care should be taken to avoid any precipitates, e.g. of salts in washing buffers or in the formaldehyde solution. The applied fixative should provide a trade-off between fast fixation of the specimen and morphological preservation. For the optimal preservation of chromatin structure, judged by the DAPI staining, an initial 2% formaldehyde solution has proven to be the best choice. A higher formaldehyde concentration of 4% seemed to alternate chromatin structure and lead to an apparent greater condensation, which was also observable as bigger nuclear pores (data not shown). According to the author's experience, there has been no observable difference in preservation quality between freshly prepared para-formaldehyde and methanol-stabilized formaldehyde (stabilized with 10% methanol), and for the sake of handling speed the latter has been used throughout the present work. A quenching step (e.g. with 100 mM Glycine / 1x PBS) helps to saturate all remaining formaldehyde residues after fixation. Dehydrating fixatives like methanol-acetic acid or ethanol should be avoided as they considerably change the nuclear morphology. Some antibodies (e.g. Rat α PCNA [16D10]), however, rely on a methanol fixation step to gain access to their epitope. This issue can be circumvented by applying a first fixation step with formaldehyde and subsequently fixing with methanol-acetic acid. This step-wise fixation preserves the nuclear morphology and leads to sufficient epitope accessibility.

The outcome of the immunodetection procedure heavily depends on the quality of the applied antibody. Only antibodies with a high epitope affinity and specificity, as well as low cross-

reactivity should be chosen. For antibodies detecting chromatin modifications or other exclusively nuclear epitopes, a good rule-of-thumb to judge their specificity is to look at the amount of cytoplasmic or nucleolar signals. The respective antibody shows a relatively low affinity to its epitope and therefore produces a lot of unspecific background binding, if these regions are full of signals. This kind of background signals can be reduced by performing high-stringency washing steps after the antibody incubation or by applying a more stringent mix of blocking agents. The choice of the optimal blocking agents can vary between different antibodies and should therefore be tested beforehand. A mixture of BSA together with other proteins like fish skin gelatin or casein diluted in 1x PBST, which should always be prepared freshly and filtered through a syringe filter (pore size 0.45 µm), has turned out to be a widely applicable choice. Also commercially available blocking agents, like BlockAid (Invitrogen, Darmstadt) or MAXBlock (Active Motif, La Hulpe, Belgium) have proven to be highly effective, especially for antibodies against histone modifications, which have been mainly used in this work. The concentration of the applied antibody should be tested for every batch and may usually be chosen higher concentrated for 3D-SIM than for conventional imaging. However, the concentration should also not be too high as this has a disproportionally increasing effect on unspecific background signals as well and thus could be as harmful to the overall outcome as a too low concentration. If the amount of unspecific signals even outside of cells – directly on the coverslip – is relatively high, this points to a generally insufficient washing performance, which can be enhanced by washing in big volumes (e.g. 50 ml beakers) and changing the washing solution repeatedly for at least 9 rounds after each incubation step. Big fluorescent pieces of debris outside of cells can be avoided by filtering all antibody dilutions through a syringe filter (pore size 0.45 µm) directly before use, as antibodies tend to form aggregates when stored for a prolonged period or when repeatedly frozen and thawed. Moving or floating particles during acquisition make the extraction of super-resolution information impossible and cause local artifacts in the reconstruction outcome. Therefore, a post-fixation step with 4% formaldehyde should always be performed after the immuno-staining procedure. This covalently fixes all antibodies to their epitopes and further makes the stochastic antibody movement with their intrinsic on-off rates negligible.

3D-SIM, as well as other super-resolution techniques, poses high demands on the applied fluorophores in terms of intensity and photostability as it is imposes a significant higher energy load on the imaged sample than conventional microscopy. Bleaching has to be avoided in order to assure optimal super-resolution images as the reconstruction algorithm requires comparable signal intensities between the several angles and phases of the structured illumination acquisition. It has to be emphasized here that a good signal-to-background ratio is much more important than absolute signal intensity and that the former can be positively influenced by following a neat staining and washing procedure. Most modern organic dyes, e.g. from the Alexa- or ATTO-family, show a high

photostability and absolute brightness and thus are well suited for 3D-SIM imaging (Dempsey et al., 2011). On the other hand, fluorescent protein tags, like GFP and RFP etc., are very photosensitive and require a post-detection step, e.g. with labeled nanobodies – small antibody fragments derived from *Camelidae* (ChromoTek, Martinsried) (Romer et al., 2011). However, recent developments (e.g. implemented in the OMX V3 Blaze), which allow significantly higher sensitivity and faster acquisition speed (in the few millisecond range), made it possible to acquire GFP-tagged proteins even in living cells and have been successfully applied in this work to acquire super-resolution data on H2B-GFP in living HeLa cells. A list of fluorophores, which have been successfully applied for 3D-SIM imaging in the present work, is given in Table 3-2.

As a last step, any salt precipitates on the coverslips should be removed by a brief last washing step in ddH_2O. Final mounting of the sample should be performed with a non-hardening glycerol-based mounting medium containing anti-fade compounds (e.g. Vectashield), which provides the best optical properties and avoids refractive index mismatches between the mounting medium and the nucleus. A pre-incubation step in mounting medium, before the final mounting step on the glass slide in fresh mounting medium, has proven to be advantageous to remove any remaining H_2O, which could dilute the mounting medium.

Table 3-2 Fluorophores successfully applied for 3D-SIM imaging in this work

Excitation wavelength	Fluorophore
405 nm	DAPI, CF405M
488 nm	GFP (only for live-cell 3D-SIM Blaze), Alexa 488, ATTO 488
593 nm	Alexa 594

Material:

- 1x PBS (cell culture grade)
- 6-well plate
- Fixation buffer (2% formaldehyde/ 1x PBS)
- 1x PBST
- Quenching buffer (100 mM Glycine/ 1x PBST)
- Permeabilization buffer (0.5% Triton X-100/ 1x PBS)
- BlockAid or Blocking Buffer (4% BSA/ 0.5% FSG/ 1x PBST)
- High-stringency PBST
- Post-fixation buffer (4% formaldehyde/ 1x PBST)
- DAPI working solution (2.5 µg/ml DAPI in 1x PBST)
- Primary/ secondary antibodies
- ddH_2O
- Syringe filter (pore size 0.45 µm)
- 1.5 ml Reaction tube
- Coverslips mini-rack
- Watchmaker forceps
- Vacuum pump
- Humid chamber
- Soft wipes (e.g. Kimtech)
- Antifade mounting medium (e.g. Vectashield)
- Glass slide
- Nail polish

Method:

- Wash cells briefly 2x with 1x PBS (cell culture grade)
- Fixate with fixation buffer (2% formaldehyde/ 1x PBS) for 10 min. at room temperature (RT)
- Replace the fixation buffer stepwise with 1x PBST, without letting the cells dry out
- Saturate remaining formaldehyde residues with quenching buffer (100 mM glycine/ 1x PBST) for 10 min. at RT
- Wash 2x with 1x PBST
- Permeabilize cells with permeabilization buffer (0.5% Triton X-100/ 1x PBS) for 10 min. at RT
- Wash 2x with 1x PBST (*be careful not to let the cells dry when taking them out of the permeabilization buffer*)

- Incubate the cells in freshly prepared and ultrafiltrated (pore size 0.45 µm) blocking buffer (home-made or commercial) for 1 h at RT in a humid chamber
- Prepare primary antibodies in appropriate dilution in blocking buffer and preferably ultrafiltrate (pore size 0.45 µm) the solution directly before use (*Caution: you will lose about 300 – 400 µl in the filter*) or centrifuge the antibody dilution for 12 – 15 min. at ~15,000 g (maximum speed with a table-top centrifuge)
- Incubate cells in a drop (min. 30 µl for 18 x 18 mm coverslip; preferably 50 – 80 µl) of the antibody dilution for 1 h at RT in a humid chamber
- Remove all unbound antibodies by excessive washing with high-stringency 1x PBST and normal 1x PBST. Use large volumes of washing buffer (e.g. 50 ml glass beakers) and dip in the coverslips repeatedly with the help of the watchmaker forceps. To treat several coverslips at once and also minimize the risk of losing them, a coverslip mini-rack (e.g. Invitrogen) has proven to be very useful. As a first step wash 3x in high-stringency 1x PBST (contains extra 300 mM NaCl) and subsequently at least 6x with 1x PBST.
- Store coverslips in a fresh 6-well plate in 1x PBST in between washing steps

In case of two different primary antibodies, antibodies should be applied sequentially and not simultaneously to avoid possible cross-reactions (Bennett et al., 2009). For a second primary antibody, just start again at the primary incubation step here.

- Prepare secondary antibodies in appropriate dilutions (according to primary antibodies)
- Incubate cells in a drop of the secondary antibody dilution for 30 min. - 1 h at RT in a humid chamber in the dark
- Perform washing steps according to the primary antibodies
- Post-fixate the cells with 4% formaldehyde/ 1x PBST for 10 min. at RT in the dark
- Wash 2x with 1x PBST
- Counterstain DNA with DAPI (2.5 µg/ml in 1x PBST; *Caution: This concentration is about 20 times higher than in conventional protocols*) for 8-10 min. at RT in the dark
- Wash 6x with 1x PBST and 1x with ddH_2O to remove salt precipitates (*perform these steps quickly*)
- Pre-mount coverslips in a drop of non-hardening anti-fade mounting medium (e.g. Vectashield) on a flat piece of Parafilm and store in the dark
- Prepare and label appropriate number of glass slides for the final mounting step
  (*Rinse the glass slides with dH_2O briefly before use and let them air dry. Wear gloves to avoid finger prints on the glass slides*)

- Mount the coverslips in a fresh drop of mounting medium on the **back** of the glass slides (*This is to avoid a tilt of the entire slide and subsequently the imaged coverslip surface when mounting it on the OMX stage. This tilt is caused by a slight difference in thickness between the labeling area of the slide (frosting) and the transparent rest of the slide)*
- Remove all excess mounting medium with a soft-wipe tissue (e.g. KIMtech precision) by carefully and gently pressing (*Do not move the coverslip*)
- Seal the coverslip properly with nail polish

Notes:

- Always make sure to not let the cells dry out, especially after the fixation and permeabilization steps, as this will seriously compromise their morphology
- For ESCs, the permeabilization time can be increased up to 20 min. to ensure proper antibody accessibility
- Between every single washing step, all excess washing buffer should be removed from the coverslips by carefully tipping its edge on a soft-wipe tissue (e.g. KIMtech Science)
- All incubation steps (i.e. blocking, antibody incubation, DAPI-staining) can be performed on a Parafilm stretched out on a flat surface (e.g. the lid of a 6-well dish)
- Best blocking results (especially for antibodies against histone modifications) have been received with commercial blocking agents (e.g. BlockAid/ Invitrogen, MAXBlock/ Active Motif), but this should be tested for every antibody individually

3.2.2 RNA-FISH

Fluorescence *in situ* hybridization is a method to visualize specific genomic sites within fixed cells by applying complementary labeled DNA-probes against the sites of interest. RNA-FISH uses non-denaturing conditions, thus only single-stranded RNA-transcripts and not the respective genomic DNA-sites can be detected. In this work, RNA-FISH has been used to detect Xist RNA in both human and mouse morphology-preserved nuclei for super-resolution imaging. RNA-FISH can also be combined with an IF staining. It has to be kept in mind though, that formamide incubation, which is essential for RNA-FISH, has detrimental effects on epitope recognition capability of the antibodies (to which extent is dependent on the particular antibody). In some cases, it may be advantageous to perform the IF prior to the RNA-FISH, but this leads to longer exposure of the desired RNA-targets to RNase digestion and usually to a weaker signal - even with the help of RNase inhibitors. In this work, the IF-labeling has always been performed after the RNA-FISH procedure. This has been the best compromise for the antibodies applied in this work (the protocol has been adapted and modified from Chaumeil et al., 2008; Cremer et al., 2008; Markaki et al., 2013).

Generation and labeling of RNA-FISH probes (Nick-Translation)

Commercially available full-length human Xist cDNA (Origene) was used as a template for the initial random amplification using a whole genome amplification kit (GenomiPhi, GE Healthcare, Munich), according to manufacturer's instructions. Mouse Xist RNA probes were generated by PCR of exons 1a and 6 using specific primers (kindly provided by Irina Solovei, LMU Munich). Both approaches created sufficient amounts of probe DNA, which has been labeled with Biotin-dUTP using nick-translation.

Table 3-3 Nick-translation setup

Reagent	Volume	Final concentration
Xist cDNA	2 µg	40 ng/µl
10x NT buffer	5 µl	1x
β-Mercaptoethanol (100 mM)	5 µl	10 mM
dNTP-Mix	5 µl	50 µm dATP/dCTP/dGTP each 10 µm dTTP
Biotin-dUTP (1 mM)	5 µl	50 µM
ddH_2O	ad 48 µl	---
DNase I (8 U/ml)	1 µl	0.16 U/ml
DNA polymerase I (10,000 U/ml)	1 µl	200 U/ml

Material:

- 15°C water bath (in polystyrene box)
- Desired DNA in sufficient amount (i.e. minimum 2 µg)
- 10x NT buffer
- β-Mercaptoethanol (100 mM)
- dATP/dCTP/dGTP (0.5 mM each)
- dTTP (0.1 mM)
- Biotin-dUTP (1 mM)
- DNase I (2,000 U/ml)
- DNA polymerase I (10,000 U/ml)
- 1.5 ml reaction tubes
- Ice bucket
- EDTA (0.5 M)
- 1% Agarose gel
- Gelelectrophoresis chamber

Method:

- Prepare a water bath with exactly 15°C
- Dilute the DNase I stock solution (2,000 U/ml) with ice-cold ddH_2O 1:250 and keep on ice
- Mix the reagents from Table 3-3 in an 1.5 ml reaction tube on ice and mix well (do not vortex)
- Incubate in 15°C water bath for 90 min.
- Put the reaction on ice and check the length of the probes with a 1% Agarose gel and an appropriate standard ladder

Ideally, the probes should have a length between 300 – 800 bp. As too long probes increase unspecific background signals, they should be post-digested with 1 µl DNase I (diluted) for 15-30 min. at RT.

- The reaction can be stopped by adding 1 µl of 0.5 M EDTA to the reaction mix
- The labeled probes can be stored until use at -20°C

The described reaction yields a total volume of 50 µl with 40 ng/µl Biotin-labeled Xist-probe.

Cell fixation, hybridization and probe detection

Cell fixation:

Material:

- 1x PBS (cell culture grade)
- 6-well plate
- Fixation buffer (2% formaldehyde/ 1x PBS)
- 1x PBST
- 2x SSC
- 50% Formamide/2x SSC
- VRC (200 mM)
- Quenching buffer (100 mM Glycine/ 1x PBST)
- Permeabilization buffer (0.5% Triton X-100/ 1x PBS)
- Watchmaker forceps
- Vacuum pump
- Soft wipes (e.g. Kimtech)

Cells should be seeded as described in Section 3.1.5 (p. 33) about 18 h prior to fixation.

Method:

- Wash cells briefly 2x with 1x PBS (cell culture grade)
- Fixate with fixation buffer (2% formaldehyde/ 1x PBS) for 10 min. at RT
- Replace the fixation buffer stepwise with 1x PBST, without letting the cells dry out
- Saturate remaining formaldehyde residues with quenching buffer (100 mM glycine/ 1x PBST) for 10 min. at RT
- Wash 2x with 1x PBST
- Permeabilize cells with permeabilization buffer (0.5% Triton X-100/ 1x PBS) supplemented with 10 mM VRC to inhibit RNase activity for 10 min. at RT
- Wash 2x with 1x PBST (*be careful not to let the cells dry when taking them out of the permeabilization buffer*)
- Equilibrate to 2x SSC buffer
- Incubate cells in 50% formamide/ 2x SSC for at least 4 h at 4°C (*formamide evaporates at RT and is extremely toxic. Always work under the hood and keep the formamide cool)*

Probe preparation and hybridization:

Material:

- Formamide (100%, deionized)
- Biotin-labeled Xist-probes
- Salmon sperm DNA (5 mg/ml)
- Yeast t-RNA (20 mg/ml)
- C_0t-1 DNA (1 µg/µl)
- Ice-cold 100% EtOH (-20°C)
- 2x Hybridization buffer
- 1.5 ml Reaction tubes
- Watchmaker forceps
- Centrifuge
- -80°C freezer
- Ice bucket
- Thermal shaker (37°C)
- Heat block
- Water bath (37°C)
- Metal box
- Fixogum
- Soft wipes (e.g. Kimtech)
- Glass slide

For non-repetitive probes like Xist RNA, a final concentration of 20 ng/µl hybridization solution is recommended. For coverslips with an area of 18 x 18 mm a total volume of about 8 µl is required to cover all cells. For probes, which have been generated from genomic DNA, and not cDNA (in this work, human Xist-probes have been generated from cDNA, and mouse Xist has been generated from genomic DNA), an about 50-fold excess of C_0t-1 DNA has to be added to compete unspecific hybridizations. Salmon sperm DNA and yeast t-RNA are added to facilitate the precipitation of the probe DNA and to reduce background.

To save the expensive reagents and DNA-probes and in order to minimize the amount of hybridization solution per coverslip, it can be helpful to cut coverslips into smaller pieces with the help of a diamond pen (e.g. 15 x 15 mm out of 18 x 18 mm, #1.5, high precision), as high-precision coverslips are currently only commercially available with a minimum area of 18 x 18 mm.

Table 3-4 Hybridization solution setup per coverslip

Reagent	Volume	Final concentration in 8 µl hybridization solution
Biotin-labeled Xist-probe (~ 40 ng/µl)	4 µl	~ 20 ng/µl
Salmon sperm DNA (5 mg/ml)	0.2 µl	~ 100 ng/µl
Yeast t-RNA (20 mg/ml)	0.2 µl	~ 500 ng/µl
C_0t-1 DNA (1 µg/µl)	8 µl	1 µg/µl

Method:

- Mix the reagents listed in Table 3-4 (volumes are per coverslip) in an 1.5 ml reaction tube on ice
- Add 2.5x volume (i.e. 50 µl/ coverslip) of ice-cold 100% EtOH (stored at -20°C) and incubate for at least 1 h at -80°C
- Centrifuge for 30 min. at 15,000 g (maximum speed of a table-top centrifuge) at 4°C
- Discard supernatant and let the remaining EtOH evaporate in a vacuum centrifuge at 37°C for about 30 min. (*Caution: All remaining EtOH has to be evaporated before proceeding to the next step*)
- Resuspend the pellet in 4 µl formamide (100%, deionized) per coverslip in a thermal shaker at 37°C under mild shaking for 30 min.
- Denature the probes at 75°C for 7 min. on a heat block and put back on ice immediately
- Add 4 µl of 2x hybridization buffer per coverslip, mix well and store on ice until needed (*for long-term storage, hybridization solution can be stored at -20°C and has to be denatured again before use)*
- Prepare and label clean glass slides (one per hybridization) under the hood
- Place 8 µl of denatured hybridization solution on a slide
- Take cells out of the 50% formamide/ 2x SSC and remove as much of the formamide as possible by tipping the edge of the coverslip on a soft-wipe tissue in order to avoid unnecessary dilution of the hybridization solution (*work quickly, do not touch the cells and do not let the cells dry*)
- Mount the cells on the hybridization solution onto the slides and seal with fixogum
- Place the slides in a metal box and let it float in a 37°C water bath over night (~ 18 h) for hybridization

Probe detection:

All unbound probes should be removed as thoroughly as possible to minimize unspecific signals and washing steps and incubation steps should be carried out accordingly as described in Section 3.2.1 (p. 35).

Caution: Work under the hood during all steps where formamide is still present – especially with warm formamide!

Material:

- 50% formamide/ 2xSSC
- 2x SSC
- 4x SSCT
- 1x PBST
- BlockAid or Blocking Buffer (4% BSA/ 0.5% FSG/ 4x SSCT)
- Post-fixation buffer (4% formaldehyde/ 1x PBST)
- DAPI working solution (2.5 µg/ml DAPI in 1x PBST)
- Primary/ secondary antibodies
- ddH_2O
- Syringe filter (pore size 0.45 µm)
- Glass coplin jars (50 ml)
- Coverslips mini-rack
- Humid chamber
- 1.5 ml Reaction tubes
- 6-well plate
- Watchmaker forceps
- Water bath (42°C)
- Soft wipes (e.g. Kimtech)
- Glass slide
- Antifade mounting medium (e.g. Vectashield)
- Nail polish

Method:

- Pre-heat water bath to 42°C under the hood and place a sufficient amount of washing buffers inside (i.e. 150 – 200 ml are sufficient for three washing steps in one 50 ml coplin jar capable of taking up 8 coverslips – in a coverslips mini-rack)
- Gently peel of fixogum from slides by adding a big drop of 2x SSC on top of the coverslips and carefully pushing the coverslip to the side of the slide where it can be taken up without

pulling (*Do not apply mechanical force to the coverslips to avoid any morphological damage to the cells!*)

- Store coverslips in a coverslip mini-rack or 6-well plate in 2x SSC
- Wash 3 x 5 min. with 50% formamide/ 2x SSC at 42°C in the water bath under mild agitation
- Wash 3 x 5 min. with 2x SSC at 42°C in the water bath under mild agitation
- Transfer to 4x SSCT at RT and wash 3x 5 min. under mild agitation
- Incubate the cells in freshly prepared and ultrafiltrated (pore size 0.45 µm) 4x SSCT blocking buffer (home-made) for 1 h at RT in a humid chamber
- Prepare probe detection antibodies in appropriate dilution in blocking buffer (*Here: Streptavidin – Alexa 488 or Streptavidin – Alexa 594, both 1:*200) and ultrafiltrate (pore size 0.45 µm) the solution directly before use (*Caution: you will lose about 300 – 400 µl in the filter*)
- Incubate cells in a drop (min. 30 µl for 18 x 18 mm coverslip; preferably 50 – 80 µl) of the antibody dilution for 1 h at RT in a humid chamber
- Remove all unbound antibodies by washing at least 9x in large volumes of 4x SSCT (compare Section 3.2.1, p. 35)
- In case of several probes, detect the other probes in subsequent steps accordingly
- Switch to 1x PBST buffer

In case of a combined RNA-FISH/Immunofluorescence labeling, perform the IF (with primary and secondary antibody incubation) after the probe detection step, here.

- Post-fixate the cells with 4% formaldehyde/ 1x PBST for 10 min. at RT in the dark
- Wash 2x with 1x PBST
- Counterstain DNA with DAPI (2.5 µg/ml in 1x PBST; *Caution: This concentration is about 20 times higher than in conventional protocols*) for 8-10 min. at RT in the dark
- Wash 6x with 1x PBST and 1x with ddH_2O to remove salt precipitates (*perform these steps quickly*)
- Pre-mount coverslips in a drop of non-hardening anti-fade mounting medium (e.g. Vectashield) on a flat piece of Parafilm and store in the dark
- Prepare and label appropriate number of glass slides for the final mounting step (*Rinse the glass slides with dH_2O briefly before use and let them air dry. Wear gloves to avoid finger prints on the glass slides*)
- Mount the coverslips in a fresh drop of mounting medium on the **back** of the glass slides (*This is to avoid a tilt of the entire slide and subsequently the imaged coverslip surface when*

mounting it on the OMX stage. This tilt is caused by a slight difference in thickness between the labeling area of the slide (frosting) and the transparent rest of the slide)

- Remove all excess mounting medium with a soft-wipe tissue (e.g. KIMtech precision) by carefully and gently pressing (*Do not move the coverslip*)
- Seal the coverslip properly with nail polish

3.2.3 DNA-FISH

DNA-FISH is a widely used technique for visualizing specific DNA-sites of various size scales by using complementary fluorescently labeled DNA-sequences, which are able to hybridize to their desired target sites after denaturation. Here, DNA-FISH has been used to visualize entire X chromosome territories in human and mouse nuclei. The whole-chromosome probes, so called paints, were provided by the Cremer Lab and have been generated by flow-cytometry sorting of individual chromosomes and subsequent amplification and labeling using degenerated primers (DOP-PCR) (protocol has been adapted from Cremer et al., 2008; Markaki et al., 2013).

Labeling of whole chromosome DNA-FISH probes (DOP-PCR)

The flow-sorted chromosomes serving as the substrate for probe generation have been labeled and amplified using **D**egenerated **O**ligonucleotide **P**rimer – **P**olymerase **C**hain **R**eaction (**DOP-PCR**), which is a method to create a pool of heterogeneous and short DNA-fragments covering most of the target sequence (there is a certain degree of overrepresentation of repetitive over single-copy sites in the resulting probe pool, in fact) and which is the method of choice for small amounts of template-DNA (Telenius et al., 1992).

The first steps in a DOP-PCR are the primary and secondary amplification of the desired template DNA (without labeling) using degenerated 6MW-primers[1] (the detailed procedure is described in Cremer et al., 2008).

For subsequent labeling DOP-PCRs, a master-mix can be prepared (see Table 3-5), which contains all reagents apart from Taq-Polymerase and template DNA and which can be stored at -20°C for several years.

[1] 6MW-primer sequence: 5’ - CCG ACT CGA GNN NNN NAT GTG G - 3’

Table 3-5 Labeling DOP-PCR master-mix setup

Reagent	Volume	Final concentration
GeneAmp PCR buffer 10x	100 µl	50 mM KCl, 10 mM Tris, pH 8.3
$MgCl_2$ (25 mM)	80 µl	2 mM
6MW-primer (100 µM)	20 µl	2 µM
ACG-Mix (each 2 mM)	50 µl	100 µM each
dTTP (1 mM)	80 µl	80 µM
Biotin- (or DIG- or DNP-)dUTP (1 mM)	20 µl	20 µM
ddH_2O	620 µl	---

Material:

- Secondary DOP-PCR DNA (approx. 30 – 200 ng/µl)
- GeneAmp PCR buffer (10x)
- $MgCl_2$ (25 mM)
- dACG-Mix (2 mM each)
- dTTP (1 mM)
- Biotin-(or DIG- or DNP-)dUTP (1 mM)
- Taq-Polymerase (5 U/µl)
- DNase I (2,000 U/ml)
- NT-buffer (10x)
- 1.5 ml reaction tubes
- Ice bucket
- Thermocycler
- 1% Agarose gel
- Gelelectrophoresis chamber

Method:

- Mix master-mix reagents listed in Table 3-5 in a 1.5 ml reaction tube (sufficient for 20 amplification reactions á 50 µl)
- Mix 48 µl master-mix with 2 µl DNA (secondary DOP-PCR product, ~ 30 – 200 ng) and 0.5 µl Taq-Polymerase (5 U/µl) on ice
- Perform PCR in a thermocycler according to Table 3-6

Table 3-6 Labeling DOP-PCR conditions

Number of cycles	Reaction	Temperature	Time
1	Initial denaturation	94°C	3 min.
20 – 25	Denaturation	94°C	1 min.
	Annealing	56°C	1 min.
	Extension	72°C	0.5 min.
1	Final extension	72°C	5 min.

- Check length of labeled probes on a 1% agarose gel. Probes should show a smear between ~200 – 1500 bp
- If probes are too long incubate them for 20 min. at RT with the reagents as described in Table 3-7

Table 3-7 Label DOP-PCR post-digestion

Reagent	Volume
Label DOP-PCR DNA	50 µl
NT-buffer (10x)	10 µl
DNase I (1:1000 in ddH_2O)	10 µl
ddH_2O	30 µl

- Labeled probes can be stored at -20°C for several years or used directly

Cell fixation, hybridization and probe detection

Cell fixation:

Material:

- 1x PBS (cell culture grade)
- 6-well plate
- Fixation buffer (4% formaldehyde/ 1x PBS)
- 1x PBST
- 2x SSC
- 50% Formamide/2x SSC
- Quenching buffer (100 mM Glycine/ 1x PBST)
- Permeabilization buffer (0.5% Triton X-100/ 1x PBS)
- 20% Glycerol/ 1x PBS
- Liquid N_2 in Dewar container
- 0.1 N HCl
- Watchmaker forceps
- Vacuum pump
- Soft wipes (e.g. Kimtech)

Cells should be seeded as described in Section 3.1.5 (p. 33) about 18 h prior to fixation.

Method:

- Wash cells briefly 2x with 1x PBS (cell culture grade)
- Fixate with fixation buffer (4% formaldehyde/ 1x PBS) for 10 min. at RT (*Caution: For DNA-FISH, a higher concentration of fixative has proven to be advantageous in preserving nuclear structure during denaturation, than the standard 2% formaldehyde*)
- Replace the fixation buffer stepwise with 1x PBST, without letting the cells dry out
- Saturate remaining formaldehyde residues with quenching buffer (100 mM glycine/ 1x PBST) for 10 min. at RT
- Wash 2x with 1x PBST
- Permeabilize cells with permeabilization buffer (0.5% Triton X-100/ 1x PBS) for 10 min. at RT
- Wash 2x with 1x PBST (*be careful not to let the cells dry when taking them out of the permeabilization buffer*)
- Incubate in 20% Glycerol/ 1x PBS for at least 1 h at RT
- 3x freezing/thawing in liquid N_2 and storage in 20% Glycerol/ 1x PBS in between to increase accessibility to the nucleus for the probes

- Wash 2x with 1x PBS
- Incubate in 0.1 N HCl for exactly 5 min. at RT to remove cytoplasmic material
- Wash 2x with 1x PBST
- Equilibrate to 2x SSC buffer
- Incubate cells in 50% formamide/ 2x SSC for at least 4 h (preferably over night) at 4°C (*formamide evaporates at RT and is extremely toxic. Always work under the hood and keep the formamide cool)*

Notes:

- The liquid N_2 step is best carried out by pouring some liquid N_2 (~ 5 – 10 ml) into an appropriate small container (e.g. polystyrene box, small Dewar container etc.). Take the coverslips directly out of the 20% Glycerol/ 1x PBS and hold them into the liquid N_2 with the help of watchmaker forceps for about 5 – 10 s until you hear a characteristic cracking sound. Place the coverslip on a prepared soft-wipe tissue and let it completely thaw for about 20 – 30 s. Be careful not to let it dry out. Place it back into the 20% Glycerol/ 1x PBS and repeat the procedure.
- The 0.1 N HCl treatment is to remove all excess cytoplasmic components. As the size of the cytoplasm may vary from cell type to cell type, so does the incubation time of this step. 5 min. are a good starting point, but you may want to monitor this step under a phase contrast microscope and make sure to stop before the cells detach.
- Formamide is extremely toxic and evaporates at RT! Be sure to keep it at low temperatures and always work under the hood.

Probe preparation and hybridization:

Material:

- Formamide (100%, deionized)
- Labeled paint probes (labeling DOP-PCR product; 30 – 200 ng/ µl)
- Salmon sperm DNA (5 mg/ml)
- Yeast t-RNA (20 mg/ml)
- C_0t-1 DNA (1 µg/µl)
- Ice-cold 100% EtOH (-20°C)
- 2x Hybridization buffer
- 1.5 ml Reaction tubes
- Watchmaker forceps
- Centrifuge
- -80°C freezer
- Ice bucket
- Thermal shaker (37°C)
- Heat block
- Water bath (37°C)
- Metal box
- Fixogum
- Soft wipes (e.g. Kimtech)
- Glass slide

For whole-chromosome paint probes, 2 µl of labeled DOP-PCR product/ µl of final hybridization mix is recommended. For probes, which have been generated from genomic DNA an about 50-fold excess of C_0t-1 DNA has to be added to compete unspecific hybridizations. Salmon sperm DNA and yeast t-RNA are added to facilitate the precipitation of the probe DNA and to reduce unspecific hybridization background.

To save the expensive reagents and DNA-probes and in order to minimize the amount of hybridization solution per coverslip, it can be helpful to cut coverslips into smaller pieces with the help of a diamond pen (e.g. 15 x 15 mm out of 18 x 18 mm, #1.5, high precision), as high-precision coverslips are currently only commercially available with a minimum area of 18 x 18 mm.

The following method describes the quantities needed for a final 8 µl/ per coverslip hybridization mix.

Method:

- Mix ~ 500 ng of labeled DOP-PCR probe DNA together with 2 µg salmon sperm DNA, 5 µg yeast t-RNA and ~ 5 – 10 µg of C_0t-1 DNA together in an 1.5 ml reaction tube on ice
- Add 2.5x volume of ice-cold 100% EtOH (stored at -20°C) and incubate for at least 1 h at -80°C
- Centrifuge for 30 min. at 15,000 g (maximum speed of a table-top centrifuge) at 4°C
- Discard supernatant and let the remaining EtOH evaporate in a vacuum centrifuge at 37°C for about 30 min. (*Caution: All remaining EtOH has to be evaporated before proceeding to the next step*)
- Resuspend the pellet in 4 µl formamide (100%, deionized) per coverslip in a thermal shaker at 37°C under mild shaking for 30 min.
- Add 4 µl of 2x hybridization buffer per coverslip, mix well and store on ice until needed (*for long-term storage, hybridization solution can be kept at -20°C)*
- Denature probe DNA for 3 min. at 86°C in a heat block and place them on ice immediately afterwards
- Prepare and label clean glass slides (one per hybridization) under the hood
- Place 8 µl of denatured hybridization solution on a slide
- Take cells out of the 50% formamide/ 2x SSC and remove as much of the formamide as possible by tipping the edge of the coverslip on a soft-wipe tissue in order to avoid unnecessary dilution of the hybridization solution (*work quickly, do not touch the cells and do not let the cells dry*)
- Mount the cells on the hybridization solution onto the slides and seal with fixogum (*Do not proceed until fixogum has dried completely!*)
- An optional pre-hybridization step can be included here by letting the mounted cells rest in hybridization solution for 1 – 3h to ensure proper penetration of probe DNA throughout the sample
- Denature probes and nuclear DNA simultaneously by placing the slides on a 76°C heat block for exactly 2 min.
- Place the slides in a metal box and let it float in a 37°C water bath for 3 days for hybridization

Probe detection:

All unbound probes should be removed as thoroughly as possible to minimize unspecific signals and washing steps and incubation steps should be carried out accordingly as described in Section 3.2.1 (p. 35).

Caution: Work under the hood during all steps where formamide is still present – especially with warm formamide!

Material:

- 0.1 x SSC
- 2x SSC
- 4x SSCT
- 1x PBST
- BlockAid or Blocking Buffer (4% BSA/ 0.5% FSG/ 4x SSCT)
- Post-fixation buffer (4% formaldehyde/ 1x PBST)
- DAPI working solution (2.5 µg/ml DAPI in 1x PBST)
- Primary/ secondary antibodies
- ddH_2O
- Syringe filter (pore size 0.45 µm)
- Glass coplin jars (50 ml)
- Coverslips mini-rack
- Humid chamber
- 1.5 ml Reaction tubes
- 6-well plate
- Watchmaker forceps
- Water bath (37°C, 60°C)
- Soft wipes (e.g. Kimtech)
- Glass slide
- Antifade mounting medium (e.g. Vectashield)
- Nail polish

Method:

- Pre-heat two water baths to 37°C, and 60°C respectively, under the hood and place a sufficient amount of washing buffers inside (i.e. 150 – 200 ml are sufficient for three washing steps in one 50 ml coplin jar capable of taking up 8 coverslips – in a coverslips mini-rack)
- Gently peel of fixogum from the slides by adding a big drop of 2x SSC on top of the coverslips and carefully pushing the coverslip to the side of the slide where it can be taken up without pulling (*Do not apply mechanical force to the coverslips to avoid any morphological damage to the cells!*)
- Store coverslips in a coverslip mini-rack or 6-well plate in 2x SSC
- Wash 3 x 5 min. with 2x SSC at 37°C in the water bath under mild agitation

- Perform stringent washing step with 3 x 5 min. washing in 0.1 x SSC at 60°C
- Transfer to 4x SSCT at 37°C and wash 3x 5 min. under mild agitation
- Incubate the cells in freshly prepared and ultrafiltrated (pore size 0.45 µm) 4x SSCT blocking buffer (home-made) for 1 h at RT in a humid chamber
- Prepare probe detection antibodies in appropriate dilution in blocking buffer (*Here usually: Streptavidin – Alexa 488 or Streptavidin – Alexa 594, both 1:*200) and ultrafiltrate (pore size 0.45 µm) the solution directly before use (*Caution: you will lose about 300 – 400 µl in the filter*)
- Incubate cells in a drop (min. 30 µl for 18 x 18 mm coverslip; preferably 50 – 80 µl) of the antibody dilution for 1 h at RT in a humid chamber
- Remove all unbound antibodies by washing at least 9x in large volumes of 4x SSCT (compare Section 3.2.1, p. 35)
- In case of several probes, detect the other probes in subsequent steps accordingly
- Switch to 1x PBST buffer

In case of a combined RNA-FISH/Immunofluorescence labeling, perform the IF (with primary and secondary antibody incubation) after the probe detection step, here.

- Post-fixate the cells with 4% formaldehyde/ 1x PBST for 10 min. at RT in the dark
- Wash 2x with 1x PBST
- Counterstain DNA with DAPI (2.5 µg/ml in 1x PBST; *Caution: This concentration is about 20 times higher than in conventional protocols*) for 8-10 min. at RT in the dark
- Wash 6x with 1x PBST and 1x with ddH_2O to remove salt precipitates (*perform these steps quickly*)
- Pre-mount coverslips in a drop of non-hardening anti-fade mounting medium (e.g. Vectashield) on a flat piece of Parafilm and store in the dark
- Prepare and label appropriate number of glass slides for the final mounting step (*Rinse the glass slides with dH_2O briefly before use and let them air dry. Wear gloves to avoid finger prints on the glass slides*)
- Mount the coverslips in a fresh drop of mounting medium on the **back** of the glass slides (*This is to avoid a tilt of the entire slide and subsequently the imaged coverslip surface when mounting it on the OMX stage. This tilt is caused by a slight difference in thickness between the labeling area of the slide (frosting) and the transparent rest of the slide)*
- Remove all excess mounting medium with a soft-wipe tissue (e.g. KIMtech precision) by carefully and gently pressing (*Do not move the coverslip*)

- Seal the coverslip properly with nail polish

3.2.4 Relocating cells before and after 3D-FISH

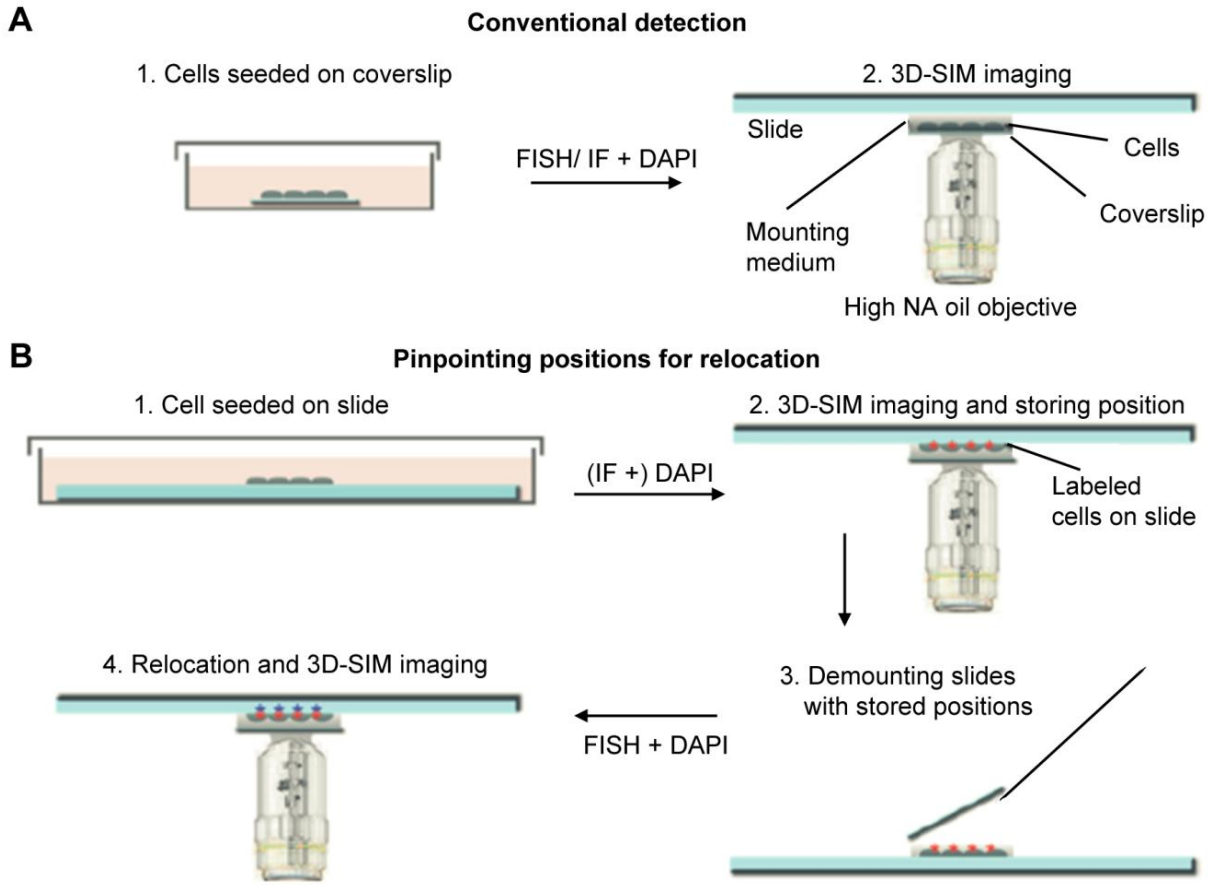

Figure 3-1 Relocation scheme for multiple acquisition of identical cells. (**A**) Shown is the conventional detection scheme with cells being seeded on coverslips, labeled according to the desired FISH- or IF-protocol and mounted on a slide in antifade mounting medium. (**B**) Shown is a versatile and easy method to relocate identical cells for multiple imaging, e.g. for subsequent IF and DNA-FISH or RNA-FISH and DNA-FISH, by seeding the cells on slides instead of coverslips. This allows the storage of exact cell positions during acquisition, which does not change after additional treatment and can easily be retraced. Figure modified after (Markaki et al., 2013).

In some cases it may be desirable to acquire the same cell multiple times, i.e. before and after a certain treatment to monitor differences without taking the phenotypical differences of individual cells within one cell population into account. Some treatments, e.g. DNA-FISH, are potentially also quite harmful to the preservation of other target structures and may hamper the quality of other parallel stainings, like IFs or RNA-FISH. In these cases, it may help to temporarily separate the two labeling procedures and to perform the harmful DNA-FISH after the entire IF- or RNA-FISH procedure, including acquisition. One has to keep in mind though, that seeding cells onto the slides (which is essential for the relocation) causes problems for 3D-SIM imaging, as the cells have to be imaged through the coverslips and a layer of mounting medium (see Figure 3-1). This causes spherical aberrations and refractive index mismatches, both resulting in misleading reconstruction artifacts and low resolution gain if not counteracted, because high NA oil objectives are optimized to a

distance directly on top of coverslips. However, two things may help to counteract these problems. The first is trying to remove as much of the mounting medium as possible (ideally to a remaining height of less than 10 µm) to minimize the distance between objective and cell, and second to choose an immersion oil with a higher refractive index (i.e. 1.514 or 1.516, instead of the conventional 1.512 for standard imaging).

In the present work, this method has been used to explore the changes imposed to nuclear and chromatin morphology before and after DNA-FISH treatment.

3.2.5 Replication labeling with EdU and click-chemistry reaction

Replicating DNA can be visualized by incorporation of 5-ethynyl-2-deoxyuridine (EdU) into the newly synthesized strand and a subsequent detection of EdU with so called "click"-chemistry (Buck et al., 2008; Salic and Mitchison, 2008). This reaction uses Cu^{2+} catalysis to covalently bind a fluorophore, carrying an azide-group, to an incorporated nucleotide, carrying an ethynyl-group, in this case EdU (see Figure 3-2). Furthermore, this method omits a DNA denaturation step, which is essential for the traditional replication labeling with 5-Bromo-2-deoxyuridine (BrdU) and thus is better suited for super-resolution imaging as it provides higher degree of morphology preservation.

In this work, EdU replication labeling has been performed to analyze the chromatin environment around sites of replication, which have been labeled with an anti-PCNA antibody. This antibody requires a methanol-fixation step to be able to recognize its epitope. A conventional formaldehyde fixation, followed by methanol-fixation has proven to be an optimal trade-off to preserve nuclear morphology for super-resolution imaging and to ensure proper epitope accessibility at the same time.

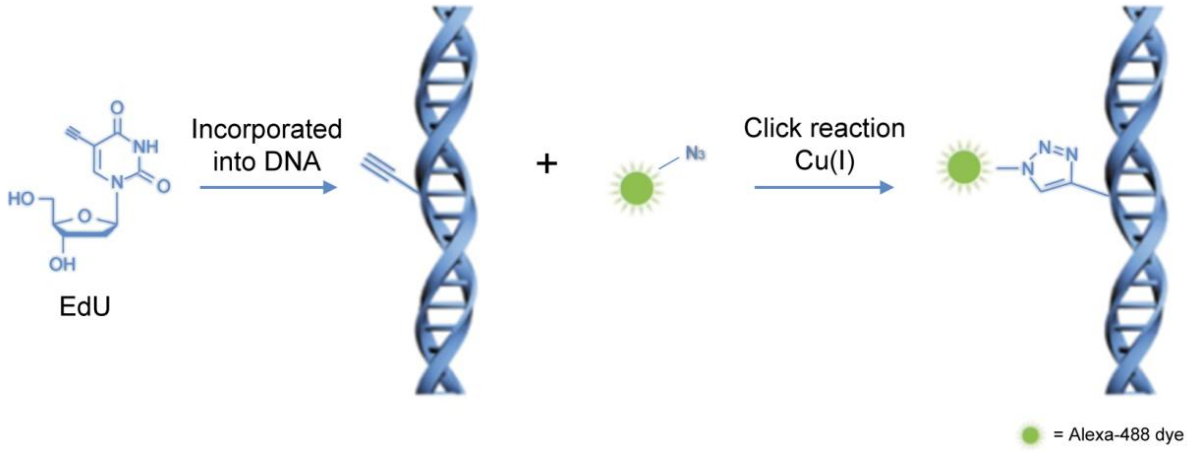

Figure 3-2 Illustration of EdU-detection using click-chemistry. EdU gets incorporated into newly synthesized DNA during replication. An azide-coupled fluorophore (Alexa 488) gets covalently bound to the ethynyl-group under Cu^{2+} catalysis. Figure modified after (Buck et al., 2008).

Material:

- 1x PBS (cell culture grade)
- 6-well plate
- Cell culture medium
- EdU (10 mM)
- Fixation buffer (2% formaldehyde/ 1x PBS)
- 1x PBST
- Quenching buffer (100 mM Glycine/ 1x PBST)
- 100% Ice-cold methanol
- BlockAid or Blocking Buffer (4% BSA/ 0.5% FSG/ 1x PBST)
- Primary/ secondary antibodies
- 1.5 ml/ 2 ml Reaction tube
- Coverslips mini-rack
- Watchmaker forceps
- Vacuum pump
- Humid chamber
- Soft wipes (e.g. Kimtech)

Method:

- Seed desired cells to a density of about 60- 80% on coverslips (as described in Section 3.1.5, p. 33)
- Take 1 ml adapted medium from the supernatant of growing cells and mix with 1 ml fresh cell culture medium
- Add EdU (10 mM) to a final concentration of 10 – 20 µM and mix well
- Aspirate old medium from growing cells and add 2 ml of the EdU containing medium
- Incubate cells at 37°C in CO_2 incubator for the desired pulse length (*Here: 5 – 10 min.)*
- Aspirate EdU medium, wash 2x with 1x PBS and add fresh cell culture medium for desired time or fixate cells immediately
- To fixate the cells, wash 2x with 1x PBS
- Fixate cells with fixation buffer (2% formaldehyde/ 1x PBS) for 10 min. at RT
- Stepwise replace with 1x PBST
- Quench remaining formaldehyde residues with 10 min. incubation in quenching buffer (100 mM Glycine/ 1x PBST) at RT
- Wash 2x with 1x PBST

Optional: For subsequent IF using the anti-PCNA antibody (rat α PCNA, 1:20), perform another fixation/permeabilization step with 100% ice-cold methanol for 5 min. at 4°C, here. Replace methanol stepwise with 1x PBST, accordingly to formaldehyde fixations

- Permeabilize and block cells as described in Section 3.2.1 (p. 35; *In case of methanol fixation, permeabilization can be omitted!*)
- Prepare click-reaction cocktail (Table 3-8)
- Incubate cells in click-reaction cocktail for 30 min. at RT in a humid chamber

Table 3-8 EdU click-reaction cocktail

Reagent	Volume	Final concentration
Tris-HCl (1 M, pH 7.0)	10 µl	100 mM
$CuSO_4$ (100 mM)	4 µl	4 mM
Sodiumascorbat (1 M, *fresh*)	5 µl	50 mM
Azide dye (10 mM)	0.2 µl	20 µM
ddH_2O	80 µl	- - -

- Wash very well, at least 14x in 1x PBST and discard all washing containers afterwards (*remaining click-cocktail is detrimental to IF-procedure*)
- Perform additional IF, DAPI-staining and mounting as described in Section 3.2.1 (p. 35)

3.3 3D-SIM imaging

3.3.1 Basic principles

SIM exploits an optical phenomenon called Moiré effect by applying a sinusoidal, striped illumination pattern onto the sample in order to extract the super-resolution information (Gustafsson, 2000; Heintzmann and Cremer, 1999). Light emitted from the unknown sample structure interferes with light from this regularly shaped pattern, which has a spatial frequency closely above the resolution limit. The resulting emitted interference light creates so called Moiré fringes, which are big enough to be resolved and collected by the microscope objective, but also contain frequency information of finer structures from the underlying unknown sample, below the resolution limit. As the stripe pattern covers parts of the sample information and is only effective in one direction, it has to be shifted (5 phases) and rotated (3 x 120° = 360°) in order to cover the entire field of view. This results in a total of 15 single acquisitions per z-section, adding up to a total of about 1,000 raw data images per color channel for the 8 µm thickness of a typical mammalian nucleus. An *in silico* post-acquisition image reconstruction step extracts the super-resolution information out these SI raw data images. By transferring the collected interference images (stripe pattern + unknown sample structure) into frequency space (Fourier transformation), the inherent super-resolution higher frequency information can be mathematically extracted. Converting the result back into real space provides a reconstructed image with doubled resolution in x,y direction (see Figure 3-3 for the SIM principle and Figure 3-6 for the reconstruction process). In 3D-SIM, additional information from above or below the focal plane is collected, too. Hence, a stripe-like modulation pattern is created in z-direction, ultimately resulting in a super-resolution image with doubled resolution in all three spatial dimensions, equivalent to an eight-fold increased volumetric resolution compared to conventional wide-field microscopy (Gustafsson et al., 2008; Schermelleh et al., 2008). The stripe pattern has typically been created by passing the excitation light beam through a diffraction grating module, which has to be mechanically shifted and rotated (Dobbie et al., 2011). Recent developments included, for example, the use of Piezo-driven structural light modulators or LED-generated stripe-modulations, which offer a much faster acquisition speed than the mechanical phase grating (Dan et al., 2013; Hirvonen et al., 2009; Xu et al., 2013).

In absolute numbers, 3D-SIM is able to achieve lateral resolutions of about 100 – 130 nm and about 250 – 350 nm in axial direction, depending on the wavelength. Introducing non-linear effects, as in the so called saturated SIM (SSIM) or in non-linear SIM (NL-SIM), equivalent to STED, allows to reach theoretically unlimited resolution (Gustafsson, 2005; Rego et al., 2012). However, this imposes extremely high energies to the sample and requires normally unachievable photostability of the applied fluorophores. Thus, 3D-SIM offers an ultimately limited increase in resolution, unlike PALM/STORM or STED. However, 3D-SIM provides several other advantages, which are particularly

useful in cell biology, like simultaneous multi-color imaging using standard fluorescent dyes, 3D in-depth imaging of up to 20 µm and fast acquisition speed, which recently even made multi-color super-resolution live-cell imaging an easily applicable tool for the standard researcher (Fiolka et al., 2012; Hirvonen et al., 2009; Kner et al., 2009; Shao et al., 2011). Taken together, all these benefits provide a wide range of applicability and already led to a series of publications (Baddeley and Chagin, 2010; Brown et al., 2011; Markaki et al., 2012; Strauss et al., 2012) (for reviews see Cardoso et al., 2012; Huang et al., 2010; Schermelleh et al., 2010; Smeets et al., 2013a, *in press*).

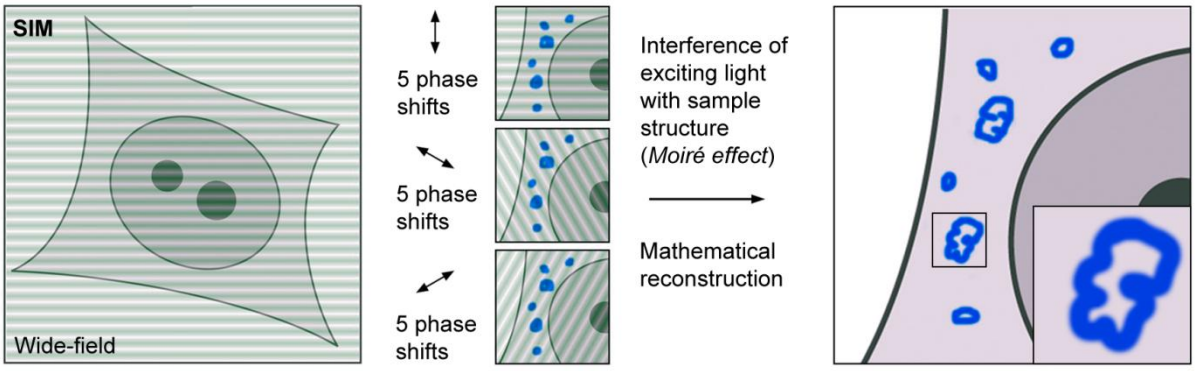

Figure 3-3 Schematic illustration of the SIM principle. The sample gets wide-field illuminated with a stripe-like pattern. Emitted light from the unknown sample structure creates an interference image with the known stripe pattern resulting in the creation of Moiré fringes. 15 images per z-section get recorded with 5 phase shifts and 3 rotations. Underlying SR information of the sample structure gets mathematically reconstructed from the recorded interference images. Figure adapted and modified after (Schermelleh et al., 2010).

Comparing the resolution of conventional wide-field microscopy and 3D-SIM

To illustrate the advantages of 3D-SIM and to compare the outcome with the corresponding wide-field image, an IF staining against the mitochondrial inner-matrix protein COX IV and against the neuronal marker protein Beta-tubulin III has been performed in mouse neuronal cells that have been differentiated from an ESC culture (see Figure 3-4, A).

A wide-field image that is identical to its corresponding 3D-SIM image – simply at lower resolution – can be generated from the 3D-SIM raw data by creating an average intensity projection of the five phase shift images for every z-section. Subsequently, the resulting wide-field image stack can be subjected to deconvolution, if desired. By this approach, identical images can directly be compared at three different levels of resolution. Intensity line plot profiles demonstrate the doubling in resolution for 3D-SIM images in lateral as well as in axial direction, when measuring peak intensity widths, a commonly used method to quantify resolution (Figure 3-4, B). It has to be noted that the depicted resolution values have been measured in the red channel (excitation at 593 nm, and emission at ≥ 620 nm) and are therefore not the best possible values. Even smaller distances can be resolved using shorter wavelengths.

Due to its advantages over other super-resolution techniques and of course due to its 8-fold increased volumetric resolution over conventional microscopy, 3D-SIM provides the possibility, e.g.

to re-address some of the remaining open questions in XCI and in studying higher-order chromatin organization.

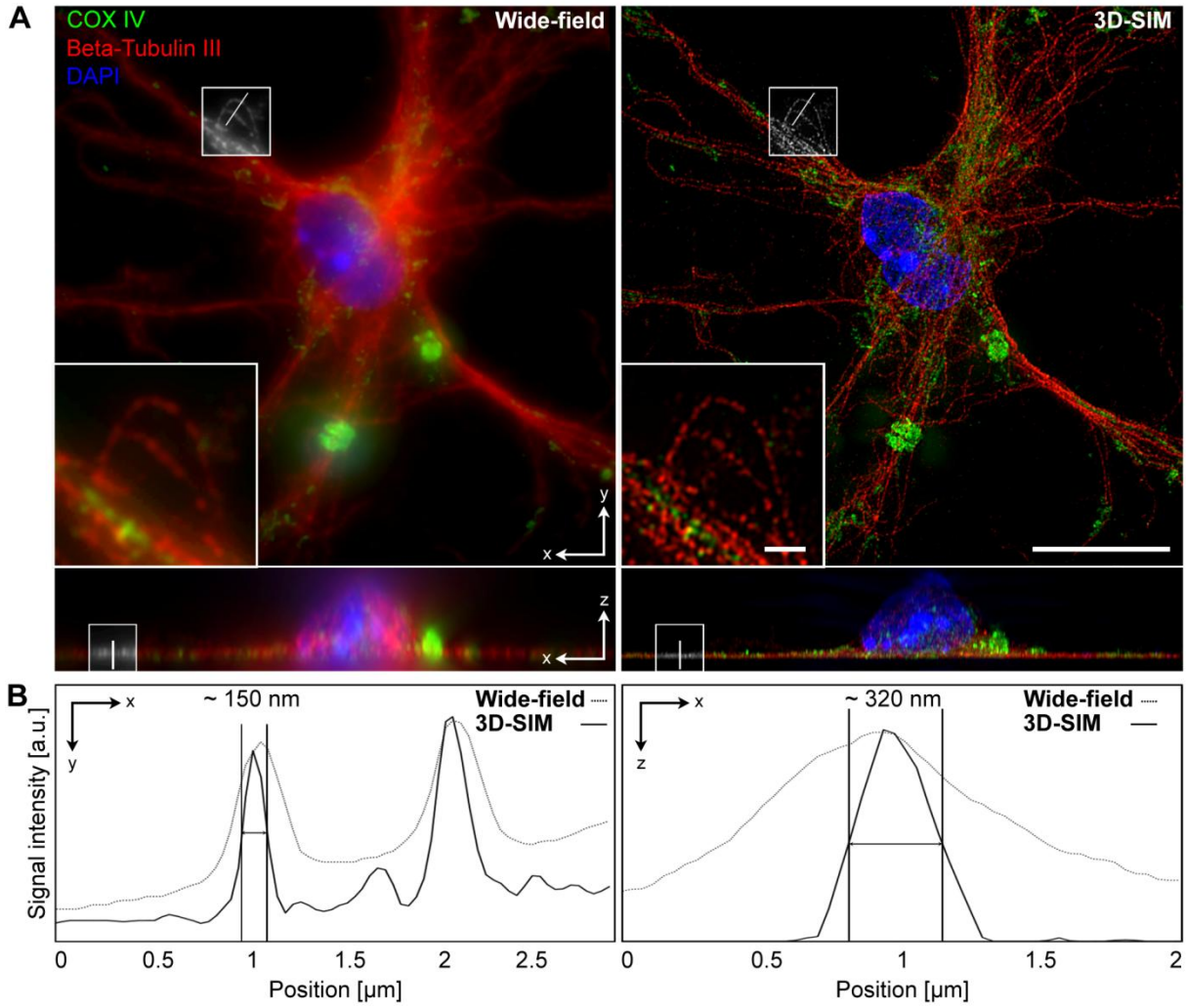

Figure 3-4 Comparison between conventional wide-field and 3D-SIM resolution. (A) Maximum intensity projections of an IF against COX IV and Beta-tubulin III in a mouse neuronal cell. Left panel shows the resolution typically achievable with conventional wide-field and right panel with 3D-SIM resolution. Lower panels depict orthogonal maximum intensity projections of the same nucleus. Scale bar 10 µm, insets 0.5 µm. **(B)** Intensity line profile plots for the red channel from the areas depicted in (A). Two-fold increased resolution of 3D-SIM compared to wide-field in lateral and axial direction is demonstrated by measurements of full-width, half maximum (FWHM) of individual peaks. Mouse neuronal cells have been differentiated from ESCs with the kind help of Fabio Spada (LMU Munich). Figure modified after (Smeets et al., 2013a, *in press*).

A major part of the present work has been to apply and optimize 3D-SIM for applications in cell and nuclear biology. Protocols for various different labeling techniques that are summarizing and cumulating this work are described in the sections above. 3D-SIM poses very high demands on sample quality, and especially signal-to-background ratio, and an overall cleanness of the sample, which has to be free from any dust, remaining oil or mounting medium. After having prepared the perfect sample, several things still have to be considered during 3D-SIM acquisition, which are described in the following sections.

3.3.2 3D-SIM imaging and system calibration

Setup of the Deltavision OMX V3 Prototype (Applied Precision Imaging/ GE Healthcare)

Figure 3-5 OMX V3 prototype setup. The OMX V3 prototype system consists of several components including a conventional pDV wide-field system (green), whose stage is calibrated to the OMX stage allowing eye-piece sample pre-screening in order to collect certain regions of interest within the sample and to visually judge sample quality. The actual OMX V3 3D-SIM system is located within an insulated microscope enclosure (yellow), which also contains the mechanical phase grating device generating the structured illumination pattern. Laser lines are mounted on an open table within a separate laser enclose (purple), also harboring all electronic equipment necessary for hardware control. Laser enclosure and microscope enclosure are only connected via two multimode laser optical fiber cables separately conducting the SI and the wide-field light path. Super-resolution information gets reconstructed from the SI raw data, channel-aligned and stored on the high-performance user workstation (red) using build-in algorithms of the commercial SoftWorx 4.0 software.

The current Deltavision OMX systems are based on a high numerical aperture wide-field deconvolution microscope, which has been radically re-designed for maximum mechanical stability (Carlton et al., 2010; Dobbie et al., 2011; Schermelleh et al., 2008; Smeets et al., 2013a, *in press*). The

entire setup is shown in Figure 3-5, and includes a personalDV wide-field devonvolution microscope (pDV) that can be used for pre-screening the sample and saving the positions of certain regions of interest. The pDV stage is calibrated to the OMX stage in the OMX microscope enclosure. The OMX V3 consists of a laser and electronics enclosure, which are physically separated from the microscope, and which harbors three laser lines that can be directed via two separate light paths – SI and wide-field. The two multimode fiber cables get mechanically shaken to ensure even illumination over the entire field of view and are connected with the microscope enclosure. The SI-fiber is directed through a phase grating generating the structured-illumination pattern, which can be mechanically rotated and shifted. Apart from the phase grating, the entire light path does not contain any moving parts. During acquisition, the objective remains fixed, while only the slide stage is moving. After excitation, the emitted light is collected by a high numerical aperture objective and after passing through a dichroic mirror set directed to one of three EMCCD cameras, one for every wavelength. The super-resolution information gets computationally reconstructed from the acquired structured-illumination raw data at the attached user workstation using built-in algorithms of the commercial SoftWorx 4.0 (Applied Precision Imaging/ GE Healthcare).

Considerations on acquisition settings

Several aspects during data acquisition and post-processing are important for an artifact-free imaging and reconstruction result using 3D-SIM. Those include (**1**) the correct system calibration using fluorescent beads to acquire Optical Transfer Functions (OTFs) for every single color-channel. The OTF is the Fourier Transformation of the PSF that describes the factor by which a microscope inherently blurs and deteriorates an ideal sub-diffraction sized point-like object due to its resolution limit and optical properties. The information from these measurements can later be used to mathematically subtract these inherent system uncertainties from any recorded image data from unknown sample structures. OTFs are influenced by the applied wavelength, which means that individual OTFs have to be generated for every color channel. They have to be updated every few months or after every major change in the system setup. OTFs also behave differently depending on the different refractive index of the applied immersion oil and thus have to be recorded for all commonly used immersion oils individually. This leads to (**2**) the choice of the correct immersion oil's refractive index. The Deltavision OMX systems come with a selection of about 20 different immersion oils with increasing refractive indices in steps sizes of 0.002. Depending on the desired application, immersion oils with different refractive indices have proven to be ideal. Generally, for fixed samples and rather flat cell types, a refractive index of 1.512 is optimal as it gives the best contrast close to the coverslips. For thicker cell types like ES-cells, a higher refractive index of 1.514 has proven advantageous as it shifts the contrast maximum away from the coverslip. For the different color

channels, a rule of thumb is, the longer the wavelength, the higher the refractive index. Close to the coverslip, the ideal refractive index for 405 nm (DAPI) is 1.510, for 488 nm (Alexa-/ ATTO-488) it is 1.512 and for 593 nm (Alexa-/ ATTO-594) the ideal refractive index is 1.516. Thus, a good trade-off for samples containing all three colors is to use an 1.512 immersion oil. The choice of the correct refractive index can be controlled by looking at an orthogonal section of a fluorescent bead (or another point-like object). The cone of blurred out-of-focus light should be symmetrical above and below the bead. (**3**) Choice of camera and acquisition mode: For the Deltavision OMX V3 system, the commercial software SoftWorX 4.0 (Applied Precision Imaging/ GE Healthcare) offers several acquisition options. Table 3-9 lists acquisition settings for standard three-color fixed samples that have been typically applied in this work. It has to be noted that bleaching stability during acquisition is much more important than total signal intensity and that all acquisition parameters should be chosen to minimize the amount and intensity of light exposed to the sample. The limiting factor in this sense is signal-to-background ratio, which can be influenced in many perspectives and also depends strongly on the nature of the signal. Abundant chromatin stainings, like DAPI or specific histone modifications, show more out-of-focus blur from signals above or below the focal plane and therefore need a much higher absolute signal intensity than small and distinct foci, which can be imaged with as little as 1,000 counts to reach a sufficient signal-to-background ratio. The camera mode can be chosen for every channel individually. Here, the electron multiplying charge-coupled device (EMCCD) mode enhances every collected photon with an adjustable factor and therefore enhances weak signals and also helps to reduce exposure time and thus minimizes bleaching. This mode should be chosen for the 488 nm and 593 nm channels, as any signals there are typically from Alexa- or ATTO fluorophores, which bleach upon too long exposure times. Yet, the drawback of this camera mode is that it also increases camera-noise, which has a negative effect on the signal-to-background ratio. If affordable by photostability, the CCD mode – without signal enhancement – should be chosen, as it does not introduce extra camera noise. This is ideal for very photostable signals, like DAPI, where this mode should always be chosen. DAPI is a special case due to its extreme photostability. This allows choosing exposure times that push the DAPI signal almost into saturation (65,535 counts) without suffering from significant bleaching and therefore providing the best possible signal-to-background ratio. (**4**) The field of view should be chosen as small as possible to reduce the resulting file size (~1 GB of raw data for a three color 512 x 512 pixel, 8 µm image stack). The same is true for the acquired z-range, which furthermore contributes to minimize bleaching as fewer z-sections mean fewer acquisitions. The z-range should always start and end entirely out of the desired structure (i.e. nucleus), as this will cause reconstruction artifacts otherwise.

Table 3-9 Typical OMX V3 acquisition settings for three color fixed samples of mammalian nuclei

	Wavelength	Settings	Notes
Acquisition mode	- - -	Sequential	Standard setting ⇨ No bleed-through
		Simultaneous	Only when bleed-through is wanted (e.g. Alignment check)
Light path	- - -	SI	Structured Illumination
Camera mode	405 nm	CCD 5 mHz	
	488 nm	EMCCD 10 mHz	
	593 nm	EMCCD 10 mHz	
EMCCD Multiplier	405 nm	- - -	
	488 nm	3000 – 3400	
	593 nm	3000 – 3400	
Exposure time	405 nm	20 – 50 ms	Use entire 16-bit range
	488 nm	20 – 100 ms	At least 1,000 counts; avoid bleaching
	593 nm	20 – 100 ms	
Transmission %	405 nm	50 – 100%	
	488 nm	100%	
	593 nm	100%	

3.3.3 3D-SIM post-processing and data analysis

Image reconstruction

After acquisition of the 3D-SIM raw data, the super-resolution information is computationally obtained with the help of specific algorithms (for a detailed description of the reconstruction process see Gustafsson et al., 2008). In short, the basic principle that is exploited in this process is the so called Moiré effect, which occurs when two or more regularly shaped structures optically interfere with each other (see Figure 3-6, A). In 3D-SIM, a regularly shaped stripe pattern is projected into the focal plane and produces and interference image with the unknown sample structure, which can be measured and recorded. Because the stripe pattern is only effective in one direction, it has to be shifted laterally (5 phases) and rotated three times (3 x 120° = 360°), which adds up to 15 images per z-section, in order to cover the entire field of view (see Figure 3-6, B). In the OMX V3 setup, three z-stacks (z-step size = 0.125 µm) are recorded sequentially, each with a different angle, whereas switching between the different laser lines for multi-color acquisitions is performed sequentially at every single z-section.

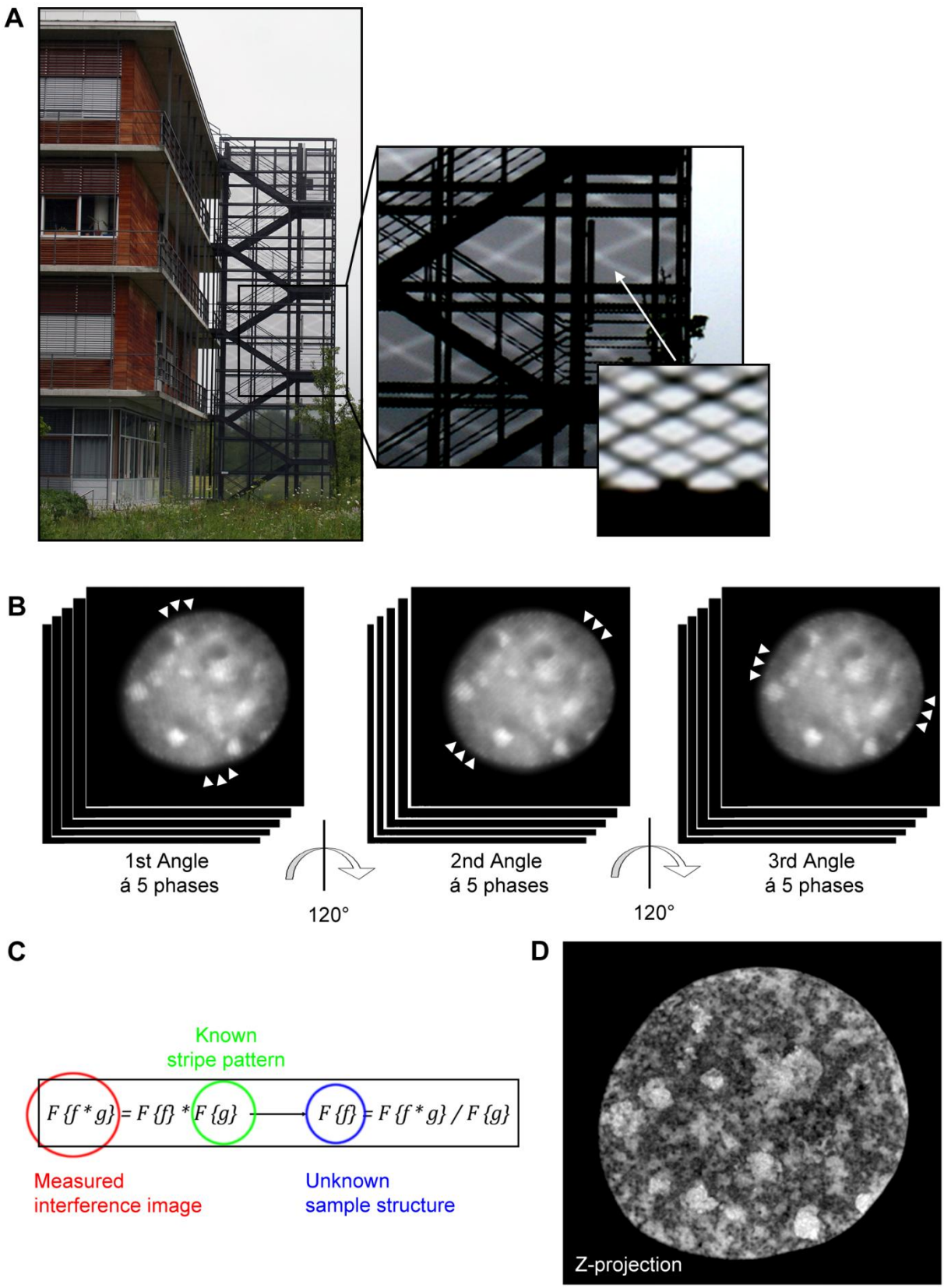

Figure 3-6 Principle of 3D-SIM reconstruction exploits the Moiré effect in the interference between known stripe pattern and unknown sample structure. (A) Moiré effect at an emergency staircase outside the LMU Biocenter, Munich. **(B)** The structured illumination acquisition process with phase-shifting and rotating the stripe pattern in total 15 times per z-section. **(C)** Main formula used by the reconstruction algorithm, solved for the unknown sample structure. **(D)** Z-projection of the nucleus shown in (B) at 3D-SIM resolution.

Due to the Moiré effect, the interference images contain information about the underlying sample structure – beyond the level of conventional resolution – which has been shifted into the resolvable range and thus can be collected by the objective of the microscope. This information can be extracted from the acquired structured illumination images by transforming them into frequency space, a mathematical process that is called Fourier Transformation. Instead of depicting an image in real space, where every pixel contains a position and an intensity information, it can also be depicted in frequency space without losing any of its information. It is just another way of showing an image, but has the advantage that mathematical calculations can be performed more easily than in real space. In frequency space, the image contains the exact same number of pixels, but here every pixel is not specified by an intensity, but by a frequency or sine wave, with the amplitude of the frequency corresponding to the real space value of the pixel (= intensity) and the wavelength of the frequency corresponding to its distance from the image center. High-frequencies are far away from the center and correspond to small distances / fine details in real space (Carlton, 2008). Going back to the first assumption, the acquired structured illumination images are interference images of the known stripe pattern and the unknown underlying sample structure, or mathematically speaking, they are a multiplication of the two. This means that this simple equation can be converted to solve for the unknown sample structure by dividing the measured interference image by the known stripe pattern in frequency space (see Figure 3-6, C). By doing this for all the different phases and angles in several adjacent z-sections (minimum 8 z-sections / 1 µm) and converting the extracted information back into real space, a super-resolution image with doubled resolution in all three dimensions – corresponding to an eight-fold increased volumetric resolution – can be computationally reconstructed (see Figure 3-6, D).

Channel alignment

The OMX V3 setup uses separate cameras for every single color channel to maximize mechanical stability by avoiding any moving components, like switching filter sets or mirrors, and to increase acquisition speed (as described above). Nonetheless, this implies a major drawback and makes a proper alignment of the different color channels in order to allow any conclusions or interpretations about the localization of acquired signals absolutely necessary.

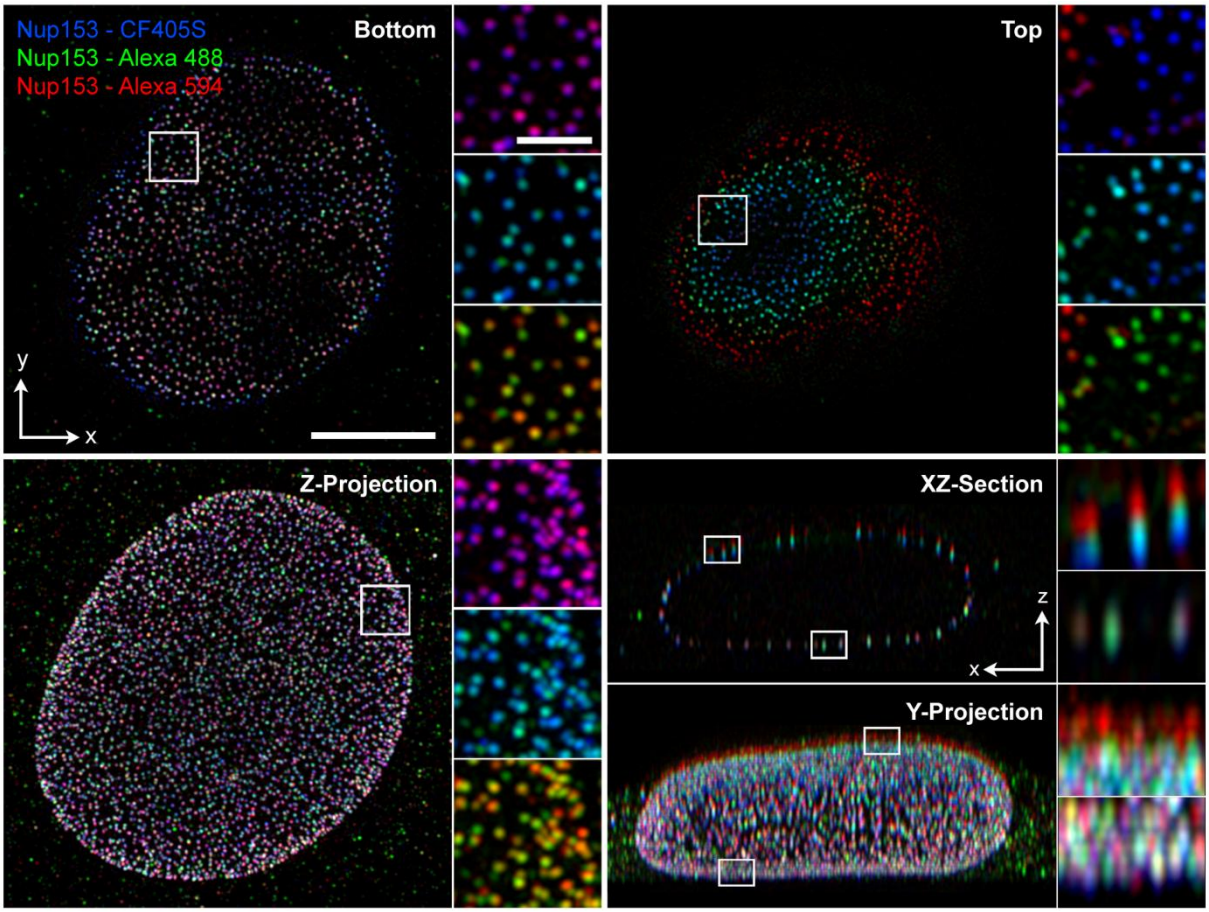

Figure 3-7 Simultaneous three-color labeling to control for sample specific channel alignment and chromatic aberration. Immunostaining in a mouse C127 cell using a primary antibody against Nup153, a nuclear pore component, and three differently labeled secondary antibodies. Upper panels show a single z-section from the bottom and top end of the nucleus. Lower panels show maximum z-projections from the same nucleus. Scale bar 5 µm, insets 1 µm. Figure modified after (Smeets et al., 2013a, *in press*).

After having reconstructed the 3D-SIM raw data, the next step is to perform the channel alignment, which occurs in two parts. The first is to physically align the three cameras to each other as good as possible (< few pixels deviation) and to avoid any tilting between them, both of which should have been done already prior to data acquisition. The second step is to perform an *in silico* alignment applying a best-fit algorithm (transformation, translation and rotation) using a suitable reference structure (e.g. 0.5 µm Tetraspeck beads/ Invitrogen, Darmstadt) to determine the system-specific alignment parameters and to apply them to every color-channel individually. It has to be noted that an alignment using only beads is not sufficient for the requirements of a three-dimensional biological sample. As beads are attached directly to the surface of the coverslip, they only reflect the best possible fit at the bottom of any sample (see Figure 3-7). The further the signal is away from the coverslip, the bigger is the axial misalignment due to chromatic aberration, where longer wavelengths are diffracted more strongly than shorter wavelengths. Figure 3-7 shows an example, where signals have been aligned to show the best fit at the bottom of the sample, next to the coverslip, leading to substantial misalignment at the top of this – rather flat – nucleus. This effect is, of course, also present in conventional microscopy, but is usually neglected there due to the poor

axial resolution. Most biological samples, like mammalian nuclei, have a thickness of more than 5 µm, which leads to the necessity to align the color channels to a best fit in the middle of the sample or directly at the region of interest, either using biological samples as reference structures in addition to standard bead samples or e.g. by using bead "sandwich-samples", with beads attached to the coverslip and to the slide. Figure 3-7 also shows that even with the best possible alignment (i.e. upper left panel, at the bottom of the nucleus), the colocalization between two or more color channels is never complete in a biological sample at this level of resolution. This appearance of misalignment is caused by differential spatial orientation and/or binding competition and/or variations in fluorophore / epitope ratio of the applied antibodies (Smeets et al., 2013a, *in press*).

Data preparation

The reconstructed and aligned images are saved as 32-bit .dv stacks. For any further processing, analysis or presentation, they have been converted into 16-bit composite .tif stacks using ImageJ (http://imagej.nih.gov/ij/). As the reconstruction software is usually not using the entire 32-bit range, the intensity histogram can easily be shifted into the positive range maintaining the absolute and relative intensity differences between pixels and without losing any information.

Chromatin density segmentation

One widely used method in this work was to statistically compare chromatin density in several parts of the nucleus with each other, according to the DAPI staining. In particular, chromatin density of the Xi has been compared to ten other random regions of the same size and volumetric shape. For this purpose, a novel tailor-made data analysis tool has been developed together with Prof. Volker Schmid (Institute for Statistics, LMU Munich), which is based on a hidden Markov random field model classification, combining a finite Gaussian mixture model with a spatial model (Potts model) implemented in the open-source statistics software R (http://www.r-project.org/). DAPI-stained chromatin was segmented into seven density classes with equal intensity variance in 3D over the entire nuclear volume. This approach allowed threshold-independent signal intensity classification at the voxel level, not only based on the intensity of an individual voxel, but also considering the classification of surrounding voxels (for a detailed description see Zhang et al., 2001). This classification is a deliberate simplification (compared to e.g. 65,535 grey levels in 16-bit images), but provided good visual discrimination of regions with different chromatin density and allowed the statistical comparison of chromatin compaction within different areas of a nucleus or between several samples and cell types. Nucleoli, visually defined by their clearly shaped border were excluded from classification. Class 1 represents voxels with intensities approximately around background level (i.e. virtually no detectable DNA), while class 7 assigns highest chromatin density.

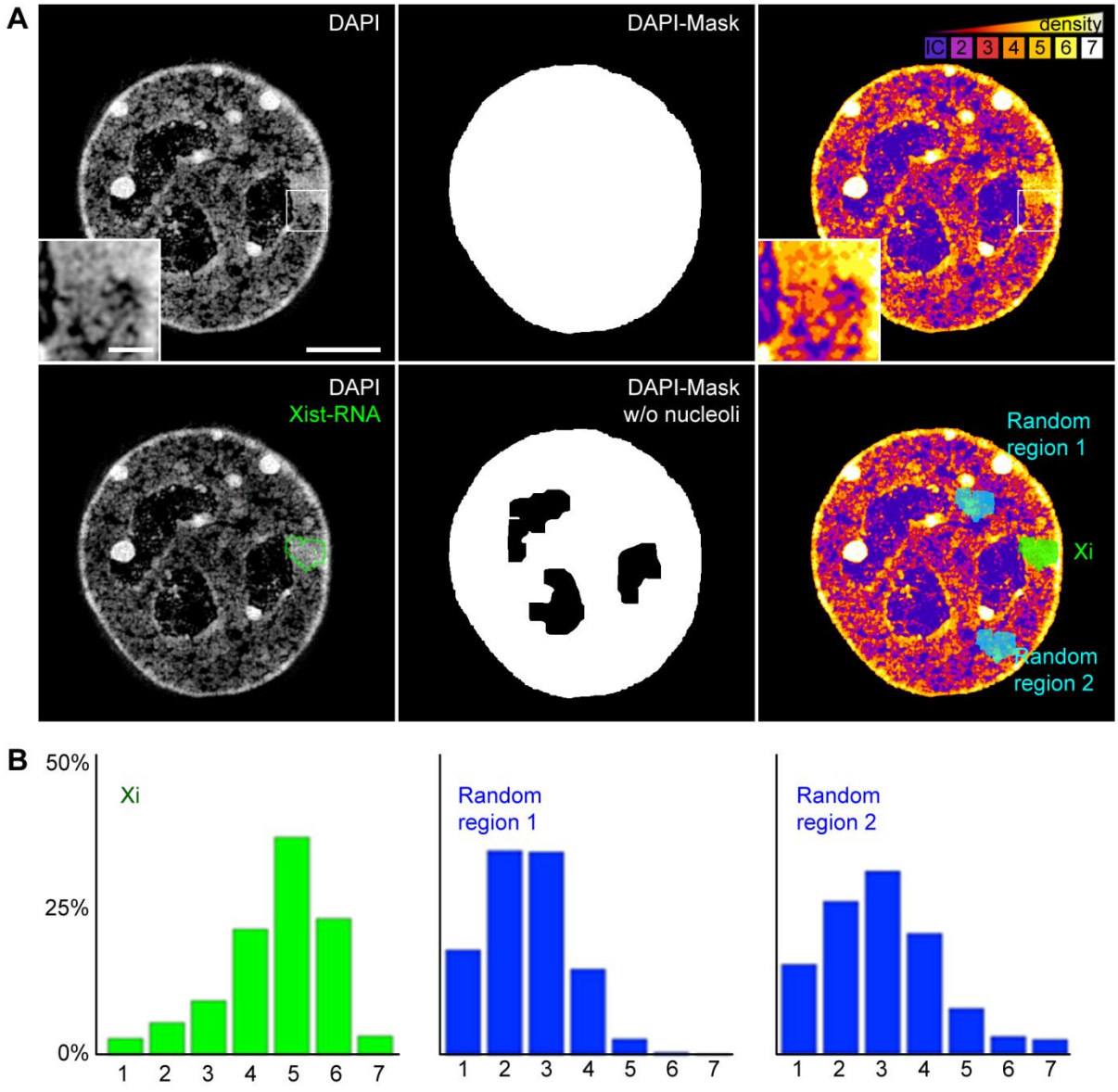

Figure 3-8 Scheme of chromatin density segmentation procedure. (A) A three-dimensional DAPI-mask is created from the DAPI signal and all signals outside are excluded. DAPI signal is divided into seven equal variance chromatin density classes (upper right panel). Xist-RNA signal defines the Xi-volume (lower left panel). Nucleoli are semi-automatically excluded from the DAPI mask and result is controlled visually before proceeding. The Xi mask gets shifted into ten random volumes within the nucleus apart from the nucleoli. Scale bar 5 µm, inset 1 µm. **(B)** Distribution of chromatin density classes from the volumes depicted in (A).

The workflow of this analysis is shown in Figure 3-8. It makes no significant difference for the outcome of the analysis, whether 16-bit or 8-bit data sets are used as input files (as they are going to be reduced to 7 “grey values”/ 7 classes anyway), but using 8-bit image stacks as input significantly reduces computing time and processing work load, which can be a limiting factor for this analysis. Prior to the segmentation, a 3D masks was generated in ImageJ to define the nuclear space according to the DAPI signal. All signals outside the DAPI-mask are not considered further. A mask to define the Xi region(s) within the nuclei is created using the Xist RNA signal by setting a visual threshold and unifying the result by using the “Dilate” (Process -> Binary -> Dilate) and “Fill Holes” (Process -> Binary -> Fill Holes) functions in ImageJ. To create a nucleoli mask (nucleoli should not be considered

as a random region), a threshold has to be set, which includes all nucleoli as good as possible. All minor holes in the DAPI signal, which shall not be counted as nucleoli, can be removed from this mask by several rounds of “Dilate”, followed by the same number of “Erode” (Process -> Binary -> Erode) operations. The result was then visually compared with the original DAPI-signal and possibly adapted if necessary. The final result can then be “multiplied” with the original DAPI-mask using the “Image Calculator” function (Process -> Image Calculator). Last, the chromatin density segmentation has been performed in R using the tailor-made script and the original DAPI signal (8- or 16-bit), the DAPI-mask, the Xi mask and the nucleoli mask as input files. The script segments the DAPI signal into seven density classes according to the definitions described above and also shifts the Xi mask randomly within the nuclear volume (excluding the nucleoli) to create a random control group for the Xi density. It results with a tif-stack, showing the density segmentation, as well as txt-files showing the density class distribution in the Xi and the ten random regions as output. The density distribution can then be averaged, provided with standard deviations, and compared with other results as desired.

Colocalization analysis

Another widely used approach in this work was colocalization analysis between different structures of interest. For a quantitative assessment of colocalization the Pearson’s coefficient (PC) and the Manders’ colocalization coefficients M1 and M2 were determined. The Pearson’s coefficient correlates intensities for the respective two color channels on a voxel-by-voxel basis, ranging from [-1] and [+1], where [-1] would correspond to a perfect inverse, [+1] to a perfect positive correlation, and uncorrelated signals yielding values around [0]. M1 and M2 measure the proportion of overlap between two channels relative to the total amount of a signal contributing to each channel. Here, an intensity threshold has to be set manually, since this approach does not integrate the information on the grey value ratios between the two channels at each single voxel.

Colocalization analysis was performed using the JACoP plug-in for ImageJ (Bolte and Cordelières, 2006). Prior to the analysis, the area of interest has been manually cut out for each single data set in order to keep distortions from Xi-unrelated signals to a minimum by manually creating a mask using either Xist RNA or H3K27me3 as reference.

At a later stage of this thesis, an additional evaluation approach has been developed, applied and kindly provided by Michal Gdula (University of Oxford, Oxford, UK), which uses centroid determination of individual signals to measure mean distance distributions between two classes of signals. This approach has been applied in the evaluation of colocalization between different PRC2 components and Xist RNA.

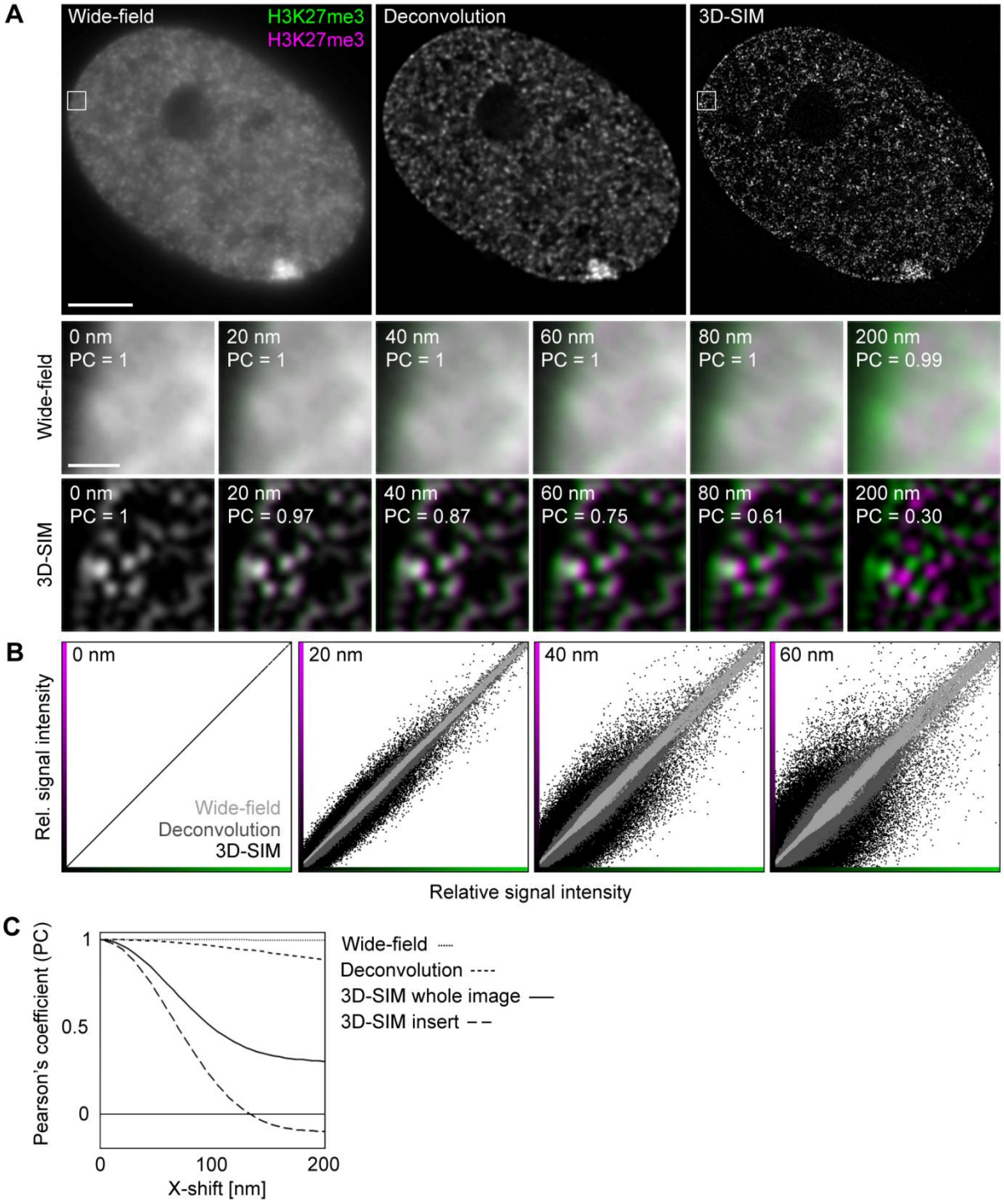

Figure 3-9 Colocalization values are dependent on the degree of resolution. (A) Single z-section of a typical IF staining at three different levels of resolution. One image has been copied into two different color channels (green and magenta). Lower panel shows a stepwise shift of the magenta channel in x-direction relative to the green one at defined distances and corresponding Pearson's coefficient (PC) at conventional wide-field and 3D-SIM resolution. Scale bar 5 µm, inset 0.5 µm. **(B)** Relative pixel intensity plots from the images shown in (A) at three different levels of resolution and with two color channels shifted next to each other at defined step sizes. **(C)** Pearson's coefficient as a function of the applied channel shifts. Note that at the level of 3D-SIM resolution, already small shifts lead to a significant drop in correlation, whereas for conventional microscopy, almost no drop can be observed under 200 nm. Figure modified after (Smeets et al., 2013a, *in press*).

Of note, at 3D-SIM resolution – even after perfect channel alignment – two kinds of signals will never appear as perfectly colocalizing, even if they detect the same target structures (e.g. one primary antibody detected by two differently labeled secondary antibodies). The inherent variation of an IF

staining is determined by the spatial orientation of an antibody complex, which can add up a distance of about 15 – 20 nm between epitope and fluorophore (Dong and Shannon, 2000; Silverton, 1977). For two differentially labeled fluorophores detecting the same epitope, this distance has to be doubled, which results in a size range of 30 – 40 nm that is already resolvable with 3D-SIM (Figure 3-9, A). Figure 3-9, B and C show that with 3D-SIM signals at a distance of ≥ 60 nm are already clearly resolvable as separate and thus yield according colocalization values. Therefore, it has to be noted that due to the higher resolution of 3D-SIM compared to conventional microscopy, colocalization values that have been obtained from different systems cannot be compared with each other.

Statistical analysis

To test the statistical significance of the outcome of the chromatin density segmentation or of the colocalization analyses, a Mann-Whitney U test has been performed using Microsoft Excel. This test compares two independent groups of results consisting of a small number of measurements (n) with each other. If the p-value of such a measurement, which describes the likelihood of a given result being a mere coincidence, is smaller than 0.05, then a result can be called statistically significant.

4 Results

4.1 Assessing the suitability of 3D-FISH for 3D-SIM

3D-FISH is a commonly used and widely distributed method to specifically visualize genomic sequences and analyze their position both during metaphase and interphase (Cremer et al., 2008; Foster and Bridger, 2005; Németh et al., 2010; Neusser et al., 2007). Yet, one major drawback is the necessity to denature the sample DNA in order to render it accessible for the detection with labeled probes. Denaturation requires the application of harsh thermal or chemical conditions, which potentially introduce small scale chromatin alterations that can counteract any benefits in resolution gain by 3D-SIM. Studies with conventional microscopy could not detect any major deteriorations of chromatin structure due to the FISH-treatment when comparing living to formaldehyde-fixed and ultimately to 3D-FISH-treated cells at this level of resolution. In contrast, at electron microscopic resolution chromatin structure appeared clearly destroyed (Solovei et al., 2002).

In the present work, it has been assessed at 3D-SIM resolution what kind of changes in chromatin structure are being introduced by the FISH treatment and especially the heat denaturation step (Markaki et al., 2012). A tailored 3D-FISH protocol has been applied, which has been optimized for structural preservation, and which also describes a method to relocate certain cells for multiple acquisitions under different fixation conditions with the 3D-SIM setup (Markaki et al., 2013). Several DAPI-stained C2C12 nuclei, previously seeded onto glass slides, have been imaged with 3D-SIM and their positions have been stored for relocation (for further details see Section 3.2.4, p. 57). Then, cells have been unmounted, subjected to (mock-) 3D-FISH treatment – including heat denaturation – DAPI stained for a second time and imaged again after relocation of previously acquired cells. Afterwards, the two image stacks, before and after FISH treatment, have been aligned as well as possible (see Figure 4-1, A). The entire nuclei showed a certain amount of shrinkage compared to the formaldehyde fixation and structural detail, especially in euchromatic areas, appeared affected. Nuclear regions with an *a priori* more compacted structure, like perinucleolar or peripheral heterochromatin, or chromocenters, seemed to be relatively resistant to the FISH treatment, which can be observed, for example, by the relatively well preserved chromatin voids underneath nuclear pores (see Figure 4-1, B).

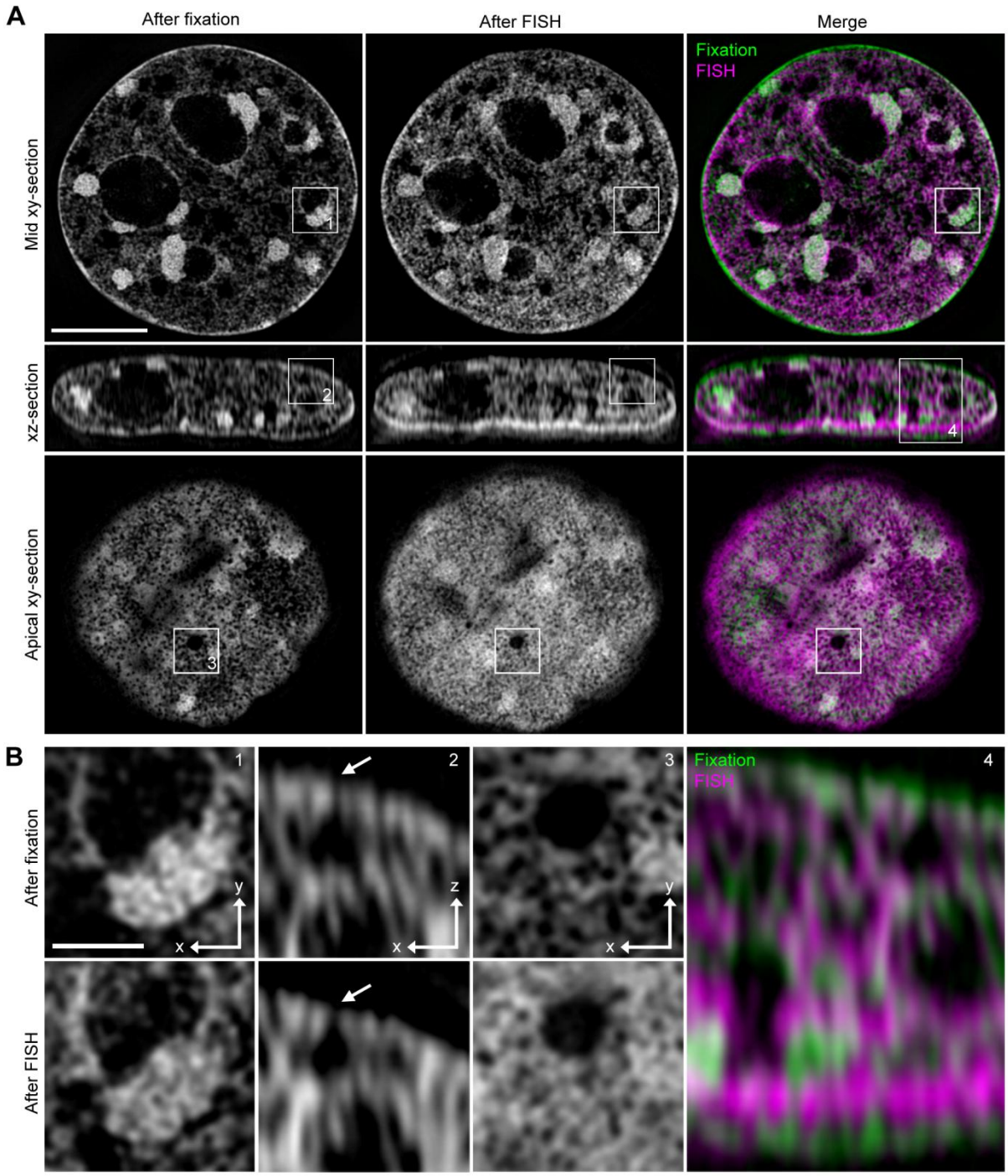

Figure 4-1 Effects on DAPI-stained chromatin before and after 3D-FISH treatment monitored in a single cell. (A) Single optical z-sections of a DAPI-stained C2C12 nucleus from a mid- and an apical xy-plain and an orthogonal mid xz-plain. Merging of the two signals shows a certain amount of shrinkage and a general broadening of euchromatic chromatin areas. Scale bar 5 µm. **(B)** Magnifications from the areas indicated in (A) depict a loss of structural detail and deterioration especially of euchromatic chromatin. More compacted chromatin sites, e.g. facultative heterochromatin around nucleoli, peripheral heterochromatin, including chromatin voids underneath nuclear pores (arrows) or chromocenters are surprisingly well preserved after the FISH treatment. Scale bar 1 µm. Figure modified after (Markaki et al., 2012).

These observations have also been quantified using a specifically designed chromatin density segmentation approach that has been developed together with Prof. Volker Schmid (Institute for Statistics, LMU Munich) and that is dividing the entire nucleus into seven different equal variance chromatin density classes according to the DAPI staining (for details about the algorithm and the

work-flow see Section 3.3.3, p. 71). This approach is a deliberate simplification of the data, but allows to statistically compare – in a user-independent manner – chromatin compaction between cells from different samples or, as in this case, cells before and after specific treatment with each other (see Figure 4-2, A). After FISH-treatment, a clear shift towards higher chromatin density classes could be observed with a particular increase of classes 5 and 6 and a corresponding loss of classes 1 and 2 (see Figure 4-2, B). This effect may be explained by the loss of structural detail due to the heat denaturation step that may especially deteriorate the structure of *a priori* decondensed chromatin sites and thus lead to an overall more homogenous appearance (in agreement to the visual impression in Figure 4-1).

Next, the impact of the 3D-FISH treatment on proteins of the nuclear envelope has been assessed at 3D-SIM resolution. The nuclear envelope is known as a functional compartment generally recruiting genes subjected to silencing. However, the picture might not be as simple, as not all genes located at the nuclear periphery are transcriptionally repressed (Deniaud and Bickmore, 2009; Kind and van Steensel, 2010). Especially the nuclear pores have emerged as a possible candidate to form a transcriptionally active micro-environment in this otherwise repressed nuclear neighborhood (Arib and Akhtar, 2011; Capelson et al., 2010; Egecioglu and Brickner, 2011; Vaquerizas et al., 2010). 3D-Immuno-FISH experiments with improved 3D-SIM resolution will be necessary in the future to shed light on this particular and on other related open questions.

In the present work, 3D-Immuno-FISH against Lamin B, the most common member of the Lamin family, and Nup 153, a component of the nuclear pore complex, has been performed (see Figure 4-3). The spatial relation of these two nuclear envelope proteins has already been analyzed in a pioneering work using 3D-SIM (Schermelleh et al., 2008). After 3D-Immuno-FISH, those two proteins maintain well preserved with no observable difference before and after 3D-FISH treatment, which is a prerequisite for future studies about the transcriptional chromatin

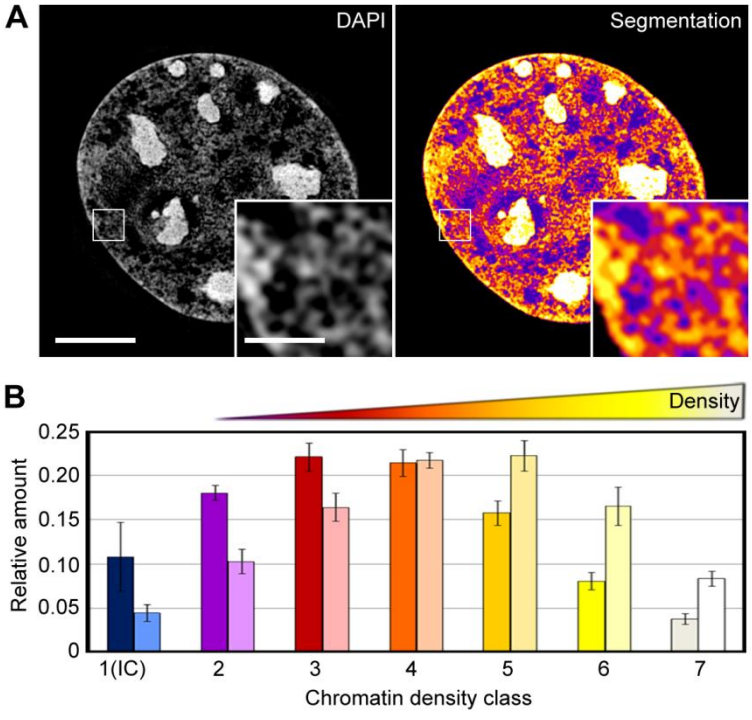

Figure 4-2 Quantification of chromatin density before and after FISH treatment. (A) Example of a single optical z-section of a DAPI-stained formaldehyde-fixed C2C12 nucleus (left) subjected to chromatin density segmentation (right). Scale bar 5 µm, inset 1 µm. **(B)** Quantification of chromatin density before (dark bars) and after (light bars) FISH treatment (n = 20). Bars show average values with respective standard deviation. Figure modified after (Markaki et al., 2012).

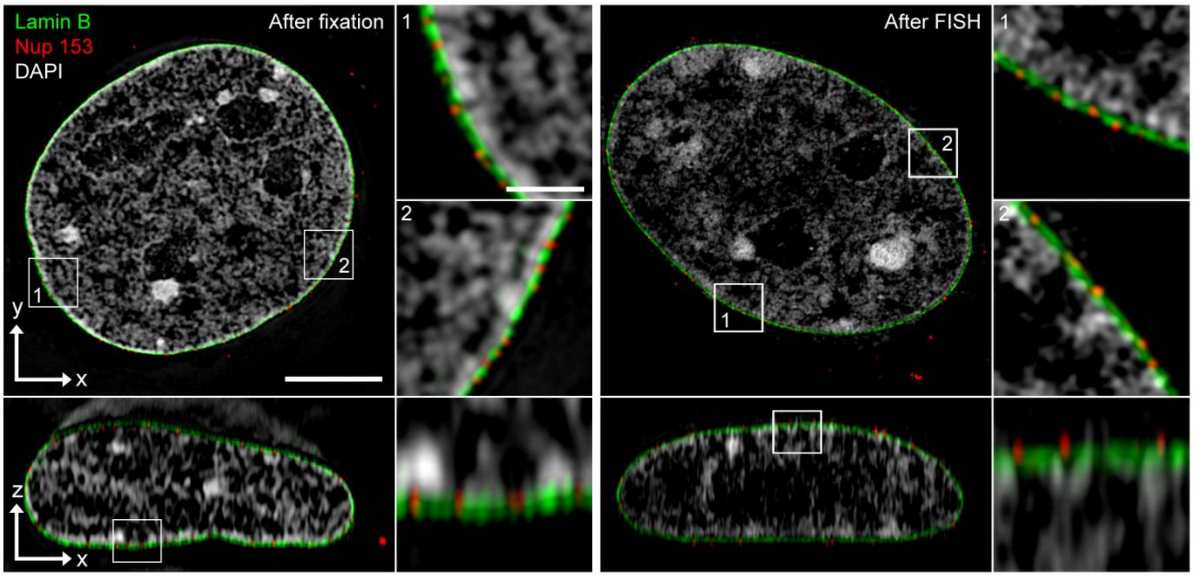

Figure 4-3 Effect of FISH treatment on nuclear envelope proteins before and after FISH treatment. Single optical z-sections of C2C12 cells subjected to an IF against Lamin B and Nup 153, part of the nuclear pore complex. These components of the nuclear envelope show no deterioration after the FISH treatment and maintain their spatial integrity. Scale bar 5 µm, insets 1 µm. Figure modified after (Markaki et al., 2012).

environment of the nuclear envelope (for further details see (Markaki et al., 2012).

In summary, 3D-FISH treatment has a clear deteriorating effect on chromatin structure on a scale, which is not visible by conventional microscopy, but becomes resolvable at 3D-SIM resolution. This negative effect, which is mostly caused by the necessary heat denaturation step, becomes already evident by DAPI staining, most dominantly in decondensed euchromatic sites, whereas generally more compacted nuclear areas seem to be less prone to alterations. Also, other nuclear structures like the nuclear envelope seem to be quite resistant to the 3D-FISH treatment and may well be a possible target for future studies combining 3D-FISH and 3D-SIM.

4.2 X chromosome inactivation analyzed with super-resolution 3D-SIM – Implications for a novel structural role for Xist RNA in XCI

The main focus of this work was to analyze the influence of epigenetic modifications on higher-order chromatin architecture. In this respect, Barr body formation during XCI acts as a paradigm due to the major chromatin re-organization, which is taking place during this process, and which is only based on epigenetic differences – not sequence differences – between Xa and Xi. To present, conventional light microscopy has been one of the major tools applied in studying higher-order chromatin structure, but as most processes are taking place at length scales below its reach many open questions remain unsolved so far. With the help of 3D-SIM, it is now possible in the present work to re-address some of these open questions and to contribute to new models about how epigenetic silencing of an entire chromosome is achieved during XCI and to draw conclusions about how chromatin is generally organized within the nucleus.

4.2.1 The chromatin architecture of the Barr body

Chromatin structure

A first approach to address chromatin organization of the Barr body and to compare it with the rest of the nucleus is to perform a DAPI staining and to image the result with 3D-SIM (see Figure 4-4, A, left). At conventional wide-field and subsequent deconvolution resolution, the Barr body appears as a uniformly compacted structure, whereas only at 3D-SIM resolution a complex folding sub-structure – with areas of decondensed chromatin even within the Barr body – emerges. DNA-FISH using whole-chromosome paint probes against Chr. X reveals that the compacted Barr body structure, as depicted by the DAPI staining, actually involves the entire X chromosome without any decondensed periphery (see Figure 4-4, A, mid and right). Instead, areas of decondensed chromatin can emerge throughout the entire Barr body volume, but are possibly skewed towards its periphery. The Xa territory on the other hand is clearly much more decondensed and cannot be distinguished from surrounding autosomal chromatin by the DAPI staining.

To quantify chromatin compaction within and around the Barr body, the tailored chromatin density segmentation approach that has been developed together with Prof. Volker Schmid (Institute for Statistics, LMU Munich). The outcome of this approach is also shown at the level of resolution achievable with wide-field and deconvolution for an exemplary Barr body and an autosomal region of the same nucleus. 3D-SIM resolution clearly offers a more complex view and shows that the Barr body harbors chromatin of all density classes, whereas for the two cases of conventional microscopy, it seems as if the Xi territory would consist of concentric layers of only the highest density classes with increasing compaction towards its center (see Figure 4-4, B). In autosomal chromatin, the

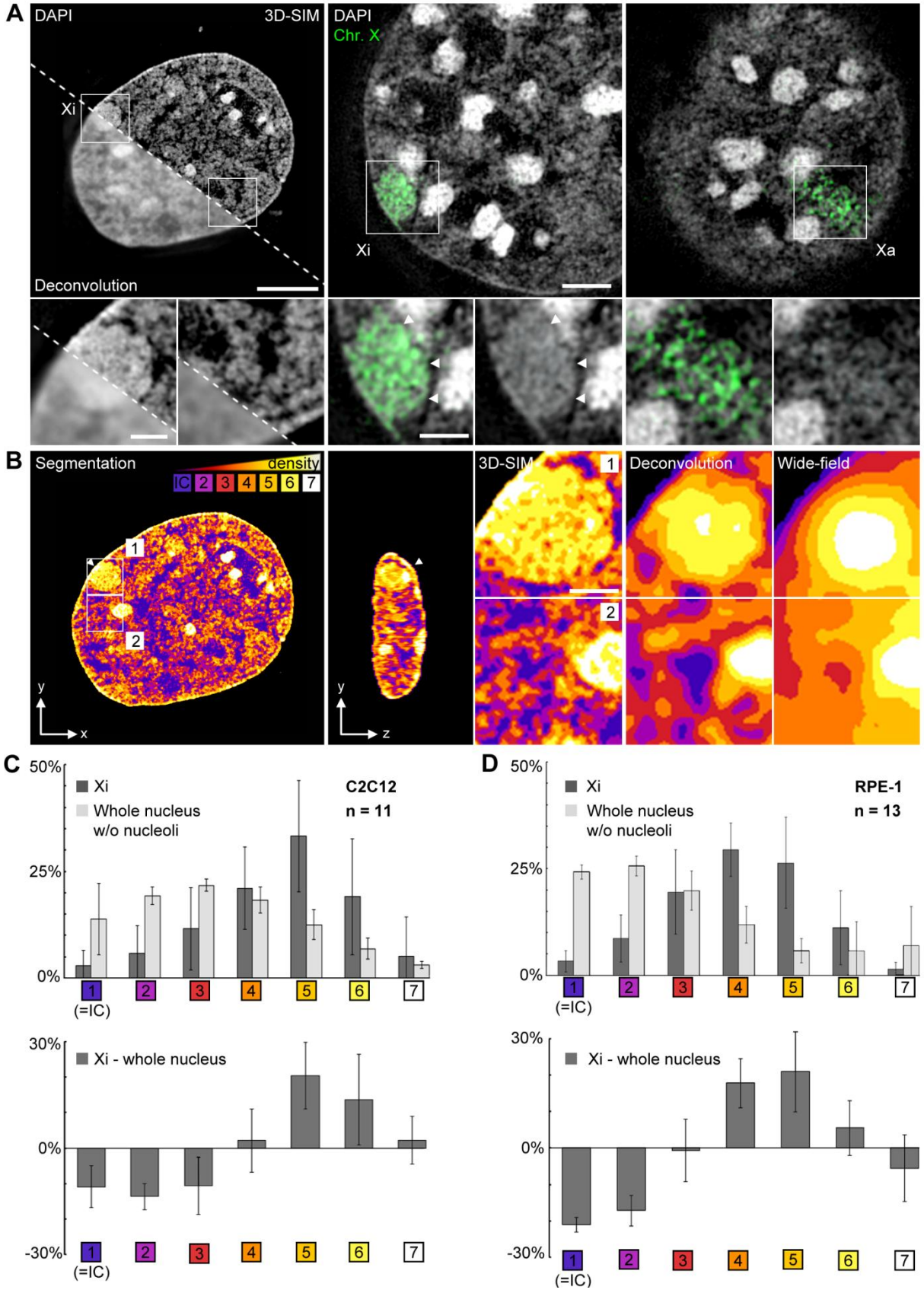

Figure 4-4 Mouse somatic C2C12 cell Barr body architecture at 3D-SIM resolution. (A) Left: Single optical z-section of a DAPI-stained mouse somatic C2C12 at wide-field + deconvolution (lower left) and 3D-SIM resolution (upper right). Insets show two exemplary sites of a Barr body and an autosomal region. Scale bar 5 µm, insets 1 µm. **Mid:** DNA-FISH using whole-chromosome paint probe against Chr. X together with DAPI. Arrowheads indicate that compacted chromatin in the DAPI staining coincides with Chr. X paint at the Xi. **Right:** Xa of the same nucleus at another z-section. Scale bar 2 µm, insets 1 µm. **(B)** *In silico* 3D chromatin density segmentation of the same nucleus shown in (A). Box 1 shows an exemplary region of

the Barr body and Box 2 from a neighboring autosomal region at 3D-SIM, wide-field + deconvolution and wide-field resolution. Scale bar 1 µm. **(C)** Quantification of chromatin density of 11 C2C12 nuclei in the Xi compared to the rest of the respective nucleus without nucleoli. Lower histogram depicts the difference between Xi and the rest of the nucleus in every chromatin density class. Indicated are average values with respective standard deviations. **(D)** The histograms are results of the same quantification approach from 13 human RPE-1 nuclei. Figure adapted from (Smeets et al., 2013b, *submitted*).

degree of chromatin compaction is locally highly variable, but typically consists of a compacted chromatin core (class 4 – 6) that is surrounded by the ANC network consisting of lower chromatin classes (2 – 3) and occasionally pervaded by wide IC lacunae, which is mainly reflected by a DAPI intensity below background level (class 1). In mouse nuclei, the highest density class 7 mainly represents the chromocenters.

Quantification of chromatin compaction (n = 11) reveals that the Xi in somatic mouse C2C12 cells is enriched in the high density classes 5 – 6 with a clear under-representation of the low density classes 1-3, but nevertheless contains all density classes. In contrast, autosomal chromatin in the entire nucleus (without nucleoli) is mostly built-up of the low density classes 1 – 3, with a high proportion of lowest density class 1, (see Figure 4-4, C). In human RPE-1 cells (n = 13) chromatin compaction in the Xi seems less pronounced and can be observed by a slight skewing towards lower density classes. Here, the highest over-representation can be found in classes 4 – 5 (see Figure 4-4, D).

This observation led to the assumption that Barr bodies might be more compacted in nuclei of mice than in those of humans. To further test this, the same evaluation has been carried out in Mouse Embryonic Fibroblasts (MEF) and Human Fibroblasts (HFb) (data not shown). However, no difference in Xi compaction could be observed between these two cell lines. The ratio was rather opposite, with the HFb Barr body being slightly more compacted – resembling C2C12 in this respect – than the MEF Barr body – resembling RPE-1. Thus, differences in Barr body compaction are rather cell-type than species-specific.

Active and repressive histone modifications

In order to analyze where active and repressive histone modifications are located in respect to chromatin and also to substantiate the chromatin density classification, an IF against H3K27me3 and H3K4me3 has been performed in C2C12 cells.

The repressive H3K27me3, typically enriched in facultative heterochromatin sites like the Xi or the nuclear periphery, coincides very well with sites of compacted chromatin and can mainly be found within condensed chromatin as depicted by DAPI staining (see Figure 4-5, A). However, in some cases it can also be found spanning the whole distance from the interior of a compacted chromatin site up to the border region between chromatin and the IC (e.g. Boxes 1 and 2). The active histone mark H3K4me3 on the other hand, is almost exclusively found in decondensed euchromatic regions at the periphery of compacted chromatin sites, at the interface to the IC.

Quantification of the preferred localization of the two histone modifications has been performed using the chromatin segmentation approach (n = 10; see Figure 4-5, B and C). It revealed that H3K27me3 is mostly enriched in chromatin classes 5 – 6 at the Xi, whereas H3K4me3 is significantly shifted to lower classes with enrichment at classes 3 – 4. In order to provide a more detailed localization distribution, the same analysis has also been performed with 32 instead of 7 chromatin density classes. Here, specific distribution of the two histone marks becomes even more apparent (see Figure 4-5, B). It has to be noted however that the Xi – as anticipated - does not contain many

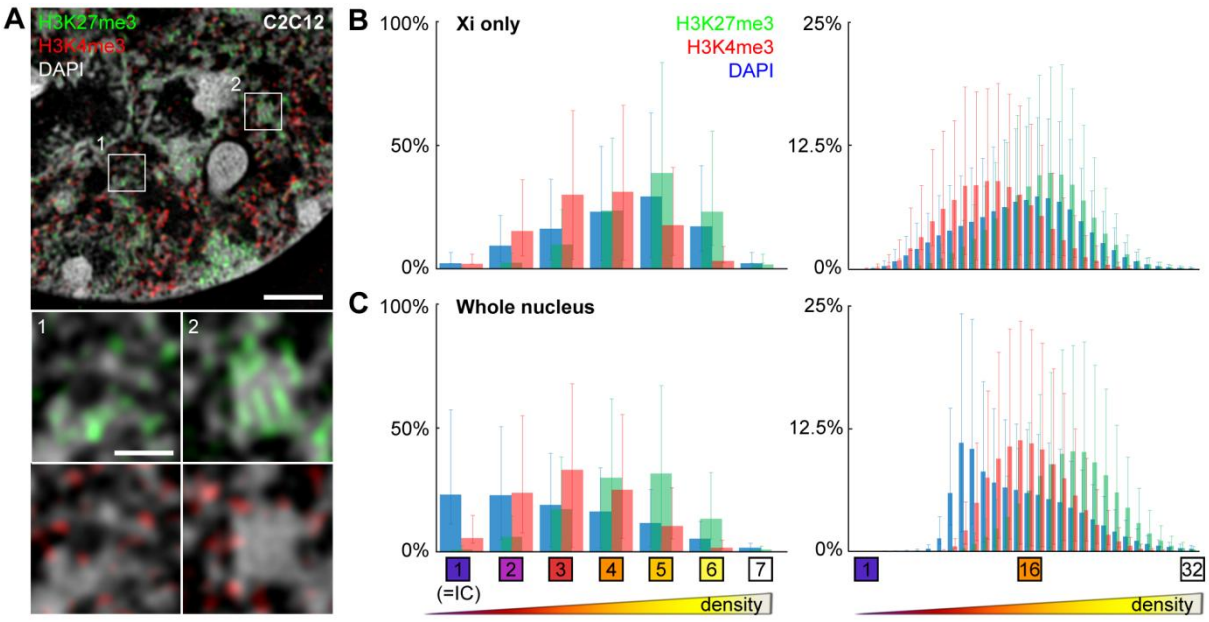

Figure 4-5 Localization of active and repressive histone modifications in respect to chromatin. (A) Single optical z-section of an IF against H3K27me3 and H3K4me3 in a C2C12 nucleus. H3K27me3 is preferably located within compacted chromatin regions, whereas H3K4me3 is preferably located within the PR, the transcriptionally competent border region between compacted chromatin and the IC. Scale bar 2 µm, inset 0.5 µm. **(B)** Quantification (n = 10) of H3K27me3 and H3K4me3 localization within DAPI chromatin density classes of signals within the Xi of the respective nuclei. Left panel: DAPI has been segmented into 7 equal variance density classes. Right panel: DAPI has been segmented into 32 equal variance density classes to better resolve histone localization. Histograms depict average values and bars define maximum and minimum values. **(C)** Same quantification as in (B), but from signals of the entire nuclei. Figure adapted from (Smeets et al., 2013b,*submitted*).

H3K4me3 signals, but the few remaining signals effectively reflect a distribution pattern similar to the entire nucleus (see Figure 4-5, C).

In summary, qualitative and quantitative analyses showed that active and repressive histone modifications are located within different chromatin compartments, coinciding with different distinguishable and resolvable chromatin density classes as determined by DAPI staining. This result comprises a good control that the different chromatin density classes can on average be linked to different functional compartments, with low density classes typically showing signs of transcriptionally active and high density classes of transcriptionally repressed chromatin.

Spatial organization of transcription

In a recently published work, the authors could show that active transcription is occurring exclusively within the PR, the locally confined zone with a diameter of 50 – 150 nm next to compacted chromatin sites, which becomes only resolvable with 3D-SIM and not with conventional light microscopy (Markaki et al., 2010). To analyze localization of transcription within the Barr body, an IF against RNAP II (Ser2P) and a RNA-FISH against Xist RNA has been performed in C2C12 and RPE-1 cells. In both cell types, active transcription could be found throughout the nucleus, but locally restricted to the PR, the interface between compacted chromatin and the IC. In mouse C2C12 nuclei, almost no signs of active transcription can be found within the Xist RNA volume of the Barr body (see Figure 4-6, A). Note that this is in line with the increased compaction found in this cell line and with the fact that mice display only ~3% XCI escape genes as opposed to ~15% in humans (Berletch et al., 2011).

In human RPE-1 nuclei, RNAP II signals could occasionally be found even within the Barr body (see Figure 4-6, B). But again, active transcription was found exclusively within the PR, which means in the case of the generally compacted Barr body structure that transcription required or resulted in a locally confined chromatin decondensation

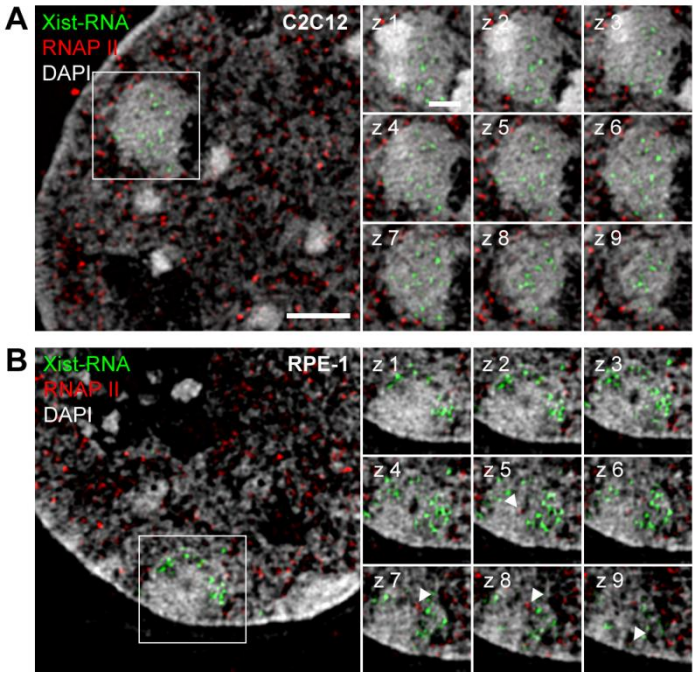

Figure 4-6 Spatial organization of active transcription in respect to chromatin in the Xi. **(A)** Single optical z-section of an RNA-FISH against Xist RNA and an IF against actively elongating RNAP II (Ser2P) in a C2C12 nucleus. Right panel shows subsequent z-sections of the depicted area (z-step size 0.125 µm). **(B)** shows the same staining in a human RPE-1 nucleus. Arrowheads indicate that RNAP II can be occasionally found within sites of decondensed chromatin even within the Barr body of RPE-1 cells. C2C12 Barr bodies are usually more compacted and show no active RNAP II signals. Scale bar 2 µm, inset 1 µm. Figure adapted from (Smeets et al., 2013b*, submitted*).

and that the functional compartment harboring transcription is, both in autosomal or Xi chromatin, in principle always identical.

Spatial distribution of replication

Besides transcription, DNA replication is one of the most important nuclear processes. A lot is known about the basic molecular events occurring during DNA replication, however, there is still a huge lack of knowledge how chromatin environment around replication foci during S-phase is organized in space and time (Baddeley and Chagin, 2010; Chagin et al., 2010). To test where in respect to higher-order chromatin architecture replication is taking place, a series of EdU pulse-chase labeling experiments together with an IF against PCNA, the main molecular loading platform directly at the replication fork, has been performed (Moldovan et al., 2007). Again, the Barr body has been used as a model system for the entire nucleus.

EdU has been added to the cell culture medium as described in Section 3.2.5 (p. 58) for a pulse length of 5 min and cells have been either fixed immediately for subsequent IF against PCNA, or EdU has been removed and cells have been fixed after variable chase time lengths (10 min – 60 min) (see Figure 4-7). The EdU gets incorporated into newly synthesized DNA and PCNA signals directly mark the position of replication forks. For 3D-SIM acquisition, cells in mid S-phase have been selected, the time point at which facultative heterochromatin including the Xi gets replicated.

Cells, which have been fixed directly after the EdU pulse show a vast amount of colocalization between EdU and PCNA signals, both of which are located within decondensed regions of the Barr body (see Figure 4-7, A). The replication fork and newly synthesized DNA have not had enough time to separate and are obviously still part of a very decondensed chromatin environment. The same picture is still true for cells with 10 min chase time between EdU pulse and fixation. Only after 20 min chase time, a clear separation between the two signal classes becomes visible, which is fully developed after 60 min chase time. At these late time points past 20 min chase time, the PCNA signals indicating the position of the presently active replication forks are still located within decondensed chromatin sites, as visible by DAPI staining, whereas the newly synthesized DNA is already re-packed into the compacted chromatin of the Barr body. This observation illustrates that large-scale chromatin reorganization events as necessary, e.g. during replication, are taking place within a locally defined space and reorganization between DNA unpacking and re-compaction occurs at size scales of possibly only 50 – 200 nm, and thus beyond the limit of conventional resolution. Further, Barr body and autosomal chromatin show obviously no apparent differences in separation rate between the two signal classes (see Figure 4-7, B), which argues that chromatin organization in the Barr body is not fundamentally different compared to autosomal chromatin.

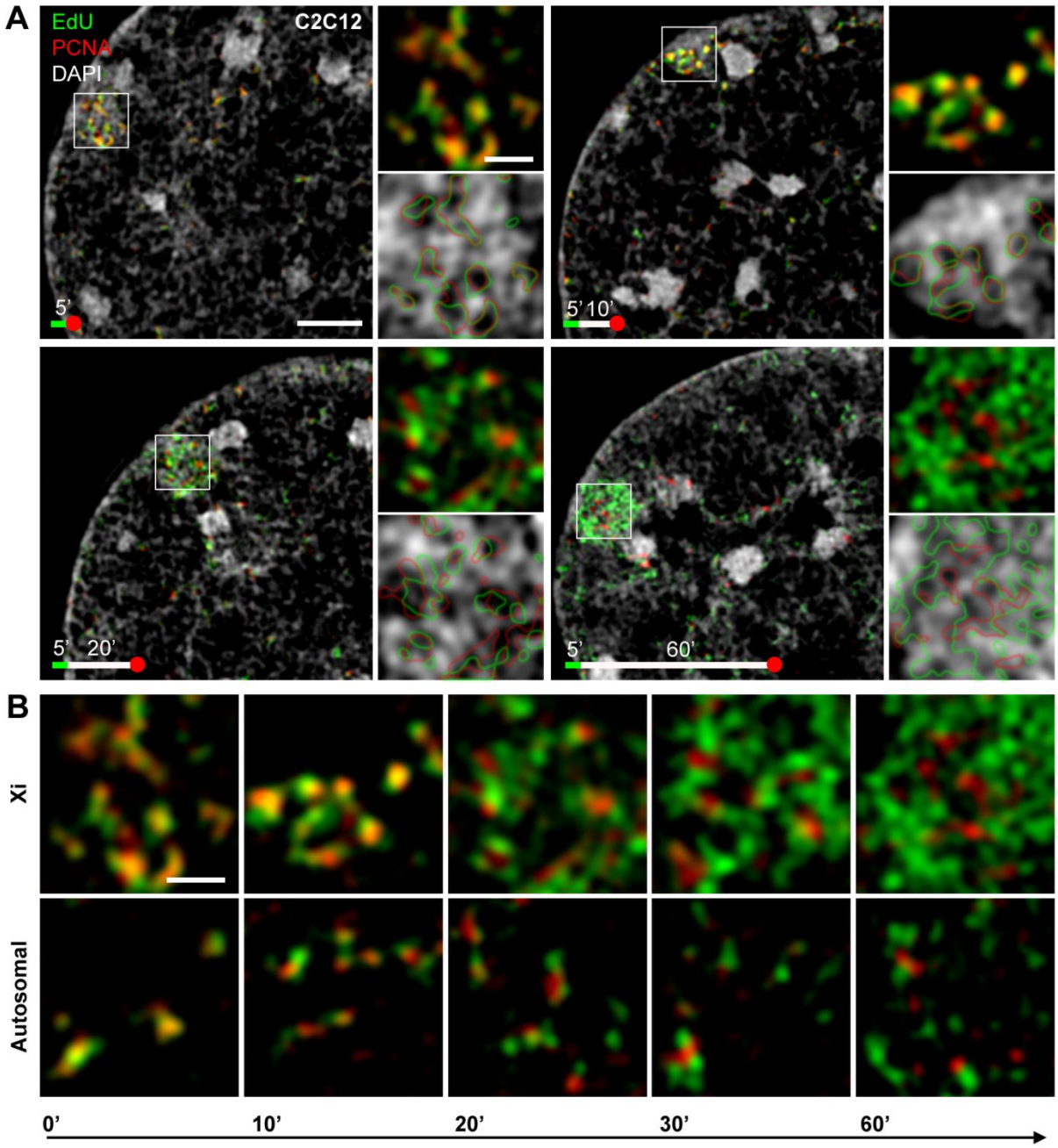

Figure 4-7 Spatial distribution of active transcription in respect to chromatin in the Xi. (A) Single optical z-sections of a series of pulse-chase experiments in C2C12 cells with 5 min. EdU pulses and an IF against PCNA after fixation. Upper insets show only EdU and PCNA signals at the Xi and lower signals show respective chromatin environment with outlined position of EdU and PCNA signals. Scale bar 2 µm, insets 0.5 µm. **(B)** Time series of EdU and PCNA signals separation rate from Xi and autosomal regions of the cells depicted in (A). 30 min. is not shown in (A). Scale bar 0.5 µm. Data generated and kindly provided by Susanne Fiedler during the course of her Bachelor thesis (Fiedler, 2011).

In summary, the functional relevant chromatin compartment, in which replication is taking place is again – as for transcription – the border region between compacted chromatin and IC, which is commonly referred to as PR, therefore providing further evidence for the until now not unequivocally accepted CT-IC model. Moreover, the finding that the separation rate between replication fork and newly synthesized DNA is not distinguishable argues that the principle underlying chromatin organization is very similar.

Contiguous ANC network pervades the entire nucleus including the Barr body

In the last two paragraphs of this work, it has been shown that transcription and replication are located within a decondensed chromatin environment, where they possibly have access to all kinds of essential nuclear factors, like RNAP II, transcription factors, histone modifiers or the replication machinery. This provides a further functional link between chromatin decondensation as seen by DAPI and an active nuclear compartment (ANC) serving as a hub for all major nuclear processes as proposed by the CT-IC model (Cremer and Cremer, 2010; Lanctôt et al., 2007; Markaki et al., 2010; Niedojadlo et al., 2011).

Here, it has been tested whether the ANC really forms an interconnected network that can be followed throughout the entire nucleus and whether the Xi is also part of this system. Optical z-sections of a DAPI-stained C2C12 nucleus show that autosomal chromatin regions are built-up of highly variable and probably very dynamic clusters of compacted chromatin, which are pervaded by relatively large regions without or little DAPI staining (IC-lacunae). Neighboring Xi chromatin, on the other hand, is also built-up of compacted chromatin clusters of variable intensity and shape and is also pervaded by regions of

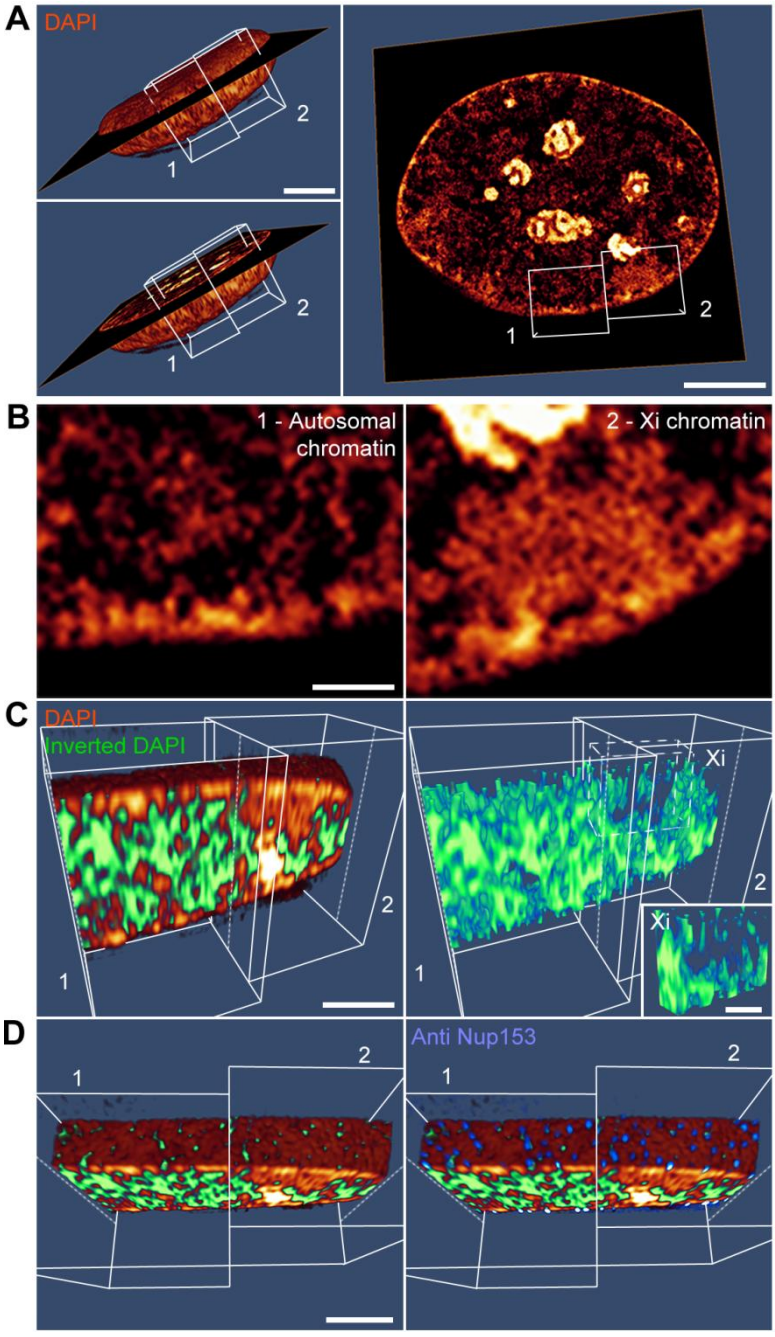

Figure 4-8 3D rendering of chromatin and the ANC in a C2C12 nucleus. (A) 3D rendering of a DAPI-stained C2C12 nucleus. Left panels indicate the positions of exemplary autosomal (1) and Xi chromatin (2). Right panel shows a single optical z-section of this nucleus. Scale bar 2 µm. **(B)** Magnifications of the exemplary regions shown in (A). Scale bar 0.5 µm. **(C)** 3D rendering of DAPI staining and the inverted DAPI signal, which reflects the – per definition – DNA-free IC, from areas (1) and (2). Right panel shows only the 3D rendering of the IC and dashed lines mark the position of the Xi. Scale bar 2 µm. **(D)** Top-view of the same volume renderings as in (C). IF against Nup153, a component of the nuclear pore complex confirms that the IC ultimately leads to nuclear pores. Figure adapted from (Smeets et al., 2013b*, submitted*).

lesser chromatin density. The Xi is obviously mostly lacking bigger IC lacunae, but importantly still shows narrow channels of lower DAPI intensity throughout the Xi (see Figure 4-8, A and B). 3D-volume rendering using the commercial software Amira reveals that chromatin clusters are interconnected with each other and form a contiguous network of large resolvable bundles throughout the entire nucleus. To visualize the ANC, the inverted DAPI signal has been used, which has been volume rendered as well. Whereas autosomal chromatin is pervaded by a broad network of ANC channels and lacunae, the Xi has retained only a narrow, rudimental – but nevertheless still present – ANC system (see Figure 4-8, C). However, corresponding to autosomal chromatin, the ANC of the Barr body also forms a contiguous network, which is connected to the ANC of the rest of the nucleus and/or can ultimately be followed through peripheral heterochromatin to nuclear pores (see Figure 4-8, D).

Live-cell 3D-SIM confirms general features of chromatin architecture and verifies DAPI as a suitable chromatin marker

In order to be able to judge the impact of fixation on the appearance of chromatin organization, live-cell super-resolution 3D-SIM imaging of HeLa H2B-GFP cells has been performed using the OMX V3 Blaze setup (API/ GE Healthcare, Micron Imaging Facility, University of Oxford, UK). In the present work, live-cell super-resolution has been performed world-wide for the first time on mammalian cell nuclei, to the author's knowledge to date. H2B-GFP comprises a good control for whole-chromatin stainings as it is almost fully incorporated into chromatin with only a negligible free unbound fraction and non-preferential incorporation throughout the genome (Kimura and Cook, 2001).

Comparison between living and formaldehyde-fixed HeLa H2B-GFP cells reveals no observable difference in overall chromatin structure. Characteristic properties of nuclear architecture like a chromatin-free IC network or chromatin voids underneath nuclear pores are present both in living and fixed cells to an obviously similar degree (see Figure 4-9, A). Thus, these fundamental features of chromatin organization do not represent fixation artifacts.

Furthermore, H2B-GFP could be used to control how suitable DAPI staining is as a whole-chromatin marker. DAPI has been used throughout this study due to its unreached photostability, appropriate emission in the blue range, low unspecific background and easy applicability. Still, DAPI has been reported to have a staining preference for AT-rich sequences, which may impede with detection of GC-rich sequences and thus have a negative effect on its suitability as a whole-chromatin marker (Chazotte, 2011). Simultaneous imaging of H2B-GFP and DAPI in formaldehyde-fixed and permeabilized stably expressing HeLa cells, prepared under standard IF conditions, resulted in a vast amount of overlap between the two chromatin stainings even at sites of very decondensed chromatin (see Figure 4-9, B). Also heterochromatic sites like the nuclear periphery and their

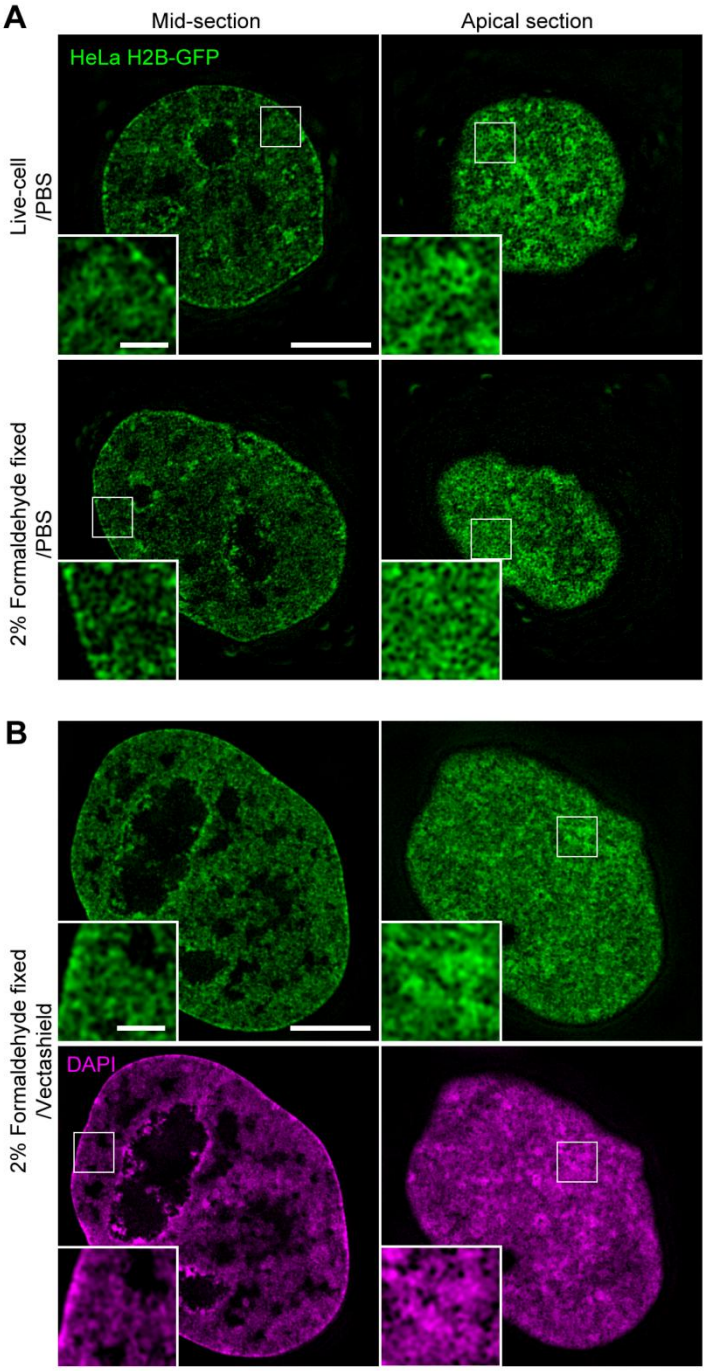

Figure 4-9 Live-cell super-resolution imaging of HeLa H2B-GFP cells. (A) Upper panel shows a living HeLa cell stably expressing H2B-GFP mounted in 1x PBS and imaged with an OMX V3 Blaze 3D-SIM setup (University of Oxford, UK). Lower panel shows a cell of the same cell line that has been fixed with 2% formaldehyde and mounted and imaged under the same conditions. Scale bar 5 µm, inset 1 µm. **(B)** HeLa H2B-GFP has been formaldehyde fixed, permeabilized, DAPI stained and mounted in Vectashield, all under standard IF conditions, and also acquired on the OMX V3 Blaze system. Scale bar 5 µm, inset 1 µm. Figure adapted from (Smeets et al., 2013b,*submitted*).

characteristic chromatin voids underneath the nuclear pores could be considered identical between both markers.

These results confirmed the general suitability of DAPI staining and the applied formaldehyde-fixation protocol for analysis of chromatin structure at 3D-SIM resolution.

In summary, the Barr body constitutes an overall more compacted chromatin entity compared to autosomal chromatin. Nevertheless, all chromatin density classes are still present in the surprisingly heterogeneous higher-order folding structure, as revealed by chromatin density segmentation at 3D-SIM resolution. Moreover, no decondensed periphery, harboring all X-linked genes, around a compacted core, consisting of all X chromosome repetitive elements, could be found as hypothesized in earlier studies carried out with conventional microscopy (Chaumeil et al., 2006; Clemson et al., 2006; Wutz, 2011). Instead, the entire X chromosome sequence seems to contribute to the compacted Barr body structure. On the smaller scale of individual resolvable chromatin bundles, the segmentation of chromatin into different density classes could be confirmed and functionally linked to a specific enrichment of the active histone modification H3K4me3 to the PR and of the repressive histone modification H3K27me3 to the core of compacted chromatin bundles. Sites of active transcription as well as sites of DNA replication proved to be restricted to the ANC. This was the case

both for Barr body and for autosomal chromatin, with the sole difference that vast decondensed regions (IC lacunae) can be found throughout autosomal chromatin – probably organized in a highly dynamic but very small scale fashion – whereas in the Barr body decondensation is locally very restricted and the still present ANC appears narrowed and collapsed. Here, opening of the surrounding chromatin environment is probably a prerequisite or direct effect of nuclear processes like transcription and DNA replication. Analyzing chromatin architecture in 3D revealed that chromatin bundles are interconnected throughout the entire nucleus and that the chromatin permeating ANC compartment comprises an interconnected network, too, which ultimately leads to nuclear pores. Furthermore, the Barr body is equally connected to this fundamental nuclear organization system and does not represent a uniformly compacted inaccessible entity, as could have easily been concluded with conventional resolution microscopy. Last, super-resolution imaging of H2B-GFP in living and fixed cells confirmed that any data about chromatin structure generated under IF conditions as described in this work, is not suffering from fixation artifacts. Concomitantly, it could be verified that DAPI staining, which has been used here as the standard DNA counterstaining dye due to its photochemical properties, is generally suited as a whole-chromatin marker and does not propagate any bias in chromatin coverage.

All these findings lead to the conclusion that chromatin organization in the Barr body reflects a special case of an otherwise conventional nuclear architecture.

4.2.2 Xist RNA is preferentially located within decondensed chromatin sites in somatic cells

The 17 kb long (human), or 15 kb (mouse) respectively, non-coding RNA Xist is the key initiator of XCI during embryogenesis and continues to play a vital role in Barr body maintenance even in fully differentiated somatic cells. Yet, how Xist RNA is able to play this role, whether and which other factors are involved in this process, is until today mostly elusive. In fact, it is even unclear, if Xist RNA is directly binding to DNA or if it is dependent on protein mediators to ensure its propagation along the X chromosome *in cis* and to initiate and maintain the entire chromosome's transcriptional silencing. Due to fact that Xist is an RNA, which makes it *per se* sensitive to degradation and because of its relatively big length, makes Xist RNA quite difficult to analyze with biochemical and genetic methods. Thus, microscopy techniques were commonly left as the methods of choice in studying the role of Xist RNA in Barr body formation, which in turn were limited by the lack of resolution of conventional microscopy. In the present work, 3D-SIM was applied to further investigate the

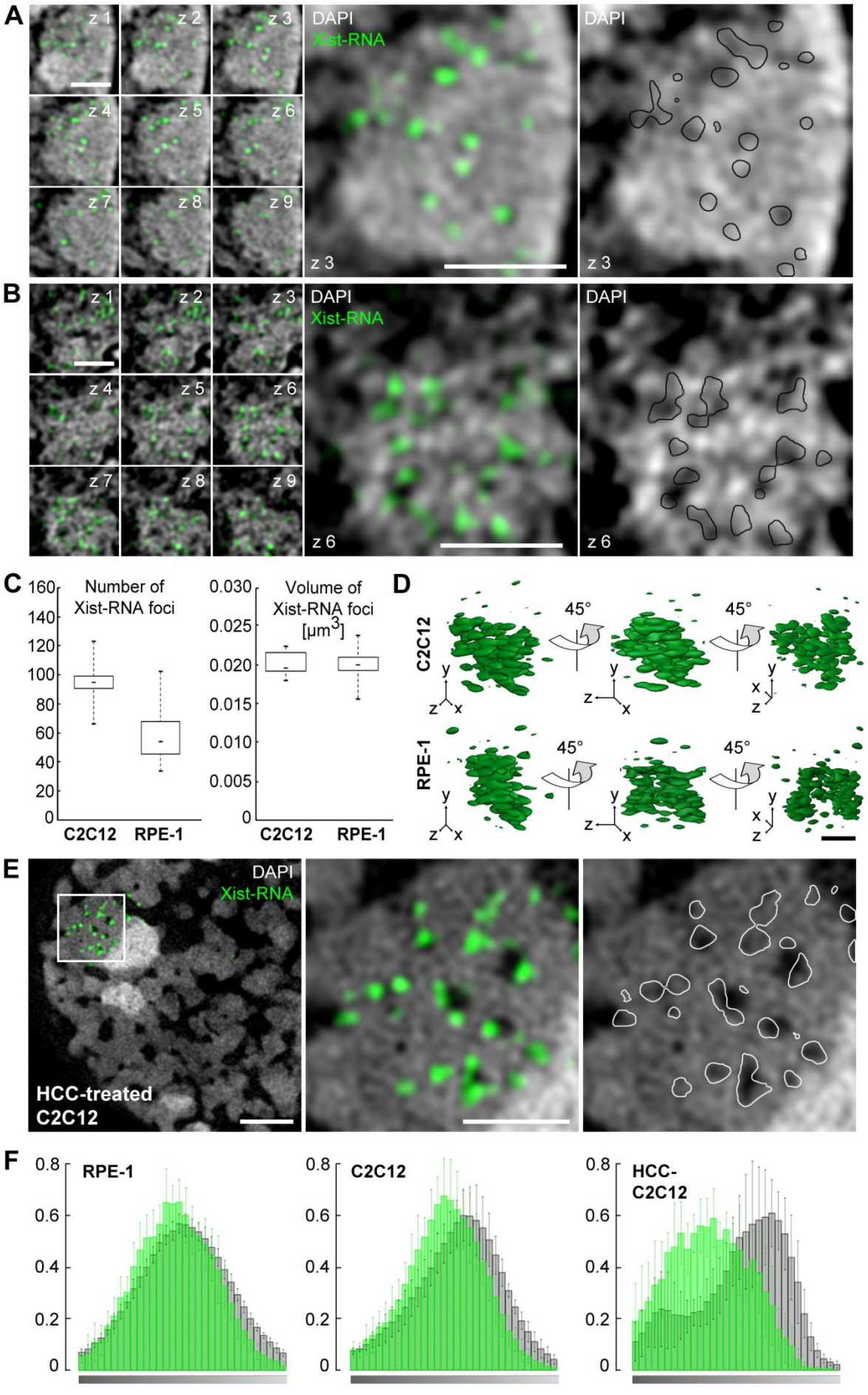
A
z 1
z 2
z 3
z 4
z 5
z 6
z 7
z 8
z 9
DAPI
Xist-RNA
z 3
DAPI
z 3
B
z 1
z 2
z 3
z 4
z 5
z 6
z 7
z 8
z 9
DAPI
Xist-RNA
z 6
DAPI
z 6
C
Number of Xist-RNA foci
160
140
120
100
80
60
40
20
0
C2C12
RPE-1
Volume of Xist-RNA foci [µm3]
0.030
0.025
0.020
0.015
0.010
0.005
0
C2C12
RPE-1
D
C2C12
RPE-1
45°
45°
45°
45°
y
z
x
E
DAPI
Xist-RNA
HCC-treated C2C12
F
RPE-1
C2C12
HCC-C2C12
0.8
0.6
0.4
0.2
0

Figure 4-10 Xist RNA is located in the decondensed regions of the Barr body in somatic cells. (A-B) Single optical z-sections (z-step size 0.125 µm) through a mouse C2C12 **(A)** and a human RPE-1 **(B)** Barr body with RNA-FISH against Xist RNA. Xist RNA can be found throughout the entire volume of the Xi, excluding the adjacent (probably Xi-) chromocenter (z 1). Magnifications illustrate that Xist RNA is preferentially being found directly within or outlining the decondensed ANC regions of the Barr body, but excluded from sites of compacted chromatin. Scale bars 1 µm. **(C)** Boxplot quantifications of individual discernible Xist RNA foci. C2C12 Xis have a median number of 95 Xist RNA foci (n = 10), RPE-1 Xis a median number of 54 (n = 22). Individual foci show very similar volumes of 0.0195 µm³ (C2C12) and 0.0198 µm³ (RPE-1) in both cell types. **(D)** 3D volume renderings of Xist RNA signals from the Xis shown in (A) and (B). Xist RNA foci adopt a variable shape varying from sub-diffraction point-like to elongated fibrillar structures. Scale bar 1 µm. **(E)** HCC treatment of a C2C12 nucleus leads to an exaggeration of pre-existing IC channels. This reversible treatment emphasizes that Xist RNA is found preferentially within decondensed areas of the Barr body. Scale bar 2 µm, insets 1 µm. **(F)** Quantification of preferred Xist RNA localization using the DAPI chromatin density segmentation approach. X-axis shows increasing DAPI intensity, y-axis shows the fraction of Xist RNA for every DAPI intensity class. Xist RNA distribution is significantly shifted towards lower density DAPI classes in all three measurements ($p < 0.001$ using Chi² test). Figure adapted from (Smeets et al., 2013b, *submitted*).

localization of Xist RNA in the Barr body to help elucidate its role in XCI, which in turn may lead to general conclusion about the organization of higher-order chromatin structure.

RNA-FISH against Xist transcripts does not require a denaturation step of the sample DNA, thus nuclear morphology remains unchanged and shows no difference to IF-treated samples, which makes RNA-FISH a generally suitable method for super-resolution analyses. RNA-FISH against Xist RNA in somatic nuclei of mouse C2C12 and human RPE-1 cells showed that Xist RNA is distributed as distinct discernible foci with variable shapes ranging from sub-diffraction sized point-like to elongated fibrillar structures throughout the entire volume of the Xi (see Figure 4-10, A, B and D). This possibly reflects locally different concentrations along the Xi sequence and varying RNA-conformations and degrees of conglomerations, but also dismisses the view of an indifferent “Xist RNA cloud” all around the Xi. In respect to chromatin, Xist RNA is not distributed evenly within the Barr body, but adapts a preferential localization within less intense DAPI-stained regions, excluding compacted chromatin sites. Mouse C2C12 cells have almost twice as many (95) discernible Xist RNA foci as human RPE-1 cells (54), whereas individual foci occupy similar volumes (~ 0.02 µm³) in both cell types arguing for a similar conformation (see Figure 4-10, C, D). To further investigate the localization of Xist RNA in respect to chromatin, C2C12 cells have been treated with osmotic conditions that reversibly induce hyper-condensation of chromatin (HCC; see Figure 4-10, E) (Albiez et al., 2006). Due to this treatment, pre-existing IC channels get widened and emphasized. This leads to an increased visibility of the preferred localization of Xist RNA within or next to sites of decondensed chromatin in the Barr body. Quantification using the DAPI density segmentation approach revealed that the preferred localization of Xist RNA within less condensed chromatin is highly significant ($p < 0.001$, Chi² test; see Figure, 4-10, F).

To further visualize the preferred localization of Xist RNA within low density chromatin, the Xist RNA signal has been superimposed over a chromatin density segmented C2C12 nucleus (see Figure 4-11, A). Here, Xist RNA signals are clearly located within density dips in most cases. However, in absolute terms these dips correspond to the relatively high classes 4 and 5, which can be explained by the generally high density of the Barr body compared to surrounding autosomal regions. Nevertheless,

these Xist RNA signals harboring chromatin sites may have a quite high intensity in absolute terms, in the context of the Barr body, they reflect low density chromatin, part of the ANC channel system. This fact becomes much clearer when the Xist RNA signals get superimposed onto chromatin, where only the Xi, not the entire nucleus, has been subjected to segmentation (see Figure 4-11, B).

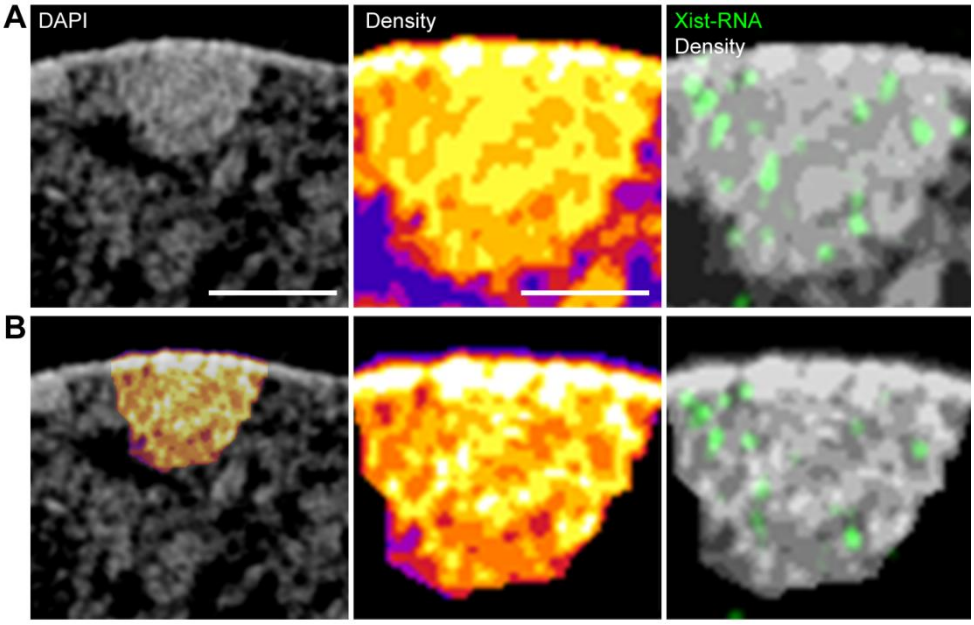

Figure 4-11 Preferential localization of Xist RNA within low density chromatin classes. (A) Entire C2C12 nucleus has been chromatin density segmented and Xist RNA signal has been superimposed afterwards. Scale bar 2 µm, inset 1 µm. **(B)** The Xi has been cut out prior to segmentation and the analysis has been applied only to the Xi, resulting in a finer segmentation of the Xi chromatin. Figure adapted from (Smeets et al., 2013b, *submitted*).

4.2.3 Xist RNA strongly colocalizes with the ANC-enriched nuclear matrix protein SAF-A

Earlier studies have provided evidence that the nuclear matrix protein SAF-A is important for Xist RNA attachment to the Xi. Hints came from the observation that SAF-A:GFP fusion proteins are enriched on the Xi and specific SAF-A knock-down leads to release of Xist RNA from the Xi (Hasegawa et al., 2010; Helbig and Fackelmayer, 2003). Yet, final evidence remained inconclusive as experiments with conventional microscopy showed no colocalization with Xist RNA. SAF-A even appeared to be excluded from the Xi when using SAF-A specific antibodies.

Using 3D-SIM and an improved high-affinity SAF-A antibody (raised against the full-length mouse SAF-A isoform; kindly provided by A. Tattermusch, Brockdorff Lab, University of Oxford, UK) showed that in C2C12 cells SAF-A is exclusively located within the transcriptionally competent ANC, but was clearly under-represented at the Xi compared to the staining in the entire nucleus (see Figure 4-12, A). However, some remaining SAF-A signals could still be detected within the narrow ANC of the Xi, too, where they showed a close – though not complete – spatial overlap with Xist RNA. In contrast to C2C12, RPE-1 cells showed a generally reduced pan-nuclear SAF-A abundance and the very sparse remaining signals in the Xi provided almost no colocalization with Xist RNA (see Figure 4-12, B).

These observations may be explained by a Xi-specific post-translational modification of SAF-A that is not well recognized by the antibody (see also Hasegawa and Nakagawa, 2011). This antibody detection issue may be even stronger in human cells as the antibody has been raised against the mouse SAF-A isoform and sequence alignment confirms about 10% divergence between the two isoforms (data not shown). HCC-treatment in C2C12 cells further emphasized the under-representation of SAF-A from the Xi, where it appeared almost excluded, but still showed vast overlap with Xist-RNA at the periphery of the Xi (see Figure 4-12, C).

To further address this antibody-borne issue on SAF-A affinity, both cell lines have been transiently transfected with either mouse or human SAF-A:hrGFP fusion proteins and subsequently hybridized against Xist RNA (see Figures 4-12, D and E). The hrGFP-signal had to be post-detected with an anti-hrGFP-antibody, as the hrGFP is sensitive to formamide and thus does not survive the RNA-FISH treatment. In contrast to the IF staining, SAF-A:hrGFP has been enriched at the Xi in both cell lines, conclusive to reports in earlier studies (Helbig and Fackelmayer, 2003), but was still located exclusively within the ANC as revealed by 3D-SIM. Upon visual inspection, in C2C12 cells the overlap with Xist RNA signals appeared to be even stronger than for the former IF signal, with every Xist RNA focus being associated to a SAF-A signal throughout the entire Xi. In line with this, hSAF-A:hrGFP colocalization with Xist RNA appeared highly increased in RPE-1 cells, too, providing further evidence for the proposed antibody-borne issue.

Quantification of colocalization between the different signal pairs confirmed that there is a strong spatial interaction between SAF-A and Xist RNA, both in mouse and human cells (see Figure 4-12, F). It should be noted here that colocalization values strongly depend on the resolution of the applied system and that at 3D-SIM resolution two signals already appear as being separate at a distance of more than 60 – 80 nm (see Figure 4-12, G; see also Section 3.3.3, p. 74). Thus, for a pair of colocalizing signals, e.g SAF-A and Xist RNA, an average distance of less than 60 – 80 nm can be assumed.

These results further pronounce a direct interaction between Xist RNA and SAF-A, strengthening evidence for its important role in XCI. The results also strongly argue for the presence of a Xi-specific post-translational modification of SAF-A, which may be either a prerequisite for its interaction with Xist RNA or a direct consequence thereof.

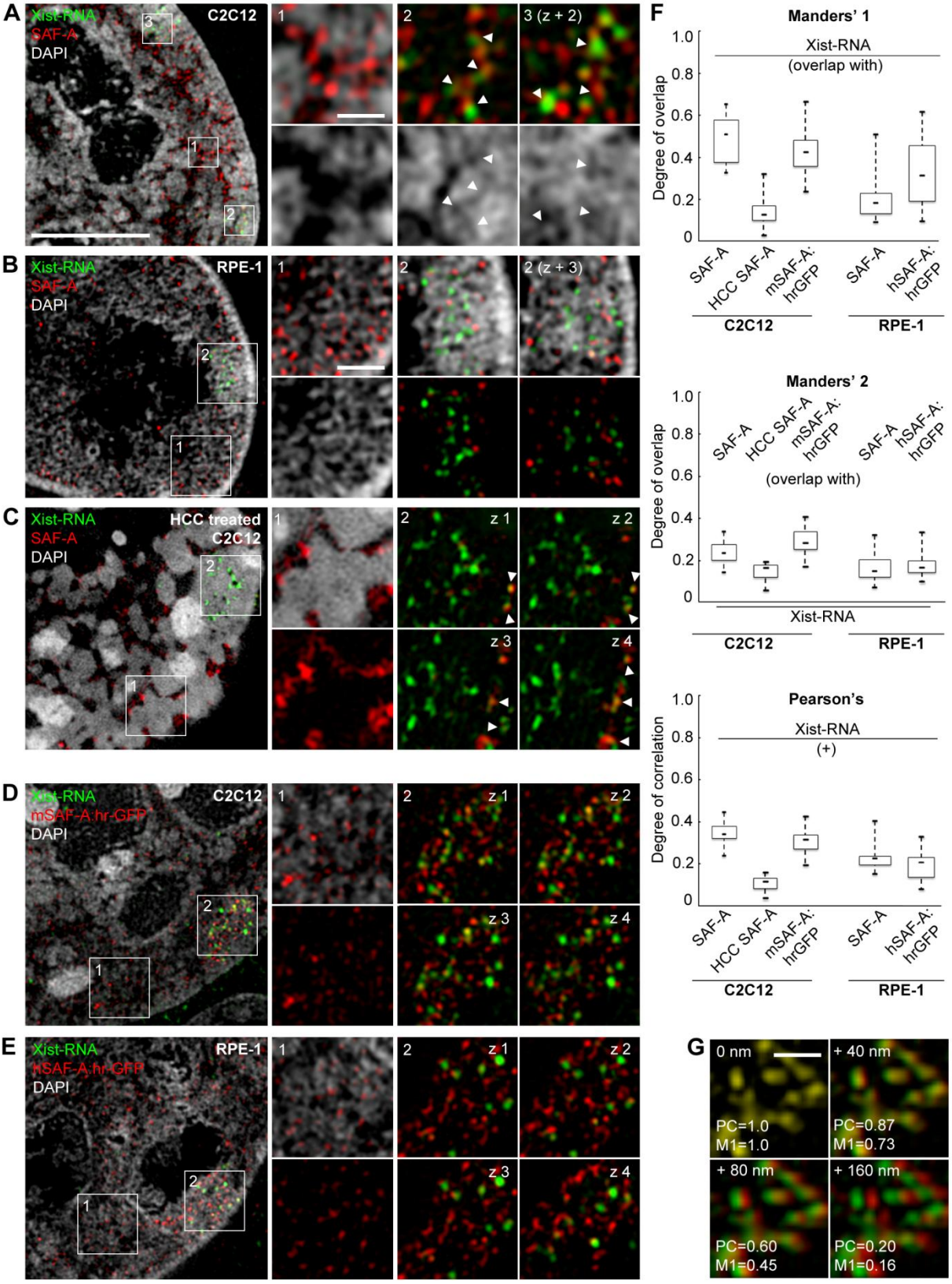

Figure 4-12 Xist RNA colocalizes with the ANC-enriched nuclear matrix protein SAF-A. (A) RNA-Immuno-FISH against the nuclear matrix protein SAF-A and Xist RNA in a C2C12 cell. **Inset 1** shows that SAF-A is exclusively found throughout the ANC of the entire nucleus. **Inset 2** and **3** illustrate under-representation of SAF-A at the Xi. However, the few remaining SAF-A signals can also be found within the small ANC of the Xi, where they form a tight – though not complete – association with Xist RNA. Scale bar 5 µm, inset 0.5 µm. **(B)** In RPE-1 cells, the SAF-A staining is less abundant than in C2C12, but still shows enrichment within the ANC of the entire nucleus (**inset 1**) and an under-representation within the Xi. In contrast to C2C12, the few remaining SAF-A signals in the Xi show almost no overlap with Xist RNA (**insets 2** and **3**). Inset scale bar 1 µm. **(C)** HCC-treated C2C12 cell emphasizes SAF-A localization within the ANC (**inset 1**) and its under-representation within

the Xi (**insets 2**). Insets 2 show subsequent z-sections (step size 0.125 µm). Arrowheads mark strong association of SAF-A with Xist RNA at the periphery of the Xi. Note extensive exclusion of SAF-A from the interior of the Xi. **(D)** C2C12 transiently transfected with mSAF-A:hrGFP and subsequent RNA-FISH against Xist RNA. Note that the SAF-A:hrGFP-fusion protein is also located within the ANC (**inset 1**), but in contrast to the IF signal is enriched at the Xi (**insets 2**). Subsequent z-sections show that Xist RNA and SAF-A:hrGFP are tightly associated throughout the Xi. **(E)** Corresponding to C2C12, RPE-1 cells transiently transfected with hSAF-A:hrGFP also show an enrichment of hSAF-A:hrGFP at within the ANC of the Xi (**insets 1 and 2**). In contrast to the IF signal, the hrGFP-fusion of SAF-A is tightly associated with Xist RNA throughout the Xi. **(F)** Quantification of colocalization (n ≥ 10) using Manders' 1 + 2 (overlap) and Pearson's (correlation) coefficients for the different combinations shown in (A)-(E). Highest Manders' values were observed for Xist RNA signals overlapping SAF-A (IF) in C2C12, as well as for Xist RNA overlapping mouse and human SAF-A:hrGFP fusions in C2C12 and RPE-1 respectively. Highest degree of correlation (Pearson's) was found between Xist RNA and SAF-A signals, with both IF and hrGFP-fusion proteins. **(G)** Idealized example of an IF signal, which has been copied into two color channels (green and red) to create a completely colocalizing image. Red channel has been shifted stepwise in defined distances in x-direction in respect to the green channel and Pearson's (PC) as well as Manders' (M1) coefficients have been determined for every step. Figure adapted from (Smeets et al., 2013b*, submitted*).

4.2.3.1 *Xist RNA shows low spatial interaction with sites of H3K27me3- and macroH2A1-marked chromatin*

Due to the limited resolution of conventional microscopy, territories of Xist RNA and repressive histone marks of the Xi, like H3K27me3 or macroH2A, have commonly been considered being widely identical (Chadwick, 2007; Chadwick and Willard, 2004; Marks et al., 2009). In some studies, stable and long-term interaction between Xist RNA and other Xi-enriched factors have been concluded from these observations, but remained doubtful to date (Jonkers and Monkhorst, 2008; Wutz, 2011).

In the last chapter, close interaction between Xist RNA and the ANC-enriched nuclear matrix

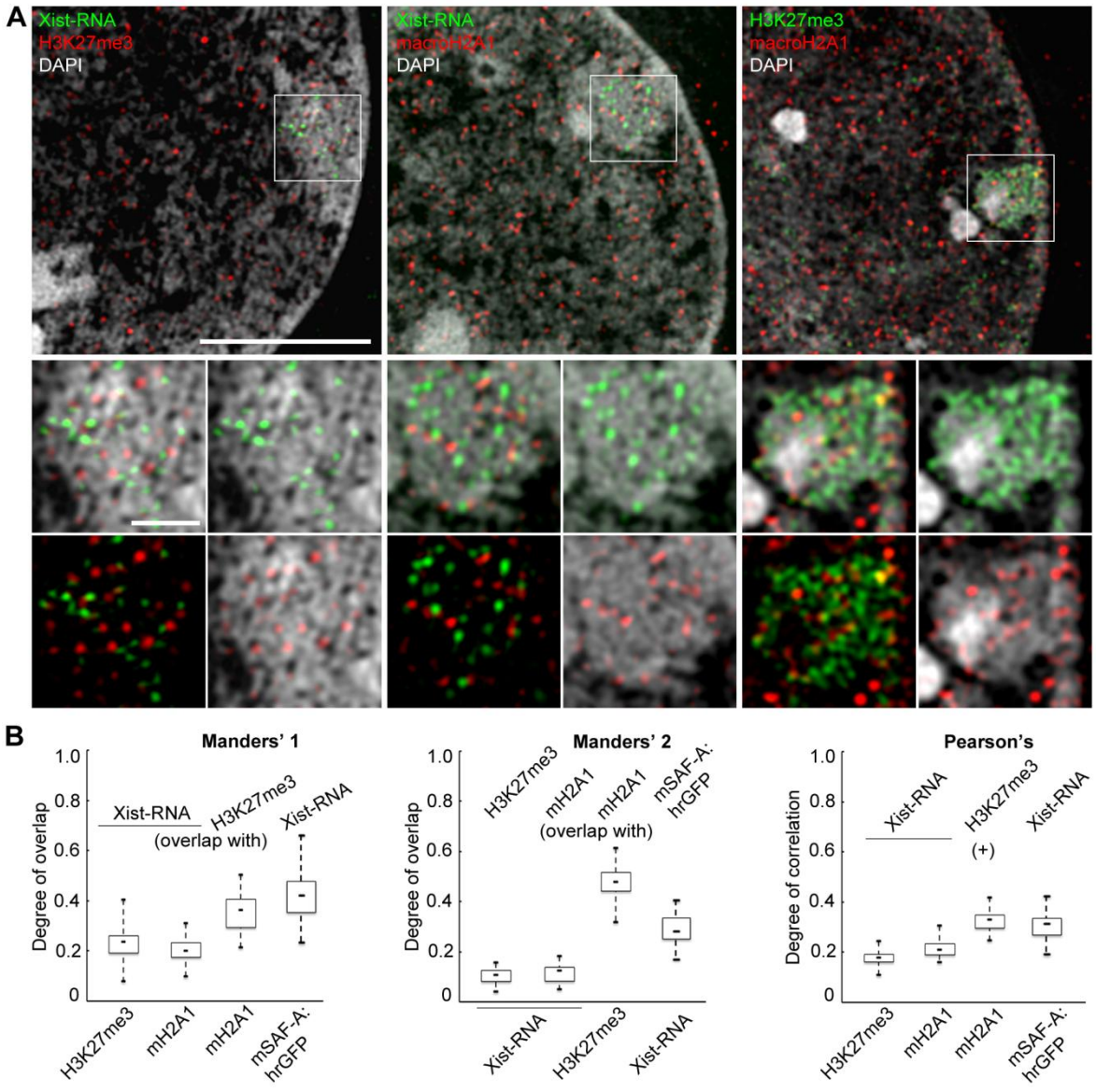

Figure 4-13 Low spatial interaction of Xist RNA with H3K27me3 and macroH2A1 in C2C12 cells. (A) Upper panels: Single optical z-sections of RNA-Immuno-FISH experiments against Xist RNA and H3K27me3 or against Xist RNA and macroH2A1, or IF against H3K27me3 and macroH2A1. **Lower panels**: Inset magnifications show different two-color combinations of the marked areas above. Scale bar 5 µm, inset 1 µm. **(B)** Quantification of colocalization using either Manders' or Pearson's coefficients. For comparison, data for Xist RNA and mSAF-A:hrGFP has been taken from Figure 4-12. Highest degree of overlap can be found between mSAF-A:hrGFP and Xist RNA or between macroH2A1 and H3K27me3. Highest degree of correlation can also be found between these two pairs. Xist RNA shows significantly lower correlation with H3K27me3 or macroH2A1, respectively ($n \geq 17$, $p < 0.05$, Mann-Whitney U test). Figure adapted from (Smeets et al., 2013b*, submitted*).

protein SAF-A could be shown. To further analyze Xist RNA localization in respect to functional chromatin compartments, Xist RNA and H3K27me3, or macroH2A1 respectively, have been imaged simultaneously with 3D-SIM in C2C12 and RPE-1 nuclei.

Visual inspection revealed little overlap between Xist RNA and H3K27me3-marked chromatin, or macroH2A1-marked chromatin respectively, whereas H3K27me3 and macroH2A1 were closely associated and overlapped partially with each other in both cell lines. Furthermore, the two repressive histone marks were enriched in sites of compacted chromatin as judged by DAPI staining

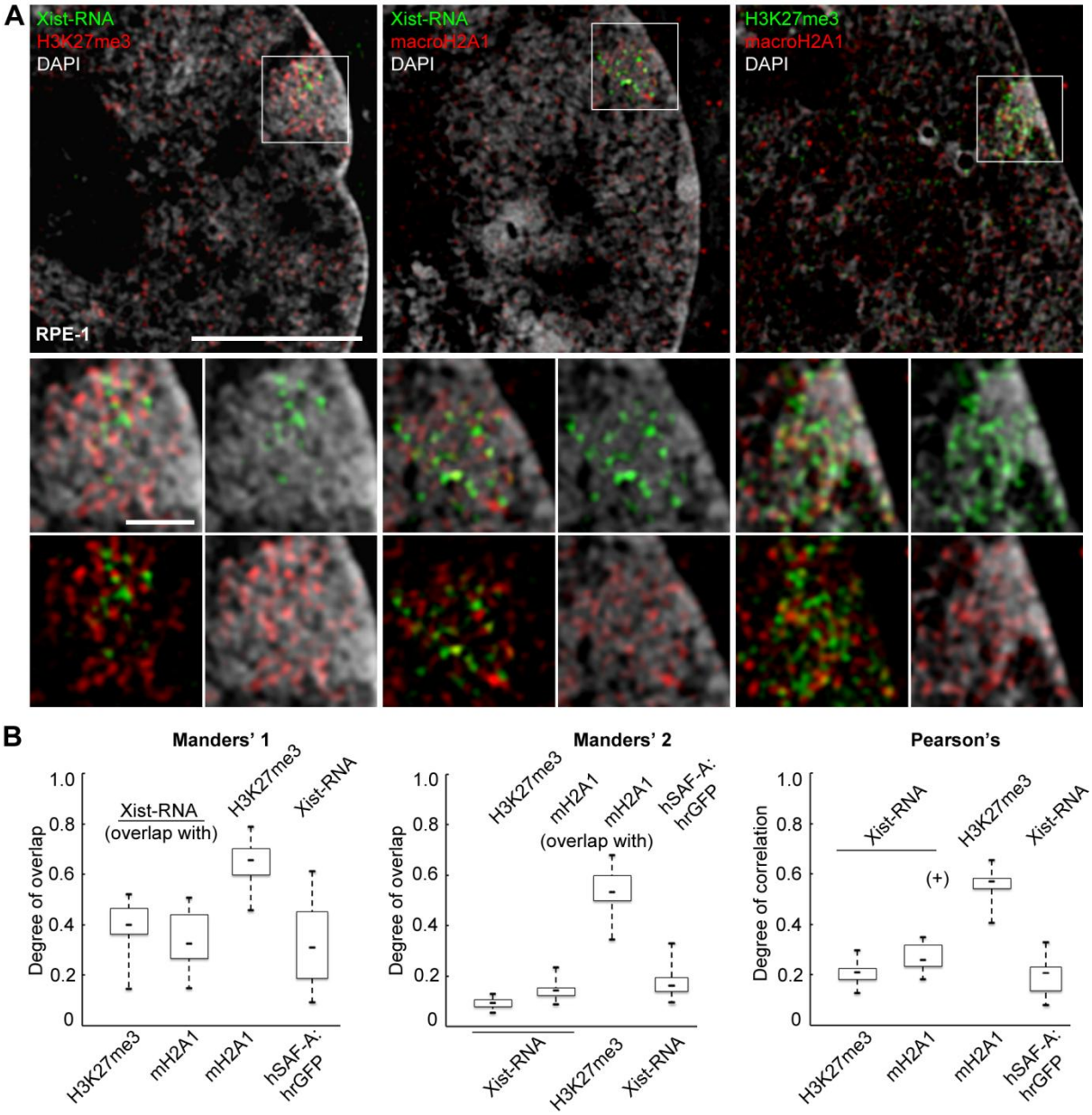

Figure 4-14 Low spatial interaction of Xist RNA with H3K27me3 and macroH2A1 in RPE-1 cells. (A) Upper panels: Single optical z-sections of RNA-Immuno-FISH experiments against Xist RNA and H3K27me3 or against Xist RNA and macroH2A1, or IF against H3K27me3 and macroH2A1. **Lower panels:** Inset magnifications show different two-color combinations of the marked areas above. Scale bar 5 µm, inset 1 µm. **(B)** Quantification of colocalization using either Manders' or Pearson's coefficients. For comparison, data for Xist RNA and hSAF-A:hrGFP has been taken from Figure 4-12. Highest degree of overlap can be found between macroH2A1 and H3K27me3. Highest degree of correlation can also be found for this pair. Xist RNA shows significantly lower correlation with H3K27me3 or macroH2A1, respectively ($n \geq 14$, $p < 0.05$, Mann-Whitney U test). Figure adapted from (Smeets et al., 2013b,*submitted*).

(see Figures 4-13, A and 4-14, A). A distance of more than 100 nm can be concluded from the fact that hardly any overlap can be seen between Xist RNA and the other two Xi-enriched factors, providing further evidence for the localization of Xist RNA within the ANC of the Barr body.

Quantitative analysis ($n \geq 17$ in C2C12, $n \geq 14$ in RPE-1) confirmed the visual impression that in C2C12 cells the highest amount of overlap (Manders') could be found between mSAF-A:hrGFP and Xist RNA, or between macroH2A1 and H3K27me3 on the other hand. The highest amount of correlation (Pearson's) could also be found between those two pairs. Significantly lower colocalization values were found between Xist RNA and the two compacted chromatin-enriched markers H3K27me3 and macroH2A1 (see Figure 4-13, B). In RPE-1 cells, the highest values for Manders' and Pearson's coefficients were observed between H3K27me3 and macroH2A1 as well (see Figure 4-14, B). Again, the respective colocalization coefficients were significantly reduced between Xist RNA and these two repressive markers, providing evidence for Xist RNA's spatial separation from sites of compacted chromatin within the Xi. However, absolute colocalization values for Xist RNA and H3K27me3, or macroH2A1 respectively, were higher in RPE-1 than in C2C12, which could be explained by the higher signal density in the human cell line resulting in an increase of the colocalization outcome just by mere chance due to an overall closer proximity. This may also explain why in RPE-1 cells Xist RNA shows no significantly increased colocalization with hSAF-A:hrGFP over the two repressive histone marks, although the absolute number (Manders' 1) for this pair is comparable between RPE-1 and C2C12 cells.

In summary, Xist RNA is preferentially located within low density chromatin classes of the Xi according to the DAPI-staining. This observation has been further emphasized by a strong colocalization with the ANC-enriched nuclear matrix protein SAF-A. A direct role for SAF-A in XCI through Xist RNA attachment has long been suggested, but so far no colocalization with Xist RNA could be observed. Moreover, the results in this work indicate towards a Xi-specific post-translational modification of SAF-A, either a prerequisite or the result of its interaction with Xist RNA, which can be concluded from the detrimental effect on antibody affinity within the Xi. On the other side, qualitative and quantitative analysis revealed no colocalization of Xist RNA with the repressive histone marks H3K27me3 and macroH2A1, both enriched within sites of compacted chromatin and partially overlapping with each other. Taken together with the results from the previous chapters, this indicates strongly that the statement of Xist RNA being localized within decondensed chromatin sites can be further pinpointed to be most likely coincident with the functional ANC of the Xi, where it is associated with SAF-A and locally distant from repressed compacted chromatin sites.

4.2.4 Xist RNA localization in decondensed chromatin is an intrinsic property that is already present during early spreading

Xist RNA localization during XX ESC differentiation – chromatin compaction and RNAP II exclusion occur subsequently to initial Xist RNA spreading

XCI and initial Xist RNA spreading *in cis* is taking plcae at very timepoints of embryogenesis. Next, it should be addressed whether the specific localization of Xist RNA within decondensed chromatin is an intrinsic feature that is already present during very early timepoints of differentiation or if it reflects a property that is only established in fully differentiated somatic cells. In this context it could also be validated if Xist RNA spreading has a direct impact on transcriptional silencing and/or chromatin compaction.

Using 3D-SIM, it was now possible to re-evaluate earlier studies using conventional light microscopy, where it could have been shown that Xist RNA spreading *in cis* leads to a gradual exclusion of RNAP II in early differentiating XX ESCs, but not to an increased compaction at very early stages of XCI (Chaumeil et al., 2006).

In undifferentiated XX ESCs, two distinct sites of basal Xist RNA expression, corresponding to the two Xa chromosomes – typically associated with strong RNAP II signals – could be observed clearly within the ANC in every cell (see Figure 4-15, A, Undifferentiated). The chromatin density segmentation algorithm has been applied to quantify the degree of chromatin compaction in these cells. Chromatin compaction in the nuclear volume few pixels around Xist RNA signals showed no difference to the rest of the nucleus (n = 11; see Figure 4-15, B, undifferentiated). Those distinct Xist RNA foci could be found seemingly unchanged until day 3 of differentiation (see Figure 4-15, A, Day 3). Upon day 4, the number of individual Xist RNA foci increased largely and could be found spreading – *in cis*, as judged from the local constraint – into sites of decondensed chromatin. RNAP II signals were not fully excluded and could still be found throughout the entire Xist RNA territory, though with a bias towards its periphery. Chromatin compaction is already starting to occur, but the Xist RNA territory is still widely pervaded by decondensed chromatin. Both observations argue for an incomplete transcriptional silencing at this stage (see Figure 4-15, A, Day 4). Consistently, only one day after initial Xist RNA spreading, i.e. on day 5 under the experimental conditions applied in this work, the overall picture has changed dramatically with a huge progress of chromatin compaction and an almost complete exclusion of RNAP II signals from the Xist RNA territory (see Figure 4-15, A and B, Day 5).

Number and volume measurements of individual Xist RNA foci revealed a specific spreading dynamic during differentiation. In undifferentiated XX ESCs and until day 3 of differentiation, only very few, locally strictly confined foci, but with a relatively large volume, were detectable, which argues for a high concentration of Xist RNA transcripts around the two Xist loci. After spreading between day 3

and day 5 of differentiation, under the experimental conditions applied in this work, a large and highly variable number of Xist RNA foci with small volumes, probably reflecting single transcripts were detectable. Subsequently, volumes of individual foci increase gradually and number of foci gets established around a median value of ~100 (in day 9 after differentiation and somatic C2C12) (Figure 4-15, C).

On day 9, all features of the Xi have arrived at a stage that is comparable to somatic C2C12 cells in about 90% of the cells within the population. RNAP II signals are predominantly excluded, the number and volume of individual Xist RNA foci is almost identical to those in C2C12 cells, and chromatin compaction in the Xist RNA territory has obviously increased further (see Figure 4-15, A, B, Day 9).Overall, these changes resulted in a Xi Barr body that is indistinguishable from its somatic C2C12 counterpart.

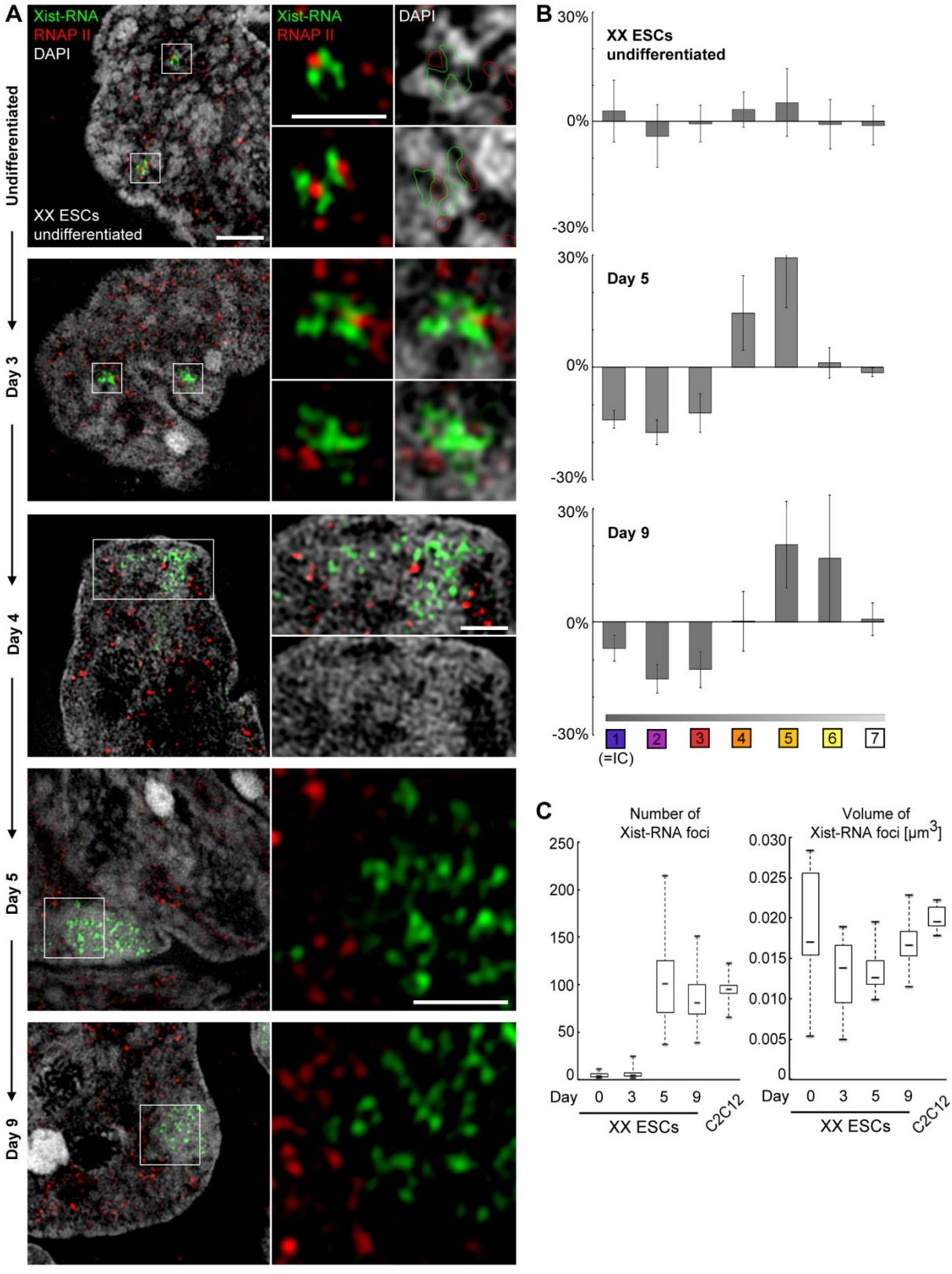

Figure 4-15 Timecourse of Xist RNA spreading, chromatin compaction and transcriptional silencing during early timepoints of XX ESC differentiation. (A) Single optical z-sections of XX ESCs at different timepoints of differentiation ranging from undifferentiated until day 9 of differentiation. Cells have been stained with RNA-Immuno-FISH against Xist RNA and against RNAP II (Ser2P). Scale bar 2 µm, inset 1 µm. **(B)** Chromatin density segmentations from undifferentiated XX ESCs (n = 11), day 5 of differentiation (n = 10) and day 9 of differentiation (n = 10). **(C)** Quantification of number and volume of individual Xist RNA foci at different timepoints of differentiation. Data for C2C12 cells has been taken from Figure 4-10. Figure adapted from (Smeets et al., 2013b*, submitted*).

Induction of transgenic Xist RNA in male ESCs autosome 11 – incomplete chromatin compaction and persistence of transcriptional activity

Induction of transgenic Xist RNA expression on autosomes is a widely used method to analyze Xist RNA function (Chaumeil et al., 2006; Lee and Jaenisch, 1997; Tang et al., 2010; Wutz and Jaenisch, 2000). Here, a male ESC line carrying a doxycyclin-inducible Xist-transgene on Chr. 11 (tr36 ESC; kindly provided by A. Wutz, Wellcome Trust, Cambridge, UK) has been used to further assess Xist RNA localization in respect to chromatin and to analyze its impact on transcriptional silencing and chromatin compaction.

Directly after doxycyclin-induction, Xist RNA spreading into a vast territory could be observed (see Figure 4-16, A, Day 1.5). However, chromatin within the Xist RNA territory was not significantly more compacted than in the rest of the nucleus (see Figure 4-16, B, Day 3) and still a lot of RNAP II signal was present throughout the Xist RNA territory. This overall picture did not change substantially even after prolonged doxycyclin-induction for up to 10 days (see Figure 4-16, A, Day 6 and 10), where Xist RNA occupied a large nuclear volume, but chromatin compaction still could not be differentiated from surrounding chromatin and RNAP II signals persisted throughout the Xist RNA territory (see Figure 4-16, B, day 6 and 10). All these findings indicate towards the inability of Xist RNA to induce transcriptional silencing and the formation of an autosomal Barr body in this autosomal context. Under the applied experimental conditions, a slightly more compacted core enriched with H3K27me3 could be found around day 6 after induction. Although being slightly more compacted, this H3K27me3 core still did not resemble a clearly demarcated autosomal Barr body with its chromatin compaction being not comparable to differentiated XX ESCs or somatic cells (see Figure 4-16, B, Day 6 Xist and Day 6 H3K27me3). Even though the number of individual Xist RNA foci exceeded the number on its Xi counterpart by about 2-fold, this did not seem to increase the capability of Xist RNA to induce a true autosomal Barr body. In addition, the increased number of Xist RNA foci failed to accumulate into a bounded nuclear volume and were found to spread into remote nuclear areas forming Xist RNA territories with a diameter of up to ~4 µm, more than 2-fold the size of an X chromosomal Xist RNA territory (see Figure 4-16, C). These observations were independent from the pluripotent state of the tr36 ESCs, as vast expansion and preservation of RNAP II could be found to a highly variable extent even up to 10 days of differentiation (data not shown).

These findings illustrate the dependence of Xist RNA on the X-chromosomal context in order to properly induce transcriptional silencing and chromatin compaction. Apart from that, its general localization within decondensed chromatin sites was also observable in this autosomal Xist RNA cell line.

All described experiments involving the transgenic tr36 ESC line, as well as respective data acquisition, have been carried out and kindly provided by Yolanda Markaki (Cremer Lab, LMU

Munich) in close collaboration with the author of the present work, who performed all data analyses and figure preparation.

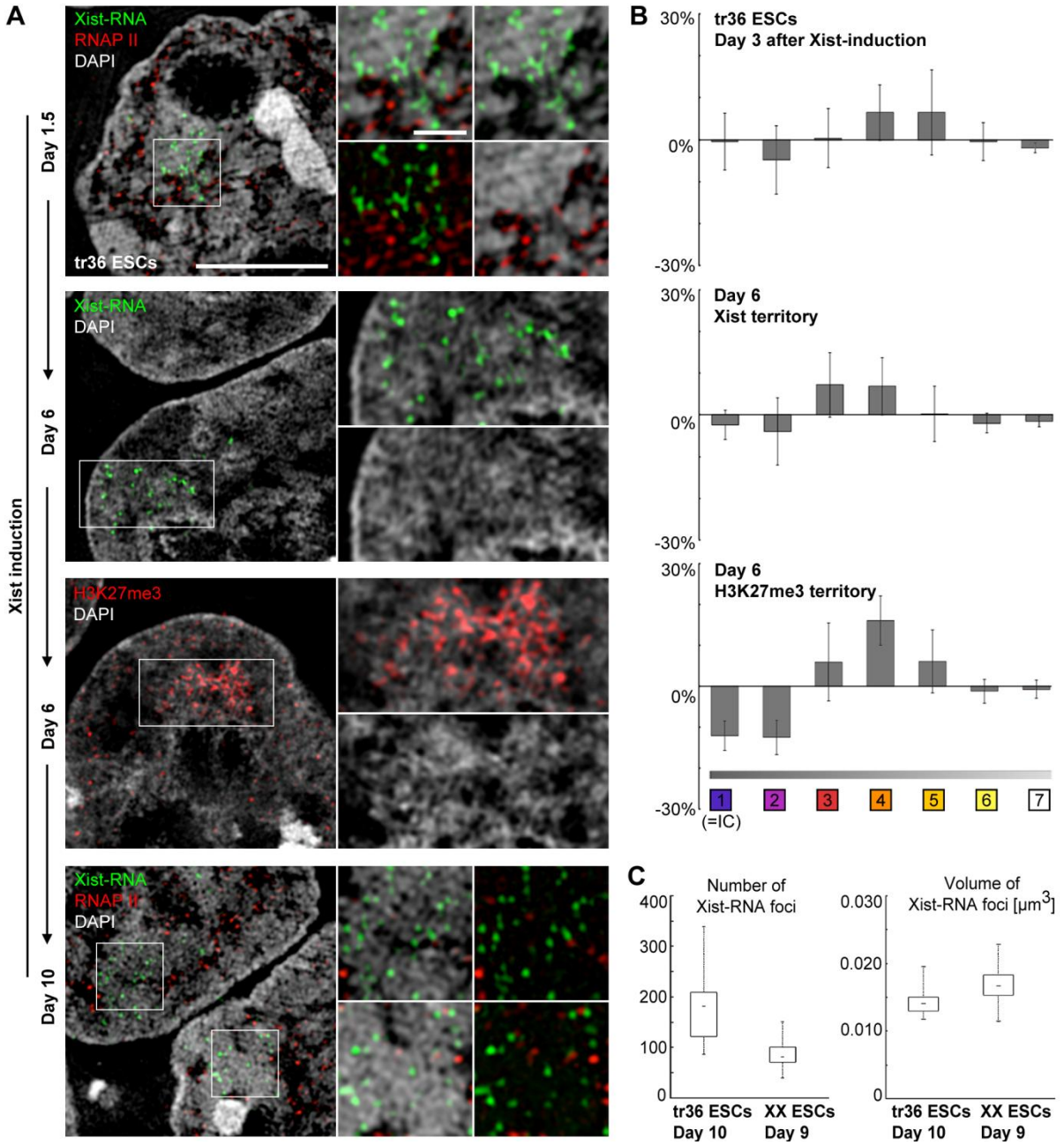

Figure 4-16 Induction of transgenic Xist RNA in male ESC autosome 11. (A) Single optical z-sections of male ESCs line carrying an inducible Xist-transgene on chromosome 11 (tr36 ESCs) at different timepoints of induction. RNA-Immuno-FISH staining against Xist RNA and RNAP II or H3K27me3, respectively. Scale bar 2 µm, inset 1 µm. **(B)** Chromatin density segmentation 3 days after induction (n = 10) or 6 days after induction using either the Xist RNA territory as reference mask (n = 11) or the H3K27me3 territory, respectively (n = 11). **(C)** Quantification of number and volume of individual Xist RNA foci, either in tr36 ESCs 10 days after induction or in XX ESCs 9 days after differentiation. Figure adapted from (Smeets et al., 2013b, *submitted*).

A manuscript about the results presented in Chapter 4.2 is currently submitted for publication (Smeets et al., 2013b, *submitted*).

4.3 Xist RNA is unlikely to interact directly with PRC2

Xist RNA is well established to be the key initiator of chromosome-wide transcriptional silencing. How this is achieved biochemically, however, is until today mostly elusive and only a few proteins have been proposed so far to possibly interact with Xist RNA directly. These are (1) the nuclear matrix protein SAF-A, the potential scaffold for Xist RNA spreading (Hasegawa et al., 2010), (2) the transcription factor YY-1, possibly tethering Xist RNA co-transcriptionally to the Xi at the XIC (Jeon and Lee, 2011) and (3) PRC2, the mediator of the Xi-enriched histone modification H3K27me3 (Zhao et al., 2008). The close spatial association provided further strong evidence for a direct interaction between Xist RNA and SAF-A as observed by 3D-SIM and described in Section 4.2.3 (p. 93) of the present work. Whereas an initial test using an anti YY-1 antibody in somatic C2C12 and RPE-1 cells revealed only sparse YY-1 throughout the entire nucleus, including the Xi, and could not detect any close association between Xist RNA and YY-1 upon qualitative examination (data not shown). But this issue will certainly need further attendance in the future and in particular experiments in differentiating cells or during early Xist RNA spreading after induction should be carried out to settle these diverging observations.

Several findings point towards an interaction between PRC2 and Xist RNA, e.g. the enrichment of PRC2 at the Xi in close colocalization to Xist RNA, both at metaphase and interphase, or the necessity of ongoing Xist RNA transcription for PRC2 recruitment (Plath et al., 2003; Silva et al., 2003; Wang et al., 2001). Moreover, biochemical studies suggested a direct interaction between Ezh2 and Suz12, both components of PRC2, and the conserved Repeat-A domain of Xist RNA (Maenner et al., 2010). Yet, the prevailing view of PRC2 recruitment to the Xi by a direct interaction with Xist RNA showed some inconsistencies that could not be easily explained (Brockdorff, 2011). In particular, the temporal preceding of Xist RNA after initial spreading compared to PRC2 (Mak et al., 2004; Okamoto et al., 2004) and an ongoing, though weakened, recruitment of PRC2 by a Repeat-A deleted Xist RNA transgene (Kohlmaier et al., 2004).

In close collaboration with Andrea Cerase (Brockdorff Lab, University of Oxford, UK), it should be assessed here with 3D-SIM resolution, if a direct spatial association of Xist RNA with different components of PRC2 is observable. As most PRC2 activity is necessary during early XCI in order to establish H3K27me3 enrichment at the future Xi, a transgenic male ESC line carrying an inducible Xist transgene on chromosome 17 (3E; kindly provided by A. Wutz, Wellcome Trust, Cambridge, UK) has been used. Visual inspection reveals a high degree of overlap among the different components of PRC2 – Eed, Ezh2 and Suz12 (see Figure 4-17, A and B). In contrast, clear spatial separation can be found between Xist RNA signals and those three PRC2 components (see Figure 4-17, C – E). Moreover, Xist RNA colocalization with Ring1b, a member of PRC1, is not observable as well (see Figure 4-17, F).

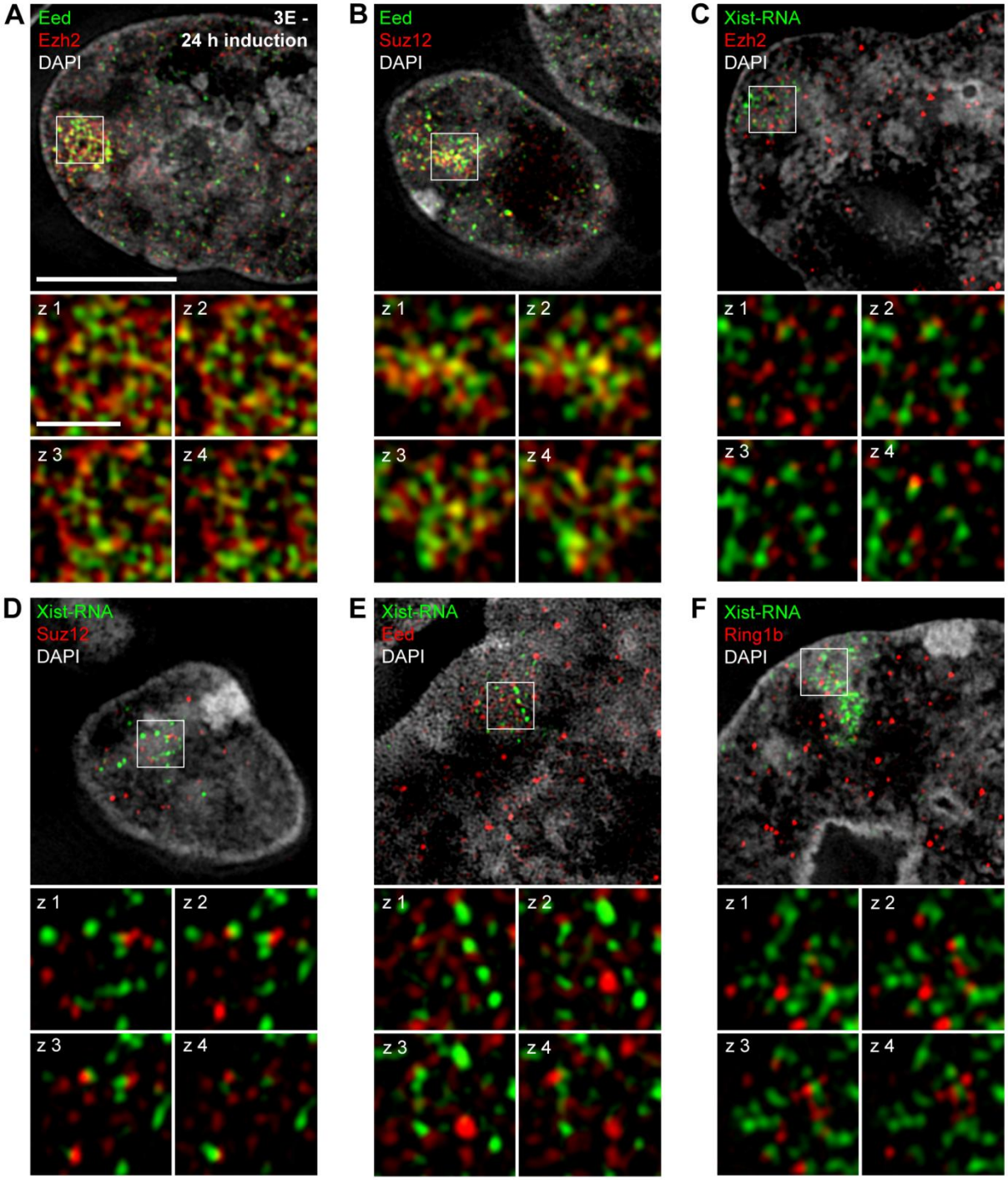

Figure 4-17 Xist RNA shows low colocalization with PRC2. Shown are single optical z-sections in 3E ESCs 24 h after Xist induction of different combinations of IFs against three different PRC2 components or RNA-Immuno-FISH against Xist RNA and those three PRC2 components or against Ring1b, a member of PRC1. Scale bar 5 µm, insets 1 µm. Z-stepsize 0.125 µm. **(A-B)** High degree of overlap between Eed and Ezh2, or between Eed and Suz12, respectively. **(C-E)** In contrast, Xist RNA shows almost no overlap with these three members of PRC2. **(F)** Xist RNA shows also no overlap with Ring1b. Figure adapted and modified from (Cerase et al., 2013, *submitted*).

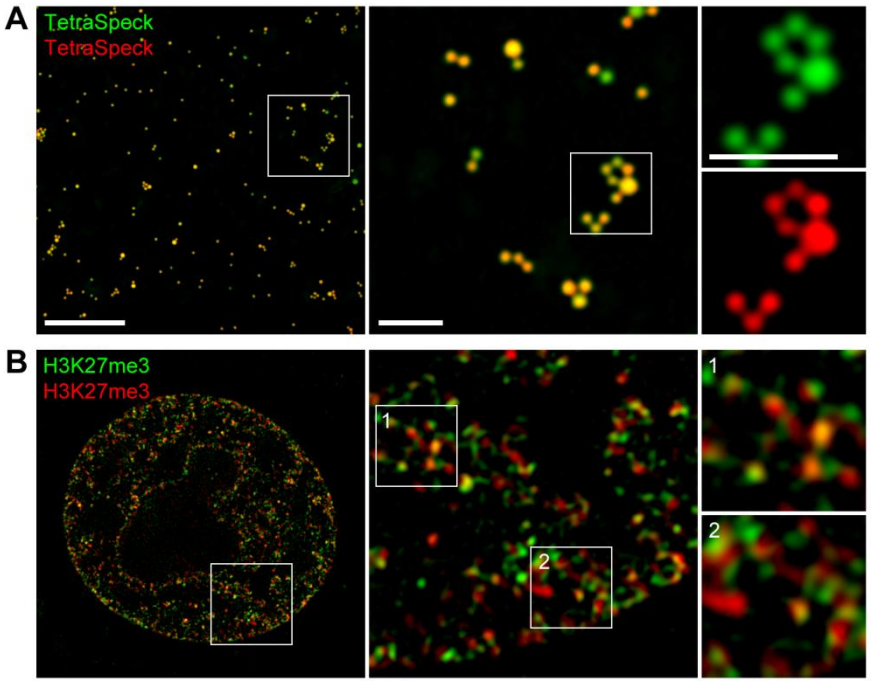

Figure 4-18 Control for intrinsic system and IF protocol uncertainties. (A) 3D-SIM imaging of TetraSpeck beads (0.2 µm, Invitrogen) reveals extent of inherent system-specific mis-alignment between two channels. **(B)** IF using one primary antibody (against H3K27me3) and two differently labeled secondary antibodies revealing inherent uncertainties due to the variable spatial orientation of all components of the antibody-fluorophore complex and the distance between epitope and fluorophore within the resolvable range. Scale bar 5 µm, insets 1 µm. Figure adapted and modified from (Cerase et al., 2013, *submitted*).

Two important control experiments have been performed to be able to judge these results in the context of intrinsic system uncertainties of 3D-SIM and the intrinsic uncertainties of an antibody detection scheme at this level of resolution (as already described in Section 3.3.3, p. 73). 3D-SIM imaging of TetraSpeck beads (0.2 µm, Invitrogen) is an adequate means to control for microscope-related variations hampering colocalization analyses (e.g. variations within different areas of the field of view or non-counteractable camera misalignment; see Figure 4-18, A). The degree of colocalization uncertainty intrinsic to the IF protocol using primary and secondary antibody labeling, i.e. introduced by the distance between epitope and actually detected fluorophore, has been assessed by detecting one primary antibody (against H3K27me3) with two differently labeled secondary antibodies (see Figure 4-18, B). Assuming a length of about 10 nm for an IgH antibody (Dong and Shannon, 2000; Silverton, 1977), the distance between epitope and fluorohpore may add up to about 20 nm, which has to be doubled to about 40 nm when two different color channels are involved. Regarding that all components of the antibody-fluorophore complex may occupy a random spatial orientation results in a considerable intrinsic uncertainty, which is already well resolvable with 3D-SIM (for further details see Smeets et al., 2013a, *in press*).

Still, quantification (n = 15) of colocalization using Pearson's and Manders' coefficients confirmed the visual impression. The PRC2 members, Eed and Ezh2, or Eed and Suz12 respectively, provided a Pearson's coefficient that was almost comparable with the H3K27me3-control experiment. The amount of Eed signals overlapping Ezh2, or Suz12, (M1) was even higher than in the control, which may well be explained by the higher signal density in the 17i territories. Yet, Xist RNA showed a highly significant reduction in colocalization, both for Pearson's and Manders' coefficients, in respect to all of the PRC2 components and to Ring1b (see Figure 4-19, A and B). Using a novel evaluation

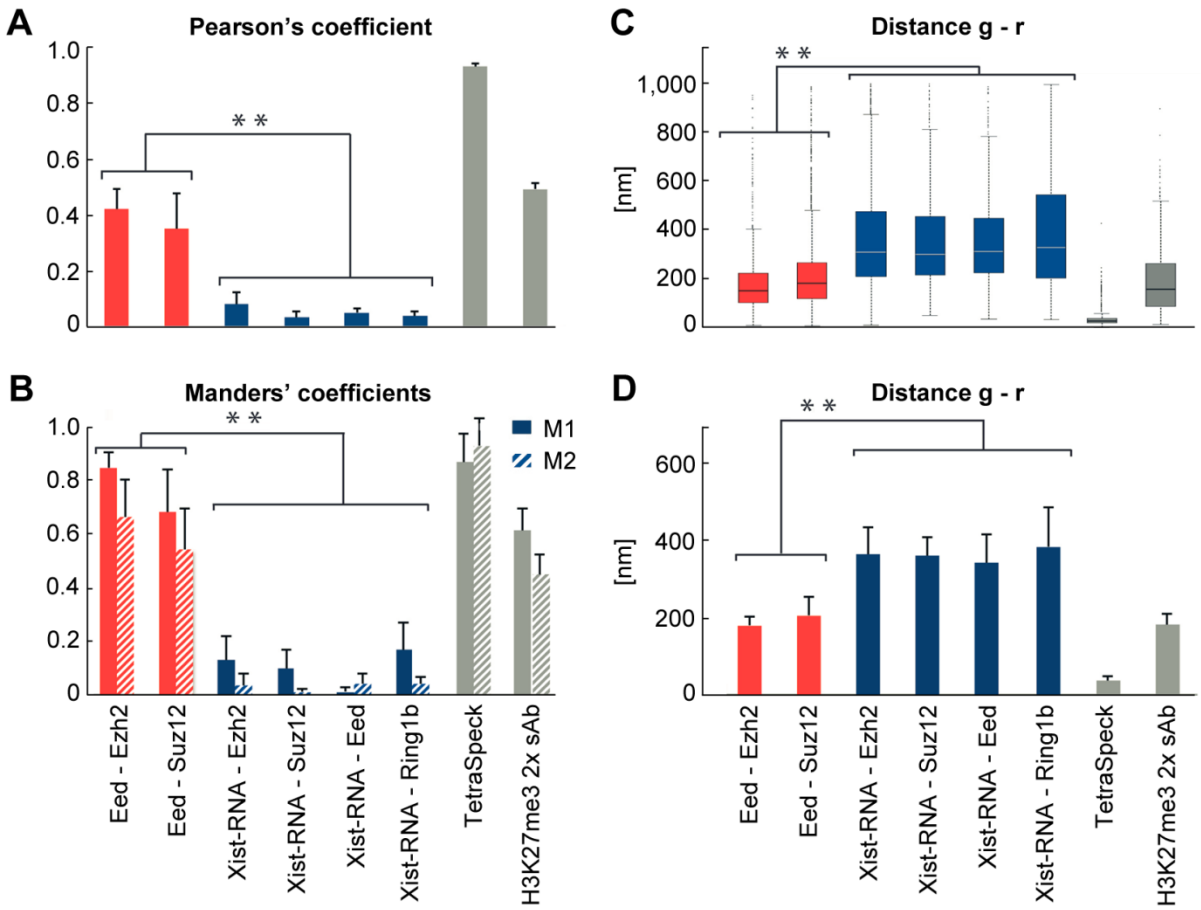

Figure 4-19 Quantification of colocalization and distance distribution of Xist RNA and PRC1/2 in 3E ESCs. (A-B) Average histograms including confidence intervals of Pearson's coefficients (degree of correlation) and Manders' coefficients (degree of overlap) (n = 15). Two stars mark highly significant differences. **(C-D)** Box-plots or average histograms of distance distributions between centroid positions of green and red channel signals within the 17i. Figure adapted and modified from (Cerase et al., 2013, *submitted*).

approach developed by Michal Gdula (University of Oxford, UK), the distances between centroids of red and green signals could be determined and depicted either as box-plots (see Figure 4-19, C) or average histograms including confidence intervals (see Figure 4-19, D). Both evaluations revealed a highly significantly different distribution. On average, the individual components of PRC2 are about 150 – 200 nm apart, whereas Xist RNA is on average about 400 nm apart. Subtracting the two control uncertainties of about 20 nm – for system uncertainties – and about 150 nm – for IF uncertainties – results in a minimal possible distance of 0 – 50 nm among the PRC2 members and 150 – 250 nm between Xist RNA and PRC1/2.

The experiments in this chapter have been performed, imaged and presented by the author of this work in close collaboration with Andrea Cerase (Brockdorff Lab, University of Oxford, UK). The data analyses in Figure 4-19 has been developed, performed and kindly provided by Michal Gdula (University of Oxford, UK). A manuscript including the results of Chapter 4.3 is currently submitted for publication (Cerase et al., 2013, *submitted*).

5 Discussion

Two major aspects have been addressed in the present thesis. First, what are the detrimental effects of the DNA-FISH treatment on small-scale chromatin structures and to what degree could super-resolution microscopy contribute to the understanding of higher-order chromatin organization in the near future? Second, how is chromatin organized in the Barr body of mammalian nuclei, a classical model system for epigenetically silenced chromatin? In particular, is there a difference between the general functional chromatin architecture of the Barr body and autosomal CTs and is there something like functional chromatin compartmentalization within the Barr body that could harbor essential nuclear processes? Xist RNA is the key initiator and regulator of XCI during early embryogenesis, but also in fully differentiated cells. Yet, how it is able to fulfill this role remains mostly elusive. In this respect, it might help to shed light on the yet unknown three-dimensional localization environment of Xist RNA and several other important Xi-enriched factors and their spatial relations to each other. Optimized staining and data analysis tools for 3D-SIM have been developed and applied in this work to pinpoint the localization and spatial organization of Xist RNA in respect to chromatin, but also to other Xi-enriched factors with suggested roles in XCI, in order to draw conclusions about its function and to integrate the results into a general model about higher-order chromatin architecture.

5.1 3D-FISH studies can benefit from super-resolution microscopy despite inherent detrimental effects

3D-FISH with its potential to specifically visualize certain DNA-sequences on the single-cell level has become an indispensible method in the cell biological toolbox. It has essentially contributed to a wide range of discoveries starting from the observation of chromosomes being organized in CTs, down to findings about the transcription-dependent localization of single-genes, which led to the current understanding of higher-order chromatin organization principles (Cremer and Cremer, 2010; Foster and Bridger, 2005; Németh et al., 2010; Neusser et al., 2007). Yet, DNA-FISH has the inherent drawback that it requires a denaturation step of the target DNA in order to render it accessible for the labeled probes. With conventional diffraction-limited light microscopy, this potentially destructive denaturation step does not seem to alter chromatin structure significantly, which has thus been neglected so far in 3D-FISH studies (Hepperger et al., 2007; Solovei et al., 2002). Moreover, the capability of 3D-FISH as a tool to understand higher-order chromatin organization on the single cell level, especially in the light of recent developments in 3C-based approaches and their findings of chromatin being organized in distinct CDs/TADs, has reached a limit due to the resolution restrictions of light microscopy (Bickmore and van Steensel, 2013; Krijger and de Laat, 2013).

Here, changes introduced to the samples by the DNA-FISH procedure, especially by the heat denaturation step, have been assessed at the super-resolution level on DAPI-stained cell nuclei. The relocalization procedure that has been applied to do so (compare Section 3.2.4, p. 57), allows to directly compare changes in chromatin structure, which have been introduced by the DNA-FISH treatment without having to take cell-specific variations into account. The chromatin density segmentation approach allowed to statistically quantify the DNA-FISH-induced changes in higher-order chromatin structure in an unbiased user-independent fashion. The observed shift of chromatin density classes towards higher density in combination with the visual inspection depicting a more homogenous chromatin appearance in the DAPI staining, both argues for skewed deterioration of the more decondensed chromatin sites. In contrast, the overall nuclear morphology and in particular more compacted heterochromatin sites at chromocenters or in perinuclear and perinucleolar regions is generally rather well preserved. This has been exemplified in apical z-sections containing chromatin voids underneath nuclear pores (the depiction of nuclear pore complexes in the DAPI staining), which illustrate a generally high degree of preservation. Also, the nuclear envelope, visualized by immunostaining against Lamin B and Nup153, seems relatively unaffected by the DNA-FISH treatment without any qualitative differences at the level of 3D-SIM resolution.

The peripheral heterochromatin associated with the nuclear envelope is usually known as a nuclear sub-compartment, where transcriptionally silenced genes are located to (Akhtar and Gasser, 2007; Cremer et al., 2006; Guelen et al., 2008; Meister et al., 2010). This observation led to the notion that relocation of genes to the nuclear periphery is sufficient to induce gene silencing. Some experiments gathered evidence favoring this view, by e.g. showing that induced tethering of genes to the lamina led to shut down of that particular genomic site or observing relocation of the CFTR gene locus towards the nuclear interior upon activation and vice versa positioning to the periphery upon silencing (Finlan et al., 2008; Muck et al., 2012; Reddy et al., 2008). Yet, this model may be over-simplistic and a number of examples have been found showing repressed genes within the nuclear interior, away from perinuclear or perinucleolar heterochromatin, and even actively transcribed genes that move towards the periphery as a consequence of their activation (Kumaran and Spector, 2008; Luo et al., 2009). The later phenomenon has been suggested to be linked to nuclear pore complexes, which probably form a transcriptionally active micro-environment within the nuclear periphery and allow the synergistic expression of clusters of genes as well as the quick export of mRNA into the cytoplasm. However, so far most studies in this direction have been performed in budding yeast, where it could be observed that active genes are usually associated with nuclear pores proteins and a series of inducible genes are relocated towards nuclear pores upon their activation (Casolari et al., 2004; Ishii et al., 2002). Studies in Drosophila argued in the same direction and found nuclear pore proteins, e.g. involved in the transcriptional up-regulation of the male X

chromosome (Vaquerizas et al., 2010). Also, nuclear pore proteins, including Nup153, were found to be associated with active genes even in the nuclear interior, away from the nuclear envelope (Capelson et al., 2010; Kalverda et al., 2010). In mammals, evidence for a role of nuclear pore proteins in the regulation of transcriptional activity is rather sparse, but one study further emphasized the evolutionary conservation of their role by describing the formation and maintenance of a so called heterochromatin exclusion zone around the nuclear pore complexes, possibly ensuring proper steric access of large macromolecules like the transcription machinery (Krull et al., 2010). To date the role of nuclear pore complexes in gene regulation in mammals, especially on the single-cell level, is still rudimentary and has been partially hampered by the limited resolution of conventional microscopy (for review see Arib and Akhtar, 2011; Deniaud and Bickmore, 2009; Egecioglu and Brickner, 2011).

The results in this work demonstrate that DNA-FISH-induced chromatin deterioration becomes visible on the resolution level of 3D-SIM. This may affect higher-order chromatin conformation predominantly within the euchromatic inner regions of the nucleus. Still, FISH studies focusing on the nuclear envelope and heterochromatic sites, which seem mostly unaffected by the DNA-FISH treatment, will in particular profit from the combination of DNA-FISH and 3D-SIM as suggested by the results of the present work. Current developments in the FISH technique like COMBO-FISH or generation of defined repeat-free probe pool sets, both using small oligo-nucleotide probes, will further increase the benefit from single-cell DNA-FISH analyses with super-resolution imaging in the future (Beliveau et al., 2012; Boyle et al., 2011; Müller et al., 2010; Yamada et al., 2011). In terms of the general applicability of 3D-FISH for studies at the 3D-SIM resolution level, there may well be possible benefits in combining those two techniques in the future depending on the respective addressed questions under the precaution that possible negative side-effects are always duly considered.

5.2 X chromosome inactivation at 3D-SIM resolution

5.2.1 The Barr body is a special case of conventional nuclear architecture

The data presented in this work supports the CT-IC model claiming the presence of two sponge-like, spatially interacting networks, with chromatin being built of interconnected CDs and a DNA-free IC network permeated by small-scale chromatin loops within the perichromatin region ranging between 50 – 150 nm (Albiez et al., 2006; Cremer and Cremer, 2010; Hihara et al., 2012; Markaki et al., 2010). Due to the lack of resolution, which makes it mostly impossible – even with 3D-SIM – to distinguish between IC and PR in the Barr body according to the DAPI-staining, those two compartments shall be addressed as the active nuclear compartment (ANC), which is the functionally important

compartment that harbors all major nuclear processes. Opposed to the ANC are the sites of compacted chromatin, which harbor silenced genes and show no or only a insignificant fraction of decondensed, transcriptionally active chromatin loops. This functional compartment shall be termed passive nuclear compartment (PNC), here. The PNC consists of a highly dynamic, interconnected network of CDs/TADs, on average varying in size between 200 kb – 1 Mb as recently suggested by an increasing number of 3C-based studies (Bickmore and van Steensel, 2013; Dixon et al., 2012; Lieberman-Aiden et al., 2009; Nora et al., 2012).

The Barr body does not seem to be surrounded by a border zone of decondensed chromatin, as it could have easily be misinterpreted with conventional microscopy, which partially led to the hypothesis of all X-linked genes being recruited to this peripheral rim (Chaumeil et al., 2006; Clemson et al., 2006; Wutz, 2011). Here, the ANC has been shown to permeate the nuclear volume and to be also connected to the Barr body, allowing access to nuclear macromolecular complexes and ultimately leading to nuclear pore complexes facilitating nuclear export. The ANC can be resolved with 3D-SIM and is visible as sites of low density chromatin classes by DAPI-staining – even throughout the Barr body. Though, the possibility that the Xi periphery is a more favorable environment for the transcription of escape genes cannot be fully excluded. Thus, a skewed positioning of X-linked genes – especially escapees – towards the periphery remains a legitimate model view (Splinter et al., 2011). In line with this view, more recent studies found X-linked genes throughout the Barr body volume (Calabrese et al., 2012; Teller et al., 2011). Ultimately, the question where exactly X-linked genes can be found in the Barr body – only in the periphery or throughout its entire volume – can only be unequivocally answered in future studies using next-generation probe pools, e.g. against all X chromosomal intronic sequences (Boyle et al., 2011).

Moreover, the ANC, as defined by the DAPI-staining and the quantitative chromatin density segmentation, has been substantiated further as a functionally significant chromatin compartment by the preferential enrichment of the active histone modification H3K4me3 as well as actively elongating RNAP II. In contrast, the repressive marker H3K27me3 is preferentially located within the PNC, reflecting high-density chromatin classes. Although, the Barr body is mainly deprived of active histone marks and transcription, those markers can occasionally be found in the Barr body, too, and in particular within the ANC. Thus, the results of the present work propose that the higher compaction of the Barr body is mainly a result of a narrowing and partial collapse of the ANC. Thanks to the preservation – though major narrowing – of this chromatin compartment, the ANC is able to widen immediately when required to do so, e.g. during replication (or upon osmotic induction of chromatin hypercondensation), where it is still able to act as a hub for necessary large-scale chromatin remodeling, even within the compacted Barr body. In agreement, it could be shown that sites of replication, as visualized by PCNA, are located within the ANC during Barr body replication,

but that newly replicated DNA is re-compacted into the PNC after 20 – 30 min further emphasizing the dynamics of small-scale chromatin organization.

In summary, 3D-SIM data presented in this work revealed that the Barr body maintains principle features of higher-order chromosomal organization, similar to all other autosomal CTs. An ANC is still visible throughout the Barr body using DAPI-staining and although active chromatin marks, like H3K4me3 or active transcription, are mostly lacking within the Xi territory, they can still occasionally be observed within the ANC of the Xi. During replication or upon induction, the ANC of the Barr body is set to widen immediately, thus maintaining its principal functionality comparable to the autosomal ANC, to which it is still connected. The PNC is interconnected in 3D and enriched with repressive histone marks, like H3K27me3, throughout the entire nucleus. It is surrounded by a locally confined PR, harboring transcriptionally competent small-scale chromatin loops, and interspearsed by an interconnected IC network. 3D-SIM imaging of H2B-GFP in living and fixed HeLa cells provided evidence that formaldehyde fixation as performed in the present work does not induce fixation artifacts and also that DAPI is a suitable whole-chromatin marker with sufficient chromatin coverage capacity.

5.2.2 Implications of the focal localization of Xist RNA within the ANC

A major unanswered question in XCI is how Xist RNA is able to fulfill its function of silencing one entire chromosome (and only one). Partially due to the lack of resolution of conventional microscopy, it is not even clear whether Xist RNA follows some kind of sequence specificity in its spreading along the Xi chromosome, whether it forms multimers to do so, or whether it is just distributed randomly along the Xi. The present study demonstrated that Xist RNA is distributed as individual foci throughout the entire volume of the Barr body, thus arguing for a site-specific localization of individual Xist RNA foci and against the view of an omnipresent Xist-cloud. The absolute number of individual discernible foci was far below the estimated copy number of 300 – 1,000 of Xist RNA transcripts, which argues for a multimerization of Xist RNA, with variable concentration or conformation along the Xi sequence (Buzin et al., 1994; Sun et al., 2006).

The observations that Xist RNA is preferentially located within the ANC of the Xi suggests that it is either only very sparsely associated with certain DNA sequences at all (in case of a true IC next to Xist RNA) or intermingled with small-scale chromatin loops (in case of the PR). The latter would be in agreement with older cytogenetic findings that Xist RNA is preferentially found on gene-rich, G-light bands on metaphase spreads or more recent high-throughput epigenomic mapping studies using allele-specific ChIP-sequencing (Duthie et al., 1999; Marks et al., 2009; Pinter et al., 2012). Thus, one may speculate that Xist RNA is fulfilling a yet unrecognized, sequence-independent role in XCI by sterically blocking the access of the transcription machinery or other activating factors to XCI-

silenced genes. This idea fits also to the observation that Xist RNA distribution within interphase is not an immobile state, but is displaying a constant transcription-dependent turnover throughout the entire volume of the Xi even in fully differentiated cells (Clemson et al., 1996; Ng et al., 2011). In this respect one also has to keep in mind that RNA-FISH experiments on fixed samples are only reflecting temporal snapshots in an actually dynamic and mobile process. Besides, gene silencing on the Xi is dependent on ongoing Xist RNA transcription in order to maintain long-term gene silencing modifications, like DNA-methylation or histone de-acetylation, which is hinting towards a role of Xist RNA beyond the simple recruitment of other downstream-acting factors (Csankovszki et al., 2001). A structural role of Xist RNA in Xi formation has recently been supported by a study using chromosome conformation capturing proposing a structural, transcription-independent role for Xist RNA in the maintenance of the Xi-conformation (Splinter et al., 2011). In agreement with this proposed role, a recent study reported about the possibility of sequence-independent interactions of Xist RNA with chromatin (Pennisi, 2013). A sequence-independent, structural function of Xist RNA would also explain why LINE-1 sequences facilitate the formation of a compacted, repressive chromatin compartment, but do not seem to be strictly necessary for Xist RNA function (Cantrell et al., 2009; Tang et al., 2010). The idea of repetitive elements as the major driving forces for the localization of entire CTs has recently been brought up in a review summarizing latest 3C-based insights in chromatin architecture (Krijger and De Laat, 2013). In the case of XCI, the X chromosome with its enrichment in LINE-1 sequences may just respond more adequately to Xist RNA-induced chromatin compaction than autosomes by forming large heterochromatic chromatin blocks, which in turn act as a favorable environment for repressive chromatin modifications and gene silencing. Very strong support for the proposed sequence-independent structural function of Xist RNA as proposed by the data presented in this thesis came from a recent 3C-based study in ESCs with inducible autosomal Xist RNA and in fully differentiated cells, which came to a very similar conclusion. It is the first study to take the three-dimensional chromatin organization for Xist RNA's function and spreading in XCI into account (Engreitz et al., 2013). These observations using molecular high-content analyses hence complement very well the single cell super-resolution microscopy-based findings presented in this thesis.

5.2.3 Implications of the spatial correlation between Xist RNA and ANC-enriched SAF-A, but not with repressed chromatin

The nuclear matrix protein SAF-A (hnRNP U) has been shown to play an essential role in XCI and Xist RNA attachment. Initial evidence came from the observation that SAF-A:GFP fusion proteins are enriched at the Xi in somatic cells and that knock-down of SAF-A led to release of Xist RNA from the Xi (Hasegawa et al., 2010; Helbig and Fackelmayer, 2003). For long time, SAF-A has been known to

possess a DNA- and a RNA-binding motif and a recent *in silico* study predicted a high interaction probability between SAF-A and Xist RNA (Agostini et al., 2013; Fackelmayer et al., 1994). Yet, final evidence remained inconclusive as experiments with conventional microscopy showed no colocalization with Xist RNA. SAF-A even appeared to be excluded from the Xi when using SAF-A specific antibodies (for reviews see Hasegawa and Nakagawa, 2011; Tattermusch and Brockdorff, 2011).

The strong spatial correlation between SAF-A and Xist RNA observed with 3D-SIM provide a plausible explanation for the previously reported discrepancy between microscopic data and biochemical analyses. The results further indicate a Xi-specific post-translational modification of SAF-A, which can be concluded from the observed epitope masking effect, and which may be a prerequisite or the result of its interaction with Xist RNA. It can also be speculated that binding of Xist RNA is causing multimerization of SAF-A molecules, which in turn may act as a scaffold for Xist RNA spreading along the Xi, after its initial tethering by YY1 (Jeon and Lee, 2011). This view is very intriguing as it offers another explanation how Xist RNA is able to spread along the Xi in a sequence-independent manner within the ANC of the Barr body and subsequently accumulating at certain (gene-rich) genomic sites, where it may cause its inhibiting function.

This is further substantiated by a very low spatial interaction observed for Xist RNA and markers of repressed chromatin, like H3K27me3 and macroH2A1. Using 3D-SIM, the data provided support for the CT-IC model, as Xist RNA and SAF-A have been found to be localized within the decondensed ANC of the Barr body as opposed by repressive chromatin marks, which have been shown to be localized within the compacted PNC. Together, these two observations argue for a functional relevance of the spatial separation of these two compartments and moreover provide a novel model of Xist RNA spreading and function.

5.2.4 Localization of Xist RNA within the ANC is an intrinsic property already at early differentiating XX ESCs

Analysis of early differentiation at the onset of XCI provided evidence that the localization of Xist RNA into decondensed chromatin sites – reflecting the ANC – is an intrinsic property, which is not just established in fully differentiated cells. Initial Xist RNA spreading is followed by an exclusion of RNAP II, which occurred concomitantly with chromatin compaction (Chaumeil et al., 2006). Of note, chromatin compaction and full RNAP II exclusion was observed on Day 5 of differentiation, which is one day after the initial spreading of Xist RNA, under the experimental conditions used in this work. It could have been shown that chromatin compaction on the Xi can be induced through a novel PRC2- and H3K27me3-independent pathway involving SMCHD1 and the HP1-binding HBiX1 (Nozawa et al., 2013). This is in line with another recent study showing the need for chromatin compaction as a

prerequisite of PRC2-induced H3K27me3-enrichment during early XCI (Yuan et al., 2012). Thus, one may speculate that spreading of Xist RNA leads to inactivation of X-linked gene promoters as a first step through the loss of active histone modifications (Marks et al., 2009). This in turn may lead to RNAP II exclusion and concomitant local chromatin compaction. These early events, which may be partially facilitated by a structural role of Xist RNA as suggested by the results of the present work, are then followed by the accumulation of silencing chromatin modifications and subsequent long-term silencing. The observed increased chromatin compaction after 9 days of differentiation, which is not distinguishable from somatic C2C12 cells, as visualized by 3D-SIM, is likely to be the result of these progressively acquired long-term silencing modifications, like DNA-methylation, histone de-acetylation or incorporation of repressive histone variants.

5.2.5 3D-SIM reveals incomplete silencing within an autosomal Barr body

Xist RNA was predominantly found within the ANC of the tr36 inducible autosomal ES cell line indicating that spreading occurs normally in respect to functional chromatin compartments and providing further evidence that the localization of Xist RNA within this active compartment is indeed an intrinsic property. Nevertheless, Xist RNA obviously fails to induce the generation of an autosomal Barr body with the same features as its Xi counterpart, as seen with 3D-SIM, which argues for an impaired silencing capacity within this autosomal context. It has been reported by one group that Xist RNA is tethered to the Xi via YY1 within the so called nucleation center at the XIC (Jeon and Lee, 2011). One possibility, which may account for the widely recognized incomplete Xist RNA-induced gene silencing of autosomes is that autosomal chromatin around the transgene insertion site lack this YY1 nucleation center. As a result, Xist RNA may only be inadequately tethered to the autosome, which would also explain the observed vast expansion of the Xist RNA volume that has an about 2-fold increased diameter than its X-chromosomal counterpart. Still, this option does not explain why the present Xist RNA fails to induce proper gene silencing as it does on the X chromosome.

Undisputedly, the X chromosome has acquired some evolutionary adaptation, which facilitates its susceptibility for chromosome-wide silencing. One of the oldest hints for this idea was the discovery of the increased fraction of repetitive LINE-1 sequences on the X chromosome, which has led to the formulation of the LINE-1 hypothesis, claiming that these repetitive elements act as waystations for Xist RNA spreading (Bailey et al., 2000; Lyon, 1998). Although the data presented in this thesis argue against a direct interaction between Xist RNA and LINE-1 sequences, those repetitive elements might still facilitate the formation of a repressive chromatin compartment (Tang et al., 2010). The obtained 3D-SIM data presented in this thesis suggests that LINE-1 sequences, instead of being direct waystations for Xist RNA spreading, facilitate the formation of a repressive chromatin compartment,

which is hampered in the autosomal context and thus leads to the observable incomplete silencing effects.

5.2.6 Xist RNA does not interact directly with PRC2

Parallel epigenomic ChIP-on-chip analyses (carried out by Andrea Cerase, Brockdorff Lab; data not shown; Cerase et al., 2013, *submitted*) revealed that sites of Xist RNA-mediated gene silencing during initial Xist RNA spreading, analyzed using inducible 3E ESCs, showed negative correlation with novel sites of PRC2-mediated H3K27me3 deposition. This was an unexpected observation, especially as other results from these experiments were well in line with earlier studies, by e.g. showing that the first sites of H3K27me3 deposition after early Xist RNA induction were predominantly gene-bodies (Calabrese et al., 2012; Pinter et al., 2012).

In order to gain further inside into this discrepancy, these epigenomic mapping experiments have been complemented with 3D-SIM analyses. Surprisingly, no spatial correlation and significant median distances of 150 – 200 nm have been found between Xist RNA and different PRC2 members. It is unlikely that those observations are the result of epitope masking phenomena, as several different antibodies against different components of the PRC2, as well as against one PRC1 component, have been applied and the predicted secondary structure of Xist RNA and also the EM structure of the PRC2 complex suggest otherwise (Ciferri et al., 2012; Maenner et al., 2010). Although several studies provide evidence for a direct recruitment of PRC2 by Xist RNA, the possibility remains that they are describing indirect binding effects, and in fact this interaction could never be proven by UV-cross-linking experiments being the most sensitive and robust tool available so far. On the other hand, it is not yet clear, what the alternative recruitment models would be. Nonetheless, several other studies provided further evidence for an indirect, Xist RNA-independent recruitment of PRC2 to the Xi. As already mentioned above, one study could show that chromatin compaction is induced independently of PRC2 and H3K27me3 and that this is turn is a prerequisite for PRC2 recruitment, as proposed by another independent study (Nozawa et al., 2013; Yuan et al., 2012) (for review about PRC2 recruitment see Brockdorff, 2013).

5.2.7 Summary of novel insights about nuclear architecture gained by 3D-SIM and outlook on future directions

Single optical mid-sections of a DAPI-stained C2C12 nucleus confirm that the subchromosomal organization of the Barr body does not fundamentally differ from autosomal chromosomes (see Figure 5-1, A). Both consist of 3D-interconnected compacted CDs/TADs of variable shape, which are probably highly dynamic, and where individual CDs/TADs usually cannot be observed separately due to their clustering. These observations are well in line with recent conclusions from the results of

novel chromosome conformation capture techniques, but also with theoretical *in silico* models about chromatin organization based on known chromatin features and dynamics (for reviews see Dekker et al., 2013; Marti-Renom and Mirny, 2011; Mirny, 2011). Here, diameters of individual ~500 kb CDs/TADs have been determined by a simple model calculation to be on average ~360 nm[2]. Compacted CD/TAD cores are enriched in repressive chromatin modifications (like H3K27me3 or macroH2A1) and are surrounded by less condensed chromatin, probably containing small-scale chromatin loops and harboring essential nuclear processes like transcription and replication (Figure 5-1, B). This functional region is enriched with active histone marks like H3K4me3 in autosomal chromatin, which has not been resolvable yet with conventional microscopy. How the compacted cores of individual CDs/TADs are organized remains highly speculative today, and has therefore not be addressed any further here, but it will surely become a field of intensive investigation in the nearer future. The entire nucleus is also pervaded by another, by definition DNA-free, IC channel network, which occasionally forms larger IC-lacunae, known to contain macromolecular complexes like splicing speckles or PML bodies. Here, the PR and IC are collectively referred to as the ANC. It could be shown that the ANC is ultimately leading towards nuclear pores and that it does not reflect a fixation artifact, thus implying and reinforcing its functional importance. The ANC is found to be enriched with SAF-A, thus linking the presence of a suggested nuclear matrix with this functional chromatin compartment. A narrowed, but still present, ANC is also clearly visible within the Barr body. Although, in the Barr body larger IC-lacunae are very rare, they can still be observed occasionally and coincide with active histone marks and active transcription, thus possibly harbor XCI escape genes. The collapsed ANC of the Barr body is still able to fulfill its functional role as a hub for replication or rarely occurring expression of escape genes, which leads to a widening of this preformed channel system, and which can even be chemically inducible by e.g. hyperosmotic conditions.

Xist RNA has been shown to be preferentially located within this narrow ANC of the Barr body, where it strongly colocalizes with SAF-A. This interaction is very likely to cause a Xi-specific post-

[2] According to recent 3C-based studies, an average CD/TAD is comprised of ~500 kb of DNA, which according to the CT-IC model and confirmed by the 3D-SIM data in this thesis would be organized in all kinds of compaction states (Bickmore and van Steensel, 2013; Dixon et al., 2012; Lieberman-Aiden et al., 2009; Nora et al., 2012). The entire Barr body has a volume of about 8 – 10 µm³ (roughly 2 x 2 x 2 µm in C2C12 cells). Given the total genomic size of ~170 Mbp of the mouse X chromosome results in an average volume of ~0.0235 µm³ per CD/TAD. Assuming a sphere-like shape, results in a diameter of ~360 nm per CD/TAD. It is reasonable to assume a sphere-like shape here as this sphere would not be homogenous, but also include all possible ANC regions, because the initial volume value has been deduced from the total Xi volume, which equally includes all possible compaction states. Of note, this value is just an average number, which might vary substantially *in vivo* and between individual CDs/TADs. However, this value is far above the resolvable limit of 3D-SIM and the fact that no regularly shaped entities are observable within chromatin stainings implies that individual CDs/TADs are highly variable and dynamic structures, which are moreover interconnected throughout the nucleus. This calculation is not supposed to provide an exact number, but rather give a rough estimate of size scales for discussions and future experiments.

translational modification of SAF-A, which may induce its polymerization and thus act as an anchor system for the sequence-independent spreading of Xist RNA throughout the Xi. This post-translational modification may also explain the observed enrichment of SAF-A:GFP at the Xi (Fackelmayer et al., 1994; Hasegawa et al., 2010; Helbig and Fackelmayer, 2003). The fact that Xist RNA is not distributed evenly but as distinct foci may also help to explain its role in XCI. An intriguing explanation is the accumulation of Xist RNA at non-repetitive sites, possibly reflecting genic sites or regulatory elements, which has already been hypothesized in studies on metaphase spreads or in more recent high-throughput epigenomic studies (Duthie et al., 1999; Marks et al., 2009; Pinter et al., 2012). Here, it could block the access for the transcription machinery, hence, offering a novel mechanism for Xist RNA-induced gene silencing. Another (parallel) mode of action might be the induction of locally constrained chromatin compaction, which in turn mediates the recruitment of other silencing machinery. This is also in line with the observation that Xist RNA is not directly colocalizing with PRC2, as previously assumed, and that PRC2 may rather be recruited through indirect effects, like the Xist RNA-induced chromatin compaction (Brockdorff, 2013; Cerase et al., 2013, *submitted*; Yuan et al., 2012).

Lastly, a first attempt has been made to integrate the findings of this work into a refined model of higher-order chromatin architecture of both Barr body and autosomal chromatin at the nucleosomal level (see Figure 5-1, C). There is still a vast lack of understanding how higher-order chromatin structure is organized within the interphase nucleus between the level of the 10 nm DNA-fiber and chromosome territories. This is mainly due to historical methodological limitations of EM on the one side and conventional light microscopy on the other side. Recent developments in surpassing the resolution limit of light, like the 3D-SIM data in this work, but also improvement of sequencing depth in 3C-based techniques or advancements in theoretical physical modeling of chromatin properties have started to close this gap. It will need further attempts in the future to integrate all these different areas to be able to truly understand how chromatin is organized on the nucleosomal level within CDs/TADs and how their structure and dynamics are able to fulfill the various needs like genome integrity, transcriptional regulation, fast and reliable access to specific genomic loci or rapid and accurate replication.

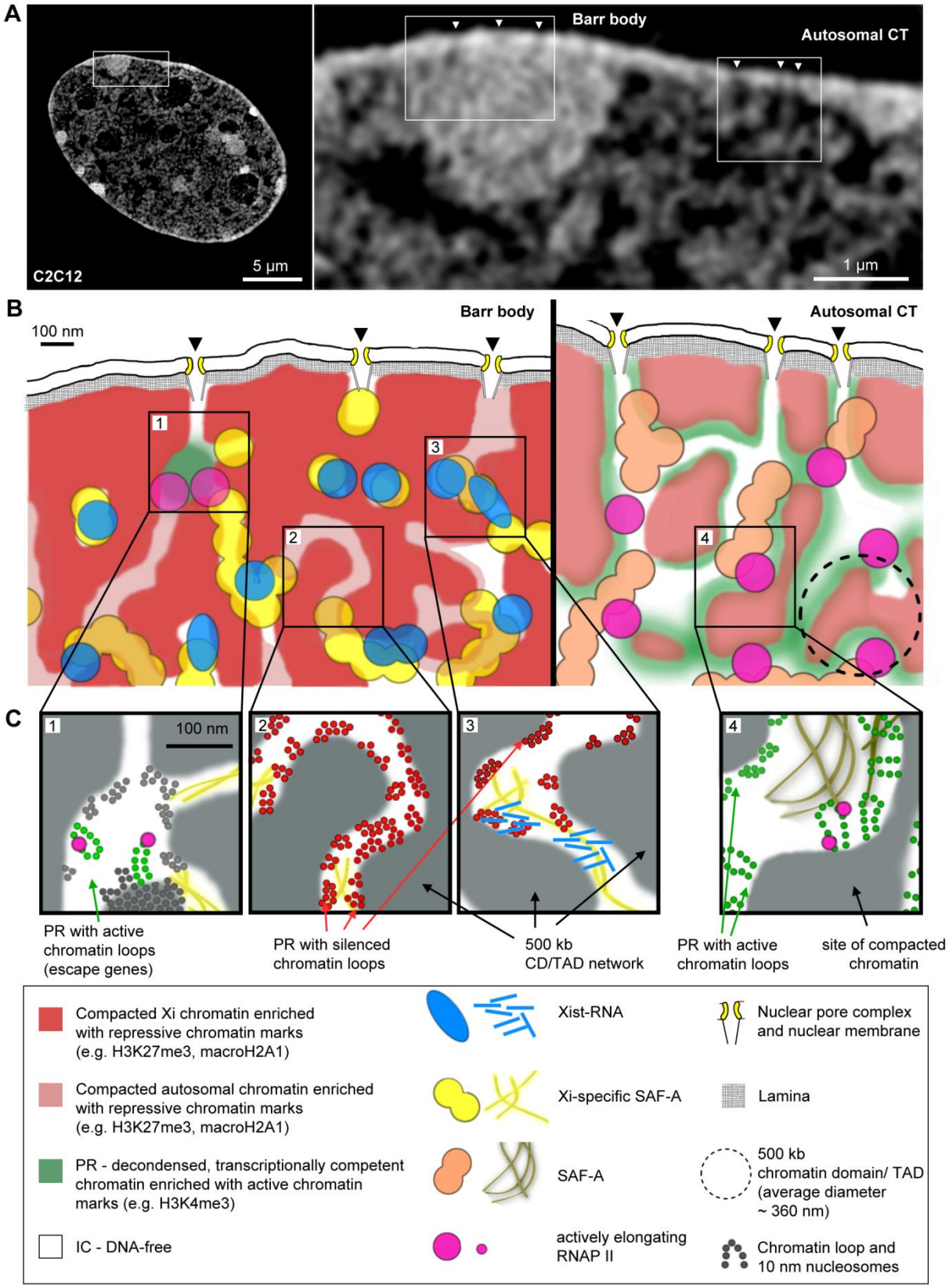

Figure 5-1 In-scale summary about the organization of Barr body and autosomal chromatin together with distribution of Xi-specific chromatin marks and other factors including a hypothetical outlook. (A) Single optical z-section of a DAPI-stained C2C12 nucleus. White boxes display typical Barr body and neighboring autosomal chromatin. Arrowheads point at nuclear pores. **(B)** Summary of nuclear architecture of Barr body and autosomal chromatin including the distribution of some of the analyzed factors in this work. Scheme is drawn to scale using the marked areas in (A) as a reference at the resolution achievable with 3D-SIM. Dotted circle indicates the ~ 360 nm average diameter of a 500 kb CD/TAD as determined by theoretical calculations. Its diameter is above the level of 3D-SIM resolution almost by factor of 3. **(C)** Hypothetical model view about the chromatin architecture at 4 exemplary nuclear sites drawn roughly to scale. **(Inset 1)**

Decondensed sites harboring escape genes can potentially emerge throughout the nucleus. Individual chromatin loops, enriched with active histone marks, can reach out of the compacted chromatin environment and be transcribed in the PR region, where they have also access to the nuclear ANC. **(Inset 2)** Typical site of repressed Barr body chromatin. Only very small-scale and still compacted chromatin loops, enriched with repressive histone marks, reach out of the compacted CD/TAD core into the ANC. The ANC network is only very narrow and can occasionally disappear completely when opposing chromatin loops come together. Neighboring or opposing chromatin loops do not overlap or intermingle to minimize detrimental entanglement effects. However, IC channels are prone to emerge and widen again upon need, e.g. during replication or via osmotic induction (HCC). **(Inset 3)** Xist RNA spreads along Xi-specific SAF-A, which probably polymerizes within the Barr body, either as consequence or prerequisite of Xist RNA interaction. Xist RNA undergoes multimerization and potentially accumulates at genic sites throughout the Barr body, where it blocks the access of the transcription machinery and thus contributes to the maintenance of Xi-linked gene silencing. It may also have a functional role in causing or maintaining chromatin compaction, which is a prerequisite for the accumulation of repressive chromatin modifications. **(Inset 4)** Autosomal chromatin is comprised of interconnected CDs/TADs of variable shape and highly dynamic. Individual CDs/TADs cannot be separated visually. Compacted cores of CDs/TADs are enriched with repressive histone marks and surrounded by decondensed chromatin enriched in active chromatin marks and harboring nuclear processes like transcription and replication. Autosomal chromatin is, unlike the Barr body, pervaded by wider IC lacunae, which are known to carry large macromolecular complexes like splicing speckles or PML bodies, and are ultimately leading towards the nuclear pores. Figure adapted from (Smeets et al., 2013b*, submitted*).

The data obtained with 3D-SIM presented in this thesis, substantiated and expanded the current CT-IC model of chromatin architecture that is mainly based on observations with conventional microscopy and EM, but has not been commonly accepted because of these methodological constraints. 3D-SIM data presented here has also provided a basis to make first promising attempts to integrate and complement high-throughput data of 3C-based whole-population studies on chromatin architecture with findings and model views based on the single-cell level. Lastly, 3D-SIM probably uncovered a yet unknown functional role of Xist RNA in gene silencing and maintaining the Barr body structure, which will contribute to the understanding of XCI reflecting a fundamental process in mammalian epigenetic regulation and chromatin architecture and will probably lead to a reappraisal of commonly accepted models about Xist RNA and its role in XCI.

6 Appendix

6.1 Abbreviations

3C	Chromosome conformation capturing
3E ESC	Mouse male embryonic stem cell line carrying an inducible Xist RNA transgene on Chromosome 17
2D / 3D	2-dimensional / 3-dimensional
ANC	Active nuclear compartment
bp	Base-pair
CD	Chromatin domain
CT	Chromosome territory
DAPI	4',6-diamidino-2-phenylindole
ESC	Embryonic stem cell
EtOH	Ethanol
FISH	Fluorescence *in situ* hybridization
HCC	Hypercondensation of chromatin
HFb	Human fibroblast
hrGFP	Humanized recombinant GFP
HSA	Human (*Homo sapiens*)
HybMix	Hybridization Mixture
IC	Interchromatin compartment
IF	Immunofluorescence
kb	Kilobase
LIF	*Leukaemia Inhibitor Factor*
Mb	Megabase
MEF	Mouse embryonic fibroblast
MMU	Mouse (*Mus musculus*)
NA	Numerical aperture
OTF	Optical transfer function
PALM	Photoactivated localization microscopy
PNC	Passive nuclear compartment
PR	Perichromatin region
PRC	*Polycomb Repressive Complex*
PSF	Point spread function

RNAP II	RNA-Polymerase II Ser2P
RT	Room temperature
SIM	Structured illumination microscopy
STED	Stimulated emission depletion microscopy
STORM	Stochastic optical reconstruction microscopy
TAD	Topology associated domain
tr36 ESC	Mouse male embryonic stem cell line carrying an inducible Xist RNA transgene on Chromosome 11
VRC	Vanadyl ribonucleoside complex
Xa / Xi	Active / Inactive X chromosome
XCI	X chromosome inactivation
XIC	X inactivation center
Xist	*X inactive specific transcript*
Xm	Maternal X chromosome
Xp	Paternal X chromosome
XX ESC	Female embryonic stem cell

6.2 Materials and equipment

6.2.1 Cell lines

Table 6-1 Cell lines

Cell line	Cell type	Medium	Source
3E ESC	Mouse male embryonic stem cells carrying a doxycyclin-inducible Xist-transgene on Autosome 17	ES-Medium (on Feeder cells)	kindly provided by A. Wutz, Wellcome Trust, Cambridge, UK
C127	Mouse mammary gland carcinoma cells	DMEM + 10% FCS + 0.1% Gentamycin	
C2C12	Mouse myoblast cells	DMEM + 20% FCS + 0.1% Gentamycin	kindly provided by C. M. Cardoso, Technical University Darmstadt
Feeder cells	Mitomycin-treated MEF cells	ES- or DMEM	kindly provided by C. Hepperger, LMU Munich
HeLa H2B-GFP	Stably expressing H2B-GFP	DMEM + 10% FCS + 0.1% Gentamycin	
HeLa Kyoto	Human cervix carcinoma cells (immobilized)	DMEM + 10% FCS + Pen./Strep.	
HFb	Human primary fibroblasts	DMEM + 10% FCS + 0.1% Gentamycin	kindly provided by I. Solovei, LMU Munich
MEF	Mouse primary embryonic fibroblasts	DMEM + 10% FCS + 0.1% Gentamycin	kindly provided by I. Solovei, LMU Munich
RPE-1	Human retina pigment epithelial cells	DMEM/Ham's F12 + 10% FCS + 0.1% Gentamycin	kindly provided by F. Eckhardt-Schupp, Helmholtz Zentrum Munich
tr36 ESC	Mouse male embryonic stem cells carrying a	N2B27 ES-Medium (for feeder-free conditions)	kindly provided by A. Wutz, Wellcome Trust Cambridge, UK

	doxycyclin-inducible Xist-transgene on Autosome 11		
XX ESC (clone 16.7)	Mouse female embryonic stem cells	N2B27 ES-Medium (for feeder-free conditions)	kindly provided by J. T. Lee, Harvard Medical School, USA

6.2.2 Chemicals and reagents

Table 6-2 Chemicals and reagents

Chemical	Manufacturer
4',6-Diamidin-2-phenylindole (DAPI)	Roche Diagnostics, Mannheim
β-Mercaptoethanol	Sigma-Aldrich, Munich
B27 (50x)	Invitrogen, Darmstadt
BlockAid Blocking Buffer	Invitrogen, Darmstadt
BSA (fraction V, powder)	AppliChem, Darmstadt
BSA (purified)	New England Biolabs, Frankfurt
Dextransulfate	Amersham-Pharmacia Biotech, Braunschweig
Dimethylsulfoxide (DMSO)	AppliChem, Darmstadt
Disodiumhydrogenphosphate (Na_2HPO_4)	AppliChem, Darmstadt
Doxycyclin	Sigma-Aldrich, Munich
Dulbecco's modified Eagle's medium (DMEM) GlutaMAX, high glucose, with L-Glutamine	Sigma-Aldrich, Munich
Dulbecco's modified Eagle's medium (DMEM) GlutaMAX, high glucose, with L-Glutamine, without Phenol Red	Sigma-Aldrich, Munich
Dulbecco's modified Eagle's medium (DMEM) GlutaMAX/ Ham's F12 (1:1, v/v), high glucose, with L-Glutamine	Sigma-Aldrich, Munich
EDTA	Merck, Darmstadt
Ethanol absolute	Merck, Darmstadt
Fetal calf serum (FCS)	PAA Laboratories, Pasching/Austria
Fetal calf serum (FCS), ES grade	PAA Laboratories, Pasching/Austria
Fish skin gelatine (FSG)	Sigma-Aldrich, Munich
Formaldehyde (37%, stabilized with 15% methanol)	AppliChem, Darmstadt

Formamide (100%, deionized)	Merck, Darmstadt
Gelatine	Sigma-Aldrich, Munich
Gentamycin	Sigma-Aldrich, Munich
Glycerol	Merck, Darmstadt
Glycine	Carl Roth, Karlsruhe
HEPES (1M)	PAA Laboratories, Pasching/Austria
Hydrochloric acid (HCl) 1N	Merck, Darmstadt
Isopropanol	Merck, Darmstadt
LIF (Leukaemia Inhibitor Factor) ESGRO	Chemicon/Millipore, Temecula, CA, USA
Lipofectamine 2000	Invitrogen, Darmstadt
Magnesium chloride ($MgCl_2$)	Sigma-Aldrich, Munich
N2 (200x)	Millipore, Billerica, MA, USA
Neurobasal medium	Invitrogen, Darmstadt
Nitrogen, liquid (N_2)	Air-Liquide, Düsseldorf
Non-essential amino acids (100x)	PAA Laboratories, Pasching/Austria
Opti-MEM I Reduced Serum Medium	Invitrogen, Darmstadt
PBS (cell culture grade)	Sigma-Aldrich, Munich
Penicillin/Streptomycin	Seromed Biochrom, Berlin
Potassium chloride (KCl)	Carl Roth, Karlsruhe
Potassium dihydrogenphosphate (KH_2PO_4)	Merck, Darmstadt
Sodium acetate	Merck, Darmstadt
Sodium chloride (NaCl)	Carl Roth, Karlsruhe
Sodium citrate	Calbiochem, Darmstadt
Sodium hydroxide (NaOH)	Carl Roth, Karlsruhe
Tris-HCl	Sigma-Aldrich, Munich
Triton X-100	Carl Roth, Karlsruhe
Trypsin-EDTA	Sigma-Aldrich, Munich
Tween-20	Carl Roth, Karlsruhe
Vanadyl ribonucleoside complex (VRC)	New England Biolabs, Frankfurt
Vectashield antifade medium	Vector Laboritories
W1 (Polyoxyethylene ether W1)	Sigmal-Aldrich, Munich

6.2.3 Buffers, solutions and media

Table 6-3 Buffers, solutions and media

Buffer/solution	Components	Notes
Blocking buffer (IF)	4% BSA	10 g BSA (fraction V, powder)
	0.5% FSG	266 µl FSG (47% stock solution)
	1x PBST/4x SSCT	50 ml 1x PBST **or** 4x SSCT
		Ultrafiltrate (pore size 0.45 µm)
DAPI working solution	2.5 µg/ml DAPI in 1x PBST	50 µl DAPI stock solution (500 µg/ml)
		in
		10 ml 1x PBST
		vortex well
ESC-Medium (with feeder		**500 ml:**
cells)	85% DMEM GlutaMAX	425 ml DMEM
	15% FCS (ESC-grade)	75 ml FCS (ESC-grade)
	1% Pen./Strep.	5 ml Pen./Strep.
	1x non-essential amino acids	5 ml non-essential amino acids
	1 µM β-Mercaptoethanol	5 ml β-Mercaptoethanol (100 µM)
	$1x10^3$ U/ml LIF	50 µl LIF ($1x10^7$ U/ml)
Fixation Buffer		**40 ml:**
	2% Formaldehyde	2 ml Formaldehyde (37%)
	1x PBS	38 ml 1x PBS
Formamide (50%) in 2x	50% Formamide	250 ml Formamide
SSC	50% 4x SSC	250 ml 4x SSC
		Adjust to pH 7.2 – 7.4 (Important!)
Freezing medium		**10 ml:**
	DMEM	7 ml DMEM
	20% FCS	2 ml FCS
	10% DMSO	1 ml DMSO
Gelatine solution (0.2%)		**200 ml:**
	1x PBS (cell culture grade)	200 ml 1x PBS
	0.2% Gelatine	0.4 g Gelatine
		autoclave
Quenching buffer		**100 ml:**
	1x PBST	100 ml 1x PBST

	100 mM Glycine	0.75 g Glycine
2x Hybridization buffer		**100 µl:**
	4x SSC	20 µl 20x SSC
	20% Dextransulfate	40 µl Dextransulfate (50%)
	20% BSA (purified)	20 µl BSA
	10% VRC (for RNA-FISH only)	10 µl VRC
		10 µl ddH_2O
Live-cell medium	DMEM (without Phenol Red)	45 ml DMEM
	10% FCS	5 ml FCS
	Gentamycin 1:1000	5 µl Gentamycin
	25mM HEPES	1.25 ml HEPES (1M)
N2B27 + 2i ES-Medium	*N2 Medium:*	
(for feeder-free	DMEM/ Ham's F12 (1:1)	124.5 ml DMEM/ Ham's F12 (1:1)
conditions)	1x N2 (1:200)	0.625 ml N2 (200x)
	50 µg/ml BSA Fraction V	83.5 µl BSA Fraction V (from 75 mg/ml stock)
	B27 Medium:	
	Neurobasal medium	122.5 ml Neurobasal medium
	1x B27(without retinoic acid)	2.5 ml B27 (50x)
	Mix 1:1 and add:	
	1 µM β-Mercaptoethanol	2.5 ml β-Mercaptoethanol (100 µM)
	20% Knockout Serum Replacement	50 ml Knockout Serum Replacement
	1x 10^3 U/ml LIF	30 µl LIF (1x 10^7 U/ml)
	1% Pen./Strep.	3 ml Pen./Strep.
	3 µM CHIR99021	70 µl CHIR99021 (10.7 mM)
	1 µM PD0325901	125 µl PD0325901 (2 mM)
10x Nick-translation (NT)		**100 ml:**
buffer	500 mM Tris-HCl (pH 7.5)	50 ml 1M Tris-HCl (pH 7.5)
	50 mM $MgCl_2$	5 ml 1M $MgCl_2$
	0.05% BSA	50 mg BSA
		45 ml ddH_2O
PBS Buffer (pH 7.4)		**10x PBS:**
	137 mM NaCl	80 g NaCl

	2.7 mM KCl	2 g KCl
	8.0 mM Na_2HPO_4	21.07 g Na_2HPO_4 x 7 H_2O
	1.5 mM KH_2PO_4	2 g KH_2PO_4
		Ad 1 l ddH_2O and adjust to pH 7.4 with HCl
		autoclave
1x PBST	0.02% Tween-20 in 1x PBS	200 µl Tween-20 in 1 l 1x PBS
High-stringency PBST		**400 ml:**
	300 mM NaCl	7.01 g NaCl
	1x PBST	400 ml 1x PBST
		(adds an extra 300 mM NaCl for higher protein binding stringency)
Permeabilization Buffer		**40 ml:**
	1x PBST	38 ml 1x PBST
	0.5% Triton X-100	2 ml Triton X-100 (10% stock solution)
Post-fixation buffer		**40 ml:**
	4% Formaldehyde	4 ml Formaldehyde (37%)
	1x PBST	36 ml 1x PBST
SSC Buffer (pH 7.0)		**20x SSC:**
	150 mM NaCl	175.3 g NaCl
	15 mM Na-citrate	88.2 g Na-citrate
		Ad 1 l ddH_2O and adjust to pH 7.0 with NaOH
		Autoclave
		Use ddH2O to dilute down to 4x, 2x and 0.1x SSC
4x SSCT	0.02% Tween-20 in 4x SSC	200 µl Tween-20 in 1 l 4x SSC

6.2.4 Enzymes, nucleotides and kits

Table 6-4 Enzymes, nucleotides and kits

Reagent	Manufacturer
6MW-Primer (5' – CCG ACT CGA GNN NNN NAT GTG G – 3')	MWG-Biotech, Ebersberg
Biotin-dUTP	Roche Diagnostics, Mannheim

BrdU (5-Bromo-2-deoxyuridine)	Invitrogen, Darmstadt
dATP, dCTP, dGTP, dTTP (100 mM)	Roche Diagnostics, Mannheim
Digoxigenin-dUTP	Roche Diagnostics, Mannheim
Dnase I (grade II)	Roche Diagnostics, Mannheim
DNA-Polymerase I	Roche Diagnostics, Mannheim
EdU (5-ethynyl-2-deoxyuridine)	Baseclick, Tutzing
GeneAmp PCR buffer (10x)	Applied Biosystems, Darmstadt
GenomiPhi Amplification Kit	GE Healthcare, Munich
Mouse C_0t-1 DNA	Invitrogen, Darmstadt
PCR buffer D (5x)	Invitrogen, Darmstadt
Pepsin	Sigma-Aldrich, Steinheim
Salmon sperm DNA	Invitrogen, Darmstadt
Taq-Polymerase	Amersham-Pharmacia Biotech, Braunschweig
Yeast t-RNA	Invitrogen, Darmstadt

6.2.5 Antibodies

Table 6-5 Primary antibodies

Antibody	Dilution	Manufacturer
Rab α ATRX (H-300)	1:200	Santa Cruz, Santa Cruz, CA, USA
M α BrUTP	1:200	Sigma-Aldrich, Steinheim
M α Digoxigenin	1:200	Sigma-Aldrich, Steinheim
M α Eed	1:100	kindly provided by Brockdorff Lab, University of Oxford, UK
Rab (mAb) α Ezh2 (DC29)	1:200	Cell Signaling, Danvers, MA, USA
Rab α H3K4me3	1:500	Active Motif, La Hulpe, Belgium
M α H3K27me3	1:500	Active Motif, La Hulpe, Belgium
Rab α H3K27me3	1:500	Active Motif, La Hulpe, Belgium
Rab α hrGFP	1:100	Agilent Technologies, Palo Alto, CA, USA
Goat α LaminB	1:200	Santa Cruz, Santa Cruz, CA, USA
Rab α macroH2A1	1:500	Active Motif, La Hulpe, Belgium
M α Nup153 (QE5)	1:100	Abcam, Cambridge, UK
Rat α PCNA (16D10)	1:500	kindly provided by A. Rottach, Leonhardt Lab, LMU Munich

M α Ring1B	1:100	kindly provided by H. Koseki, RIKEN, Yokohama, Japan
M α RNAP II Ser2P	1:100	kindly provided by D. Eick, LMU Munich
Rab α SAF-A	1:200 – 1:500	kindly provided by A. Tattermusch, Brockdorff Lab, University of Oxford, UK
Rab (mAb) α Suz12 (D39F6)	1:200	Cell Signaling, Danvers, MA, USA

Table 6-6 Secondary Antibodies

Antibody	Dilution	Manufacturer
Donkey α M – Alexa 488	1:500	Invitrogen, Darmstadt
Donkey α M – Alexa 594	1:500	Invitrogen, Darmstadt
Goat α Rab – Alexa 488	1:500	Invitrogen, Darmstadt
Donkey α Rab – Alexa 594	1:500	Invitrogen, Darmstadt
Goat α Rat – Alexa 488	1:500	Invitrogen, Darmstadt
Donkey α Rat – Alexa 594	1:500	Invitrogen, Darmstadt
Streptavidin – Alexa 488	1:200	Invitrogen, Darmstadt
Streptavidin – Alexa 594	1:200	Invitrogen, Darmstadt
Goat α M – CF405S	1:100	Biotium, Hayward, CA, USA
Goat α M – CF405M	1:100	Biotium, Hayward, CA, USA
GFP-Booster IV – Atto 488	1:20 – 1:100	Chromotek, Martinsried

6.2.6 Equipment and hardware

Table 6-7 Equipment and hardware

Device	Note	Manufacturer
Autoclave	Varioklav	Heraeus, Hanau
Centrifuge	Biofuge pico	Heraeus, Hanau
Centrifuge	Rotina 38R	Hettich Zentrifugen, Tuttlingen
Centrifuge	JA-14	Beckman Coulter, Krefeld
CO_2 Incubator	BBD 6220	Thermo Fisher Scientific, Schwerte
Heat block	DB 2-D	Techne, Cambridge, UK
Laminar flow cabinet	Heraeus Hera safe	Thermo Fisher Scientific, Schwerte
Pipette Aid	PIPETBOY acu	INTEGRA Biosciences, Fernwald
Table-top centrifuge	Centrifuge 5424	Eppendorf, Hamburg
Thermoshaker	Thermomixer comfort	Eppendorf, Hamburg
Thermocycler	Mastercycler gradient	Eppendorf, Hamburg

Vacuum centrifuge	Vacuumconcentrator	Bachhofer, Reutlingen
Vortex mixer	Neolab 7-2020	Neolab, Heidelberg
Water bath	SW-20C	JULABO, Seelbach
Water purification system	Milli-Q Plus	Millipore, Schwalbach

6.2.7 Glass and plastic consumables

Table 6-8 Glass and plastic consumables

Consumable	Notes	Manufacturer
µ-dish	35 mm, high	Ibidi, Martinsried
6-well dish		Greiner Bio One, Frickenhausen
Coverslip mini-rack		Invitrogen, Darmstadt
Cryo-tubes	1.8 ml	Greiner Bio One, Frickenhausen
Falcon tubes	15 ml, 50 ml	Becton Dickinson, San Jose, CA, USA
Fixogum		Marabuwerke, Tamm
Glass bottles	100 ml, 250 ml, 500 ml, 1 l	Schott, Stafford, UK
Glass coverslips (high precision thickness, 0.170 mm ± 0.005 mm)	18 x 18 mm 22 x 22 mm 24 x 60 mm	Carl Roth, Karlsruhe
Glass slides (iced)	26 x 76 mm (SuperFrost)	Menzel-Gläser, Braunschweig
Nail polish		Rimmel, London, UK
Nitril gloves		Neolab, Heidelberg
Parafilm		Neolab, Heidelberg
Pasteur pipettes	3 ml	Becton Dickinson, San Jose, CA, USA
Reaction tubes	1.5 ml, 2 ml	Eppendorf, Hamburg
QuadriPerms		Greiner Bio One, Frickenhausen
Serological pipettes	1 ml, 2ml 5 ml, 10 ml, 25, ml	Sarstedt, Nürnbrecht Costar, Corning, USA
Soft wipes	Kimtech Science (green and black)	Kimberly-Clark Europe, Surrey, UK
Sterile filters	pore size 0.45µm	Satorius, Göttingen
Sterile syringes	1 ml, 5 ml, 20 ml	Schubert & Weiss, Munich
Tissue culture flasks	T25 (25 cm^2)	Greiner Bio One, Frickenhausen

	T75 (75 cm^2)	
Tissue culture dish	p100 (10 cm^2)	Greiner Bio One, Frickenhausen
Watchmaker forceps		Dumont, Montiguez, Switzerland

6.2.8 Miscellaneous

Table 6-9 Miscellaneous

Various devices	
+4°C fridge	Microwave oven
-20°C / -80°C freezer	Pipette tips
Alarm clock	Polystyrene boxes
Humid chamber	Precision scale
Ice machine	Slide holders
Liquid N_2 tank	Slide storage containers
Magnetic stirrer	UV-lamp
Metal box	Vacuum pump

6.2.9 Microscopes

Table 6-10 Microscopes

Microscopes		
3D-SIM setup Munich	**Deltavision OMX V3 Prototype**	Applied Precision Imaging/ GE Healthcare, Amersham, UK
Objective	UPlan S Apo 100x / 1.4 NA oil objective (Olympus)	
Lasers	405 nm 600 mW diode laser (Power technology) 488 nm 200 mW VECSEL (Coherent) 592.5 nm 300 mW diode laser (MPB Communications)	
Cameras	Cascade II:512 16-bit EMCCD (Photometrics)	
Software	SoftWorx 4.0	

3D-SIM setup Oxford, UK	**Deltavision OMX V3 Blaze**	Applied Precision Imaging/ GE Healthcare, Amersham, UK
Objectives	Plan Apochromat 100x / 1.4 NA oil objective (Olympus) Plan Apochromat 63x / 1.4 NA oil objective (Olympus) with heater unit	
Lasers	405 nm 600 mW diode laser (Power technology) 488 nm 200 mW VECSEL (Coherent) 564 nm 200 mW VECSEL (Coherent) 592.5 nm 300 mW diode laser (MPB Communications)	
Cameras	14-bit Edge sCMOS (PCO)	
Software	SoftWorx 4.0	

Wide-field deconvolution microscope	**personalDV**	Applied Precision Imaging/ GE Healthcare, Amersham, UK
Objectives	Plan Apo N 63x / 1.42 NA oil objective (Olympus) UPlan S Apo 10x / 0.40 NA UPlan FL N 4x / 0.13 NA	
Fluorescence filters	DAPI (Ex: 350/50 nm, Em: 455/50 nm) FITC (Ex: 490/20 nm, Em: 525/36 nm) TRITC (Ex: 555/25 nm, Em: 605/52 nm) Cy5 (Ex: 645/30 nm, Em: 705/72 nm) 250 W Xenon Arc lamp	
Camera	12-bit CoolSNAP HQ² CCD camera	
Software	SoftWorx 4.0	

Spinning Disc microscope	**Axio Observer D1**	Carl Zeiss, Jena
Objectives	A-Plan 10x / 0.25 NA Ph1 LD-Plan NEOFLUAR 20x / 0.6 NA Ph2 Plan NEOFLUAR 40x oil / 1.3 Ph3 Plan Apochromat 63x oil / 1.4 NA Plan Apochromat 100x oil / 1.4 NA	
Fluorescence filter sets	DAPI (G 265 nm, FT 395 nm, BP 445/50 nm) FITC (FT 495 nm, BP 525/50 nm) Cy3.5v1 (FT 585 nm, BP 620/60 nm) UV-Filter for life-cell observations 3RD Millenium Longpass Filter LC-3RD/450LP-25	
Spinning Disc Confocal Unit	Ultra *View* VoX	Perkin Elmer, Waltham, MA, USA
FRAP	FRAP photokinesis Unit	
Camera	EMCCD camera	
Software	Volocity 5.3	

LED Phase contrast microscope	**EVOS fl**	AMG, Bothell, WA, USA
Objectives	Plan Fluor 40x / 0.65 NA Plan Fluor 20x / 0.45 NA Plan Fluor 10x / 0.30 NA Plan PH2 10x / 0.25 NA UPlan FL N 4x / 0.13 PhP	
Fluorescence filters	DAPI (Ex: 375nm, Em: 447 nm) GFP (Ex: 470 nm, Em: 525 nm) RFP (Ex: 531 nm, Em: 593 nm) LED-Illumination Phase contrast	
Camera	Sony ICX285AL CCD	

6.2.10 Image processing, analysis and other software

Table 6-11 Software

Software	Manufacturer
Adobe CS4	Adobe Systems, Inc.
Amira 5.2.2	Visage Imaging
ImageJ v.1.47	Wayne Rasband http://rsb.info.nih.gov/ij/
Microsoft Office 2007	Microsoft Corp.
R v.2.15.0	Kurt Hornik http://CRAN.R-project.org/doc/FAQ/R-FAQ.html
SoftWorx 4.0	Applied Precision Imaging/GE Healthcare
Volocity 5.3	Perkin Elmer

7 References

Abbe, E. (1873). Beiträge zur Theorie des Mikroskops und der mikroskopischen Wahrnehmung. *Archiv für mikroskopische Anatomie*.

Adkins, N. L., Watts, M. and Georgel, P. T. (2004). To the 30-nm chromatin fiber and beyond. *Biochimica et biophysica acta* **1677**, 12–23.

Agostini, F., Cirillo, D., Bolognesi, B. and Tartaglia, G. G. (2013). X-inactivation: quantitative predictions of protein interactions in the Xist network. *Nucleic acids research* **41**, e31.

Agrelo, R., Souabni, A., Novatchkova, M., Haslinger, C., Leeb, M., Komnenovic, V., Kishimoto, H., Gresh, L., Kohwi-Shigematsu, T., Kenner, L., et al. (2009). SATB1 defines the developmental context for gene silencing by Xist in lymphoma and embryonic cells. *Developmental Cell* **16**, 507–16.

Akhtar, A. and Gasser, S. M. (2007). The nuclear envelope and transcriptional control. *Nature reviews. Genetics* **8**, 507–17.

Albiez, H., Cremer, M., Tiberi, C., Vecchio, L., Schermelleh, L., Dittrich, S., Küpper, K., Joffe, B., Thormeyer, T., Von Hase, J., et al. (2006). Chromatin domains and the interchromatin compartment form structurally defined and functionally interacting nuclear networks. *Chromosome Research* **14**, 707–33.

Arib, G. and Akhtar, A. (2011). Multiple facets of nuclear periphery in gene expression control. *Current opinion in cell biology* **23**, 346–53.

Arthold, S., Kurowski, A. and Wutz, A. (2011). Mechanistic insights into chromosome-wide silencing in X inactivation. *Human genetics* **130**, 295–305.

Augui, S., Filion, G. J., Huart, S., Nora, E., Guggiari, M., Maresca, M., Stewart, A. F. and Heard, E. (2007). Sensing X chromosome pairs before X inactivation via a novel X-pairing region of the Xic. *Science* **318**, 1632–6.

Bacher, C. P., Guggiari, M., Brors, B., Augui, S., Clerc, P., Avner, P., Eils, R. and Heard, E. (2006). Transient colocalization of X-inactivation centres accompanies the initiation of X inactivation. *Nature cell biology* **8**, 293–9.

Baddeley, D. and Chagin, V. (2010). Measurement of replication structures at the nanometer scale using super-resolution light microscopy. *Nucleic acids research* **38**, e8.

Bailey, J. A., Carrel, L., Chakravarti, A. and Eichler, E. E. (2000). Molecular evidence for a relationship between LINE-1 elements and X chromosome inactivation: The Lyon repeat hypothesis. *Proceedings of the National Academy of Sciences of the United States of America* **97**, 6634–6639.

Bannister, A. J. and Kouzarides, T. (2011). Regulation of chromatin by histone modifications. *Cell research* **21**, 381–95.

Barakat, T. S., Gunhanlar, N., Pardo, C. G., Achame, E. M., Ghazvini, M., Boers, R., Kenter, A., Rentmeester, E., Grootegoed, J. A. and Gribnau, J. (2011). RNF12 activates Xist and is essential for X chromosome inactivation. *PLoS genetics* **7**, e1002001.

Barr, M. and Bertram, E. (1949). A morphological distinction between neurones of the male and female, and the behaviour of the nucleolar satellite during accelerated nucleoprotein synthesis. *Nature*.

Beletskii, a, Hong, Y. K., Pehrson, J., Egholm, M. and Strauss, W. M. (2001). PNA interference mapping demonstrates functional domains in the noncoding RNA Xist. *Proceedings of the National Academy of Sciences of the United States of America* **98**, 9215–20.

Beliveau, B. J., Joyce, E. F., Apostolopoulos, N., Yilmaz, F., Fonseka, C. Y., McCole, R. B., Chang, Y., Li, J. B., Senaratne, T. N., Williams, B. R., et al. (2012). Versatile design and synthesis platform for visualizing genomes with Oligopaint FISH probes. *Proceedings of the National Academy of Sciences of the United States of America* **109**, 21301–6.

Belmont, A. (2006). Mitotic chromosome structure and condensation. *Current opinion in cell biology* **5**, 632–638.

Bennett, B. T., Bewersdorf, J. and Knight, K. L. (2009). Immunofluorescence imaging of DNA damage response proteins: optimizing protocols for super-resolution microscopy. *Methods* **48**, 63–71.

Berletch, J. B., Yang, F., Xu, J., Carrel, L. and Disteche, C. M. (2011). Genes that escape from X inactivation. *Human genetics* **130**, 237–45.

Betzig, E., Patterson, G. H., Sougrat, R., Lindwasser, O. W., Olenych, S., Bonifacino, J. S., Davidson, M. W., Lippincott-Schwartz, J. and Hess, H. F. (2006). Imaging intracellular fluorescent proteins at nanometer resolution. *Science* **313**, 1642–5.

Bian, Q. and Belmont, A. S. (2012). Revisiting higher-order and large-scale chromatin organization. *Current opinion in cell biology* **24**, 359–66.

Bickmore, W. A. and Van Steensel, B. (2013). Genome Architecture: Domain Organization of Interphase Chromosomes. *Cell* **152**, 1270–1284.

Bird, A. (2002). DNA methylation patterns and epigenetic memory. *Genes & development* **16**, 6–21.

Blewitt, M. E., Gendrel, A.-V., Pang, Z., Sparrow, D. B., Whitelaw, N., Craig, J. M., Apedaile, A., Hilton, D. J., Dunwoodie, S. L., Brockdorff, N., et al. (2008). SmcHD1, containing a structural-maintenance-of-chromosomes hinge domain, has a critical role in X inactivation. *Nature genetics* **40**, 663–9.

Bolte, S. and Cordelières, F. P. (2006). A guided tour into subcellular colocalization analysis in light microscopy. *Journal of microscopy* **224**, 213–32.

Bolzer, A., Kreth, G., Solovei, I., Koehler, D., Saracoglu, K., Fauth, C., Müller, S., Eils, R., Cremer, C., Speicher, M. R., et al. (2005). Three-dimensional maps of all chromosomes in human male fibroblast nuclei and prometaphase rosettes. *PLoS biology* **3**, e157.

Bönisch, C., Schneider, K., Pünzeler, S., Wiedemann, S. M., Bielmeier, C., Bocola, M., Eberl, H. C., Kuegel, W., Neumann, J., Kremmer, E., et al. (2012). H2A.Z.2.2 is an alternatively spliced

histone H2A.Z variant that causes severe nucleosome destabilization. *Nucleic acids research* **40**, 5951–64.

Borsani, G., Tonlorenzi, R., Simmler, M., Dandolo, L., Arnaud, D., Capra, V., Grompe, M., Pizzuti, A., Muzny, D., Lawrence, C., et al. (1991). Characterization of a murine gene expressed from the inactive X chromosome. *Nature* **351**, 325–329.

Boyle, S., Rodesch, M. J., Halvensleben, H. a, Jeddeloh, J. a and Bickmore, W. a (2011). Fluorescence in situ hybridization with high-complexity repeat-free oligonucleotide probes generated by massively parallel synthesis. *Chromosome Research* **19**, 901–9.

Branco, M. R., Ficz, G. and Reik, W. (2012). Uncovering the role of 5-hydroxymethylcytosine in the epigenome. *Nature reviews. Genetics* **13**, 7–13.

Brockdorff, N. (2011). Chromosome silencing mechanisms in X-chromosome inactivation: unknown unknowns. *Development* **138**, 5057–65.

Brockdorff, N. (2013). Noncoding RNA and Polycomb recruitment. *RNA* **19**, 429–42.

Brockdorff, N., Ashworth, A., Kay, G., Cooper, P., Smith, S., McCabe, V., Norris, D., Penny, G., Patel, D. and Rastan, S. (1991). Conservation of position and exclusive expression of mouse Xist from the inactive X chromosome. *Nature* **351**, 329–331.

Brown, C., Ballabio, A., Rupert, J., Lafreniere, R., Grompe, M., Tonlorenzi, R. and Willard, H. F. (1991a). A gene from the region of the human X inactivation centre is expressed exclusively from the inactive X chromosome. *Nature* **349**, 38–45.

Brown, C., Lafreniere, R., Powers, V., Sebastio, G., Ballabio, A., Pettigrew, A., Ledbetter, D., Levy, E., Craig, I. and Willard, H. F. (1991b). Localization of the X inactivation centre on the human X chromosome in Xq 13. *Nature* **349**, 83–84.

Brown, A. C. N., Oddos, S., Dobbie, I. M., Alakoskela, J.-M., Parton, R. M., Eissmann, P., Neil, M. A. A., Dunsby, C., French, P. M. W., Davis, I., et al. (2011). Remodelling of cortical actin where lytic granules dock at natural killer cell immune synapses revealed by super-resolution microscopy. *PLoS biology* **9**, e1001152.

Buck, S. B., Bradford, J., Gee, K. R., Agnew, B. J., Clarke, S. T. and Salic, A. (2008). Detection of S-phase cell cycle progression using 5-ethynyl-2'-deoxyuridine incorporation with click chemistry, an alternative to using 5-bromo-2'-deoxyuridine antibodies. *BioTechniques* **44**, 927–9.

Buzin, C. H., Mann, J. R. and Singer-Sam, J. (1994). Quantitative RT-PCR assays show Xist RNA levels are low in mouse female adult tissue, embryos and embryoid bodies. *Development* **120**, 3529–36.

Calabrese, J. M., Sun, W., Song, L., Mugford, J. W., Williams, L., Yee, D., Starmer, J., Mieczkowski, P., Crawford, G. E. and Magnuson, T. (2012). Site-specific silencing of regulatory elements as a mechanism of X inactivation. *Cell* **151**, 951–63.

Cantrell, M. A., Carstens, B. C. and Wichman, H. A. (2009). X chromosome inactivation and Xist evolution in a rodent lacking LINE-1 activity. *PloS one* **4**, e6252.

Capelson, M., Liang, Y., Schulte, R., Mair, W., Wagner, U. and Hetzer, M. W. (2010). Chromatin-bound nuclear pore components regulate gene expression in higher eukaryotes. *Cell* **140**, 372–83.

Cardoso, M. C., Schneider, K., Martin, R. M. and Leonhardt, H. (2012). Structure, function and dynamics of nuclear subcompartments. *Current opinion in cell biology* **24**, 79–85.

Carlton, P. (2008). Three-dimensional structured illumination microscopy and its application to chromosome structure. *Chromosome Research* **16**, 351–365.

Carlton, P. M., Boulanger, J., Kervrann, C., Sibarita, J.-B., Salamero, J., Gordon-Messer, S., Bressan, D., Haber, J. E., Haase, S., Shao, L., et al. (2010). Fast live simultaneous multiwavelength four-dimensional optical microscopy. *Proceedings of the National Academy of Sciences of the United States of America* **107**, 16016–22.

Carrel, L. and Willard, H. F. (2005). X-inactivation profile reveals extensive variability in X-linked gene expression in females. *Nature* **434**, 400–4.

Casolari, J. M., Brown, C. R., Komili, S., West, J., Hieronymus, H. and Silver, P. a (2004). Genome-wide localization of the nuclear transport machinery couples transcriptional status and nuclear organization. *Cell* **117**, 427–39.

Cerase, A., Smeets, D., Tang, Y. A., Gdula, M., Spivakov, M., Leleu, M., Moindroit, B., Tattermusch, A., Demmerle, J., Nesterova, T. B., et al. (2013). Spatial separation of Xist-RNA and Polycomb proteins revealed by 3D-SIM. *Proceedings of the National Academy of Sciences of the United States of America, submitted*.

Chadwick, B. P. (2007). Variation in Xi chromatin organization and correlation of the H3K27me3 chromatin territories to transcribed sequences by microarray analysis. *Chromosoma* **116**, 147–57.

Chadwick, B. P. and Willard, H. F. (2004). Multiple spatially distinct types of facultative heterochromatin on the human inactive X chromosome. *Proceedings of the National Academy of Sciences of the United States of America* **101**, 17450–5.

Chagin, V. O., Stear, J. H. and Cardoso, M. C. (2010). Organization of DNA replication. *Cold Spring Harbor perspectives in biology* **2**, a000737.

Charlesworth, B. (1996). The evolution of chromosomal sex determination and dosage compensation. *Current biology* **6**, 149–62.

Chaumeil, J., Le Baccon, P., Wutz, A. and Heard, E. (2006). A novel role for Xist RNA in the formation of a repressive nuclear compartment into which genes are recruited when silenced. *Genes & Development* **20**, 2223–2237.

Chaumeil, J., Augui, S., Chow, J. C. and Heard, E. (2008). Combined Immunofluorescence , RNA Fluorescent In Situ Hybridization , and DNA Fluorescent In Situ Hybridization to Study Chromatin Changes , Transcriptional Activity , Nuclear Organization , and X-Chromosome Inactivation. In *The Nucleus: Volume I: Nuclei and Subnuclear Components*, pp. 297–308.

Chazotte, B. (2011). Labeling nuclear DNA using DAPI. *Cold Spring Harbor protocols* **2011**, pdb.prot5556.

Chow, J. C., Ciaudo, C., Fazzari, M. J., Mise, N., Servant, N., Glass, J. L., Attreed, M., Avner, P., Wutz, A., Barillot, E., et al. (2010). LINE-1 activity in facultative heterochromatin formation during X chromosome inactivation. *Cell* **141**, 956–69.

Ciferri, C., Lander, G. C., Maiolica, A., Herzog, F., Aebersold, R. and Nogales, E. (2012). Molecular architecture of human polycomb repressive complex 2. *eLife* **1**, e00005–e00005.

Clemson, C., McNeil, J., Willard, H. F. and Lawrence, J. B. (1996). XIST RNA paints the inactive X chromosome at interphase: evidence for a novel RNA involved in nuclear/chromosome structure. *The Journal of cell biology* **132**, 259–275.

Clemson, C. M., Hall, L. L., Byron, M., McNeil, J. and Lawrence, J. B. (2006). The X chromosome is organized into a gene-rich outer rim and an internal core containing silenced nongenic sequences. *Proceedings of the National Academy of Sciences of the United States of America* **103**, 7688–7693.

Cremer, T. and Cremer, M. (2010). Chromosome territories. *Cold Spring Harbor perspectives in biology* **2**, a003889.

Cremer, T., Cremer, M., Dietzel, S., Müller, S., Solovei, I. and Fakan, S. (2006). Chromosome territories--a functional nuclear landscape. *Current opinion in cell biology* **18**, 307–16.

Cremer, M., Grasser, F., Lanctôt, C., Müller, S., Neusser, M., Zinner, R., Solovei, I. and Cremer, T. (2008). Multicolor 3D fluorescence in situ hybridization for imaging interphase chromosomes. *Methods in molecular biology* **463**, 205–39.

Crews, D. (2003). Sex determination: where environment and genetics meet. *Evolution & development* **55**, 50–55.

Csankovszki, G., Nagy, a and Jaenisch, R. (2001). Synergism of Xist RNA, DNA methylation, and histone hypoacetylation in maintaining X chromosome inactivation. *The Journal of cell biology* **153**, 773–84.

Dan, D., Lei, M., Yao, B., Wang, W., Winterhalder, M., Zumbusch, A., Qi, Y., Xia, L., Yan, S., Yang, Y., et al. (2013). DMD-based LED-illumination super-resolution and optical sectioning microscopy. *Scientific reports* **3**, 1116.

De Napoles, M., Mermoud, J. E., Wakao, R., Tang, Y. A., Endoh, M., Appanah, R., Nesterova, T. B., Silva, J., Otte, A. P., Vidal, M., et al. (2004). Polycomb group proteins Ring1A/B link ubiquitylation of histone H2A to heritable gene silencing and X inactivation. *Developmental cell* **7**, 663–76.

Dekker, J., Marti-Renom, M. A. and Mirny, L. A. (2013). Exploring the three-dimensional organization of genomes: interpreting chromatin interaction data. *Nature reviews. Genetics* **14**, 390–403.

Dempsey, G. T., Vaughan, J. C., Chen, K. H., Bates, M. and Zhuang, X. (2011). Evaluation of fluorophores for optimal performance in localization-based super-resolution imaging. *Nature methods* **8**, 1027–36.

Deng, X., Hiatt, J. B., Nguyen, D. K., Ercan, S., Sturgill, D., Hillier, L. W., Schlesinger, F., Davis, C. A., Reinke, V. J., Gingeras, T. R., et al. (2011). Evidence for compensatory upregulation of

expressed X-linked genes in mammals, Caenorhabditis elegans and Drosophila melanogaster. *Nature genetics* **43**, 1179–85.

Deniaud, E. and Bickmore, W. A. (2009). Transcription and the nuclear periphery: edge of darkness? *Current opinion in genetics & development* **19**, 187–91.

Dickie, M. (1954). The tortoiseshell house mouse. *Journal of Heredity* **45**, 158–159.

Dietzel, S., Jauch, A., Kienle, D., Qu, G., Holtgreve-Grez, H., Eils, R., Münkel, C., Bittner, M., Meltzer, P. S., Trent, J. M., et al. (1998). Separate and variably shaped chromosome arm domains are disclosed by chromosome arm painting in human cell nuclei. *Chromosome Research* **6**, 25–33.

Dixon, J. R., Selvaraj, S., Yue, F., Kim, A., Li, Y., Shen, Y., Hu, M., Liu, J. S. and Ren, B. (2012). Topological domains in mammalian genomes identified by analysis of chromatin interactions. *Nature* **485**, 376–80.

Dobbie, I. M., King, E., Parton, R. M., Carlton, P. M., Sedat, J. W., Swedlow, J. R. and Davis, I. (2011). OMX: a new platform for multimodal, multichannel wide-field imaging. *Cold Spring Harbor protocols* **2011**, 899–909.

Dong, Y. and Shannon, C. (2000). Heterogeneous immunosensing using antigen and antibody monolayers on gold surfaces with electrochemical and scanning probe detection. *Analytical chemistry* **72**, 2371–6.

Donohoe, M. E., Silva, S. S., Pinter, S. F., Xu, N. and Lee, J. T. (2009). The pluripotency factor Oct4 interacts with Ctcf and also controls X-chromosome pairing and counting. *Nature* **460**, 128–32.

Duszczyk, M. M., Wutz, A., Rybin, V. and Sattler, M. (2011). The Xist RNA A-repeat comprises a novel AUCG tetraloop fold and a platform for multimerization. *RNA* **17**, 1973–82.

Duthie, S. M., Nesterova, T. B., Formstone, E. J., Keohane, a M., Turner, B. M., Zakian, S. M. and Brockdorff, N. (1999). Xist RNA exhibits a banded localization on the inactive X chromosome and is excluded from autosomal material in cis. *Human molecular genetics* **8**, 195–204.

Egecioglu, D. and Brickner, J. H. (2011). Gene positioning and expression. *Current opinion in cell biology* **23**, 338–45.

Engreitz, J. M., Pandya-Jones, A., McDonel, P., Shishkin, A., Sirokman, K., Surka, C., Kadri, S., Xing, J., Goren, A., Lander, E. S., et al. (2013). The Xist lncRNA Exploits Three-Dimensional Genome Architecture to Spread Across the X Chromosome. *Science* 1–13.

Escamilla-Del-Arenal, M., Da Rocha, S. T. and Heard, E. (2011). Evolutionary diversity and developmental regulation of X-chromosome inactivation. *Human genetics* **130**, 307–27.

Fackelmayer, F., Dahm, K., Renz, A., Ramsperger, U. and Richter, A. (1994). Nucleic-acid-binding properties of hnRNP-U/SAF-A, a nuclear-matrix protein which binds DNA and RNA in vivo and in vitro. *European Journal of Biochemistry* **757**, 749–757.

Fakan, S. and Hancock, R. (1974). Localization of newly-synthesized DNA in a mammalian cell as visualized by high resolution autoradiography. *Experimental cell research* **83**, 95–102.

Fang, J., Chen, T., Chadwick, B., Li, E. and Zhang, Y. (2004). Ring1b-mediated H2A ubiquitination associates with inactive X chromosomes and is involved in initiation of X inactivation. *The Journal of biological chemistry* **279**, 52812–5.

Fiedler, S. (2011). Untersuchung zur Dynamik der DNA Replikation mit Hilfe von hochauflösender Lichtmikroskopie (3D-SIM).

Filippova, G. N., Cheng, M. K., Moore, J. M., Truong, J.-P., Hu, Y. J., Tsuchiya, K. D. and Disteche, C. M. (2005). Boundaries between Chromosomal Domains of X Inactivation and Escape Bind CTCF and Lack CpG Methylation during Early Development. *Developmental Cell* **8**, 31–42.

Finlan, L. E., Sproul, D., Thomson, I., Boyle, S., Kerr, E., Perry, P., Ylstra, B., Chubb, J. R. and Bickmore, W. A. (2008). Recruitment to the nuclear periphery can alter expression of genes in human cells. *PLoS genetics* **4**, e1000039.

Fiolka, R., Shao, L., Rego, E. H., Davidson, M. W. and Gustafsson, M. G. L. (2012). Time-lapse two-color 3D imaging of live cells with doubled resolution using structured illumination. *Proceedings of the National Academy of Sciences of the United States of America* **109**, 5311–5.

Foster, H. a and Bridger, J. M. (2005). The genome and the nucleus: a marriage made by evolution. Genome organisation and nuclear architecture. *Chromosoma* **114**, 212–29.

Fussner, E., Ching, R. W. and Bazett-Jones, D. P. (2011). Living without 30nm chromatin fibers. *Trends in biochemical sciences* **36**, 1–6.

Gaspar-Maia, A., Qadeer, Z. A., Hasson, D., Ratnakumar, K., Leu, N. A., Leroy, G., Liu, S., Costanzi, C., Valle-Garcia, D., Schaniel, C., et al. (2013). MacroH2A histone variants act as a barrier upon reprogramming towards pluripotency. *Nature communications* **4**, 1565.

Gilchrist, S., Gilbert, N., Perry, P. and Bickmore, W. A. (2004). Nuclear organization of centromeric domains is not perturbed by inhibition of histone deacetylases. *Chromosome Research* **12**, 505–16.

Grant, J., Mahadevaiah, S. K., Khil, P., Sangrithi, M. N., Royo, H., Duckworth, J., McCarrey, J. R., Vandeberg, J. L., Renfree, M. B., Taylor, W., et al. (2012). Rsx, a metatherian RNA with Xist-like properties. *Nature* **487**, 254–258.

Graves, J. (2006). Sex chromosome specialization and degeneration in mammals. *Cell* **124**, 901–914.

Greaves, I. K., Rangasamy, D., Devoy, M., Marshall Graves, J. A. and Tremethick, D. J. (2006). The X and Y chromosomes assemble into H2A.Z-containing facultative heterochromatin following meiosis. *Molecular and cellular biology* **26**, 5394–405.

Gribnau, J. and Grootegoed, J. A. (2012). Origin and evolution of X chromosome inactivation. *Current opinion in cell biology* **24**, 397–404.

Gruetzner, F., Ashley, T., Rowell, D. M. and Marshall Graves, J. A. (2006). How did the platypus get its sex chromosome chain? A comparison of meiotic multiples and sex chromosomes in plants and animals. *Chromosoma* **115**, 75–88.

Guelen, L., Pagie, L., Brasset, E., Meuleman, W., Faza, M. B., Talhout, W., Eussen, B. H., De Klein, A., Wessels, L., De Laat, W., et al. (2008). Domain organization of human chromosomes revealed by mapping of nuclear lamina interactions. *Nature* **453**, 948–51.

Gunkel, M., Erdel, F., Rippe, K., Lemmer, P., Kaufmann, R., Hörmann, C., Amberger, R. and Cremer, C. (2009). Dual color localization microscopy of cellular nanostructures. *Biotechnology journal* **4**, 927–38.

Gustafsson, M. G. L. (2000). Surpassing the lateral resolution limit by a factor of two using structured illumination microscopy. *Journal of microscopy* **198**, 82–7.

Gustafsson, M. G. L. (2005). Nonlinear structured-illumination microscopy: wide-field fluorescence imaging with theoretically unlimited resolution. *Proceedings of the National Academy of Sciences of the United States of America* **102**, 13081–6.

Gustafsson, M. G., Shao, L., Carlton, P. M., Wang, C. R., Golubovskaya, I. N., Cande, W. Z., Agard, D. A. and Sedat, J. W. (2008). Three-dimensional resolution doubling in wide-field fluorescence microscopy by structured illumination. *Biophysical journal* **94**, 4957–4970.

Hall, L. and Lawrence, J. (2010). XIST RNA and architecture of the inactive X chromosome: implications for the repeat genome. *Cold Spring Harbor symposia on quantitative biology* **27**, 345–356.

Harper, P. S. (2011). Mary Lyon and the hypothesis of random X chromosome inactivation. *Human genetics* **130**, 169–74.

Hasegawa, Y. and Nakagawa, S. (2011). Revisiting the function of nuclear scaffold/matrix binding proteins in X chromosome inactivation. *RNA biology* **8**, 735–9.

Hasegawa, Y., Brockdorff, N., Kawano, S., Tsutui, K. K. and Nakagawa, S. (2010). The matrix protein hnRNP U is required for chromosomal localization of Xist RNA. *Developmental cell* **19**, 469–76.

Heard, E., Rougeulle, C., Arnaud, D., Avner, P., Allis, C. D. and Spector, D. L. (2001). Methylation of histone H3 at Lys-9 is an early mark on the X chromosome during X inactivation. *Cell* **107**, 727–738.

Heintzmann, R. and Cremer, C. G. (1999). Laterally modulated excitation microscopy: improvement of resolution by using a diffraction grating. In *BiOS Europe'98* (ed. Bigio, I. J., Schneckenburger, H., Slavik, J., Svanberg, K., and Viallet, P. M.), pp. 185–196.

Helbig, R. and Fackelmayer, F. O. (2003). Scaffold attachment factor A (SAF-A) is concentrated in inactive X chromosome territories through its RGG domain. *Chromosoma* **112**, 173–82.

Hell, S. W. (2007). Far-field optical nanoscopy. *Science* **316**, 1153–8.

Hell, S. W. and Wichmann, J. (1994). Breaking the diffraction resolution limit by stimulated emission: stimulated-emission-depletion fluorescence microscopy. *Optics letters* **19**, 780–2.

Hellman, A. and Chess, A. (2007). Gene body-specific methylation on the active X chromosome. *Science* **315**, 1141–3.

Henriques, R., Griffiths, C., Hesper Rego, E. and Mhlanga, M. M. (2011). PALM and STORM: unlocking live-cell super-resolution. *Biopolymers* **95**, 322–31.

Hepperger, C., Otten, S., Von Hase, J. and Dietzel, S. (2007). Preservation of large-scale chromatin structure in FISH experiments. *Chromosoma* **116**, 117–33.

Herbert, S., Soares, H., Zimmer, C. and Henriques, R. (2012). Single-molecule localization super-resolution microscopy: deeper and faster. *Microscopy and microanalysis* **18**, 1419–29.

Hess, S. T., Girirajan, T. P. K. and Mason, M. D. (2006). Ultra-high resolution imaging by fluorescence photoactivation localization microscopy. *Biophysical journal* **91**, 4258–72.

Hewitt, S. L., High, F. a, Reiner, S. L., Fisher, A. G. and Merkenschlager, M. (2004). Nuclear repositioning marks the selective exclusion of lineage-inappropriate transcription factor loci during T helper cell differentiation. *European journal of immunology* **34**, 3604–13.

Hihara, S., Pack, C.-G., Kaizu, K., Tani, T., Hanafusa, T., Nozaki, T., Takemoto, S., Yoshimi, T., Yokota, H., Imamoto, N., et al. (2012). Local nucleosome dynamics facilitate chromatin accessibility in living mammalian cells. *Cell reports* **2**, 1645–56.

Hirvonen, L. M., Wicker, K., Mandula, O. and Heintzmann, R. (2009). Structured illumination microscopy of a living cell. *European biophysics journal : EBJ* **38**, 807–12.

Huang, B., Jones, S., Brandenburg, B. and Zhuang, X. (2008a). Whole-cell 3D STORM reveals interactions between cellular structures with nanometer-scale resolution. *Nature methods* **5**, 1047–1052.

Huang, B., Wang, W., Bates, M. and Zhuang, X. (2008b). Three-dimensional super-resolution imaging by stochastic optical reconstruction microscopy. *Science* **319**, 810–3.

Huang, B., Bates, M. and Zhuang, X. (2009). Super-resolution fluorescence microscopy. *Annual review of biochemistry* **78**, 993–1016.

Huang, B., Babcock, H. and Zhuang, X. (2010). Breaking the diffraction barrier: super-resolution imaging of cells. *Cell* **143**, 1047–58.

Huynh, K. and Lee, J. (2003). Inheritance of a pre-inactivated paternal X chromosome in early mouse embryos. *Nature* **426**, 857–862.

Ishii, K., Arib, G., Lin, C., Van Houwe, G. and Laemmli, U. K. (2002). Chromatin boundaries in budding yeast: the nuclear pore connection. *Cell* **109**, 551–62.

Jeon, Y. and Lee, J. T. (2011). YY1 tethers Xist RNA to the inactive X nucleation center. *Cell* **146**, 119–33.

Jeon, Y., Sarma, K. and Lee, J. T. (2012). New and Xisting regulatory mechanisms of X chromosome inactivation. *Current opinion in genetics & development* **22**, 62–71.

Jeppesen, P. and Turner, B. M. (1993). The inactive X chromosome in female mammals is distinguished by a lack of histone H4 acetylation, a cytogenetic marker for gene expression. *Cell* **74**, 281–9.

Jones, S. a, Shim, S.-H., He, J. and Zhuang, X. (2011). Fast, three-dimensional super-resolution imaging of live cells. *Nature methods* **8**, 499–508.

Jonkers, I. and Monkhorst, K. (2008). Xist RNA is confined to the nuclear territory of the silenced X chromosome throughout the cell cycle. *Molecular and cellular biology* **28**, 5583–5594.

Jonkers, I., Barakat, T. S., Achame, E. M., Monkhorst, K., Kenter, A., Rentmeester, E., Grosveld, F., Grootegoed, J. A. and Gribnau, J. (2009). RNF12 is an X-Encoded dose-dependent activator of X chromosome inactivation. *Cell* **139**, 999–1011.

Kalhor, R., Tjong, H., Jayathilaka, N., Alber, F. and Chen, L. (2012). Genome architectures revealed by tethered chromosome conformation capture and population-based modeling. *Nature biotechnology* **30**, 90–8.

Kalverda, B., Pickersgill, H., Shloma, V. V and Fornerod, M. (2010). Nucleoporins directly stimulate expression of developmental and cell-cycle genes inside the nucleoplasm. *Cell* **140**, 360–71.

Kaufmann, R., Piontek, J., Grüll, F., Kirchgessner, M., Rossa, J., Wolburg, H., Blasig, I. E. and Cremer, C. (2012). Visualization and quantitative analysis of reconstituted tight junctions using localization microscopy. *PloS one* **7**, e31128.

Kempf, C., Staudt, T., Bingen, P., Horstmann, H., Engelhardt, J., Hell, S. W. and Kuner, T. (2013). Tissue Multicolor STED Nanoscopy of Presynaptic Proteins in the Calyx of Held. *PloS one* **8**, e62893.

Kimura, H. and Cook, P. R. (2001). Kinetics of core histones in living human cells: little exchange of H3 and H4 and some rapid exchange of H2B. *The Journal of cell biology* **153**, 1341–53.

Kind, J. and Van Steensel, B. (2010). Genome-nuclear lamina interactions and gene regulation. *Current opinion in cell biology* **22**, 320–5.

Kireev, I., Lakonishok, M., Liu, W., Joshi, V., Powell, R. and Belmont, A. S. (2008). In vivo immunogold labeling confirms large-scale chromatin folding motifs. *Nature methods* **5**, 311–313.

Klar, T. A. and Hell, S. W. (1999). Subdiffraction resolution in far-field fluorescence microscopy. *Optics letters* **24**, 954–6.

Kner, P., Chhun, B. B., Griffis, E. R., Winoto, L., Gustafsson, M. G. L. and America, N. (2009). Super-resolution video microscopy of live cells by structured illumination. *Nature methods* **6**, 339–42.

Koh, K. P. and Rao, A. (2013). DNA methylation and methylcytosine oxidation in cell fate decisions. *Current opinion in cell biology* **25**, 152–61.

Kohlmaier, A., Savarese, F., Lachner, M., Martens, J., Jenuwein, T. and Wutz, A. (2004). A chromosomal memory triggered by Xist regulates histone methylation in X inactivation. *PLoS biology* **2**, E171.

Kosak, S. T., Skok, J. A., Medina, K. L., Riblet, R., Le Beau, M. M., Fisher, A. G. and Singh, H. (2002). Subnuclear compartmentalization of immunoglobulin loci during lymphocyte development. *Science* **296**, 158–62.

Kouzarides, T. (2007). Chromatin modifications and their function. *Cell* **128**, 693–705.

Krijger, P. H. and De Laat, W. (2013). Identical cells with different 3D genomes; cause and consequences? *Current opinion in genetics & development* **23**, 1–6.

Krull, S., Dörries, J., Boysen, B., Reidenbach, S., Magnius, L., Norder, H., Thyberg, J. and Cordes, V. C. (2010). Protein Tpr is required for establishing nuclear pore-associated zones of heterochromatin exclusion. *The EMBO journal* **29**, 1659–73.

Kumaran, R. I. and Spector, D. L. (2008). A genetic locus targeted to the nuclear periphery in living cells maintains its transcriptional competence. *The Journal of cell biology* **180**, 51–65.

Küpper, K., Kölbl, A., Biener, D., Dittrich, S., Von Hase, J., Thormeyer, T., Fiegler, H., Carter, N. P., Speicher, M. R., Cremer, T., et al. (2007). Radial chromatin positioning is shaped by local gene density, not by gene expression. *Chromosoma* **116**, 285–306.

Lanctôt, C., Cheutin, T., Cremer, M., Cavalli, G. and Cremer, T. (2007). Dynamic genome architecture in the nuclear space: regulation of gene expression in three dimensions. *Nature reviews. Genetics* **8**, 104–15.

Law, J. A. and Jacobsen, S. E. (2010). Establishing, maintaining and modifying DNA methylation patterns in plants and animals. *Nature reviews. Genetics* **11**, 204–20.

Lee, J. T. (2011). Gracefully ageing at 50, X-chromosome inactivation becomes a paradigm for RNA and chromatin control. *Nature reviews. Molecular cell biology* **12**, 815–26.

Lee, J. T. and Bartolomei, M. S. (2013). X-inactivation, imprinting, and long noncoding RNAs in health and disease. *Cell* **152**, 1308–23.

Lee, J. and Jaenisch, R. (1997). Long-range cis effects of ectopic X-inactivation centres on a mouse autosome. *Nature*.

Lee, J. T. and Lu, N. (1999). Targeted mutagenesis of Tsix leads to nonrandom X inactivation. *Cell* **99**, 47–57.

Lee, J. T., Davidow, L. S. and Warshawsky, D. (1999). Tsix, a gene antisense to Xist at the X-inactivation centre. *Nature genetics* **21**, 400–4.

Li, N. and Carrel, L. (2008). Escape from X chromosome inactivation is an intrinsic property of the Jarid1c locus. *Proceedings of the National Academy of Sciences of the United States of America* **105**, 17055–60.

Lidke, D. S. and Lidke, K. A. (2012). Advances in high-resolution imaging--techniques for three-dimensional imaging of cellular structures. *Journal of cell science* **125**, 2571–80.

Lieberman-Aiden, E., Van Berkum, N. L., Williams, L., Imakaev, M., Ragoczy, T., Telling, A., Amit, I., Lajoie, B. R., Sabo, P. J., Dorschner, M. O., et al. (2009). Comprehensive mapping of long-range interactions reveals folding principles of the human genome. *Science* **326**, 289–93.

Luger, K., Mäder, A. W., Richmond, R. K., Sargent, D. F. and Richmond, T. J. (1997). Crystal structure of the nucleosome core particle at 2.8 Å resolution. *Nature* **387**, 251–260.

Luo, L., Gassman, K. L., Petell, L. M., Wilson, C. L., Bewersdorf, J. and Shopland, L. S. (2009). The nuclear periphery of embryonic stem cells is a transcriptionally permissive and repressive compartment. *Journal of cell science* **122**, 3729–37.

Lyon, M. (1960). A Further Mutation Of The Mottled Type: In the House Mouse. *Journal of Heredity* **51**, 116–121.

Lyon, M. (1961). Gene action in the X-chromosome of the mouse (Mus musculus L.). *Nature* **190**, 372–3.

Lyon, M. (1998). X-chromosome inactivation: a repeat hypothesis. *Cytogenetic and Genome Research* **137**, 133–137.

Lyon, M. (2003). The Lyon and the LINE hypothesis. *Seminars in cell & developmental biology* **14**, 313–318.

Maenner, S., Blaud, M., Fouillen, L., Savoye, A., Marchand, V., Dubois, A., Sanglier-Cianférani, S., Van Dorsselaer, A., Clerc, P., Avner, P., et al. (2010). 2-D structure of the A region of Xist RNA and its implication for PRC2 association. *PLoS biology* **8**, e1000276.

Maeshima, K., Hihara, S. and Eltsov, M. (2010). Chromatin structure: does the 30-nm fibre exist in vivo? *Current opinion in cell biology* **22**, 291–7.

Mak, W., Baxter, J., Silva, J., Newall, A. E., Otte, A. P. and Brockdorff, N. (2002). Mitotically stable association of polycomb group proteins eed and enx1 with the inactive x chromosome in trophoblast stem cells. *Current biology* **12**, 1016–20.

Mak, W., Nesterova, T. B., De Napoles, M., Appanah, R., Yamanaka, S., Otte, A. P. and Brockdorff, N. (2004). Reactivation of the paternal X chromosome in early mouse embryos. *Science* **303**, 666–9.

Manley, S., Gunzenhäuser, J. and Olivier, N. (2011). A starter kit for point-localization super-resolution imaging. *Current opinion in chemical biology* **15**, 813–21.

Markaki, Y., Gunkel, M., Schermelleh, L., Beichmanis, S., Neumann, J., Heidemann, M., Leonhardt, H., Eick, D., Cremer, C. and Cremer, T. (2010). Functional nuclear organization of transcription and DNA replication: a topographical marriage between chromatin domains and the interchromatin compartment. *Cold Spring Harbor symposia on quantitative biology* **75**, 475–92.

Markaki, Y., Smeets, D., Fiedler, S., Schmid, V. J., Schermelleh, L., Cremer, T. and Cremer, M. (2012). The potential of 3D-FISH and super-resolution structured illumination microscopy for studies of 3D nuclear architecture. *BioEssays* **34**, 412–426.

Markaki, Y., Smeets, D., Cremer, M. and Schermelleh, L. (2013). Fluorescence in situ hybridization applications for super-resolution 3D structured illumination microscopy. In *Methods in molecular biology*, pp. 43–64.

Marks, H., Chow, J. C., Denissov, S., Françoijs, K.-J., Brockdorff, N., Heard, E. and Stunnenberg, H. G. (2009). High-resolution analysis of epigenetic changes associated with X inactivation. *Genome research* **19**, 1361–73.

Marti-Renom, M. A. and Mirny, L. A. (2011). Bridging the resolution gap in structural modeling of 3D genome organization. *PLoS computational biology* **7**, e1002125.

Masui, O., Bonnet, I., Le Baccon, P., Brito, I., Pollex, T., Murphy, N., Hupé, P., Barillot, E., Belmont, A. S. and Heard, E. (2011). Live-cell chromosome dynamics and outcome of X chromosome pairing events during ES cell differentiation. *Cell* **145**, 447–58.

Mayer, R., Brero, A., Von Hase, J., Schroeder, T., Cremer, T. and Dietzel, S. (2005). Common themes and cell type specific variations of higher order chromatin arrangements in the mouse. *BMC cell biology* **6**, 44.

Meister, P., Towbin, B. D., Pike, B. L., Ponti, A. and Gasser, S. M. (2010). The spatial dynamics of tissue-specific promoters during C. elegans development. *Genes & development* **24**, 766–82.

Meyer, B., McDonel, P., Csankovszki, G. and Ralston, E. (2004). Sex and X-Chromosome-wide Repression in Caenorhabditis elegans. *Cold Spring Harbor symposia on quantitative biology* **69**, 71–80.

Migeon, B. R. (2002). X chromosome inactivation: theme and variations. *Cytogenetic and Genome Research* **99**, 8–16.

Miller, D., Summers, J. and Silber, S. (2004). Environmental versus genetic sex determination: a possible factor in dinosaur extinction? *Fertility and Sterility* **81**, 954–964.

Mirny, L. A. (2011). The fractal globule as a model of chromatin architecture in the cell. *Chromosome Research* **19**, 37–51.

Misteli, T. (2013). The cell biology of genomes: bringing the double helix to life. *Cell* **152**, 1209–12.

Moldovan, G.-L., Pfander, B. and Jentsch, S. (2007). PCNA, the maestro of the replication fork. *Cell* **129**, 665–79.

Moneron, G., Medda, R., Hein, B., Giske, A., Westphal, V. and Hell, S. W. (2010). Fast STED microscopy with continuous wave fiber lasers. *Optics express* **18**, 1302–9.

Monkhorst, K., Jonkers, I., Rentmeester, E., Grosveld, F. and Gribnau, J. (2008). X inactivation counting and choice is a stochastic process: evidence for involvement of an X-linked activator. *Cell* **132**, 410–21.

Monkhorst, K., Hoon, B. De and Jonkers, I. (2009). The probability to initiate X chromosome inactivation is determined by the X to autosomal ratio and X chromosome specific allelic properties. *PLoS One* **4**, 14.

Moreira de Mello, J. C., De Araújo, E. S. S., Stabellini, R., Fraga, A. M., De Souza, J. E. S., Sumita, D. R., Camargo, A. a and Pereira, L. V (2010). Random X inactivation and extensive mosaicism in human placenta revealed by analysis of allele-specific gene expression along the X chromosome. *PloS one* **5**, e10947.

Muck, J. S., Kandasamy, K., Englmann, A., Günther, M. and Zink, D. (2012). Perinuclear positioning of the inactive human cystic fibrosis gene depends on CTCF, A-type lamins and an active histone deacetylase. *Journal of cellular biochemistry* **113**, 2607–21.

Müller, P., Schmitt, E., Jacob, A., Hoheisel, J., Kaufmann, R., Cremer, C. and Hausmann, M. (2010). COMBO-FISH Enables High Precision Localization Microscopy as a Prerequisite for Nanostructure Analysis of Genome Loci. *International journal of molecular sciences* **11**, 4094–105.

Navarro, P., Chambers, I., Karwacki-Neisius, V., Chureau, C., Morey, C., Rougeulle, C. and Avner, P. (2008). Molecular coupling of Xist regulation and pluripotency. *Science* **321**, 1693–5.

Navarro, P., Oldfield, A., Legoupi, J., Festuccia, N., Dubois, A., Attia, M., Schoorlemmer, J., Rougeulle, C., Chambers, I. and Avner, P. (2010). Molecular coupling of Tsix regulation and pluripotency. *Nature* **468**, 457–60.

Németh, A., Conesa, A., Santoyo-Lopez, J., Medina, I., Montaner, D., Péterfia, B., Solovei, I., Cremer, T., Dopazo, J. and Längst, G. (2010). Initial genomics of the human nucleolus. *PLoS genetics* **6**, e1000889.

Neusser, M., Schubel, V., Koch, A., Cremer, T. and Müller, S. (2007). Evolutionarily conserved, cell type and species-specific higher order chromatin arrangements in interphase nuclei of primates. *Chromosoma* **116**, 307–20.

Ng, K., Daigle, N., Bancaud, A., Ohhata, T., Humphreys, P., Walker, R., Ellenberg, J. and Wutz, A. (2011). A system for imaging the regulatory noncoding Xist RNA in living mouse embryonic stem cells. *Molecular biology of the cell* **22**, 2634–45.

Niedojadlo, J., Perret-Vivancos, C., Kalland, K.-H., Cmarko, D., Cremer, T., Van Driel, R. and Fakan, S. (2011). Transcribed DNA is preferentially located in the perichromatin region of mammalian cell nuclei. *Experimental cell research* **317**, 433–44.

Nora, E. P., Lajoie, B. R., Schulz, E. G., Giorgetti, L., Okamoto, I., Servant, N., Piolot, T., Van Berkum, N. L., Meisig, J., Sedat, J., et al. (2012). Spatial partitioning of the regulatory landscape of the X-inactivation centre. *Nature* **485**, 381–5.

Nozawa, R.-S., Nagao, K., Igami, K.-T., Shibata, S., Shirai, N., Nozaki, N., Sado, T., Kimura, H. and Obuse, C. (2013). Human inactive X chromosome is compacted through a PRC2-independent SMCHD1-HBiX1 pathway. *Nature structural & molecular biology* **20**, 566–73.

Ogawa, Y., Sun, B. K. and Lee, J. T. (2008). Intersection of the RNA interference and X-inactivation pathways. *Science* **320**, 1336–41.

Ohno, S., Kaplan, W. D. and Kinosita, R. (1959). Formation of the sex chromatin by a single x-chromosome in liver cells of rattus norvegicus. *Experimental Cell Research* **18**, 415–418.

Okamoto, I., Otte, A. P., Allis, C. D., Reinberg, D. and Heard, E. (2004). Epigenetic dynamics of imprinted X inactivation during early mouse development. *Science* **303**, 644–9.

Okamoto, I., Patrat, C., Thépot, D., Peynot, N., Fauque, P., Daniel, N., Diabangouaya, P., Wolf, J.-P., Renard, J.-P., Duranthon, V., et al. (2011). Eutherian mammals use diverse strategies to initiate X-chromosome inactivation during development. *Nature* **472**, 370–4.

Olins, a L. and Olins, D. E. (1974). Spheroid chromatin units (v bodies). *Science* **183**, 330–2.

Ooi, S. K. T., O'Donnell, A. H. and Bestor, T. H. (2009). Mammalian cytosine methylation at a glance. *Journal of cell science* **122**, 2787–91.

Pandey, R. R., Mondal, T., Mohammad, F., Enroth, S., Redrup, L., Komorowski, J., Nagano, T., Mancini-Dinardo, D. and Kanduri, C. (2008). Kcnq1ot1 antisense noncoding RNA mediates lineage-specific transcriptional silencing through chromatin-level regulation. *Molecular cell* **32**, 232–46.

Pasque, V., Gillich, A., Garrett, N. and Gurdon, J. B. (2011). Histone variant macroH2A confers resistance to nuclear reprogramming. *The EMBO journal* **30**, 2373–87.

Payer, B. and Lee, J. (2008). X chromosome dosage compensation: how mammals keep the balance. *Annual review of genetics* **42**, 733–772.

Pennisi, E. (2013). Long Noncoding RNAs May Alter Chromosome's 3D Structure. *Science* **340**, 340.

Pessia, E., Makino, T., Bailly-Bechet, M., McLysaght, A. and Marais, G. A. B. (2012). Mammalian X chromosome inactivation evolved as a dosage-compensation mechanism for dosage-sensitive genes on the X chromosome. *Proceedings of the National Academy of Sciences of the United States of America* **109**, 5346–51.

Pinter, S. F., Sadreyev, R. I., Yildirim, E., Jeon, Y., Ohsumi, T. K., Borowsky, M. and Lee, J. T. (2012). Spreading of X chromosome inactivation via a hierarchy of defined Polycomb stations. *Genome research* **22**, 1864–76.

Plath, K., Fang, J., Mlynarczyk-Evans, S. K., Cao, R., Worringer, K. a, Wang, H., De la Cruz, C. C., Otte, A. P., Panning, B. and Zhang, Y. (2003). Role of histone H3 lysine 27 methylation in X inactivation. *Science* **300**, 131–5.

Polani, P., Hunter, W. and Lennox, B. (1954). Chromosomal sex in Turner's syndrome with coarctation of the aorta. *The Lancet* **264**, 256–257.

Pontier, D. B. and Gribnau, J. (2011). Xist regulation and function explored. *Human genetics* **130**, 223–36.

Pullirsch, D., Härtel, R., Kishimoto, H., Leeb, M., Steiner, G. and Wutz, A. (2010). The Trithorax group protein Ash2l and Saf-A are recruited to the inactive X chromosome at the onset of stable X inactivation. *Development* **137**, 935–43.

Ratnakumar, K., Duarte, L. F., LeRoy, G., Hasson, D., Smeets, D., Vardabasso, C., Bönisch, C., Zeng, T., Xiang, B., Zhang, D. Y., et al. (2012). ATRX-mediated chromatin association of histone variant macroH2A1 regulates α-globin expression. *Genes & development* **26**, 433–8.

Reddy, K. L., Zullo, J. M., Bertolino, E. and Singh, H. (2008). Transcriptional repression mediated by repositioning of genes to the nuclear lamina. *Nature* **452**, 243–7.

Rego, A., Sinclair, P. B., Tao, W., Kireev, I. and Belmont, A. S. (2008). The facultative heterochromatin of the inactive X chromosome has a distinctive condensed ultrastructure. *Journal of cell science* **121**, 1119–27.

Rego, E. H., Shao, L., Macklin, J. J., Winoto, L., Johansson, G. A., Kamps-Hughes, N., Davidson, M. W. and Gustafsson, M. G. L. (2012). Nonlinear structured-illumination microscopy with a

photoswitchable protein reveals cellular structures at 50-nm resolution. *Proceedings of the National Academy of Sciences of the United States of America* **109**, E135–43.

Richmond, T. J. and Davey, C. A. (2003). The structure of DNA in the nucleosome core. *Nature* **423**, 145–50.

Rinn, J. L., Kertesz, M., Wang, J. K., Squazzo, S. L., Xu, X., Brugmann, S. a, Goodnough, L. H., Helms, J. a, Farnham, P. J., Segal, E., et al. (2007). Functional demarcation of active and silent chromatin domains in human HOX loci by noncoding RNAs. *Cell* **129**, 1311–23.

Rittweger, E., Han, K. Y., Irvine, S. E., Eggeling, C. and Hell, S. W. (2009). STED microscopy reveals crystal colour centres with nanometric resolution. *Nature Photonics* **3**, 1–4.

Romer, T., Leonhardt, H. and Rothbauer, U. (2011). Engineering antibodies and proteins for molecular in vivo imaging. *Current opinion in biotechnology* **22**, 882–7.

Rouquette, J., Cremer, C., Cremer, T. and Fakan, S. (2010). Functional nuclear architecture studied by microscopy: present and future. *International review of cell and molecular biology* **282**, 1–90.

Rust, M., Bates, M. and Zhuang, X. (2006). Sub-diffraction-limit imaging by stochastic optical reconstruction microscopy (STORM). *Nature methods* **3**, 793–795.

Sado, T., Hoki, Y. and Sasaki, H. (2006). Tsix defective in splicing is competent to establish Xist silencing. *Development* **133**, 4925–31.

Sadoni, N., Cardoso, M. C., Stelzer, E. H. K., Leonhardt, H. and Zink, D. (2004). Stable chromosomal units determine the spatial and temporal organization of DNA replication. *Journal of cell science* **117**, 5353–65.

Salic, A. and Mitchison, T. J. (2008). A chemical method for fast and sensitive detection of DNA synthesis in vivo. *Proceedings of the National Academy of Sciences of the United States of America* **105**, 2415–20.

Sarma, K., Levasseur, P., Aristarkhov, A. and Lee, J. T. (2010). Locked nucleic acids (LNAs) reveal sequence requirements and kinetics of Xist RNA localization to the X chromosome. *Proceedings of the National Academy of Sciences of the United States of America* **107**, 22196–22201.

Schermelleh, L., Carlton, P. M., Haase, S., Shao, L., Winoto, L., Kner, P., Burke, B., Cardoso, M. C., Agard, D. a, Gustafsson, M. G. L., et al. (2008). Subdiffraction multicolor imaging of the nuclear periphery with 3D structured illumination microscopy. *Science* **320**, 1332–6.

Schermelleh, L., Heintzmann, R. and Leonhardt, H. (2010). A guide to super-resolution fluorescence microscopy. *The Journal of cell biology* **190**, 165–75.

Schmidt, R., Wurm, C. A., Jakobs, S., Engelhardt, J., Egner, A. and Hell, S. W. (2008). Spherical nanosized focal spot unravels the interior of cells. *Nature methods* **5**, 539–544.

Schmidt, R., Wurm, C. A., Punge, A., Egner, A., Jakobs, S. and Hell, S. W. (2009). Mitochondrial cristae revealed with focused light. *Nano letters* **9**, 2508–10.

Schoeftner, S., Sengupta, A. K., Kubicek, S., Mechtler, K., Spahn, L., Koseki, H., Jenuwein, T. and Wutz, A. (2006). Recruitment of PRC1 function at the initiation of X inactivation independent of PRC2 and silencing. *The EMBO journal* **25**, 3110–22.

Schulz, E. G. and Heard, E. (2013). Role and control of X chromosome dosage in mammalian development. *Current opinion in genetics & development* 1–7.

Sexton, T., Yaffe, E., Kenigsberg, E., Bantignies, F., Leblanc, B., Hoichman, M., Parrinello, H., Tanay, A. and Cavalli, G. (2012). Three-dimensional folding and functional organization principles of the Drosophila genome. *Cell* **148**, 458–72.

Shao, L., Kner, P., Rego, E. H. and Gustafsson, M. G. L. (2011). Super-resolution 3D microscopy of live whole cells using structured illumination. *Nature methods* **8**, 1044–6.

Shen, L. and Zhang, Y. (2013). 5-Hydroxymethylcytosine: generation, fate, and genomic distribution. *Current opinion in cell biology* **25**, 289–296.

Shogren-Knaak, M., Ishii, H., Sun, J.-M., Pazin, M. J., Davie, J. R. and Peterson, C. L. (2006). Histone H4-K16 acetylation controls chromatin structure and protein interactions. *Science* **311**, 844–7.

Silva, J., Mak, W., Zvetkova, I., Appanah, R., Nesterova, T. B., Webster, Z., Peters, A. H. F. M., Jenuwein, T., Otte, A. P. and Brockdorff, N. (2003). Establishment of histone h3 methylation on the inactive X chromosome requires transient recruitment of Eed-Enx1 polycomb group complexes. *Developmental cell* **4**, 481–95.

Silverton, E. (1977). Three-dimensional structure of an intact human immunoglobulin. *Proceedings of the National Academy of Sciences of the United States of America* **74**, 5140–5144.

Sinclair, A. H., Berta, P., Palmer, M. S., Hawkins, J. R., Griffiths, B. L., Smith, M. J., Foster, J. W., Frischauf, A.-M., Lovell-Badge, R. and Goodfellow, P. N. (1990). A gene from the human sex-determining region encodes a protein with homology to a conserved DNA-binding motif. *Nature* **346**, 240–244.

Smeets, D., Neumann, J. and Schermelleh, L. (2013a). Application of Three-Dimensional Structured Illumination Microscopy in Cell Biology – Pitfalls and Practical Considerations. In *Neuromethods*, *in press*.

Smeets, D., Markaki, Y., Tattermusch, A., Cerase, A., Popken, J., Sterr, M., Leonhardt, H., Schmid, V. J., Brockdorff, N., Schermelleh, L., et al. (2013b). Focal Xist RNA spreading in the X chromosome territory committed for inactivation is followed by a collapse of its active nuclear compartment. *PLoS biology, submitted*.

Solovei, I., Cavallo, A., Schermelleh, L., Jaunin, F., Scasselati, C., Cmarko, D., Cremer, C., Fakan, S. and Cremer, T. (2002). Spatial preservation of nuclear chromatin architecture during three-dimensional fluorescence in situ hybridization (3D-FISH). *Experimental cell research* **276**, 10–23.

Splinter, E., De Wit, E., Nora, E. P., Klous, P., Van de Werken, H. J. G., Zhu, Y., Kaaij, L. J. T., Van Ijcken, W. W., Gribnau, J., Heard, E., et al. (2011). The inactive X chromosome adopts a unique three-dimensional conformation that is dependent on Xist RNA. *Genes & development* **25**, 1–14.

Straub, T. and Becker, P. (2007). Dosage compensation: the beginning and end of generalization. *Nature Reviews Genetics* **8**, 47–57.

Strauss, M. P., Liew, A. T. F., Turnbull, L., Whitchurch, C. B., Monahan, L. G. and Harry, E. J. (2012). 3D-SIM super resolution microscopy reveals a bead-like arrangement for FtsZ and the division machinery: implications for triggering cytokinesis. *PLoS biology* **10**, e1001389.

Sun, B. K., Deaton, A. M. and Lee, J. T. (2006). A transient heterochromatic state in Xist preempts X inactivation choice without RNA stabilization. *Molecular cell* **21**, 617–28.

Szwagierczak, A., Bultmann, S., Schmidt, C. S., Spada, F. and Leonhardt, H. (2010). Sensitive enzymatic quantification of 5-hydroxymethylcytosine in genomic DNA. *Nucleic acids research* **38**, e181.

Takagi, N. and Sasaki, M. (1975). Preferential inactivation of the paternally derived X chromosome in the extraembryonic membranes of the mouse. *Nature* **256**,.

Tanasijevic, B. and Rasmussen, T. P. (2011). X chromosome inactivation and differentiation occur readily in ES cells doubly-deficient for macroH2A1 and macroH2A2. *PloS one* **6**, e21512.

Tang, Y. A., Huntley, D., Montana, G., Cerase, A., Nesterova, T. B. and Brockdorff, N. (2010). Efficiency of Xist-mediated silencing on autosomes is linked to chromosomal domain organisation. *Epigenetics & Chromatin* **10**,.

Tattermusch, A. and Brockdorff, N. (2011). A scaffold for X chromosome inactivation. *Human genetics* **130**, 247–53.

Telenius, H., Carter, N. P., Bebb, C. E., Nordenskjöld, M., Ponder, B. a and Tunnacliffe, A. (1992). Degenerate oligonucleotide-primed PCR: general amplification of target DNA by a single degenerate primer. *Genomics* **13**, 718–25.

Teller, K., Illner, D., Thamm, S., Casas-Delucchi, C. S., Versteeg, R., Indemans, M., Cremer, T. and Cremer, M. (2011). A top-down analysis of Xa- and Xi-territories reveals differences of higher order structure at ≥ 20 Mb genomic length scales. *Nucleus* **2**, 465–77.

Tian, D., Sun, S. and Lee, J. T. (2010). The long noncoding RNA, Jpx, is a molecular switch for X chromosome inactivation. *Cell* **143**, 390–403.

Tremethick, D. J. (2007). Higher-order structures of chromatin: the elusive 30 nm fiber. *Cell* **128**, 651–4.

Uphoff, S., Reyes-Lamothe, R., Garza de Leon, F., Sherratt, D. J. and Kapanidis, A. N. (2013). Single-molecule DNA repair in live bacteria. *Proceedings of the National Academy of Sciences of the United States of America* **110**, 8063–8.

Vallot, C., Huret, C., Lesecque, Y., Resch, A., Oudrhiri, N., Bennaceur-Griscelli, A., Duret, L. and Rougeulle, C. (2013). XACT, a long noncoding transcript coating the active X chromosome in human pluripotent cells. *Nature genetics* **45**, 239–41.

Vaquerizas, J. M., Suyama, R., Kind, J., Miura, K., Luscombe, N. M. and Akhtar, A. (2010). Nuclear pore proteins nup153 and megator define transcriptionally active regions in the Drosophila genome. *PLoS genetics* **6**, e1000846.

Veyrunes, F., Waters, P. D., Miethke, P., Rens, W., McMillan, D., Alsop, A. E., Grützner, F., Deakin, J. E., Whittington, C. M., Schatzkamer, K., et al. (2008). Bird-like sex chromosomes of platypus imply recent origin of mammal sex chromosomes. *Genome research* **18**, 965–73.

Wallis, M. C., Waters, P. D., Delbridge, M. L., Kirby, P. J., Pask, A. J., Grützner, F., Rens, W., Ferguson-Smith, M. A. and Graves, J. A. M. (2007). Sex determination in platypus and echidna: autosomal location of SOX3 confirms the absence of SRY from monotremes. *Chromosome Research* **15**, 949–59.

Wang, J., Mager, J., Chen, Y., Schneider, E., Cross, J. C., Nagy, a and Magnuson, T. (2001). Imprinted X inactivation maintained by a mouse Polycomb group gene. *Nature genetics* **28**, 371–5.

Waters, P. D., Wallis, M. C. and Marshall Graves, J. A. (2007). Mammalian sex--Origin and evolution of the Y chromosome and SRY. *Seminars in cell & developmental biology* **18**, 389–400.

Watson, J. D. and Crick, F. H. C. (1953). Molecular Structure of Nucleic Acids: A Structure for Deoxyribose Nucleic Acid. *Nature* **171**, 737–738.

Welshons, W. and Russell, L. (1959). The Y-chromosome as the bearer of male determining factors in the mouse. *Proceedings of the National Academy of Sciences of the United States of America* **45**, 560–566.

Westphal, V., Rizzoli, S. O., Lauterbach, M. A., Kamin, D., Jahn, R. and Hell, S. W. (2008). Video-rate far-field optical nanoscopy dissects synaptic vesicle movement. *Science* **320**, 246–9.

White, W. M., Willard, H. F., Van Dyke, D. L. and Wolff, D. J. (1998). The spreading of X inactivation into autosomal material of an x;autosome translocation: evidence for a difference between autosomal and X-chromosomal DNA. *American journal of human genetics* **63**, 20–8.

Wildanger, D., Medda, R., Kastrup, L. and Hell, S. W. (2009). A compact STED microscope providing 3D nanoscale resolution. *Journal of microscopy* **236**, 35–43.

Wilhelm, D. and Koopman, P. (2006). The makings of maleness: towards an integrated view of male sexual development. *Nature reviews. Genetics* **7**, 620–31.

Williams, R. R. E., Azuara, V., Perry, P., Sauer, S., Dvorkina, M., Jørgensen, H., Roix, J., McQueen, P., Misteli, T., Merkenschlager, M., et al. (2006). Neural induction promotes large-scale chromatin reorganisation of the Mash1 locus. *Journal of cell science* **119**, 132–40.

Wombacher, R., Heidbreder, M., Van de Linde, S., Sheetz, M. P., Heilemann, M., Cornish, V. W. and Sauer, M. (2010). Live-cell super-resolution imaging with trimethoprim conjugates. *Nature methods* **7**, 717–9.

Wutz, A. (2011). Gene silencing in X-chromosome inactivation: advances in understanding facultative heterochromatin formation. *Nature reviews. Genetics* **12**, 542–53.

Wutz, a and Jaenisch, R. (2000). A shift from reversible to irreversible X inactivation is triggered during ES cell differentiation. *Molecular cell* **5**, 695–705.

Wutz, A., Rasmussen, T. P. and Jaenisch, R. (2002). Chromosomal silencing and localization are mediated by different domains of Xist RNA. *Nature genetics* **30**, 167–74.

Xu, D., Jiang, T., Li, A., Hu, B., Feng, Z., Gong, H., Zeng, S. and Luo, Q. (2013). Fast optical sectioning obtained by structured illumination microscopy using a digital mirror device. *Journal of Biomedical Optics* **18**, 060503.

Yamada, N. a, Rector, L. S., Tsang, P., Carr, E., Scheffer, a, Sederberg, M. C., Aston, M. E., Ach, R. a, Tsalenko, a, Sampas, N., et al. (2011). Visualization of fine-scale genomic structure by oligonucleotide-based high-resolution FISH. *Cytogenetic and genome research* **132**, 248–54.

Yang, F., Babak, T., Shendure, J. and Disteche, C. M. (2010). Global survey of escape from X inactivation by RNA-sequencing in mouse. *Genome research* **20**, 614–22.

Yuan, W., Wu, T., Fu, H., Dai, C., Wu, H., Liu, N., Li, X., Xu, M., Zhang, Z., Niu, T., et al. (2012). Dense chromatin activates Polycomb repressive complex 2 to regulate H3 lysine 27 methylation. *Science* **337**, 971–5.

Zhang, Y., Brady, M. and Smith, S. (2001). Segmentation of brain MR images through a hidden Markov random field model and the expectation-maximization algorithm. *IEEE transactions on medical imaging* **20**, 45–57.

Zhao, J., Sun, B. K., Erwin, J. A., Song, J.-J. and Lee, J. T. (2008). Polycomb proteins targeted by a short repeat RNA to the mouse X chromosome. *Science* **322**, 750–6.

8 Acknowledgements

First, I'd like to thank **Heinrich Leonhardt** for being my Doktorvater, for providing me with an optimal working environment that was really second to none and for generously giving me the freedom to follow my own research interests.

I'd like to thank **Thomas Cremer** for being my Zweitgutachter and for the opportunity to conduct my PhD studies about such an interesting topic. Our emotional discussions about various models and your passion for science were a great inspiration. I really admire that besides all the energy you are spending on science you are never forgetting the people behind it, nor life in general.

Lothar, thank you very much for being my supervisor and for your patient help with all kinds of corrections. You always had an open ear for my problems and taught me the value of detailed work for good science. I'm especially thankful for your support and trust in offering me the opportunity to spend one exciting year in Oxford. Special thanks also to Andrea and Poldi for occasional wife-sitting and for providing me with your best Enzian and delicious dinners that I just had (!!!) to like, but surely helped me a lot to have a great time in England!

Marion, I cordially like to thank you for being the crucial person in making this thesis possible. I'd like to thank you for our endless discussions about work and life, for your patience, support and calmness in many turbulent situations, but also for staying focused on releasing the "bomb". It is unbelievable how you managed to handle the opinions and intentions of so many different people throughout the last years. Thank you very much for all you effort and a really enjoyable working environment.

Thank you, **Neil Brockdorff**, for helping me with my grant proposal and especially for your welcoming support in your lab in Oxford.

Ela **Yola**, thanks for bringing some Greek liveliness into this lazy German bunch (although I've learnt now that this is Yola-specific, not Greek-specific)! Thanks for all your help throughout the years and for being my informative connection to home.

Andreas, danke für unsere zahlreichen Squash-Matches, aus denen Du leider meist als Gewinner hervorgegangen bist (nur nicht beim nächsten Mal!), sowie für unsere Zeit als mikroskopische Weggefährten (et al.!).

Jürgen, danke für Deine stets kompetente, schnelle und zuverlässige Hilfe und vor allem danke, dass Du nie aufgegeben hast einem Biologen etwas über Migroschgobie beibringen zu wollen!

Thanks to all the excellent people that I had the chance to meet in Oxford. Especially **Andrea** for your countless help (thanks mate without you and your Napolitano tricks, life over there would have been much duller), **Anna** for the invitations to your College guest nights and **Justin** for your laid-back spirit, quiz nights, pub visits and enthusiasm.

Zuni, danke, dass ich Zeuge sein durfte als Du Dich mit „dem Zunhammer" in die Geschichtsbücher geschossen hast, der so trocken, ansatzlos und unvorhergesehen aus dem Nichts kam, wie sonst nur Dein Humor.

Jens, mein alter Roomy und Kickerbuddy, Deine Praktika, Übernachtungsgeschichten und diversen Perlen des Internets waren mir eine Freude, Deine Arbeitsweise ein Vorbild. Danke dafür!

Udo, danke für unsere zahlreichen emotionalen Diskussionen über Fußball (,von dem Du leider nichts verstehst), und dass Du meine Herzensangelegenheit, den Getränkedienst, so kompetent fortgeführt hast.

Katrin S., **Weihua**, **Wen** and **Nan**, thanks for being such great and entertaining roommates, for sharing my passion for Duplo stickers and for always creating a nice and friendly working atmosphere.

Danke an meine Bachelorettes **Veronika** und vor allem an **Susanne** für die immer nette Zusammenarbeit und für's Teilen der schönen Ergebnisse.

Fabio, thanks for all your competent and friendly help with the stem cells.

Volker, danke für die gute Zusammenarbeit und Deine Anstrengungen bei der Entwicklung der Datananalyse Tools.

Anja und **Susanne**, vielen Dank für Eure ungezählte Hilfe bei diversen Extrawürsten, und für Eure stets freundliche und offene Art, die eine Bereicherung für die gesamte Arbeitsgruppe war und ist.

Special thanks to all my past and present fellow PhD students in the Leonhardt and Cremer Labs, **Andrea B., Andrea R., Barbara, Bulti, Carina, Christine, Congdi, Danny, Garwin, Hilmar, Jens P., Jonas, Kamila, Katharina, Mengxi, Patrizia** and **Tobi**, and also to all the other people that I had the pleasure to work with in the last couple of years including **Boris, Frau Zhao, Heidi (!!), Irina, Kathrin Pflegbercht, Kourosh, Ola, Tina and Uli.** This includes all the numerous students, Bachelor(ette)s, Masters and Diploma students, which equally contributed to the always friendly working environment.

Ich möchte allen **Gutachtern** dieser Arbeit für Ihre Zeit und Ihren Aufwand danken.

Ich möchte mich herzlich bei meiner Mutter **Rosemarie**, meiner Schwester **Kathrin** und meiner **Oma**, sowie meiner ganzen Familie bedanken. Ohne Eure Unterstützung wäre diese Arbeit und vieles andere niemals möglich gewesen. Ein besonderer Dank geht auch an meine langjährigen Kumpels **Jojo** und **Schmiddi**, die erfolgreich verhindern, dass ich zu sehr in die Welt der Biologie abdrifte.

Von Herzen möchte ich mich bei meiner Frau **Palina** bedanken. Danke für Deine Unterstützung, Deine Geduld und Liebe, dafür dass wir immer zusammen lachen können, Du auch in schwierigen Zeiten immer für mich da warst und wir zusammen einfach mehr sind!

9 Publications

K. Laurence Jost, Sebastian Haase*, Daniel Smeets*, Nadine Schrode*, Jörn M. Schmiedel*, Bianca Bertulat, Hanspeter Herzel, Marion Cremer and M. Cristina Cardoso (2011). 3D-Image analysis platform monitoring relocation of pluripotency genes during reprogramming. *Nucleic Acids Research*, **39**, 17, e113

* *these authors contributed equally to this work*

Kajan Ratnakumar, Luis F. Duarte, Gary LeRoy*, Dan Hasson*, Daniel Smeets*, Chiara Vardabasso, Clemens Bönisch, Tianying Zeng, Bin Xiang, David Y. Zhang, Haitao Li, Xiawo Wang, Sandra B. Hake, Lothar Schermelleh, Benjamin A. Garcia, and Emily Bernstein (2012). ATRX-mediated chromatin association of histone variant macroH2A1 regulates alpha globin expression. *Genes and Development*, **26**, 433-8

* *these authors contributed equally to this work*

Yolanda Markaki*, Daniel Smeets*, Susanne Fiedler, Volker J. Schmid, Lothar Schermelleh, Thomas Cremer and Marion Cremer (2012). The potential of 3D-FISH and super-resolution structured illumination microscopy for studies of 3D nuclear architecture. *BioEssays*, **34**, 412-26

** both authors contributed equally to this work*

Yolanda Markaki, Daniel Smeets, Marion Cremer and Lothar Schermelleh (2013). Fluorescence *in situ* hybridization applications for super-resolution 3D structured illumination microscopy. *Nanoimaging: Methods and Protocols, Methods in Molecular Biology*, **950**, 43-64

Daniel Smeets, Jürgen Neumann and Lothar Schermelleh (2013a). Application of three-dimensional structured illumination microscopy in cell biology – pitfalls and practical considerations. *Neuromethods*, *in press.*

Daniel Smeets, Yolanda Markaki, Volker J. Schmid, Anna Tattermusch, Andrea Cerase, Michael Sterr, Jens Popken, Heinrich Leonhardt, Neil Brockdorff, Lothar Schermelleh, Thomas Cremer and Marion Cremer (2013b). Focal Xist RNA spreading in the X chromosome territory committed for inactivation is followed by a collapse of its active nuclear compartment. *PLOS Biology*, *submitted.*

Andrea Cerase, Daniel Smeets, Y. Amy Tang, Michal Gdula, Mikhail Spivakov, Marion Leleu, Benoit Moindroit, Anna Tattermusch, Justin Demmerle, Tatyana B. Nesterova, Catherine Green, Arie P. Otte, Lothar Schermelleh and Neil Brockdorff (2013). Spatial separation of Xist RNA and Polycomb proteins revealed by 3D-SIM. *PNAS*, *submitted.*

10 Eidesstattliche Erklärung

Ich versichere hiermit an Eides statt, dass die vorgelegte Dissertation von mir selbständig und ohne unerlaubte Hilfe angefertigt wurde.

München, den 16.07.2013

Daniel Smeets

Erklärung über frühere Promotionsversuche

Hiermit erkläre ich, dass diese Dissertation nicht ganz oder in wesentlichen Teilen einer anderen Prüfungskommission vorgelegt worden ist, und dass ich vor dieser Arbeit keine anderen Promotionsversuche unternommen habe.

München, den 16.07.2013

Daniel Smeets